The University of Hong Kong
Faculty of Engineering
Department of Mechanical Engineering

High-performance Tele-operated Robot Systems for Intra-operative MRI-guided Interventions

Dong Ziyang

August 2020

A thesis submitted in partial fulfilment of the requirements of
the Degree of Doctor of Philosophy
at The University of Hong Kong

Abstract of thesis entitled

"High-performance Tele-operated Robot Systems for Intra-operative MRI-guided Interventions"

Submitted by

Ziyang Dong

for the degree of Doctor of Philosophy
at The University of Hong Kong
in August 2020

Magnetic resonance imaging (MRI)-guided intervention has drawn increasing attention over the last decade. It is accredited to the capabilities in providing non-invasive and high-contrast images of soft tissues without harmful ionizing radiation, and also in monitoring the temperature change in thermal therapy procedures. These advantages prompted the adoption of MRI guidance for interventions ranging from biopsy, thermal therapy for tumor ablation, drug delivery to catheter-based procedures within cardiovascular system. However, the inherent working principle of MRI involves high-intensity magnetic and radiofrequency (RF) fields, which prevents the adoption of robotic systems containing ferromagnetic materials. Besides, precisely manipulating the instrument within the limited workspace of MRI bore remains challenging. This gives rise to the demand for precise tele-manipulation of interventional instruments under MRI guidance.

The major focus of this thesis is to develop high-performance systems regarding robotic tele-operation for intra-operative (intra-op) MRI-guided interventions. Key robotic components are investigated, including the high-fidelity magnetic resonance (MR) safe actuation, dexterous and compact robotic mechanism, and the real-time sensing and feedback control under MRI. MR safe high-performance hydraulic motors using diaphragm-sealed cylinders are proposed as the essential component for robotic actuation. The motor can provide tele-operated, dexterous control of interventional tools under MRI. The configurable motor designs are capable of generating unlimited range of continuous bidirectional rotation with high payload. With incorporation of the proposed MR safe

motors, a robotic platform is developed for bilateral stereotactic neurosurgery under intra-op MRI guidance. The compact robotic structure can enable less invasive anchorage and the accommodation inside the MR imaging head coil with a limited workspace. The simplified workflow has been validated by a pre-clinical trial under MRI. Furthermore, an MR safe robotic manipulator is developed for intracardiac catheterization, with incorporation of the proposed MR safe motors to provide dexterous manipulation of the cardiac catheter. The robot can offer functional manipulation towards cardiac electrophysiology (EP) under MRI, which is the first of its kind. A shape tracking system is proposed for the standard cardiac catheter, integrating the tracking coils and a multi-core optical fiber with fiber Bragg gratings (FBGs). Both shape and positional tracking of the bendable section could be realized. To achieve accurate and effective feedback control of the cardiac catheter, a learning-based modeling method using the shape information from FBGs is proposed, which is implemented for autonomous robotic control. The overall performance of the shape tracking and controller was demonstrated by a simulated pulmonary vein isolation (PVI) task with *ex-vivo* tissue ablation.

(Word count: 405 words)

Declaration

I declare that this thesis represents my own work, except where due acknowledgment is made, and that it has not been previously included in a thesis, dissertation or report submitted to this University or to any other institution for a degree, diploma or other qualifications.

Signed _____

Dong Ziyang

Dedication

To my parents
who have given solid support
to my journey of study

To my wife
who is always considerate and tolerant
and encouraging me to believe in myself

To my friends
who have accompanied and helped me
to maintain an optimistic attitude during the hardest period

Acknowledgements

I would like to express my sincere gratitude to my supervisor Dr. Ka-Wai Kwok, who has brought me into the field of surgical robotics and guided me with the highest standard. I have been inspired a lot by his expertise and perspectives during my study. His research passion and exploring spirit are always motivating me towards being excellent.

I am also grateful to Dr. Danny Tat Ming Chan, Dr. Alex Pui-Wai Lee and Dr. Hing-Chiu Chang, who have provided indispensable advice and assistance form clinical aspect.

I would like to thank Dr. Kit-Hang Lee and Dr. Ziyan Guo, who offered great support in my Ph.D. study. Your guidance and patience have benefited me a lot, particularly during my early Ph.D. study period when I was a freshman in research.

I am indebted to all the teammates in the research group who gave aid to my study. It is enjoyable to work with you all for discussion, conducting experiment, and even preparing manuscript before deadline. I would like to thank Xiaomei Wang, Ge Fang, Kui Wang, Zhuoliang He, Justin Di-Lang Ho, Hin Choi Fu, Wai Lun Tang, Chimlee Cheung and Martin Leong. Without your generous assistance I could not make such achievement.

Lastly but most importantly, I wish to thank my parents and wife for the unlimited support to my Ph.D. study.

Contents

List of Figures

List of Tables

Nomenclature

Acronyms

3D	Three-dimensional
AC-PC	Anterior commissure-posterior commissure
ASTM	American Society for Testing and Materials
AV	Atrioventricular
CC	Constant curvature
CSF	Cerebrospinal fluid
CT	Computed tomography
D-H	Denavit–Hartenberg
DBS	Deep brain stimulation
DC	Direct current
DICOM	Digital Imaging and Communications in Medicine
DoF(s)	Degree(s) of freedom
EA	Electroanatomic
EAM	Electroanatomic mapping
ECG	Electrocardiogram
EM	Electromagnetic
EP	Electrophysiology
FBG	Fiber Bragg grating
FDA	Food and Drug Administration
FFE	Fast field echo
FSPGR	Fast spoiled gradient recalled-echo
GUI	Graphic user interface
HCC	Hepatocellular carcinoma

HIFU	High-intensity focused ultrasound
Intra-op	Intra-operative
LA	Left atrial/atrium
LV	Left ventricle
MCP	Mid-commissural point
MER	Microelectrode recording
MR	Magnetic resonance
MRI	Magnetic resonance imaging
OFDR	Optical frequency domain reflectometry
PA	Polycaprolactam
PCC	Piecewise constant curvature
PD	Parkinson's disease
PE	Polyethylene
PEEK	Polyetheretherketone
PID	Proportional–integral–derivative
Pre-op	Pre-operative
PTFE	Polytetrafluoroethylene
PU	Polyurethane
PVC	Polyvinyl Chloride
PVI	Pulmonary vein isolation
RCM	Remote center of motion
RF	Radiofrequency
SA	Sinus
SNR	Signal-to-noise ratio
STN	Subthalamic nucleus
TSE	Turbo spin echo
VT	Ventricular tachycardia
w.r.t.	with respect to
WDM	Wavelength division multiplexing

Chapter 1

Introduction

1.1 Motivation and objectives

Magnetic resonance imaging (MRI) is a medical imaging technology. Compared to other imaging modalities (ultrasound or X-ray), MRI has demonstrated its unique and superior advantages for interventional applications: i) non-invasive imaging without harmful ionizing radiation; ii) high-contrast imaging of soft tissues; iii) intra-operative (intra-op) monitoring of pathological and physiological changes; iv) three-dimensional (3D) localization in real-time; v) monitoring of temperature variation during thermal therapy procedures. However, precise manipulation of surgical instruments for minimally invasive surgeries still remains challenging, particularly for operations in confined space under dynamic disturbance. To this end, tele-operated robotic systems have been investigated to assist the procedures, demonstrating improved surgical outcomes. However, the operation of MRI involves high-intensity magnetic and radiofrequency (RF) fields, which prevents the application of robotic systems containing ferromagnetic materials. Besides, there are still lots of technical challenges related to the application, such as undesired patient movement, confined workspace inside imaging coils, and real-time tracking and control of instruments under MRI. For MRI-guided robot-assisted interventions, it poses a strong need for compact and high-performance robotic systems to offer dexterous instrument manipulation and precise motion control.

To tackle these unmet technical challenges towards robot-assisted interventions guided by intra-operative (intra-op) MRI, I have mainly devoted efforts to the development of magnetic resonance (MR) safe high-performance actuation, dexterous robotic mechanism

with compact size, and the real-time sensing and feedback control under MRI. The major objectives of this thesis involve:

1. To design MR safe hydraulic actuators for robotic tele-operation of MRI-guided interventions, particularly for the procedures requiring precise and dexterous instrument manipulation;
2. To develop compact robotic manipulators for MRI-guided needle placement procedures, including stereotactic neurosurgery and percutaneous interventions;
3. To propose a tele-operated robotic catheter system for cardiac electrophysiology (EP) procedure under MRI guidance, which can provide high-dexterity and fast-response manipulation of cardiac catheter.
4. To validate the control performance using a model-free method based on the robotic catheter system;
5. To investigate the shape tracking and feedback control technologies for cardiac catheters. Multi-core optical fiber with fiber Bragg grating (FBG) and learning-based modeling method are involved.

1.2 Structure and contributions of thesis

Chapter 2 presents a review of the current status regarding intra-op MRI-guided robot-assisted interventions. The recent advances of intra-op MRI systems and corresponding technologies are reviewed. The MRI safety classification is introduced, serving as the fundamental standard for the development of MRI-guide robotic devices. The prior arts of MRI-guided robotic systems are reviewed, focusing on neurosurgery, percutaneous interventions, and intra-cardiovascular interventions. The trends and perspectives regarding tele-operated robotic system, MR safe/conditional actuation, real-time sensing in MRI, and high-performance control interface are presented. They are the major areas that this thesis will address.

Chapter 3 presents an MR safe hydraulic motors for robotic tele-operation of MRI-guided interventions. The hydraulic motors can offer high-fidelity and dexterous manipulation of interventional tools under MRI. The configurable MR safe motor designs are capable of offering continuous bidirectional rotation with unlimited range.

These capabilities would be comparable to the conventional electric motor for versatile applications even involving high-payload manipulation. Kinematics and dynamics models of the hydraulic motor have been studied, which can facilitate the overall design optimization and position/torque control. Motor performance, such as step response, frequency response, and accuracy, has been experimentally evaluated. The proposed hydraulic motors have been incorporated into the tele-operated robotic systems in **Chapter 4** and **Chapter 5**.

Chapter 4 introduces fluid-driven needle placement robots for MRI-guided interventions. An intra-op MRI-guided robot for bilateral stereotactic procedures is developed. Its compact design can enable robot operation within the constrained space of MRI head coil. A simulated needle insertion task of deep brain stimulation (DBS) has demonstrated an average targeting accuracy of $\leq$1.73 mm assisted by the robot. The system also incorporated MR-based wireless tracking markers, which can offer real-time 3D instrument localization with a frequency of 30-40 Hz. Moreover, to explore a more compact and flexible robot design, another prototype for percutaneous needle placement has been proposed. The compact and lightweight design can enable the direct fixture of robot on the patient body and needle targeting at multiple locations with several robots. The instrument manipulation can be conducted in an interactive way, with coarse placement made by the surgeon and fine adjustment by fluid-driven actuators. Visual feedback with light indicator can be provided during manual operation for clear and interactive operation.

Chapter 5 presents a robotic manipulator to realize robot-assisted intra-cardiac catheterization in MRI environment. It is designed particularly for cardiac EP procedure, which is an effective treatment of arrhythmia. It is the first MR safe robot for intra-cardiac EP intervention. The robot incorporated the MR safe, high-performance hydraulic actuators, which demonstrated a promising ability to tele-manipulate a cardiac EP catheter. A human-robot control interface is also presented to improve the tele-operation effectiveness. Experiments were conducted with simulated navigation and pulmonary vein isolation (PVI) tasks to validate the effectiveness for surgical operation.

Chapter 6 introduces the kinematics modeling, shape tracking and feedback control of cardiac catheter based on the robotic platform. Kinematics modeling methods, including model-free and model-based control approaches, have been applied to the robot for quantitative comparison and evaluation. A shape tracking system is also proposed, integrating a multi-core FBG fiber and tracking coils with a standard cardiac catheter. Both

shape and positional tracking of the bendable section can be achieved. A learning-based modeling method has been developed for cardiac catheters. The modeling method can use FBG-reconstructed 3D curvatures to initialize the model and update the motion mapping. Feedback control of the cardiac catheter can be realized by implementing the proposed modeling method on the MRI-guided robotic platform. The overall performance of the proposed shape tracking and feedback control approaches was demonstrated by a simulated PVI task with *ex-vivo* tissue ablation.

The main contributions of the thesis are summarized as:

1. Development of MR safe hydraulic motors for robotic tele-operation of MRI-guided interventions. The hydraulic motors can provide high-fidelity, dexterous control of interventional tools under MRI. The configurable MR safe motor designs are capable of providing unlimited range of continuous bidirectional rotation.

2. Development of a tele-operated manipulator for bilateral stereotactic neurosurgery under intra-op MRI guidance. The robotic manipulator features light-weight (145.4 g) and compact ($110.6 \times 206.8 \times 33.2$ mm^3), which can be operated inside an MR imaging head coil with limited workspace. High-performance hydraulic motors are adopted to offer MR safe actuation with minimal imaging artifacts;

3. Design of a patient-mounted robotic device for MRI-guided percutaneous procedures. The robot can provide semi-automated and interactive needle manipulation. The light-weight (189 g) and compact ($\varnothing$108 mm$\times$115 mm height) features can enable the setup of several robots for needle targeting at multiple locations.

4. Development of an MR safe robotic manipulator for intracardiac catheterization. High-performance hydraulic motors have been incorporated to provide dexterous manipulation of cardiac catheter. A robot control interface is also developed to assist the tele-operation. Experimental evaluations were conducted to validate its effectiveness.

5. Experimental validation of model-based and model-free control approaches for tele-operation of the robotic catheter platform. The model-free and model-based control approaches were implemented on the MR safe robotic catheter platform. A simulated ablation task was conducted by ten subjects for quantitative evaluation and comparison of the control approaches.

6. Development of shape tracking and feedback control methods for the flexible cardiac catheter under MRI guidance. Multi-core FBG fiber and tracking coils were integrated with a standard cardiac catheter to achieve both shape and positional tracking of the bendable section. A learning-based modeling approach is proposed for cardiac catheters, which can utilize 3D curvatures obtained from FBG fiber to initialize the model and update the motion mapping. The proposed modeling method has been implemented on an MRI-guided robotic catheter platform for feedback control.

1.3 Publications, patents and awards during Ph.D. study

Journals:

1) Z. Dong, X. Wang, J. D.L. Ho, Z. He, G. Fang, W. L. Tang, A. P.W. Lee, and K.W. Kwok, "*Shape tracking and feedback control of cardiac catheter using MRI-guided robotic platform*," **IEEE Transactions on Robotics** (under review).

2) Z. Dong, Z. Guo, K.H. Lee, G. Fang, W. L. Tang, H.C. Chang, D. T. M. Chan, and K.W. Kwok, "*High-performance continuous hydraulic motor for MR safe robotic teleoperation*," **IEEE Robotics and Automation Letters**, vol. 4, no. 2, pp. 1964–1971, 2019.

3) Z. He, Z. Dong, G. Fang, J.D.L. Ho, C.L. Cheung, H.C. Chang, C.N. Chong, Y.K. Chan, T.M. Chan, K.W. Kwok, "*Design of a Percutaneous MRI-guided Needle Robot with Soft Fluid-driven Actuator*," **IEEE Robotics and Automation Letters**, vol. 5, no. 2, pp. 2100-2107, 2020.

4) Z. Guo, Z. Dong, K.-H. Lee, C. L. Cheung, H.C. Fu, J. D. Ho, H. He, W.-S. Poon, D. T.M. Chan, and K.W. Kwok, "*Compact design of a hydraulic driving robot for intraoperative MRI-guided bilateral stereotactic neurosurgery*," **IEEE Robotics and Automation Letters**, vol. 3, no. 3, pp. 2515–2522, 2018.

5) Y. Feng, Z. Guo, Z. Dong, X.Y. Zhou, K.W. Kwok, S. Ernst, and S.L. Lee, "*An efficient cardiac mapping strategy for radiofrequency catheter ablation with active learning*," **International journal of computer assisted radiology and surgery**, vol. 12, no. 7, pp. 1199–1207, 2017.

6) K.H. Lee, K.C.D. Fu, Z. Guo, Z. Dong, M.C. Leong, C.L. Cheung, A. P.W. Lee, W. Luk, and K.W. Kwok, "*MR safe robotic manipulator for MRI-guided intracardiac*

catheterization," **IEEE/ASME Transactions on Mechatronics**, vol. 23, no. 2, pp. 586-595, 2018.

7) X. Wang, K.H. Lee, D. K. Fu, Z. Dong, K. Wang, G. Fang, S.L. Lee, A. P. Lee, and K.-W. Kwok, "*Experimental validation of robot-assisted cardiovascular catheterization: model-based versus model-free control*," **International journal of computer assisted radiology and surgery**, vol. 13, no. 6, pp. 797–804, 2018.

Peer-reviewed international conference proceeding:

1) C.L. Cheung, K.H. Lee, Z. Guo, Z. Dong, M.C.W. Leong, Y. Chen, A.P.W. Lee, K.W. Kwok., "*Kinematic-model-free positional control for robot-assisted cardiac catheterization*," in **Proceedings of the Hamlyn symposium on medical robotics**, pp. 80–81, 2016.

Patents:

1) Z. Dong, K.W. Kwok, Z. Guo, K.H. Lee, "*Fluid Powered Transmission for MRI-guided Interventions*", **US Provisional Patent**: US 62/640,302 [Filed on 8 Mar, 2018]; **PCT Patent**: PCT/IB2019/051877 [Filed on Mar 8, 2019].

2) Z. Guo, K.W. Kwok, Z. Dong, K.H. Lee, H.C. Fu, C.L. Cheung, "*Robotic Stereotactic System for MRI-guided Neurosurgery*", **US Provisional Patent**: US 62/623,280 [Filed on 29 Jan, 2018]; **PCT Patent**: PCT/CN2019/072961 [Filed on Jan 24, 2019].

3) K.W. Kwok, Z. Dong, Z. Guo, K.C.D. Fu, K.H. Lee, and C.L. Cheung, "*Robotic catheter system for MRI-guided cardiovascular interventions*," **US Non-Provisional Patent**: US 15/630,406 [pending]; **US Provisional Patent**: US 15/630,406 [Filed on Jun 24, 2016]; **PCT Patent**: PCT/CN2017/089701 [Filed on Jun 23, 2017]; **Licensed to APTUS Therapeutics Limited**.

International awards:

1) May 2019, Montreal, Canada
   Best Workshop Paper Award (Second Place) (*Sponsored by Intuitive Surgical Inc.*)
   In the 2019 IEEE International Conference on Robotics and Automation (**ICRA'19**), workshop on surgical robotics (Open Challenges and State-of-the-Art in Control System Design and Technology Development for Surgical Robotic Systems).

Workshop paper: Z. Dong, X. Wang, J. D.L. Ho, Z. He, G. Fang, W. L. Tang, A. P.W. Lee and K.W. Kwok, "*Experimental validation of autonomous motion control with standard cardiac electrophysiology catheter*."

2) May 2018, Brisbane, Australia

Best Conference Paper Award, and **Finalist of Best Medical Robotics Paper Award** (*Sponsored by Intuitive Surgical Inc.*)

In 2018 IEEE International Conference on Robotics and Automation (**ICRA'18**).

Presented paper: Z. Guo, Z. Dong, K.-H. Lee, C. L. Cheung, H.C. Fu, J. D. Ho, H. He, W.-S. Poon, D. T.M. Chan, and K.W. Kwok, "*Compact design of a hydraulic driving robot for intraoperative MRI-guided bilateral stereotactic neurosurgery*," **IEEE Robotics and Automation Letters**, vol. 3, no. 3, pp. 2515–2522, 2018.

3) June 2017, Singapore

Merit Poster Award (*Sponsored by Intuitive Surgical Inc.*)

In 2017 IEEE International Conference on Robotics and Automation (**ICRA'17**), workshop on surgical robotics (C4 Surgical Robots: Compliant, Continuum, Cognitive, and Collaborative)

Workshop paper: Z. Dong, Z. Guo, D. K.C. Fu, K.H. Lee, M. C.W. Leong, C.L. Cheung, A. P.W. Lee, W. Luk, K.W. Kwok, "*A robotic catheter system for MRI-guided cardiac electrophysiological intervention*."

4) June 2016, London, UK

Best Live Demonstration in Surgical Robot Challenge 2016

Team member: Z. Dong, Z. Guo, K.H. Lee, C.L. Cheung, M. C.W. Leong, D. K.C. Fu, J. P.T. Chan, A. P.W. Lee, K.W. Kwok

Project title: MR-conditional Catheter Robot for MRI-guided Cardiac Electrophysiological Intervention

Chapter 2

Robot-assisted Interventions under MRI Guidance

2.1 Introduction

Magnetic resonance imaging (MRI) is well-known for its superior capabilities in providing high-contrast and non-invasive images of soft tissues without harmful ionizing radiation, and also in monitoring the temperature changes during thermal therapy procedures [53]. These advantages have prompted the adoption of MRI guidance for interventions ranging from biopsy [54], thermal therapy for tumor ablation [55, 56], drug delivery [57, 58] to catheter-based procedures within cardiovascular system [59, 60].

However, high-intensity magnetic and radiofrequency (RF) fields generated by MRI scanner prevents the application of robotic systems containing ferromagnetic materials. Besides, precisely manipulating the instrument within the limited workspace of MRI bore also remains challenging. In an attempt to tackle these difficulties, a number of researches [61–64] have focused on developing tele-operated robotic platforms for interventions, demonstrating enhanced accuracy and reduced procedural time under intra-operative (intra-op) MRI guidance. The recent development of techniques for magnetic resonance (MR) safe/conditional robotics has shown great potential in MRI-guided robot-assisted interventions. MR safe/conditional actuators have been developed, enabling tele-operated robotic manipulation to optimize the surgical workflow. MR-based tracking system can achieve real-time positional localization for various robotic instruments, allowing feedback control of devices under MRI guidance.

In this chapter, the advances of intra-op MRI technology and recent development of MRI-guided robotic platforms are reviewed. The clinical motivations for tele-operated robotic systems are summarized, together with technical challenges towards a safe and effective robotic system for MRI-guided interventions. The research background of the thesis is presented in this chapter.

2.2 Intra-operative MRI technology

2.2.1 Recent advances of MRI

MRI is an imaging technology for medical applications ranging from diagnosis, disease detection, to treatment monitoring. It was firstly invented in 1970s and then went through a tremendous development over the following years. The first commercial MRI system appeared in 1980s. After that, the technique of MRI rapidly evolved over the last three decades and has become the routine diagnostic procedure [65]. Till 1996, more than ten thousand MRI scanners have been installed in the world [66]. Around 100 million MRI exams were estimated to be taken in each year, with the global quantity of operational MRI scanners at over thirty thousand [53]. Nowadays, MRI has become one of the most versatile modalities in radiology, occupying a large proportion of radiological examinations.

The fundamental MRI working principle is to excite and detect the spins of hydrogen atoms, which makes up 70% to 90% of the most tissues in human body [66]. These atom spins can be excited by strong fluctuating magnetic fields generated by the MRI machine. MRI scanner's computer can then process these signals of spin changes and reconstruct tissue images. Since the amount and status of water can have dramatic differences in various tissues, organs and tissues with different properties can be clearly distinguished in the images obtained by MRI. It makes MRI a very sensitive imaging modality for diagnosis.

Compared to other imaging modalities commonly used for diagnosis and pre-operative planning, such as X-ray or ultrasound, MRI has been proven to have many unique and superior advantages. It can provide non-invasive three-dimensional (3D) scanning with zero ionizing radiation to neither patient nor radiologist/surgeon, which is particularly beneficial to procedures requiring frequent scanning. MRI can offer high-contrast imaging of soft tissue (**Fig. 2.1a**) to visualize the morphology and anatomical structures, enabling characterization of the pathological and normal tissue. Intra-op MRI can even provide

a great variety of physiologic information, such as water diffusion, blood flow, tissue deformation and ablation progress (**Fig. 2.1b**). For instance, the physiological change of tissue originated by complete or insufficient ablation/cutting can be readily visualized in real-time by T2/diffusion-weighted MRI [67]. Functional MRI has also been invented to observe activities and functions in the brain, which is achieved by measuring hemodynamics in different regions [68]. In addition, MRI can provide precise and real-time temperature monitoring ($<1°C$), namely MR thermometry, during thermal therapy procedures [3] to monitor the heat generation and diffusion to tissues (**Fig. 2.1c**).

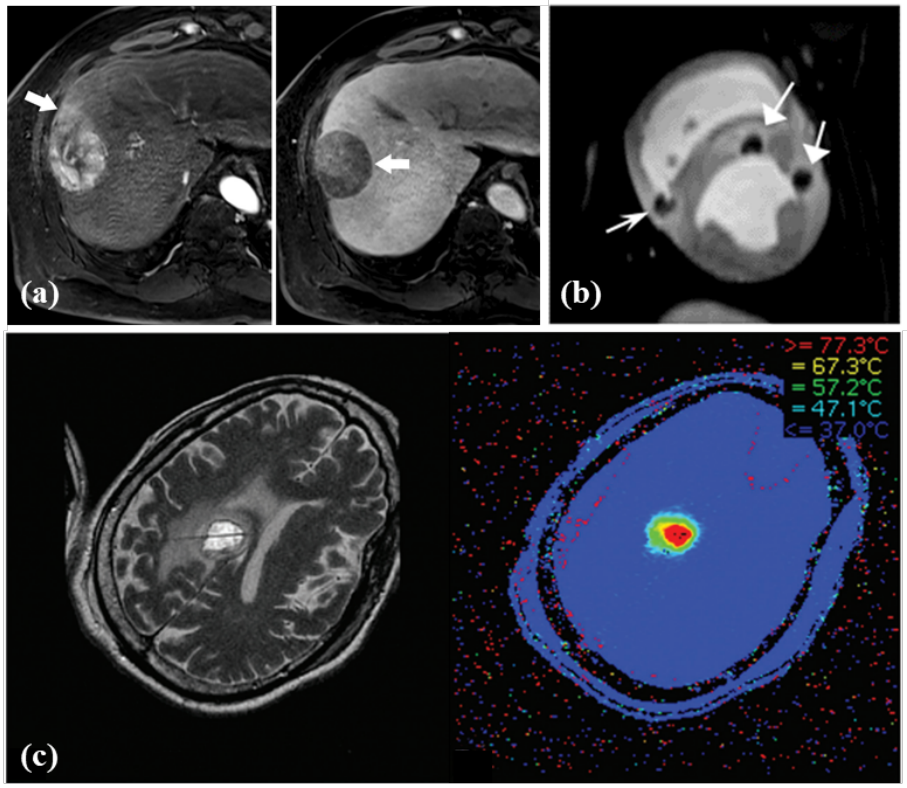

Fig. 2.1: (a) Magnetic resonance (MR) image showing the cardiac structure and lesions created by radiofrequency (RF) ablation; **(b)** T1-weighted MR images showing the hepatobiliary carcinoma; **(c)** T2 image of brain (left) and heat map during ablation (right) through MR thermometry. **Image Source**: [1–3]

2.2.2 Setup of MRI systems for intra-operative operation

To bring the MRI advantages into surgical applications, a variety of interventional or intra-op MRI systems have been developed and commercialized. Among the various designs, both low-field [69] and high-field MRI scanners [70] can be adopted. The low-field scanners generally involve open magnets with field strength varying from 0.2T to 1T. The low-field scanners equip with smaller magnets than high-field ones, hence reducing scanner size. Because of the lower field strength, the MRI room for low-field scanner has lower

standard on the electromagnetic (EM) shielding. It is feasible to build the open-magnet scanner, offering larger space for patients access for direct interventional procedures [71]. **Fig. 2.2a** shows a typical low-field MRI scanner, Signa SP system (GE Medical Systems, Milwaukee, Wisc., USA), developed by GE Healthcare. It adopts a "double-donut" magnet configuration for the 0.5T scanner. Patients can be accessed from the side and top, giving great convenience to surgical operations. It can also eliminate the need to transfer either patients or facilities. A variety of low-field systems were also commercialized, such as Polestar (Medtronic) (**Fig. 2.2b**) [72], Panorama (Philips Medical Systems MR Technologies, Vantaa, Finland) (**Fig. 2.2c**), and Magnetom (Siemens, Erlangen, Germany) (**Fig. 2.2d**). These low-field systems generally feature convenient patient access and flexible arrangement and installation, facilitating a faster surgical workflow. However, the imaging quality is greatly sacrificed in low-field scanners, which is the major drawback and limits the wide application.

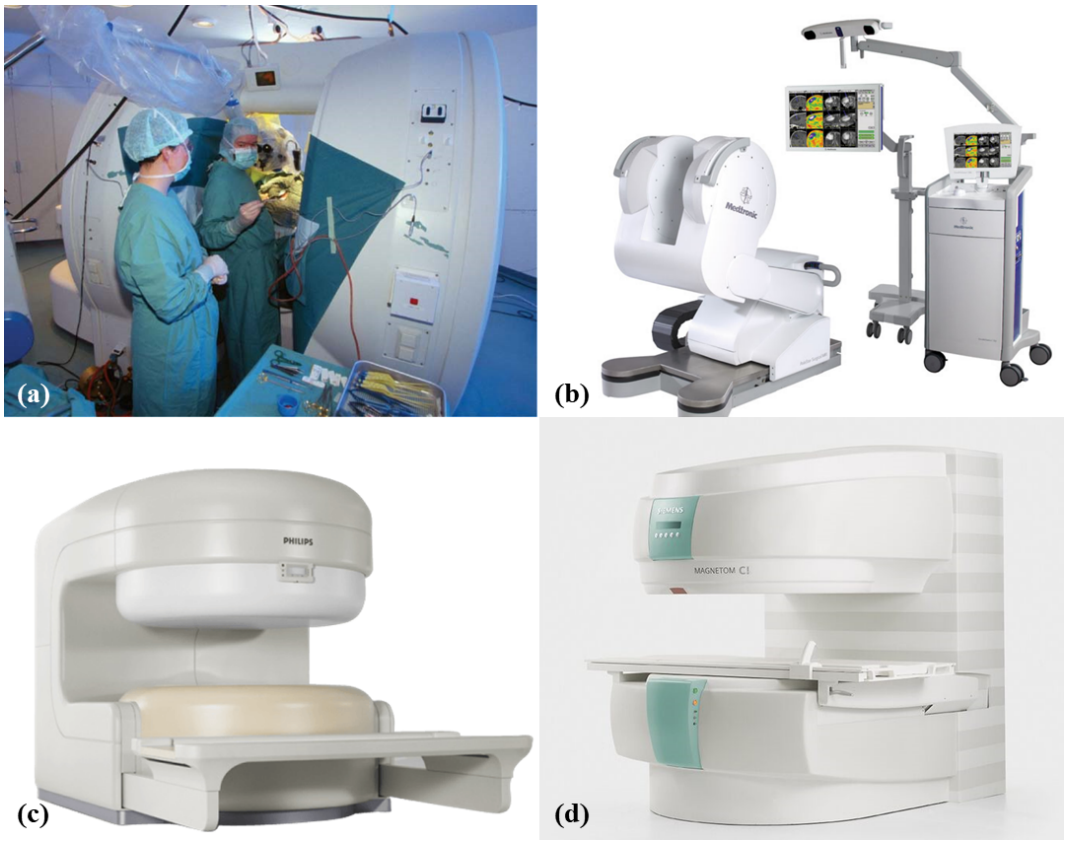

Fig. 2.2: **(a)** Signa SP system from GE Healthcare. Clinician can access the patient at the gap between the two magnets, even during MRI acquisition; **(b)** Polestar system from Medtronic. The system is optimized for cranial surgery by incorporating two smaller magnets; **(c)** Panorama interventional magnetic resonance imaging (MRI) system from Philips; **(d)** Magnetom system from Siemens. **Image Source**: [4–7].

In general, high-field scanners involve closed-bore scanners with a higher magnetic field ranging from 1.5T to 3T, which can offer higher imaging resolution and faster imaging speed. The intra-op MRI system from IMRIS Inc., Winnipeg, Canada (**Fig. 2.3a**) [73–75] is an example. This system requires two rooms to travel the magnet, while the patient is staying in the same position for operations (**Fig. 2.3b**). The system can provide the same imaging quality compared to fixed-magnet systems. Because the operating room is also used for imaging, it needs to be RF-shielded to ensure safety and prevent EM interference. Since high-field scanners involve closed MRI bore, surgeons could not access the patient in the bore during scanning. Therefore, surgical operation is generally performed after transferring the patient outside the bore. It is very labor-intensive and time-consuming for this transition between surgery and imaging mode for the high-field scanner systems.

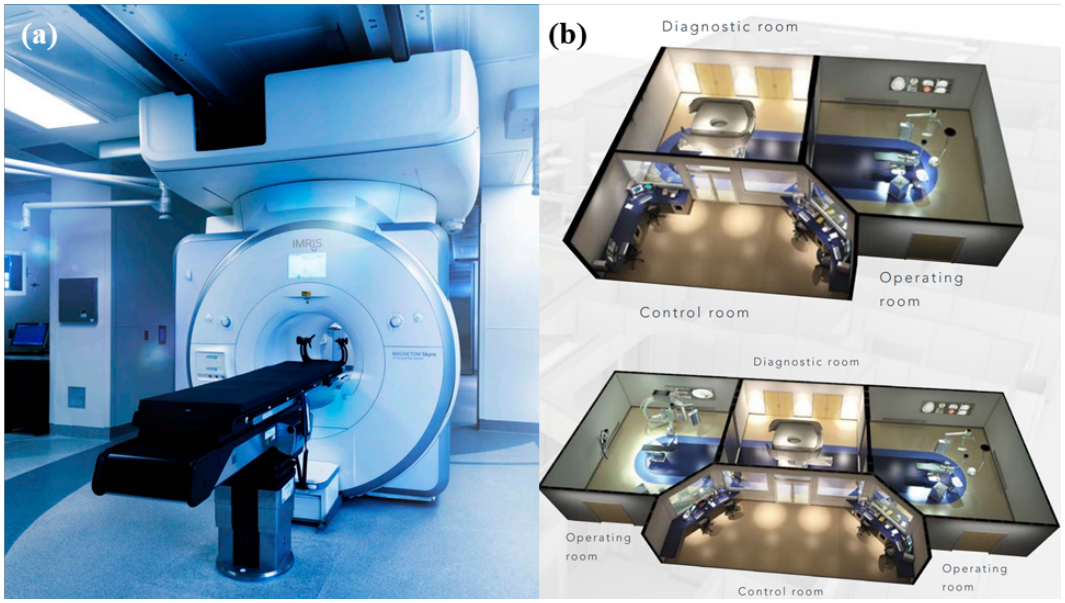

Fig. 2.3: (a) Operating suite from IMRIS Inc. with dual-room configuration. The patient table is fixed on the ground. The MRI scanner is mounted on the ceiling track and can be traveled between the two rooms; **(b)** Two types of room arrangement for the interventional MRI system from IMRIS Inc. Each contains three types of room: operating room, diagnostic room, and control room. **Image Source**: [8].

2.2.3 MRI safety classification

In order to excite and detect the tiny changes of hydrogen atoms spins for imaging, MRI scanner will generate high-intensity static magnetic field, rapidly switched magnetic fields (gradient filed), as well as pulsed RF field. These strong magnetic and RF fields would cause potential hazards (force and torque) for devices containing metallic components (**Fig. 2.4a**). Heating may also be induced in electrical cables by the fluctuating magnetic fields and RF pulses. In terms of imaging quality, implants or devices made of non-MR-safe materials

would cause image artifact by disrupting the magnetic field homogeneity (**Fig. 2.4b**). Although a certain level of artifact is acceptable in diagnosis, it may produce severe distortion in the navigation or targeting in MRI-guided interventions. To deal with the safety issue of medical devices in the MR environment, relevant standards have been published by American Society for Testing and Materials (ASTM) with the adoption of current MR safety terminology. A clear classification has been list in ASTM-2503 [76] (**Table 2.1**) about the MR safety.

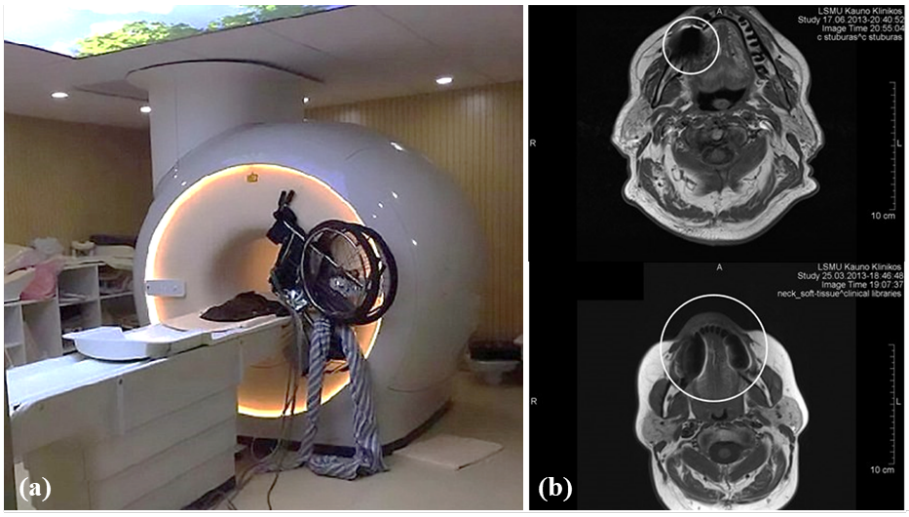

Fig. 2.4: **(a)** Safety hazard caused by strong magnet field of MRI. A wheelchair was attracted by the magnet field to hit the MRI bore; **(b)** MRI axial projections showing artifacts triggered by metallic devices (marked by circles). **Image Source**: [9, 10].

Table 2.1: MR safety classification in ASTM F2503-13 standard

Label	Term	Description
MR MR MR Safe MR Safe	MR Safe	An item that poses no known hazards resulting from exposure to any MR environment. MR Safe items are composed of materials that are electrically nonconductive, nonmetallic, and nonmagnetic.
MR MR Conditional	MR Conditional	An item with demonstrated safety in the MR environment within defined conditions. At a minimum, address the conditions of the static magnetic field, the switched gradient magnetic field and the radiofrequency fields. Additional conditions, including specific configurations of the item, may be required.
MR MR Unsafe	MR Unsafe	An item which poses unacceptable risks to the patient, medical staff or other persons within the MR environment.

In order to develop devices and systems for application in MRI, materials should follow this standard to ensure MR safety. In general, EM motors and metallic structures that are commonly used in conventional robotic systems cannot be adopted for MRI-guided interventions. The development of MR safe/conditional robotic systems requires additional efforts to achieve a functional, effective and safe design. In the next section, the recent development of MRI-guided robotic systems is summarized.

2.3 Recent development of MRI-guided robotic systems

Robotic systems were firstly adopted for medical applications in 1980s, and have made great influence on varieties of medical disciplines, including neurosurgery, orthopedic surgery, and general surgery [77–80]. Recently, researchers have developed various robotic platforms for MRI-guided interventions in an attempt to solve the technical challenges related to MRI. It is expected that robotic systems will play a more significant role in the future [81]. The prior arts of MRI-guided robotic systems for interventions are reviewed in this section. Backgrounds of surgical requirements and the recent development of corresponding robotic systems are introduced for the three surgical applications: stereotactic neurosurgery, percutaneous interventions, and intra-cardiovascular interventions.

2.3.1 Stereotactic neurosurgery

Stereotaxy is a method to localize surgical targets with the reference of an external coordinate system. In functional neurosurgery, this technique has been adopted to treat a variety of movement disorders (e.g. dystonia and Parkinson's disease (PD)), psychiatric abnormalities and epilepsy. Among these applications, PD is the second prevalent disease of the nervous system following Alzheimer's disease. The number of affected people is expected to reach 8.7 million worldwide by 2030 [82]. Deep brain stimulation (DBS) is one of the standard stereotactic procedures, providing treatment to debilitate motor symptoms of PD and dystonia. Two DBS needles with long (e.g. 300 mm) and slender ($\approx \varnothing 1.3$ mm) structure can be individually orientated by a stereotactic frame (**Fig. 2.5a**) and inserted into the patient's skull through burr holes ($\leq \varnothing 14$ mm). After reaching the deep brain areas of interest, stimulation electrodes attached on the needle will be implanted to deliver scheduled electrical impulses.

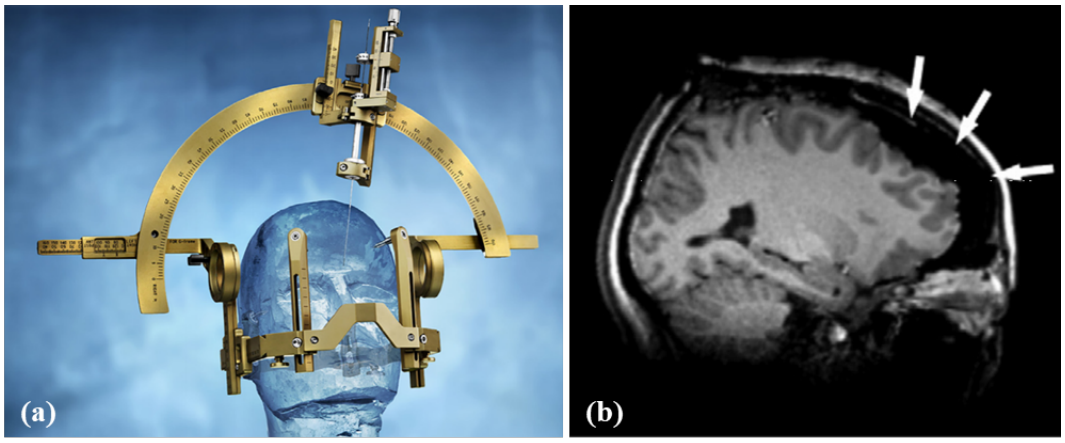

Fig. 2.5: (a) Head frame for stereotactic neurosurgery; **(b)** MR images showing brain shift caused by craniotomy. The brain deformation is marked by white arrows. **Image Source**: [11, 12].

Although physicians have established the standard workflow of stereotactic neurosurgery for more than half a century, the surgical operation is still challenging due to the complex workflow and high requirement of targeting accuracy. For example, an average error of 2-3 mm was just bearable for the needle targeting according to the records [83]. Besides, the deformation of intracranial contents occurs inevitably after craniotomy, namely "brain shift" (**Fig. 2.5b**), which would further increase the difficulty of stereotactic navigation. Gravity, cerebrospinal fluid (CSF) leakage, anesthesia, and surgical manipulation are several major causes of the brain shift. It may provoke a notable misalignment (up to 10-30 mm [84]) of the pre-operative (pre-op) planning path, resulting in a significant targeting error. To deal with this issue, conventional DBS guided by fluoroscopy/computed tomography (CT) utilizes several micro-electrode recording (MER) to verify the placement accuracy of electrodes, and simultaneously evaluates the symptoms with the awake patient under local anesthesia. These sophisticated measures give incentives to the adoption of intra-op MRI-guided stereotaxy. With the equipment of MRI, the essential brain structures and points of interest (e.g. subthalamic nucleus (STN) or ventral intermediate nucleus) can be spontaneously reflected and monitored.

There are only a few products of MR safe stereotactic systems [83, 85] which can be found in the present market, such as NexFrame® (**Fig. 2.6a**) from Medtronic Inc., USA and ClearPoint® (**Fig. 2.6b**) from ClearPoint Neuro, USA (formerly MRI Interventions). However, these products usually need intensive manual adjustment of the stereotactic frame (**Fig. 2.6b**), and frequent patient transfer in-and-out of the scanner bore, which would largely disturb the workflow. For this purpose, researchers have developed MR safe/conditional robotic platforms. SYMBIS® (also called NeuroArm, IMRIS Inc.,

Canada), is a Food and Drug Administration (FDA)-approved prototype for MRI-guided tele-operated microsurgery (**Fig. 2.7a-b**) [86]. It can conduct MRI-guided stereotaxy with one of its robot arms. To ensure the MRI compatibility, piezoelectric motors were adopted to actuate the robotic arms and MRI safe/conditional materials (e.g. titanium, polyetheretherketone (PEEK)) were used to build the robot body [16]. However, the robotic system occupied a larger space in the operational theater, which would reduce its effectiveness while being repeatedly transferred in-and-out the scanner for imaging updates.

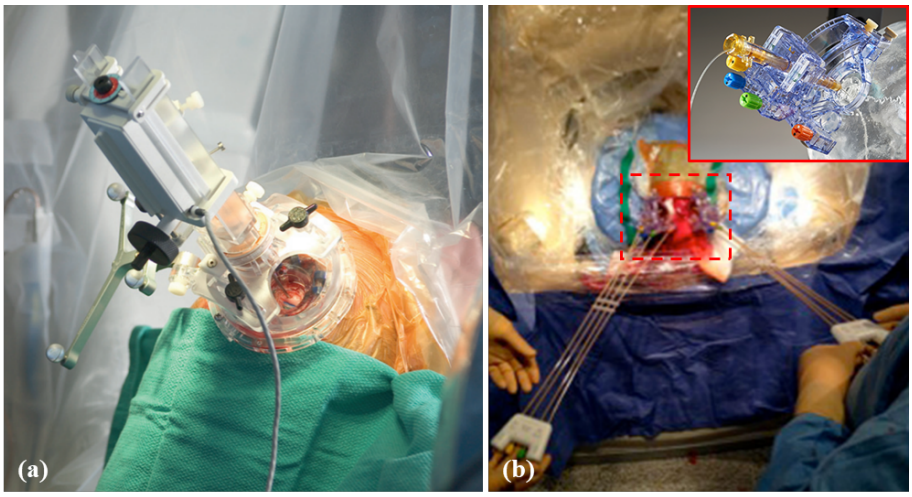

Fig. 2.6: (a) The Nexframe® platform; **(b)** ClearPoint® system from ClearPoint Neuro, USA. The frame of device was anchored on the skull and the trajectory of needle was manually adjusted. **Image Source**: [13–15].

Neuroblate® (Monteris Medical Inc., USA) (**Fig. 2.7d**) is a robotic platform which can offer two degrees of freedom (DoFs) manipulation of probe. The system was actuated by piezoelectric motors and could provide assistance for stereotactic laser ablation [56]. MR-thermometry information could be acquired in real-time to secure a safe ablation margin separated from the adjacent structures [87]. For multiple instrument insertions, the frame relocation/realignment and additional craniotomy were needed after transferring the patient back to the operating theater.

Fischer *et al.* [17, 88] have developed a research prototype for needle-based neural interventions (**Fig. 2.7c**). In terms of kinematics, the robot is similar to the traditional stereotactic frame (e.g. Leksell frame). Piezoelectric motors were utilized to drive the robot. The MR imaging quality for surgical guidance can be assured by adopting a specially designed control system, enabling the concurrent MR imaging and robot actuation. As the robot needs to be mounted on the operation table, either MRI head coil or the scanner bore (inner diameter of 1.5/3T MRI scanners usually $\varnothing 600-700$ mm) needs to be customized to enlarge the operational space for the robot.

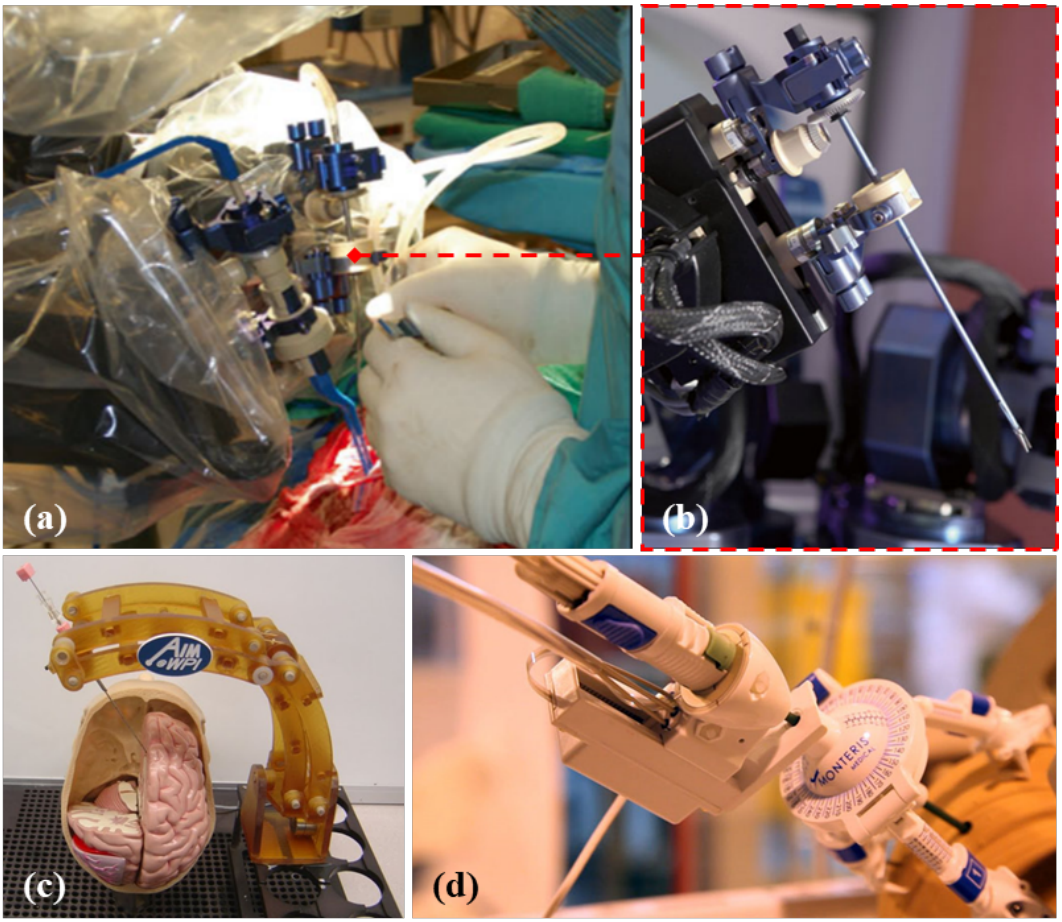

Fig. 2.7: (a) SYMBIS/NeuroArm® system developed by Deerfield Imaging, USA; **(b)** End-effector of NeuroArm system to hold surgical tools; **(c)** Table-mounted robotic system towards needle-based neural interventions; **(d)** NeuroBlate® system (Monteris Medical, Inc., USA) developed to manipulate instrument in 2 degrees of freedom (DoFs). **Image Source**: [16–18].

After reviewing the current robotic systems for MRI-guided stereotaxy, compactness and MRI compatibility can be concluded as two crucial matters affecting the efficiency and flexibility of robot setup in the hospital. However, quite a few robotic systems can be implemented into the MRI head coil, as well as perform instrument manipulation without diminishing the imaging quality during consecutive MR imaging. No platform can provide bilateral DBS, which is currently the prevalent approach for PD [89]. Besides, for most of the above systems, the positional tracking of the instrument was achieved by either passive MR fiducials or optical tracker, which may introduce high errors during the registration between the coordinates of robot and imaging [90]. In summary, there is no existing robotic system for functional neurosurgery, which adopts MR safe actuation and MR-based tracking, and can conduct stereotactic manipulation inside the MRI bore.

2.3.2 Percutaneous interventions

Percutaneous procedures are typically conducted by inserting a needle or probe through the patient's skin towards target anatomy. Percutaneous interventions can be involved in various applications, including biopsy, drainage, drug administration and tumor ablation. As one of the primary sources of cancer-related death globally [91], liver cancer is also the sixth most common type of cancer. Hepatocellular carcinoma (HCC) is the most common form of primary liver cancer and is mainly treated by liver transplantation and resection for $<$20% cases [92]. The remaining cases can be conducted by RF ablation [93], which is a standard local ablative therapy. For each insertion, an ablation needle with an outer diameter of $\varnothing$1.2-2.1 mm is advanced through patient's skin to the target region, which is generally under the guidance of ultrasound or CT. In case of a tumor with a larger diameter ($>\varnothing$3 cm) or multiple tumors, several needles would be inserted to achieve a complete ablation.

However, despite the recent development of RF ablation and other loco-regional techniques such as laser therapy, cryotherapy, microwave ablation, HCC still holds a high recurrence rate in five years at 70% [94]. The current procedure still faces challenges in dealing with tumors near vessels or organs, since the ablation cannot guarantee accurate ablative margins ($<$10 mm). As a result, the tumor recurrence rate may be increased or potential of inadvertent organ injury would be caused. Multiple paths are required for the tumors resided on the liver dome, or near the gall bladder [95]. Furthermore, liver movement caused by patient respiration would also bring difficulty to the procedure [96] during the percutaneous treatment.

In an attempt to solve these challenges, MRI has been applied as an option to ultrasound and CT guidance, demonstrating unique advantages of high-contrast imaging of soft-tissue [97] and zero ionizing radiation. The intra-op MRI can also accomplish real-time and accurate measurement ($<1^{\circ}$C) of tissue temperature, allowing estimation of ablation and its heat diffusion progress. Alternatively, laser ablation [98] can be conducted with MR thermometry and no imaging interference. Nevertheless, the precise probe placement in tumor and percutaneous needle insertion positioning still play an essential role in effective MRI-guided ablation. It demands highly skilled operators, which may also induce inter-operator variability in ablation results [99].

To minimize the probe placement variability, passive needle holders have been developed as commercial products, such as SeeStar (AprioMed, Uppsala, Sweden) and

Simplify (NeoRad AS, Oslo, Norway) [100, 101]. Passive devices can support the manual alignment of needle orientation and hold the desired direction for needle insertion. However, surgeons still have to perform intensive manual adjustments of the needle to achieve an accurate placement. It would lengthen the operation time due to the frequent transfer of the patient in-and-out the MRI scanner, so as to conduct needle adjustment.

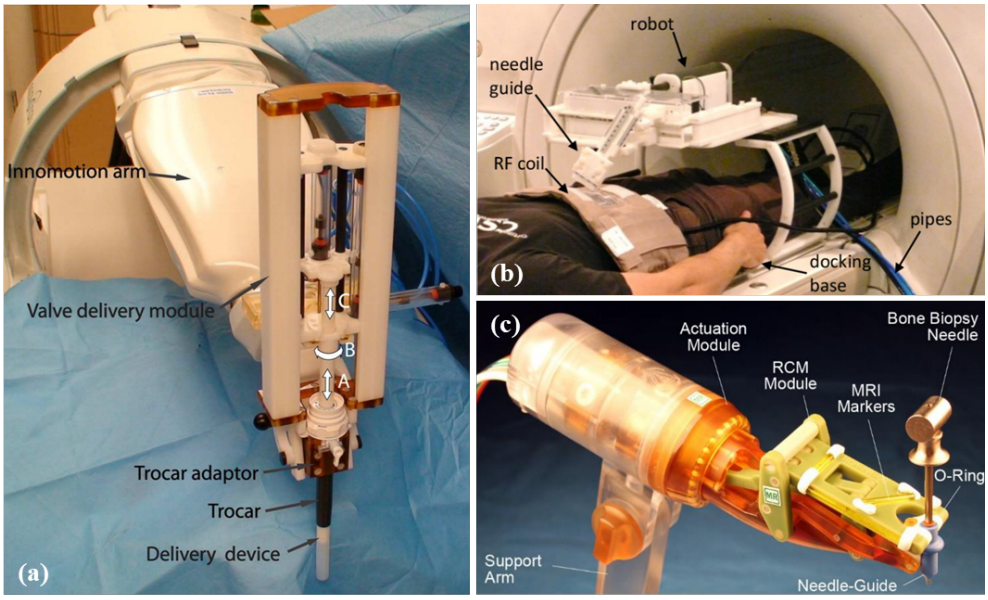

Fig. 2.8: **(a)** Innomotion robotic system from Innomedic Inc., Herxheim, Germany; **(b)** Robotic system for MRI-guided liver tumor ablation by laser; **(c)** MR safe needle-guide robot actuated by pneumatic motors. **Image Source**: [19–21].

To this end, extensive researches have been conducted towards the MR safe/conditional systems for robot-assist percutaneous procedure. A commercialized robotic system Innomotion (Innomedic Inc., Herxheim, Germany) (**Fig. 2.8a**) was developed for MRI- and CT-guided needle placement [102]. The robot was table-mounted and could provide 5-DoF needle manipulation through pneumatic actuators. The experiment demonstrated an average targeting accuracy of $<$0.5 mm by the system. Research prototypes have also been built for MRI-guided needle procedures. The 5-DoF instrument manipulator developed by Chinzei *et al.* [103] is an example. Two long rigid arms with end-effectors were extended to the surgical workspace and actuated by piezoelectric motors. All the motors were placed far from the imaging region and inside the main structure, which was mounted at the top of an open-bore intra-op MRI scanner (0.5-Tesla, Signa SP/i, GE Medical Systems, USA). Franco *et al.* [20] have developed an MRI-guided robot for tumor ablation by laser (**Fig. 2.8b**), which were under pilot studies on two patients. The robot employed a gantry to support the robot structure above the patient and could accommodate a large workspace (up to 90% volume of the liver) for needle positioning. More research prototypes have also

been developed, including the MR safe pneumatic-actuated needle robot (**Fig. 2.8c**) from Stoianovici *et al.* [21], a needle steering robot for neurosurgical ablation with concentric tubes by Comber *et al.* [104], and a robotic system for breast biopsy from Park *et al.* [105], which could be installed on an MR imaging coil inside the MRI bore.

In general, the table/floor-mounted systems can provide a fixed reference frame through the rigid structure, and can hence achieve high-accuracy needle targeting. However, their bulky structure would occupy a large footprint, which may require a specialized MRI body coil or scanner with larger clearance, as well as alteration of the surgical workflow. Moreover, the potential relative motion between the robot/needle and patient body due to respiration or accidental movement of the patient would pose a safety hazard.

Patient-mounted systems can guarantee safety regarding the patient movement, as the needle and robot have the synchronized motion with the patient. The Light Puncture Robot [22, 23] was developed for CT- and MRI-guided needle placement and actuated by pneumatic cylinders (**Fig. 2.9a**). The system could achieve a large needle tip workspace (135 mm $\times$ 120 mm) above-skin and automatic needle insertion. However, as a result, the overall system footprint was large (368 mm $\times$ 270 mm $\times$ 127 mm). A patient-mounted robot [106] was developed for MRI-guided arthrography of the pediatric shoulder (**Fig. 2.9c**), which could provide 4-DoF needle manipulation and had a diameter of $\sim \varnothing$200 mm. A robotic system for low back pain injections was developed by Li *et al.* [24], with a dimension of 219 mm $\times$ 250 mm $\times$ 87 mm. It could be anchored on the patient's body directly through the two stacked *x*-*y* table mechanisms (**Fig. 2.9b**).

Although many current systems can provide accurate and automatic needle positioning, they are typically not designed for the simultaneous use of multiple needles. Due to the relatively large footprint, most of the systems could not be deployed in multiples to overcome this limitation. In case of larger ($>\varnothing$3 cm) and/or multiple tumors, several ablations and insertions are often needed to sufficiently cover the tumor volume [107]. This would prolong the procedure if only a single-needle ablation can be conducted at each time of MRI guidance. Few studies have been focused on this issue. A patient-mounted MR conditional robotic positioner was proposed by Wu *et al.* [26], which could be fixed on the MRI loop coil (**Fig. 2.9d**). The robotic system was particularly designed for multiple needle insertions, although through a common entry point for needle insertion. This feature may restrict its applications in cases where separate entry points are required.

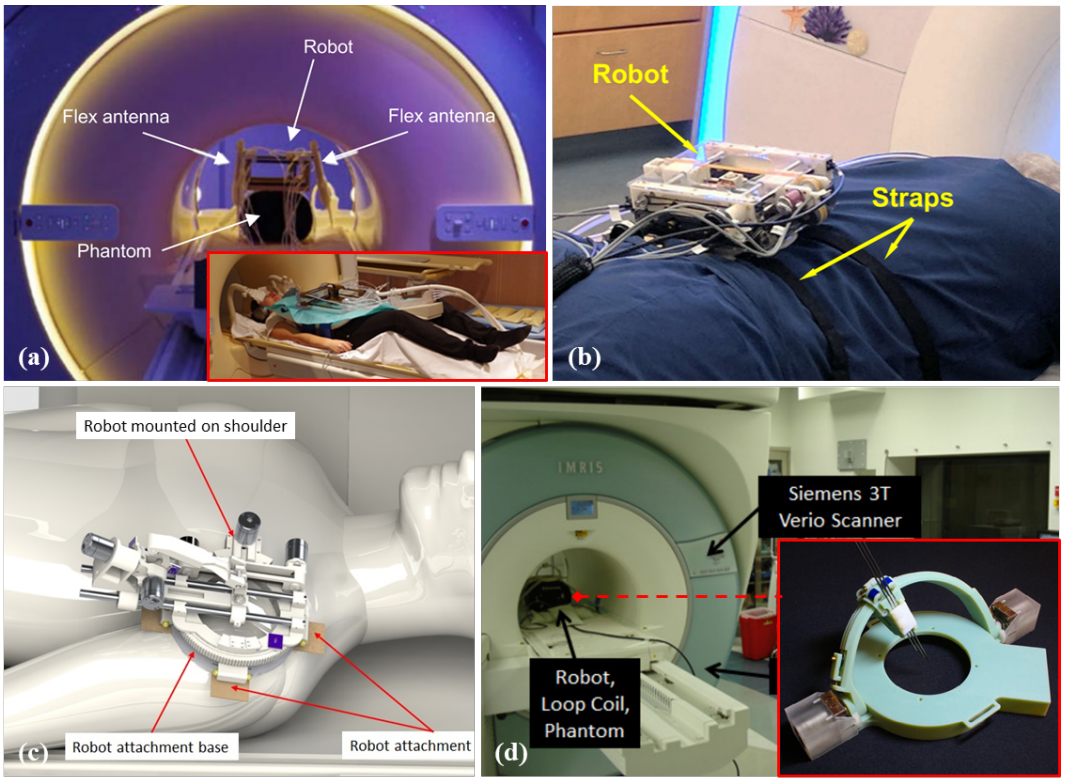

Fig. 2.9: (a) Computed tomography (CT) and MRI-compatible system for needle positioning and insertion, which was mounted on patient body. The robot was actuated by pneumatic pistons; **(b)** Patient-mounted robot for low back pain injections. The robot was anchored on patient's body by two straps; **(c)** Robot for MRI-guided arthrography, which was mounted on the patient's shoulder. The basement of robot can be attached on patient's body by adhesive pads; **(d)** MR conditional robotic positioner mounted on MRI loop coil. Multiple needle insertions can be conducted by the robot. **Image Source**: [22–26].

For MRI-guided percutaneous procedures that require multiple needle insertions, the overall procedure time could be shortened by reducing the need for rescanning, repositioning, and inserting needles for each target. It poses a strong need for a small-size patient-mounted robotic platform to conduct MRI-guided percutaneous needle placement, which could also enable the needle targeting and insertion at multiple locations.

2.3.3 Intra-cardiovascular interventions

Heart rhythm disorders, also named as arrhythmia, affect over 2.6 million people in the United States each year. Specific arrhythmias, e.g. ventricular tachycardia (VT), may induce unexpected cardiac death, causing over half a million death in the United States annually. As population age increases, these numbers would rise accordingly. Timely diagnosis and proper treatment can prevent at least 80% of the cardiac deaths. Among a variety of treatments, cardiovascular electrophysiology (EP) is an effective surgical approach, which has drawn growing attention [108, 109]. In the procedure, a long (∼1.5 m) and thin (∼⌀2.7

mm) catheter is inserted to the heart chamber from the femoral vein. Then the electrodes on the catheter tip conduct RF ablation on the target tissue, which can block the irregular electric signals that induce arrhythmias. Two significant factors govern the effectiveness and safety of the EP procedure: i) the ability to evaluate lesions and their locations, as well as to monitor the ablation progress during intra-op imaging; ii) effective manipulation of cardiac EP catheters to the target tissues for electroanatomic mapping (EAM) and RF ablation [110–112].

However, the arrhythmia recurrence rate would rise due to the formation of edema instead of necrosis, which were generally caused by insufficient RF ablation or inaccurate/incomplete electrical-circuit isolation [113]. On the contrary, excessive ablation of tissue may cause severe perforation on the cardiac wall. In light of the challenges, MRI can provide high-contrast imaging for clear visualization of cardiovascular soft tissue, as well as can enable the construction of the 3D cardiac roadmap [114, 115]. The scar tissue [116] or edema [117] resulted from completed or inadequate RF ablation can also be promptly visualized and distinguished under MRI. Numerous clinical trials have also been carried out by research groups (e.g. [118–121]), verifying the advantages of intra-op MRI-guided EP procedure.

Even assisted by the cardiac roadmap for catheter navigation, it still remains challenging to manipulate the long and flexible EP catheter, particularly due to the dynamic disturbance and the rapidly deforming cardiovascular tissue. These difficulties have stimulated the development of tele-operated robotic systems for the catheter manipulation [122–124], including the well-known commercial platforms - Hansen Sensei® X (**Fig. 2.10a**), Amigo Remote Catheter System (**Fig. 2.10b**), and Stereotaxis Niobe® system [125] (**Fig. 2.10c**). These commercial platforms have demonstrated the great potential of robotics to enhance the catheter manipulation accuracy and dexterity for intra-cardiac EP intervention. However, the catheter navigation would still be complicated due to the lack of real-time and continuous updates of patient-specific cardiac EP roadmaps. The electrophysiologists would be conservative to perform large amount of RF ablation, due to the possibly large misalignment (>5 mm) between the actual and reconstructed catheter tip positions in the roadmap or EA map. Despite the significant benefits of robot-assisted catheterization as well as the advances of intra-op MRI, there is no complete system which has been tested for MRI-guided EAM and RF ablation. This may attribute to the high demand on dexterous manipulation of the long flexible EP catheter, as well as the conventional challenge of robotic actuation in MRI environment [126].

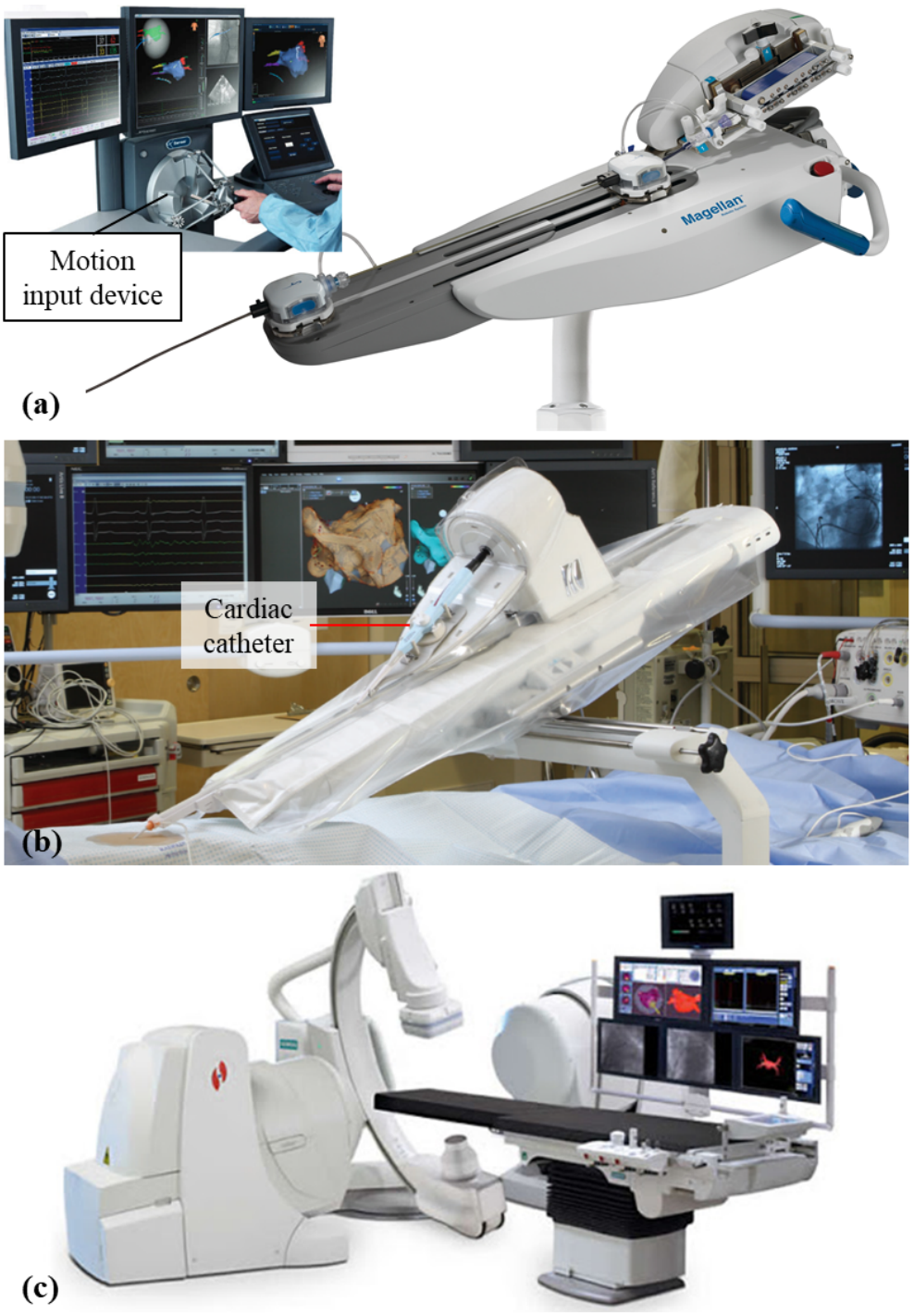

Fig. 2.10: **(a)** Sensei® X robotic system developed by Hansen Medical. Surgeon can use a motion input device to tele-operate the robotic catheter; **(b)** Amigo Remote Catheter System by Catheter Precision Inc. Cardiac catheter can be directly mounted on the robot for tele-operation; **(c)** Niobe Remote Magnetic Navigation System. The catheter tip motion can be driven by magnetic force. **Image Source**: [27–29]

2.4 Perspectives towards MRI-guided robotic system

In review of the development of MRI-guided robotics, tele-operation has become a common feature for most of the surgical robotic systems. On the other hand, there are still lots of unsolved technical difficulties in association with the robotic operation and setup in MRI. Major difficulties involve the restricted workspace within the MRI scanner bore, MRI compatibility regarding the robot actuation/material, and the real-time localization of instrument/target with sufficient imaging quality. The system design is anticipated to be more compact with improved accuracy and dexterity. The subsequent sections will present the trends and perspectives of tele-operated robotic systems under MRI environments towards high-performance robotic manipulation. These perspectives also constitute the main focus of this thesis.

2.4.1 Tele-operated robotic system

In tele-operated robotic system, the operator can remotely control the manipulator, while continuously receiving sensory or visual feedback. This type of system is also named as "master-slave system", with the control part as "master" and remote manipulator as "slave". Tele-operated robotic system has attracted significant interests and been utilized for various medical applications, including diagnostic and interventional procedures. A medical tele-operated robotic system can conduct interventional tasks remotely while involving the advantages of robotic manipulation. These features can particularly benefit the MRI-guided interventions, where the high magnetic field and confined workspace in the scanner would cause limited accessibility to the patient (**Fig. 2.11**). Most of the MRI-guided robotic systems introduced in **Section 2.3** were tele-operated, demonstrating the significance by their applications. Image and video guidance are two primary sources for the control of tele-robotic systems. The portability and transportability of the tele-operated robotic system would be affected by the image acquisition process. For the application in MRI, real-time intra-op MR imaging (**Fig. 2.11**) of the target region can be readily acquired, which can be shown together with the instrument localization for visual guidance.

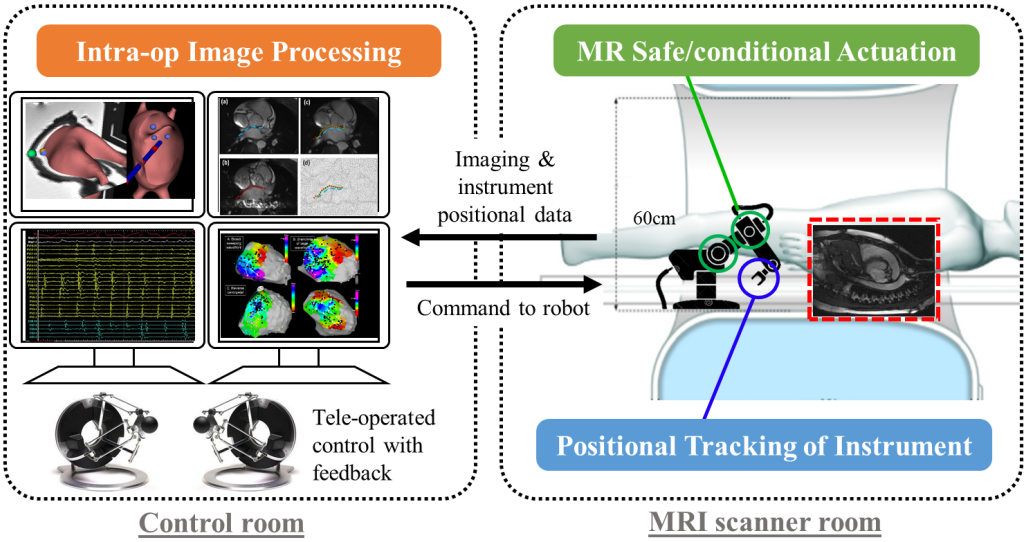

Fig. 2.11: Integrated robotic framework involving the MR safe/conditional actuation and robotic platform, tele-operation control interface, and MR image processing.

Compared to the fully autonomous systems, tele-operated robotic system would not completely replace human operation, but can involve human in the control loop. Physicians can contribute their expertise together with the precise and dexterous robotic manipulation for surgical procedures. An exemplary case is the robot-assisted stereotactic interventions. Surgeon can pre-define the instrument trajectory based on pre-operative images. And the remote manipulator can execute the task automatically by following the instruction. Another example is the da Vinci® surgical system. It can display the operating environment to surgeon through the endoscopic camera, while greatly improving the instrument maneuverability through robotic tele-operation. Regarding the safety issue, human factor is still an important constituent to ensure the safety and effectiveness of surgical procedures [127]. Experts need to continuously monitor and take control of the whole procedure to avoid any accident that the robotic system may not be able to handle.

However, contrary to the expending use of tele-operated robotic systems for MRI-guided interventions, only a few systems have been commercialized, and much fewer have been adopted in interventional practice [128]. Additional efforts are required to address technical challenges regarding: i) MR safe/conditional robotics actuation with high fidelity and fast response; ii) compact robot design to allow operation within the limited workspace of MRI scanner bore; iii) real-time localization and navigation of instrument/target under MRI; iv) high-performance control for flexible robotic instrument. The majority of the previous researches address only on a part of the above challenges and could not achieve sufficient system effectiveness for translation to clinical routine.

2.4.2 MR safe/conditional robotic actuation for tele-operated system

As introduced in previous sections, MRI is well-known for its superior capabilities in providing non-invasive and high-contrast images of soft tissues without harmful ionizing radiation, and also in monitoring the temperature changes during thermal therapy procedures [53]. These advantages prompted MRI for interventions ranging from biopsy [54], thermal therapy for tumor ablation [55, 56], drug delivery [57, 58] to catheter-based procedures within cardiovascular system [59, 60].

However, the use of ferromagnetic materials is forbidden due to the high magnetic interaction forces in MR environment (e.g. at 1.5 or 3-Tesla). Conductive materials may introduce eddy currents by EM induction, which may generate excessive heating or cause image artifact by disrupting the magnetic field homogeneity. These limitations restrict the adoption of conventional robotic actuators, i.e. electromagnet motor, for MRI-guided robots. It imposes a significant challenge to robotic design, particularly for interventions requiring precise and fast actuation, such as the manipulation of catheter inside the heart chamber. There are strong demands of high-performance actuators adopted for robotic actuation under MR environment. The actuator design should consider the long-range power transmission from the control room to MRI room, and through a waveguide in-between the rooms. Compared to the transmission distance (at least 10 meters), the length of waveguide ($\sim$30 cm) is negligible.

Piezoelectric (ultrasonic) motor is one of the prevalent choices for MRI-guided robotic actuation. It employs high-frequency current to excite precise stepping action [129–131]. It generally features compact size and high positioning accuracy (e.g. $\varnothing 23 \times 34.7$ mm^3, 5.73×10^{-6} degree per step [31]), which can give rise to a flexible robotic design and integration. **Fig. 2.12a-b** show two robot designs with the adoption of piezoelectric motors for stereotaxy [8]. However, the use of electricity with high-frequency current would inevitably introduce interference leading to image artifacts. In order to minimize the EM interference, the motors had to be placed far from the imaging region [103]. Recent study [31] attempted to use tailor-made components to attenuate EM interference. Much effort has been made in designing the EM-shield enclosures and the motor driver for low loss of signal-to-noise ratio (SNR). Nevertheless, due to the fundamental working principle of stepping and friction driven, it is challenging to apply piezoelectric motor to operations that require promising dynamics performance.

Fig. 2.12: **(a)** Robotic system driven by piezoelectric motors from PiezoMotor AB, Sweden, which was designed for MRI-guided stereotactic neurosurgery; **(b)** NeuroArm manipulator actuated by piezoelectric motors from Nanomotion, Yokneam, Israel; **(c)** Complex shielded enclosure containing the piezoelectric motor drivers, power supplies, and other accessories. **Image Source**: [8, 30, 31].

MR safe motors driven by pneumatic power have been extensively studied over the last two decades. The pressurized air (at 0.2-0.4 MPa) from the medical gas supply systems in MRI rooms can actuate the pneumatic motors and ensure no EM interference in MRI. The first MR safe pneumatic stepper motor, *PneuStep* (**Fig. 2.13a**) [32], was developed by Stoivanici *et al.*, which was also integrated into an MR safe prostate robot [132]. The motor could provide a discrete rotation at 3.33° per step. Maximum torque could reach to 640 mN-m with 3-m air hoses and air pressure at 0.83 MPa. Groenhuis *et al.* [33] developed a pneumatic stepper motor and incorporated it in an MRI-guided robot for breast biopsy (**Fig. 2.13b**). By sequentially pushing the pistons against a straight/curved rack, translational motion could be generated at a resolution of 0.25 mm [133]. This motor could

exert the highest force of 63 N at 6.5 MPa within a short transmission distance (0.5-m). But the actuation range was constrained by the rack length. Besides, various mechanisms of pneumatic motors were proposed to generate step-wise motion (**Fig. 2.13c-d**) [34, 35, 104, 134–137]. However, the high air compressibility would cause difficulties in handling the air dynamics and also the mechanical transmission delay, particularly in certain procedures demanding prompt and responsive manipulation/navigation of instruments.

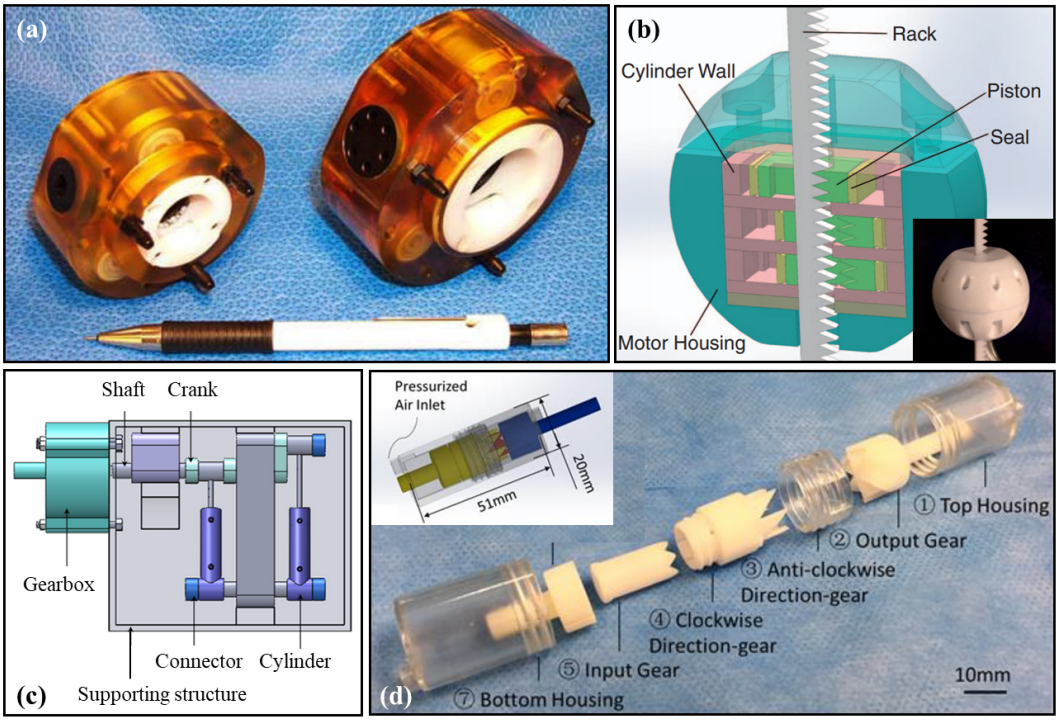

Fig. 2.13: Various designs of MR safe pneumatic motors: **(a)** MR safe pneumatic stepper motor, *PneuStep*; **(b)** Pneumatic actuator developed by Groenhuis *et al.*, which can provide linear stepping actuation; **(c)** High-torque stepper motor integrated with a gearbox; **(d)** Customizable pneumatic motor from Guo *et al.*. **Image Source**: [32–35].

Hydraulic actuation using incompressible fluid (e.g. water, oil) as transmission media can offer a much faster response and higher power density [138, 139]. However, conventional piston-cylinder paradigm would suffer from large Coulomb friction due to the tight O-ring sealing, which may introduce substantial mechanical losses and nonlinearities to the control system. Whitney *et al.* [140] developed an efficient fluid transmission based on the rolling-diaphragm-sealed metallic cylinders, which could significantly reduce the mechanical friction. However, the diaphragm could only be flipped inside out with a limited stroke, which was insufficient for operations demanding long-range motion, such as catheter navigation in EP. Although the effective stroke could be increased by gearing up the actuator, it would inevitably compromise the output torque and durability of non-metallic components.

This poses a strong incentive to develop a novel integration method of these fluid transmissions, which is MR safe and capable of providing bi-directional rotation with unlimited range and high payload. Such technique is expected to resolve many bottlenecks involved in tele-operating MRI-guided surgical apparatus. For example, high-intensity focused ultrasound (HIFU) thermal therapy [141, 142] under MRI is a noninvasive ablation approach, which currently still relies on manual positioning of a heavy ultrasound transducer array.

2.4.3 Real-time sensing and navigation in MRI

Position tracking of instrument is essential in interventions, where the positional feedback data can close the control loop for robotic navigation. The conventional use of passive MR fiducial markers has been found to be difficult in achieving responsive/continuous tracking. The complicated MRI sequence would prolong the process time of the susceptibility artifacts in the high-resolution images. Recently, paramagnetic markers could be automatically localized at high frequency (50 Hz) [143]. But it had a relatively large positional error of $\leq$4.5 mm when the MRI sequence PRIDE was used to acquire echo-phased projection in three principal axes [143].

MR-based tracking can also be achieved by attaching two tiny solenoid coils (**Fig. 2.14a**) close to the catheter tip, which were connected to an electronic receiver system via coaxial cables. It is a typical MR-*active* tracking setting, in which the coil can actively "pick up" the MR gradient field [144] along with the three principal directions for localization. By matching/tuning the receiver's circuit components for a specific MRI scanner, these coils can be highly sensitive to very local field inhomogeneity [145] without adversely affecting the image quality, providing high-resolution ($0.6\times0.6\times0.6$ mm^3) tracking performance with fast sampling rate (40 Hz) **Fig. 2.14c-d** [36].

MR-*semiactive* tracking is a state-of-the-art approach, in which coils can be integrated into small isolated resonant circuits. These coils can resonate with specific MR frequencies by means of wireless inductive coupling with the MRI system. There were no direct electrical connections with the MRI system. This can avoid resonating RF waves along with the connection of the coaxial cable, which would pose a potential heating hazard in active tracking. Using a properly programmed MR sequence to detune/trigger the isolated resonant circuit, the *semiactive* device can be visualized in the MR images. To alter the RF resonant behavior, an optical fiber could be connected to the circuit in order to illuminate

a photodiode placed parallel to a coil, which could achieve real-time imaging in an *in vivo* test [37] (**Fig. 2.14e**). MR tracking also allows real-time visualization of the catheter configuration with respect to (w.r.t.) the EP roadmap constructed from the MR images. This can provide the operator with reliable navigation guidance and consistent motion reference to aim the catheter tip at the ablation lesions imaged and registered locally around the tip (**Fig. 2.14b**).

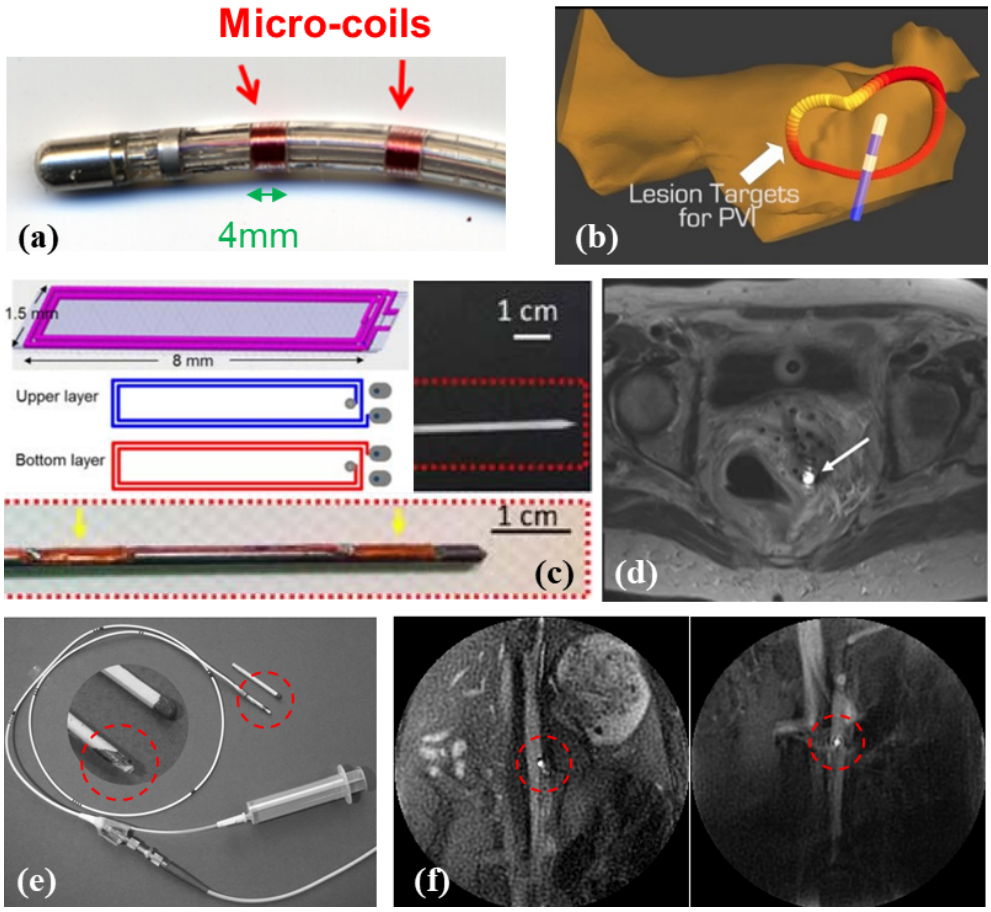

Fig. 2.14: **(a)** Tiny solenoid coils attached on the catheter tip; **(b)** Real-time visualization of the instrument configuration can be achieved based on the MR-based positional tracking; **(c)** Catheter mounted with MR-*active* tracking coils; **(d)** MR image showing the location of the active micro-coil (white arrow); **(e)** MR-*semiactive* coils mounted on a catheter; **(f)** Real-time MR images showing the intense signal spot generated by the MR-*semiactive* coils; **Image Source**: [36, 37].

2.4.4 High-performance control interface for flexible robotic instrument

Catheterization is an interventional procedure for the treatment of cardiovascular diseases. In cardiac EP for atrial fibrillation, a long (1.5-m) and flexible EP catheter is inserted from femoral vein to heart chamber to obtain an EA map [60], then to create lesion by RF ablation. The non-conductive scars created by ablation, usually on the ostia of the pulmonary veins, can isolate abnormal EP signals to treat heart rhythm disorders

(arrhythmias) [146]. This minimally invasive procedure requires delicate and consistent motion of the catheter tip via the manipulation of the catheter handle. However, even provided with X-ray visual guidance, maneuvering the distal tip to the desired location is still a challenging task. To facilitate precise manipulation, robotic catheterization has attracted increasing attention.

The conventional navigation relied on intra-op X-ray to provide a real-time navigation interface [147]. Compared with X-ray, intra-op MRI can offer high-contrast imaging of cardiovascular soft tissue [113], which can distinguish the edema [117] and scar tissue [116] resulting from inadequate or successful RF ablation. MRI-guided EP procedure has been validated by research groups with patient trials [118, 121], which have shown its potential to improve the procedure effectiveness. MR-based tracking [148, 149] can offer accurate localization of catheter under the same coordinate as imaging, which can eliminate the need for registration. This feature also allows the generation of a virtual endoscopic view from the catheter tip. The hand-to-eye coordination can hence be simplified, as the operator can control the catheter movement in the endoscopic view instead of conventional Cartesian space. Such an endoscopic visual guidance has been utilized in a simulated ablation task [150], demonstrating improved accuracy and reduced potential perforation risk.

Traditional robotic control was based on the kinematics/dynamics model of the robot configuration and motion [151–154]. The distal bendable section of a catheter could be modeled as a continuum robot. Constant curvature (CC) approach is one of the most common methods for kinematics modeling of continuum structures [151]. CC models of catheters [155, 156] have simple formulations thus facilitating convenient implementation. Catheter deflection could also be predicted from actuation force using quasi-static force-deflection models based on beam theory [157]. Another approach modeled the bendable sections as discretized rigid links with passive spherical joints, which was demonstrated in a 2D motion planning simulation [158]. However, external disturbance to the catheter, such as the pulsatile blood flow and contact with the cardiac chamber, would promptly deteriorate the reliability of these models in surgical applications. Furthermore, the accuracy of these kinematics/dynamics models strongly depends on proper selection of the structural parameters. However, cardiac EP catheters usually consist of composite materials with unknown properties. It would be time-consuming and impractical to characterize the parameters of each cardiac catheter before usage. To obtain the precise model parameter still remains crucial for accurate modeling and control.

In an attempt to avoid the complicated procedures of system identification, model-free control methods have been proposed. Online estimation of the robot kinematics can be adopted to control the catheter within a constrained workspace with unknown conditions. A proportional–integral–derivative (PID) controller was developed for a 4-tendon catheter [159], in which solely real-time position/force feedback was used to generate actuation commands. Another model-free controller introduced in [160] could estimate the Jacobian in real-time to correlate the actuator command with the sensory feedback from catheter tip. However, due to the dynamic disturbance in heart chambers, it is difficult to estimate the Jacobian with a smooth transition, particularly under contact or interaction with surroundings. It poses a strong need for precise modeling and control of standard EP catheter towards effective cardiac catheterization.

2.5 Conclusion

This chapter reviews the advances of intra-op MRI technology and recent development of MRI-guided robotic systems. The MRI safety classification is introduced, which is the basic standard for the development of robotic devices under MRI guidance. The current status of MRI-guided robotic systems is reviewed, focusing on neurosurgery, percutaneous interventions, and intra-cardiovascular interventions. In review of these systems, there are still lots of unmet technical challenges towards effective MRI-guide robot-assisted interventions. To this end, essential techniques have been investigated, including the tele-operated system configuration, MR safe robotic actuation, real-time sensing and navigation in MRI, and high-performance control of flexible instruments.

In the following content, MR safe high-performance hydraulic motors are introduced in **Chapter 3**, serving as the essential component for robotic tele-operation. The needle placement robots (**Chapter 4**) and the robotic catheter system (**Chapter 5**) are developed with incorporation of the hydraulic motors, offering dexterous instrument manipulation. Real-time shape tracking and motion control methods are proposed and validated with the robotic catheter platform, which are introduced in **Chapter 6**.

Chapter 3

MR Safe Hydraulic Actuation for Tele-operated Robotic System

3.1 Introduction

As introduced in **Chapter 2**, a variety of magnetic resonance (MR) safe/conditional robotic actuators have been developed for MRI-guided robots, in which piezoelectric and pneumatic motors were mostly adopted. However, their inevitable drawbacks have limited the wide adoption, such as the complex shielding or significant transmission delay. There still lacks choice of MR safe actuator that can provide high-fidelity and dexterous robot manipulation. In this chapter, an MR safe hydraulic actuation method is presented. The high-performance hydraulic motors can offer tele-operated, dexterous motion control under magnetic resonance imaging (MRI). The proposed hydraulic motor in three-cylinder configuration is also capable of providing continuous bidirectional rotation with unlimited range. The detailed design and mechanism of the motor are described in **Section 3.3**. Kinematics and dynamics modeling of the proposed hydraulic motor is studied in **Section 3.4**, which facilitates the overall design optimization (**Section 3.5**) and position/torque control. Motor performance, including accuracy, step response and frequency response, was also experimentally evaluated (**Section 3.6**). The key contributions of this work include:

1. Design of MR safe hydraulic motors for robotic tele-operation for MRI-guided interventions. The motor configured with three cylinders can achieve continuous bidirectional actuation in unlimited motion range. The motor can also be customized with more cylinders (>3) to provide higher output torque;

2. Kinematics and dynamics modeling of the hydraulic actuation for motor control and design optimization. Both positional and torque control can be applied. The key design parameters governing the system performance have been devised. Their design tradeoff is also presented in an analytical study.

3. Experimental validation of transmission performance. Step response, force transmission, frequency response and actuation accuracy have been evaluated for the proposed hydraulic motors.

3.2 Advances of rolling-diaphragm seals for hydraulic system

Fig. 3.1 shows a pair of cylinders enabling action-and-reaction transmission via a long hydraulic pipe (10-meter), which passed through the waveguide in-between MRI and control room. Compared to the 10-m hydraulic tube, the length of waveguide ($\sim$30 cm) would cause negligible influence on the hydraulic transmission performance. Incompressible liquid, such as water or oil, could be filled in the pipelines to ensure responsive, accurate power transmission in both directions. Considering the tradeoff between pliability and stiffness of the tube for such long-distance transmission, semi-rigid nylon tubes with outer/inner diameter of $\varnothing$6/4 mm (DG-5431101, Daoguan Inc.) were selected. Radial expansion of these tubes under loading is minimal when the transmission liquid inside is pressurized. Key components in the current prototype, such as piston rods and cylindrical housings, were 3D-printed with polymer composites (VeroWhitePlus and VeroClear, Stratasys, US), thus ensuring the MR safety. To enhance the structural rigidity and robustness in production stage, alternative choices of MR safe materials with higher strength, such as polyethylenimine and polyoxymethylene, will be explored and adopted.

Each cylinder unit contains a rolling diaphragm (MCS2018M, FEFA Inc.) made of fabric-reinforced rubber for sealing. The diaphragm can be flipped inside out, and roll over the piston rod to allow 35-mm stroke linear motion. Its working principle can inherently avert the static contact and sliding friction between the seal and cylinder, which are great concerns in the conventional O-ring-sealed hydraulic transmission [140, 161] (**Fig. 3.2**).

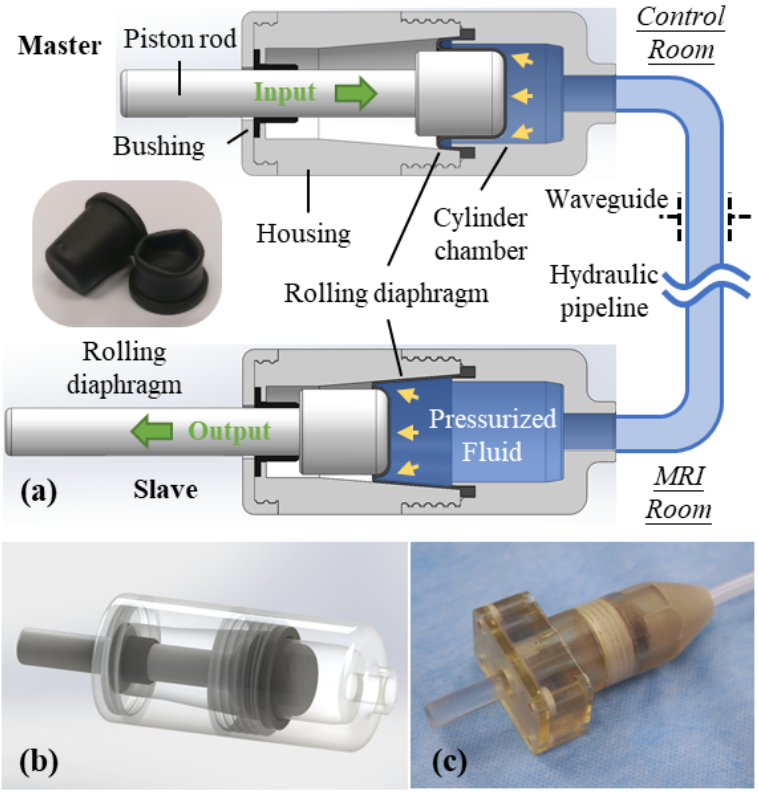

Fig. 3.1: **(a)** Pair of rolling-diaphragm-sealed cylinders enabling MR safe power transmission through a long hydraulic tube, which was channeled through the waveguide in-between control room (master control side) and MRI suite (slave robot side). The transmission can take place only when the piston rod is pushed onto the diaphragm hat. The rendered model and 3D-printed prototype of the cylinder are respectively shown in **(b)** and **(c)**.

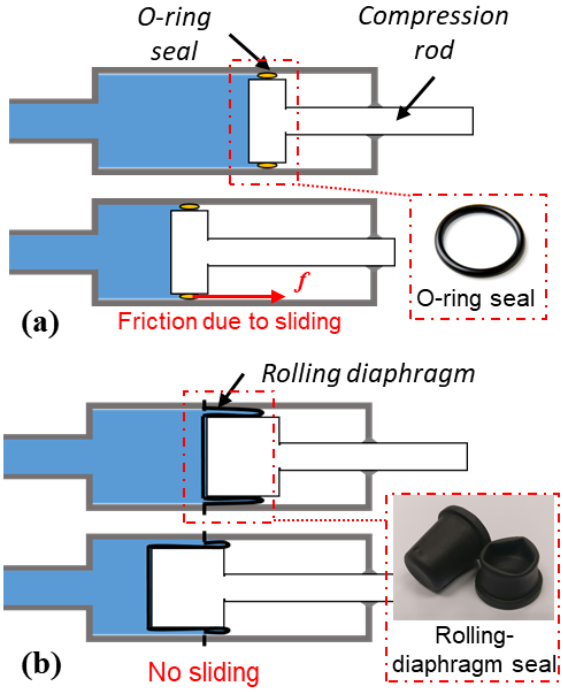

Fig. 3.2: **(a)** Traditional sealing using O-rings. Large sliding friction would be induced between the cylinder wall and the seal; **(b)** Low-friction sealing with rolling diaphragms, which can tightly seal the fluid and avoid the sliding friction.

To ensure symmetric rolling and constrain undesired ballooning/stretching of the rolling diaphragm, the diaphragm hat was kept to attach the piston head and cylinder wall tightly. As a result, the pressure reaction of the rolling diaphragm can be efficiently transmitted to the piston head.

However, the transmission can only take place when the piston rod is pushed onto the diaphragm hat. Therefore, only one pair of cylinders is *incapable* to conduct bidirectional transmission. In this light, the integration of multiple cylinders pairs is proposed to generate actuation in both directions. Two exemplary configurations are presented, with *two* (**Section 3.3.1**) and *three* pairs of cylinders (**Section 3.3.2**) arranged in parallel or radial, respectively.

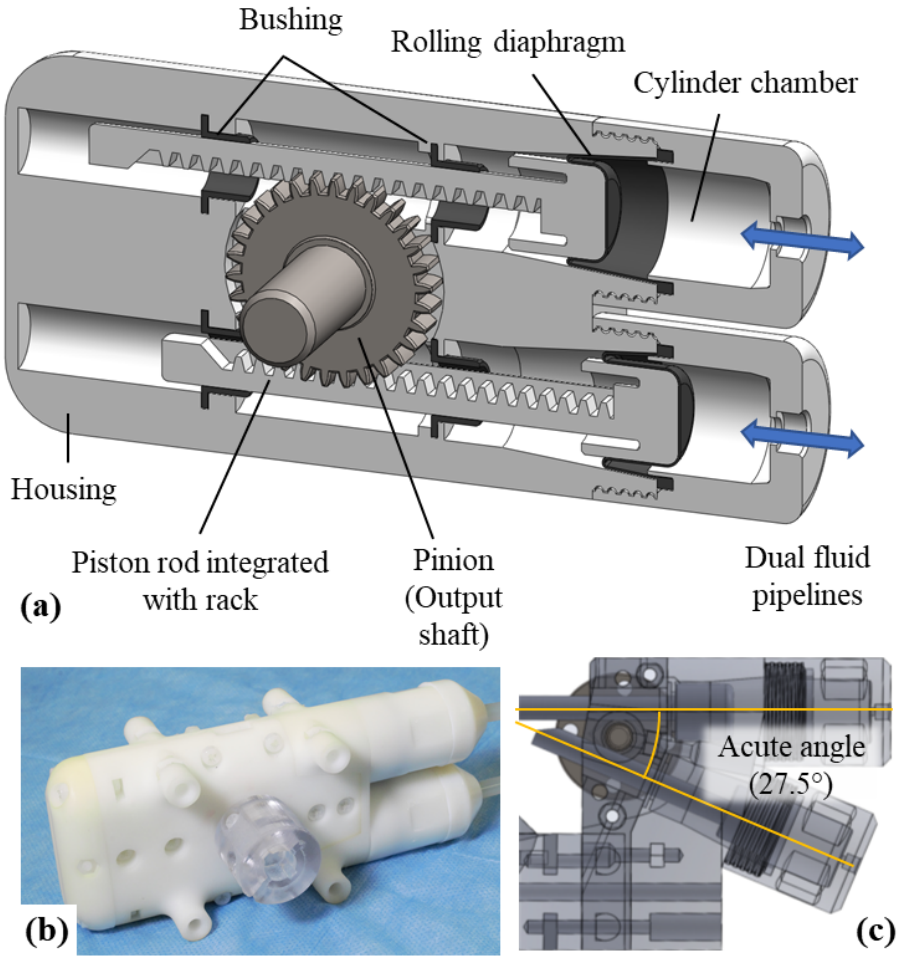

Fig. 3.3: **(a)** Section view of two-cylinder actuation unit. The rack-and-pinion mechanism can enable the bidirectional rotation. Preloading fluid pressure can minimize backlash, thereby maintaining steady contact of gear teeth; **(b)** Prototype of the actuation unit. All components are MR safe, with the housing body 3D-printed by polymer composites; **(c)** Two cylinders placed at an acute angle, giving rise to larger range of output rotation.

3.3 Multiple configurations of diaphragm-based hydraulic transmission

3.3.1 Actuation with two-cylinder configuration

Fig. 3.3a shows the section view of integrated two-cylinder actuation unit with an overall dimension of 85×60×28 mm^3. The two cylinders were placed in parallel (**Fig. 3.3a-b**). A pinion gear was located in-between and coupled with the two linear racks, which were integrated with the piston rods. This rack-and-pinion mechanism can enable bidirectional rotation of the pinion, which converts the piston's linear motion (25 mm) to pinion's rotation (±47.8°). Master-slave system can be adopted (**Fig. 3.4a**), in which the master unit was connected to the slave unit via two long hydrostatic pipelines. The master and slave parts located separately in the control room and MRI room, respectively. The slave unit can passively follow the motion of master unit which can be driven by direct current (DC) motor (**Fig. 3.4b**).

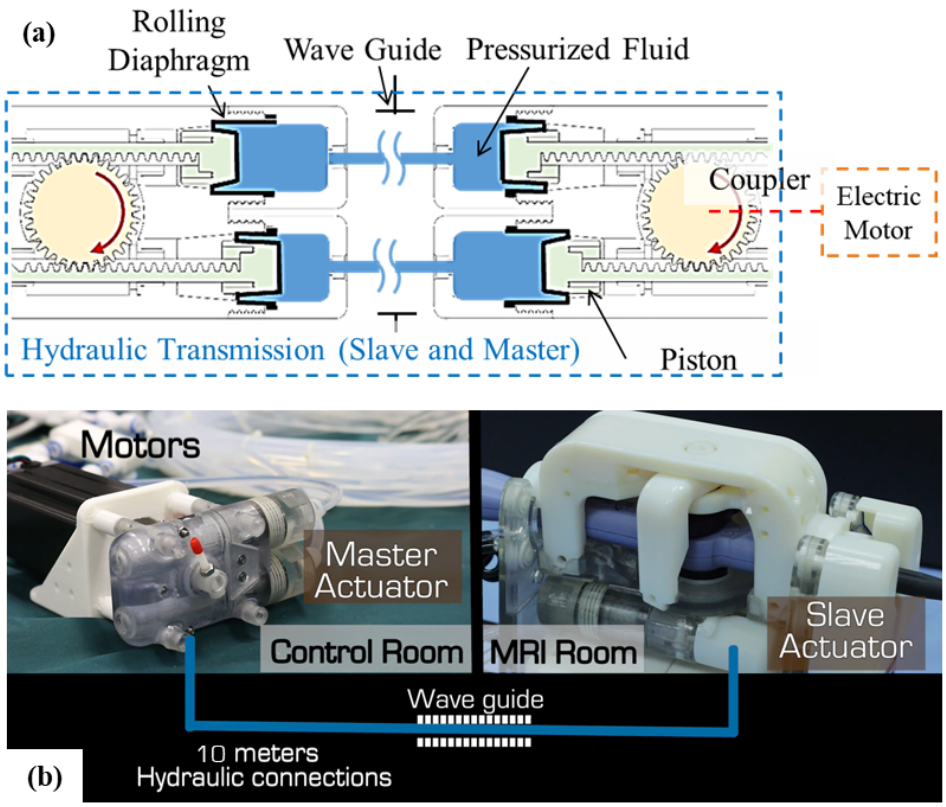

Fig. 3.4: (a) Mater-slave hydraulic transmission of the two-cylinder actuation unit for tele-operation. The slave unit can passively follow the motion of master unit driven by electric motor; **(b)** Prototype of the actuation units with a master-slave setup. Hydraulic power was transmitted by 10-meter pipelines through a waveguide in-between the control room and MRI room

The motion range of the two-cylinder design could be increased by configuring the cylinders with an acute angle, as shown in **Fig. 3.3c**. Another way to achieve the motion range increase is to vary the cylinders' cross-sectional areas at the master and slave sides, in order to form a certain transmission ratio without a gearbox. However, these methods would generally decrease the transmission accuracy and maximum torque output. Moreover, the short motion range is still far from satisfying requirements for high-precision and long-range navigation, such as needle insertion (>100 mm [162]) or electrophysiology (EP) catheterization from the femoral vein to heart chamber. To this end, a fundamental change of cylinders configuration (**Fig. 3.5**) is proposed to resolve the unmet technical challenges.

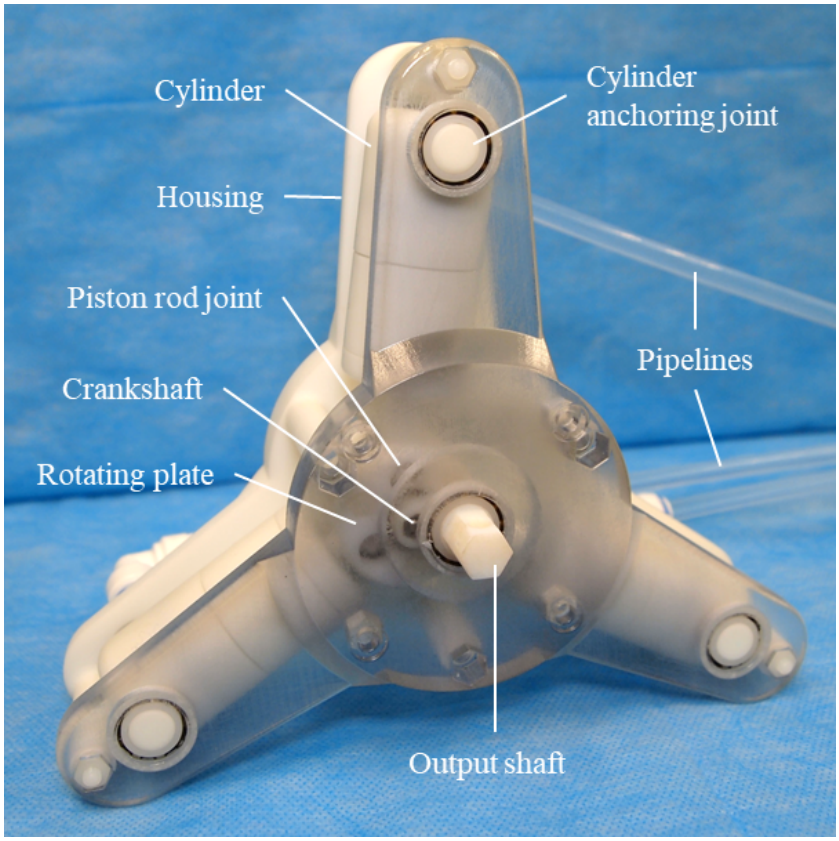

Fig. 3.5: Prototype of the three-cylinder actuation unit connected with three separate pipelines. All components are MR safe, with the structural components 3D-printed by polymer composites.

3.3.2 Continuous actuation with three-cylinder configuration

Fig. 3.5 and **Fig. 3.6a** show the prototype and 3D model of the proposed MR safe motor, respectively, which integrates three hydraulic cylinders. It has an overall dimension of $150\times140\times46$ mm^3. This design is capable of offering bidirectional, continuous and torque-controllable rotatory actuation, in contrast to aforementioned pneumatic stepper motors that only allowed stepper motion [32]. Continuous motion can be made possible by taking advantage of the rolling diaphragm seal. The low-friction sealing method can enable precise displacement/force control of each cylinder, even when connected through 10-meter hydraulic pipelines.

As shown in **Fig. 3.6b**, a rotating plate with a crankshaft coupled the piston rods to the output shaft. The rotating plate can provide a larger space for the rod anchorage, while keeping the cylinders in the same plane. The plate was fixed to the rod of cylinder C1, with others remaining flexible to revolve around the joints. While being actuated, the cylinders can rotate about the anchoring joints thus following the rod motion. This design can reduce the lateral force between the cylinder housing and piston rod, and can also keep the diaphragm centered inside the cylinder. Thus the durability of diaphragm can be enhanced with reduced internal friction.

The motor's output shaft can be simultaneously driven by all cylinders, which were radially placed with 120° intervals (**Fig. 3.6b**). This configuration aims to avoid kinematics singularity, where no output torque can be generated regardless of how the cylinders are actuated. For fluid-driven cylinders that only allow for push motion, singularity would become inevitable if only one or two cylinders are employed in a craft-shaft mechanism. This necessitates a minimum of three-cylinder design to enable smooth rotary motion. By employing more cylinders such that more than three, the actuator's allowable output torque can be increased, where more cylinders share the payload. However, the tradeoffs include larger motor dimension and increased hydraulic pipelines to connect with the cylinders. Other performance indices, such as step response or frequency response, would remain the same, as they are mainly governed by the hydraulic transmission performance.

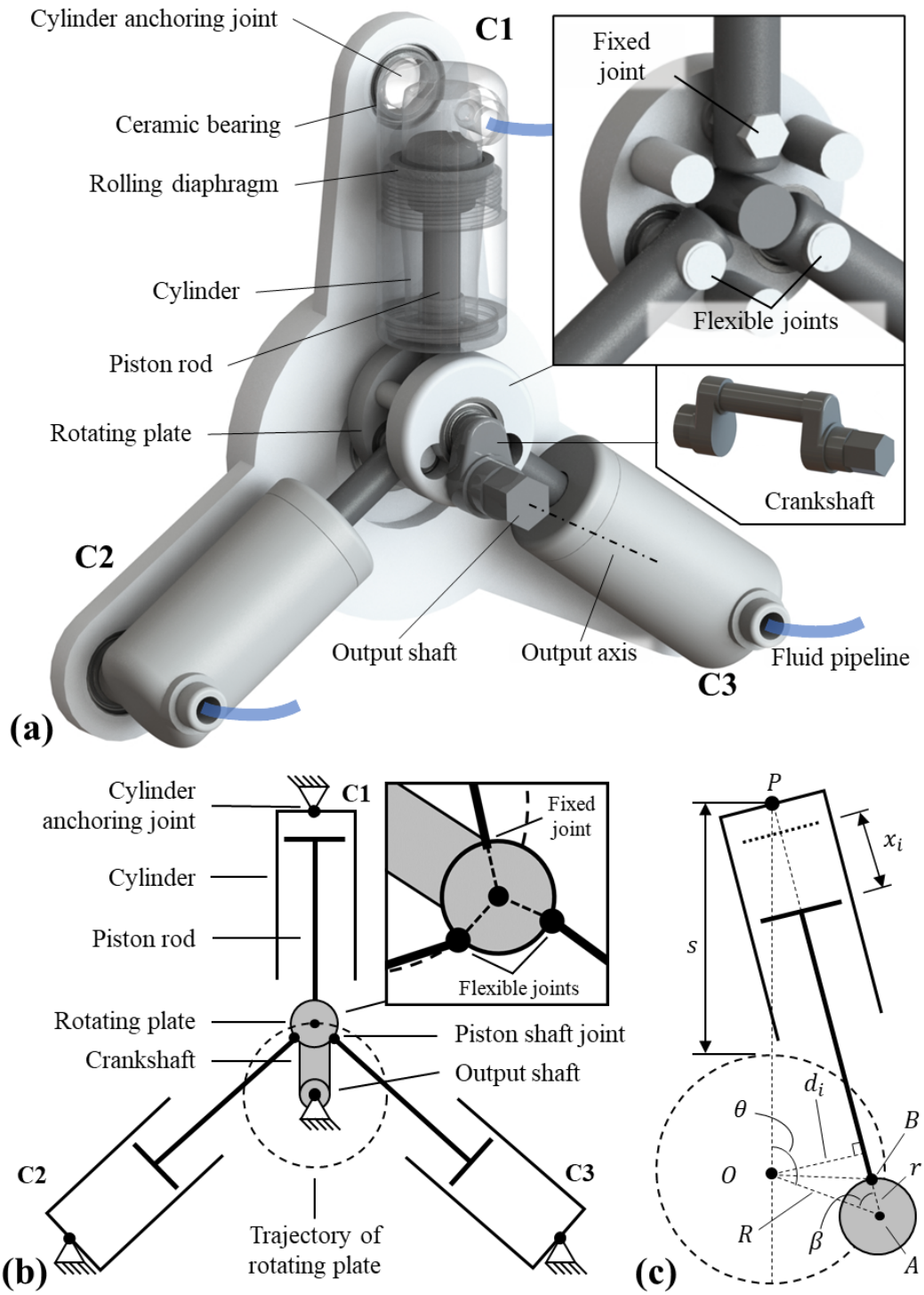

Fig. 3.6: **(a)** Design of hydraulic motor with the three-cylinder configuration. The three cylinders are radially placed/moved about the output axis; **(b)** Schematic diagram showing the coupling mechanism of output shaft and piston rods through a crankshaft and rotating plate; **(c)** Kinematics parameters denoted in a single cylinder, which are summarized in **Table 3.1**.

By varying the linear positions of cylinder shafts (**Fig. 3.7**), the continuous positional control at the output shaft can be achieved. Such a three-cylinder configuration in previous works [32] generally output stepping motion without precise positional control of each cylinder, or just delivered a continuous rotation. In this work, the adoption of rolling-diaphragm-sealed cylinders can enable precise positional adjustment of individual cylinders through the tele-operated hydraulic actuation. Then by deducing the actuator kinematics, the angular output of the three-cylinder actuator can be accurately generated by controlling the cylinders' displacement.

Table 3.1: Key parameters of three-cylinder actuator

Parameter	Description
x	Piston displacement
s	Distance from point P to the nearest point on crankshaft trajectory
θ	Angular position of the output shaft
β	Angle between the piston rod and the direction of the rotating plate relative to the output axis
r	Radius of rotating plate
R	Radius of crankshaft
d_i	Distance between the center line of the i^{th} piston rod and the rotation axis of output shaft

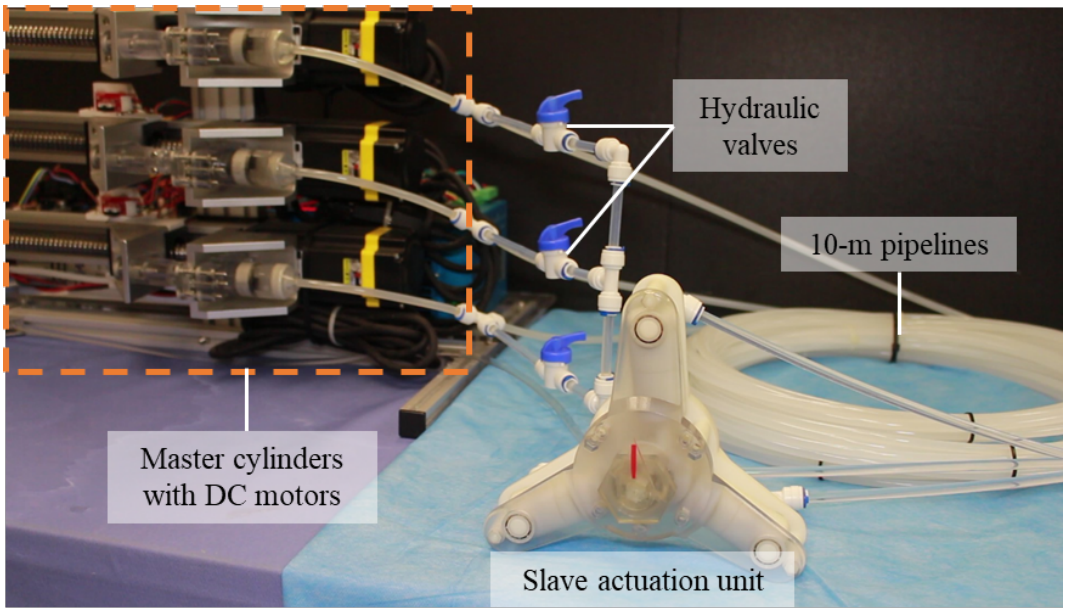

Fig. 3.7: Setup of hydraulic system for three-cylinder actuator. The continuous positional actuation at the output shaft was controlled by varying the linear positions of piston rods, which were driven by the direct current (DC) motors at master side through 10-m hydraulic pipelines.

3.4 Modeling of hydraulic motor

3.4.1 Kinematics model of slave actuator

The kinematics model of the three-cylinder configuration is derived based on the actuator geometry. Key kinematics parameters of a single cylinder are depicted in **Table 3.1**. All the components, except for the rolling diaphragm, are considered as rigid bodies. Unique solution of each piston displacement, x_i, is obtainable, corresponding to an angular position θ of the output shaft. By applying Cosine Law for the triangle *OAP* in **Fig. 3.6c**, the piston displacement of the cylinder C1 can be calculated as:

$$x_1(\theta) = \sqrt{2R(R+s)(1-\cos\theta)+s^2} - s \tag{3.1}$$

As the pistons are evenly placed in a circle, the i^{th} cylinder C_i has a phase difference $\varphi_i = (i-1)\cdot 2\pi/n$ compared with cylinder C1, where n is the total number of cylinders and equals to 3 for the three-cylinder configuration. Therefore, the piston displacements of the cylinders can be derived by adding the phase difference to θ in **Eq. 3.1**. Note that the misalignment due to the installation of rotating plate is negligible.

3.4.2 Dynamics modeling of hydraulic transmission

To identify the system properties and optimize the design parameters, we established the model of the integrated transmission system and carry out the validation, not only in simulation but also in the experimentation. Provided with the dynamics model of our proposed actuator, we can identify the key parameters that govern the system performance, which makes it possible to define a design guideline to fulfill various practical requirements and constraints.

The proposed transmission system adopts a master-slave design, with two sides connected by hydrostatic transmission pipelines. The slave side is the three-cylinder actuation unit and the master side comprises of the same number of cylinders individually driven by electric motors. The system dynamics model is derived in two parts, namely the slave actuation unit and the hydraulic transmission.

The kinematics and dynamics of the two-cylinder configuration (**Fig. 3.3**) could be formulated as $x_t = \pm r_p \cdot \theta$ and $\tau_{t1} - \tau_{t2} = I_p \cdot \ddot{\theta} + \tau_o$, respectively, with **Table 3.2**

summarizing the parameters. There are two assumptions: 1) all the components are considered as rigid body, except for the rolling diaphragm and pipelines; 2) friction at the joints is negligible. It is also applicable for the models of three-cylinder configuration.

Table 3.2: Parameters of dynamics model for two-cylinder configuration

Parameter	Parameter name
x_t	Displacement of the two piston rods
r_p	Radius of the pinion
θ	Angular position of the output shaft
$\ddot{\theta}$	Angular acceleration of the output shaft
τ_{t1}, τ_{t2}	Torques provided by the two cylinders
τ_o	Output torque
I_p	Inertia of the pinion and output shaft

For the three-cylinder configuration illustrated in **Fig. 3.6a-b**, each cylinder can only generate a unidirectional force, which comes from the fluid pressure in the pipeline. The output torque contributed by the i^{th} cylinder can then be described as $\tau_i = F_i \cdot d_i$, where F_i is the force provided by the cylinder and d_i is the offset between the center line of the i^{th} piston and the rotation axis of output shaft. From **Fig. 3.6c**, d_i could be calculated as $d_i = R \cdot \sin\beta_i$, where β_i is the angle between AO and the i^{th} piston rod axis, and R is the rotational radius. According to Sine Law, $\sin\beta_i$ can be calculated as:

$$\sin\beta_i = \frac{s \cdot \sin(\theta - \varphi_i)}{\sqrt{s^2 + R^2 - 2s \cdot R\cos(\theta - \varphi_i)}} \tag{3.2}$$

The output torque at the crankshaft is generated from the the cylinder rods as:

$$\sum_{i=1}^{n} \tau_i = I_r\ddot{\theta} + \tau_o \tag{3.3}$$

where I_r is the inertia of the rotational components, $\ddot{\theta}$ is the angular acceleration of output shaft and τ_o is the output torque. Thus, the correlation between the output torque and the forces provided by the cylinders can be described. Torque control is then made possible to be implemented on this actuator.

The dynamics model of the rolling diaphragm-based hydraulic transmission describes the relation between the input force F_{in} (master side) to the output force of F_{out} (slave side). A spring-mass-damping system (**Fig. 3.8**) is adopted to approximate the interactions between the pistons and hydraulic fluid. Their interconnection is represented by the spring elements of stiffness $2K_t$, which account for the pipeline compliance and fluid compressibility. We assume that the system damping induced by the rolling diaphragm and

fluid friction can be described by the coefficients c and B_f.

We first derive the pipeline compliance by considering that the input force F_{in} is applied at Piston 1 while the Piston 2 is being blocked. The following equations in **Eq. 3.4** describe radial stress σ_r and the hoop stress σ_θ applied on the inner pipe wall resulted from the applied pressure P, according to Lamé Formula:

$$\sigma_\theta = P \cdot \frac{D_{pi}^2 + D_{po}^2}{D_{po}^2 - D_{pi}^2},\ \sigma_r = -P \tag{3.4}$$

where D_{pi} and D_{po} represent the inner and outer diameters of the pipeline. For pipes made of isotropic material with Poisson's ratio ν and elasticity modulus E, the hoop strain is equivalent to $\varepsilon_\theta = \Delta D_{pi}/D_{pi} = (\sigma_\theta - \upsilon\sigma_r)/E$. The volume change in the pipe for an enclosed system should be equal to the change in the input cylinder, which gives $[(D_{pi} + \Delta D_{pi})^2 - D_{pi}^2]L_p = D_{in}^2 \cdot \Delta x_{in}$, where ΔD_{pi} is the change of pipe inner diameter, D_{in} is the diameter of input cylinder, Δx_{in} is the displacement of input piston and L_p is the length of pipe. Therefore, the inner diameter change of pipe could be determined by:

$$\Delta D_{pi} \approx \frac{D_{in}^2 \cdot \Delta x_{in}}{2 D_{pi} L_p} \tag{3.5}$$

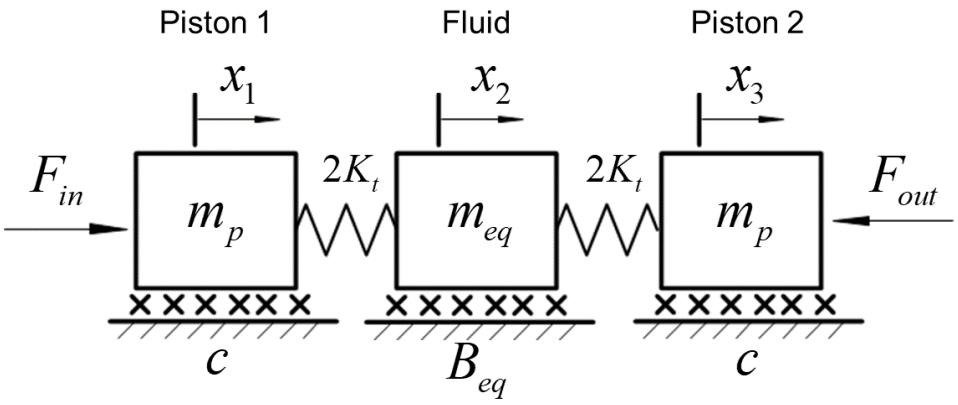

Fig. 3.8: Dynamics parameters of a single transmission pipeline. Input force F_{in} is applied to produce movement at constant velocity of piston 1, with output force F_{out} equal to zero. The cross markers "×" denote the fluid damping.

With **Eq. 3.4**, **Eq. 3.5** and the assumption that the pressure comes from the input force $F_{in} = P \cdot (\pi D_{in}^2/4)$, the pipeline stiffness K_p observed at the piston can be derived as:

$$K_p = \frac{F_{in}}{\Delta x_{in}} = \frac{\pi E D_{in}^4}{8 D_{pi}^2 L_p} \left[\frac{D_{pi}^2 + D_{po}^2 + \nu D_{po}^2 - \nu D_{pi}^2}{D_{po}^2 - D_{pi}^2} \right]^{-1} \tag{3.6}$$

The fluid stiffness resulted from compression could be modeled as $K_f = E_v \cdot {A_{in}}^2/V$,

where A_{in} is the cross-sectional area of the input cylinder, V is the total volume and E_v is the bulk modulus of fluid. The equivalent transmission stiffness K_t of the hydraulic pipe can be obtained as the series of fluid stiffness and pipeline compliance: $K_t = K_p K_f/(K_p + K_f)$.

For the system damping factors, we assume that the input force at Piston 1 is F_{in} and it produces a movement at constant velocity, given that there is *zero* loading at the Piston 2 ($F_{out} = 0$). We can hence derive the fluid head loss, which is governed by the Bernoulli equation for steady and incompressible flow between any two points in a pipe:

$$\frac{P_{in}}{\rho} + \frac{v_{in}^2}{2} + g \cdot z_{in} = \frac{P_{out}}{\rho} + \frac{v_{out}^2}{2} + g \cdot z_{out} + h_f \tag{3.7}$$

where P_{in} and P_{out} are the fluid pressures, z_{in} and z_{out} represent the elevations, v_{in} and v_{out} represent the fluid velocities, at the input and output piston respectively, h_f is the head loss ρ is the fluid density and g is the gravitational constant.

In this case, pipeline loss mainly contributes to head loss. So the local loss at the connections between cylinder and tube can be neglected. Because the pipeline loss is proportional to the length but *inversely* proportional to the diameters, the head loss in the cylinders is negligible when compared with that in the pipelines. The total pipeline loss can be approximated as $h_f = \lambda L_p {v_f}^2/(2D_{pi})$, where λ is the flow coefficient and v_f is the fluid velocity [163]. For laminar pipe flow, we can assume that $\lambda = 64/R_e$, where the Reynolds number $R_e = \rho v_f D_{pi}/\mu$, and μ is the dynamic viscosity of fluid.

Assuming that the pipes are put at the same elevation, the terms gz_{in} and gz_{out} can be eliminated. The fluid is nearly incompressible so that the velocity at the input piston and output piston is approximately equal, $v_{in} \approx v_{out}$. The pressure P_{out} is zero in our case with no load applied ($F_{out} = 0$). By observing that $F_{in} = P_{in} \cdot A_{in}$, the equivalent damping coefficient B_f can be obtained as:

$$B_f = \frac{F_{in}}{v_{in}} = 8\pi\mu L_P \left(\frac{D_{in}}{D_{pi}}\right)^4 \tag{3.8}$$

For the fluid inertia, we consider an equivalent fluid mass as observed at the piston, which can be determined by an energy calculation:

$$m_f v_{in}^2 = m_{cyl} v_{in}^2 + m_{pi} {v_f}^2 \tag{3.9}$$

where m_f is the equivalent mass of fluid, m_{cyl} is the fluid mass in cylinder, and $m_p i$ is the

fluid mass in the pipeline. Then the equivalent mass can be obtained as:

$$m_f = m_{cyl} + m_{pi}(D_{in}/D_{pi})^4 \tag{3.10}$$

The key components of the overall dynamics model of the passive fluid transmission system are shown in **Fig. 3.8**. The dynamics of the hydraulic transmission can be described by a linear differential equation as follows:

$$\mathbf{K}\mathbf{q} + \mathbf{C}\dot{\mathbf{q}} + \mathbf{M}\ddot{\mathbf{q}} = \mathbf{F} \tag{3.11}$$

where

$$\begin{cases} \mathbf{K} = \begin{bmatrix} 2K_t & -2K_t & 0 \\ -2K_t & 4K_t & -2K_t \\ 0 & -2K_t & 2K_t \end{bmatrix} & \mathbf{C} = diag\,(c, B_f, c) \\ \mathbf{M} = diag(m_p, m_f, m_p) & \mathbf{F} = \begin{bmatrix} F_{in} & 0 & -F_{out} \end{bmatrix}^T \end{cases} \tag{3.12}$$

In **Eq. 3.10**, $q = [\ q_1 \quad q_2 \quad q_3\ ]^T$ denotes the matrix containing displacements of input piston (q_1), fluid (q_2) and output piston (q_3). Damping coefficient, c, is introduced by the rolling diaphragm. The state space function can be derived as:

$$\begin{bmatrix} \dot{\mathbf{q}} \\ \ddot{\mathbf{q}} \end{bmatrix} = \begin{bmatrix} 0 & \mathbf{I} \\ -\mathbf{M}^{-1}\mathbf{K} & -\mathbf{M}^{-1}\mathbf{C} \end{bmatrix} \begin{bmatrix} \mathbf{q} \\ \dot{\mathbf{q}} \end{bmatrix} + \begin{bmatrix} 0 \\ \mathbf{M}^{-1}\mathbf{F} \end{bmatrix} \tag{3.13}$$

3.5 Design optimization of hydraulic transmission system

This section presents the design guidelines for the hydraulic system in regards to the desired system performance, including fluid transmission stiffness, transmission latency and pipeline bending stiffness. Parametric study was performed by numerical simulation of the dynamics model. The study scope includes several form factors of the transmission system, such as pipe diameter, length, thickness, materials, and cylinder diameter. Four typical pipe materials: polycaprolactam 6 (PA 6), PA 66, polytetrafluoroethylene (PTFE) and polyurethane (PU), were examined. Their nominal values adopted for the integration are listed in **Table 3.3** for reference.

Table 3.3: Values of design parameter set in simulation

Parameter	Value
Pipe inner diameter (mm)	4.0
Ratio of pipe inner diameter to thickness	4.0
Pipe material	PA 6
Pipe length (m)	10.0
Piston diameter (mm)	13.0

3.5.1 Transmission stiffness

The transmission stiffness has a compelling effect on the system repeatability and accuracy. **Fig. 3.9a-b** illustrate the trends of transmission stiffness under various pipe diameters and lengths. The stiffness decreases when the diameter or the length increases. It can also be observed that the choice of pipe material imposes a significant influence on the transmission stiffness. PA66 offers the highest transmission stiffness because it possesses the highest Young's modulus. However, the large bending stiffness of PA66 (0.17 N-m^2 with outer/inner diameter of ⌀6/4 mm) would hinder its application in conditions that requires flexible arrangement. **Fig. 3.9c** shows that the enlargement of piston diameter could also enhance the transmission stiffness, because of the increased piston diameter to pipe inner diameter ratio.

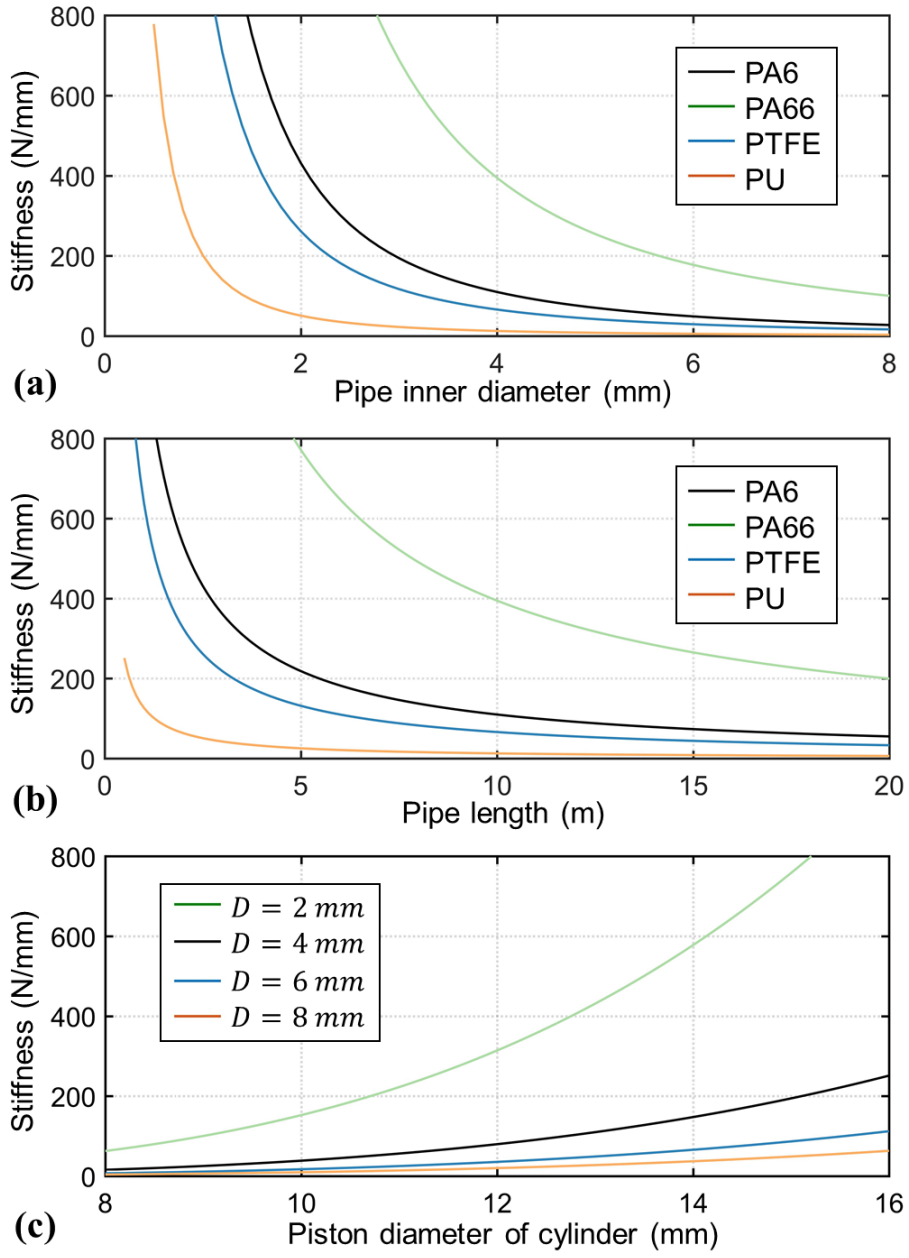

Fig. 3.9: Simulation results showing the trend of transmission stiffness against: **(a)** the pipe inner diameter; **(b)** the pipe length; and **(c)** the piston diameter. It can be observed that the stiffness profile is significantly affect by the pipe materials: polycaprolactam 6 (PA 6), polycaprolactam 66 (PA 66), polytetrafluoroethylene (PTFE) and polyurethane (PU).

3.5.2 Transmission latency

The power transmission in this system could be considered as the simultaneous occurrence of pressure and velocity changes. Such velocity of pressure transient through fluid in a closed conduit could be deduced as:

$$c_p = \left(\sqrt{\frac{\rho \psi D_{pi}}{e \cdot E} + \frac{\rho}{E_v}} \right)^{-1} \tag{3.14}$$

where the relevant parameters are described in **Table 3.4** [164]. The pipe support factor ψ is a function of the pipe material (ν), the pipe inner diameter (D_{pi}) and the pipe wall thickness (T_p), which can be calculated as following for the case of thick-walled pipe ($D_{pi}/T_p < 10$) without anchorage throughout the length [164]: $\psi = 2e(1+\upsilon)/D_{pi} + D_{pi}/(D_{pi}+T_p)$.

Table 3.4: Physical parameters

Parameter	Parameter name
c_p	Velocity of pressure transient in fluid
E_v	Bulk modulus of fluid
E	Young's modulus of pipe material
ν	Poisson's ratio of pipe material
ρ	Fluid density
D_{pi}	Pipe inner diameter
e	Pipe wall thickness
ψ	Pipe support factor

Fig. 3.10a-b show that the predicted transmission latency was around 21 ms (with the ratio of pipe inner diameter to thickness varying and pipe thickness fixed at 1 mm). The enlargement of pipe inner diameter over 2 mm would cause a slight increase of latency. But the decline of the diameter under 1 mm would bring a significant rise in latency. The latency is also proportional to the pipe length. And more rigid pipe material can reduce the transmission latency.

3.5.3 Bending stiffness

The pipelines' bending stiffness can influence the system setup by affecting the maximum tube bending curvature, which would hence affect the arrangement flexibility of the whole system. **Fig. 3.11** informs that the stiffness of the pipe will increase when the pipe diameter raises, indicating a larger bending radius and more difficult arrangement for the pipe. The materials of pipe can also result in four bending stiffness curves, ranging from 0.05 to 0.17 N-m^2.

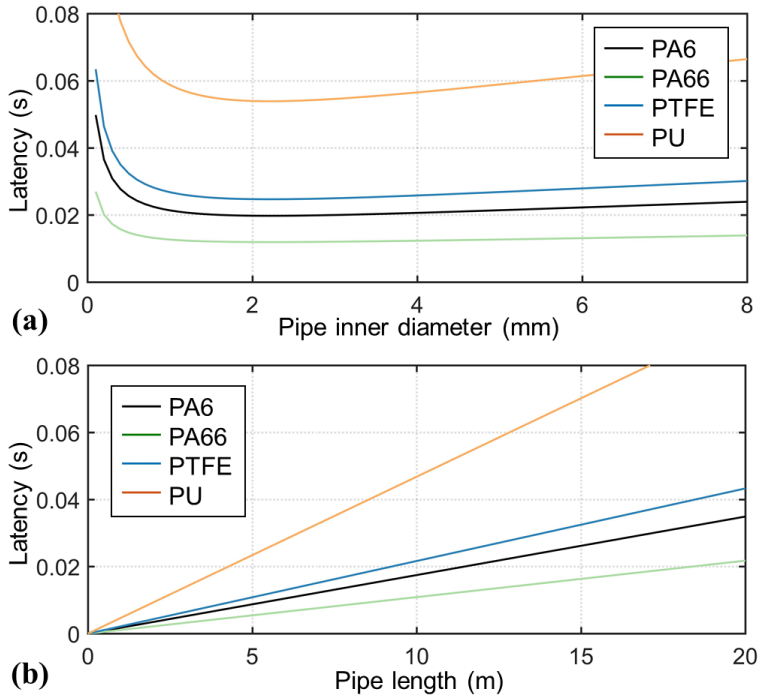

Fig. 3.10: Plot of transmission latency against: **(a)** the pipe inner diameter; **(b)** the pipe length.

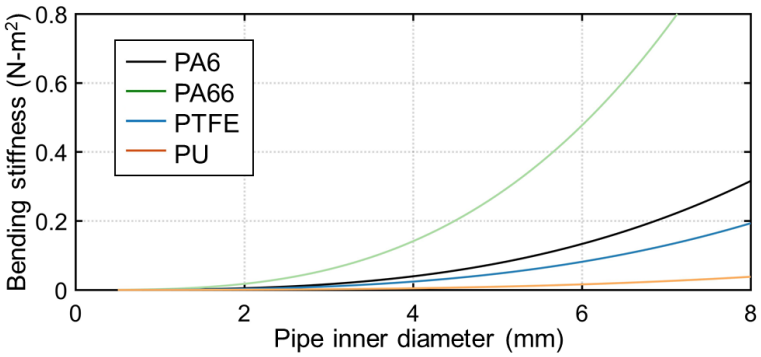

Fig. 3.11: Simulation result illustrating the trends of bending stiffness against the pipe inner diameter.

Overall, several design tradeoffs haven been investigated to account for the required dynamics performance and dedicated operating conditions. Shorter pipelines are preferable as a general design rule to reduce the fluid inertia, give rise to a higher transmission stiffness, and decrease the transmission latency. For surgical applications that emphasize positional accuracy, such as breast or prostate biopsy, pipelines with a smaller diameter and pistons with a larger diameter should be adopted to enhance the transmission stiffness. However, a small pipe diameter ($<$ 1 mm) would dramatically increase transmission latency and damping, which would deteriorate the control and stability. Therefore, the pipeline diameter shall be expanded to accommodate for applications that require a fast dynamic response, such as tele-manipulation of a catheter in a master-slave manner.

3.5.4 Towards maintaining a reliable hydraulic system

To enhance the transmission efficiency, the liquid in pipelines can be preloaded at the same pressure (0.05-0.2 MPa) before operation. It can increase the transmission stiffness in three ways: 1) reducing the volume of micro air bubbles that have been inadvertently drawn into the pipelines during their connection; 2) pre-stretching the rolling diaphragm that is naturally flexible in shape; 3) reducing the gear backlash, where the rack and pinion tooth being pushed tightly in contact under the preloaded pressure. **Fig. 3.12a-b** respectively demonstrate the setup and pipeline schematic of the preloading system for the two-cylinder actuator. A water reservoir was connected to the pipelines in order to prevent entering of air bubbles. The fluid in pipelines can be pre-loaded by a pressurized air source or air pump before actuation. Upon the motor actuation, the valves are closed to isolate the two hydraulic pipelines, thus enabling the master-slave hydraulic actuation. This preloading system can be readily used for actuators with more than two cylinders by adding extra pipelines.

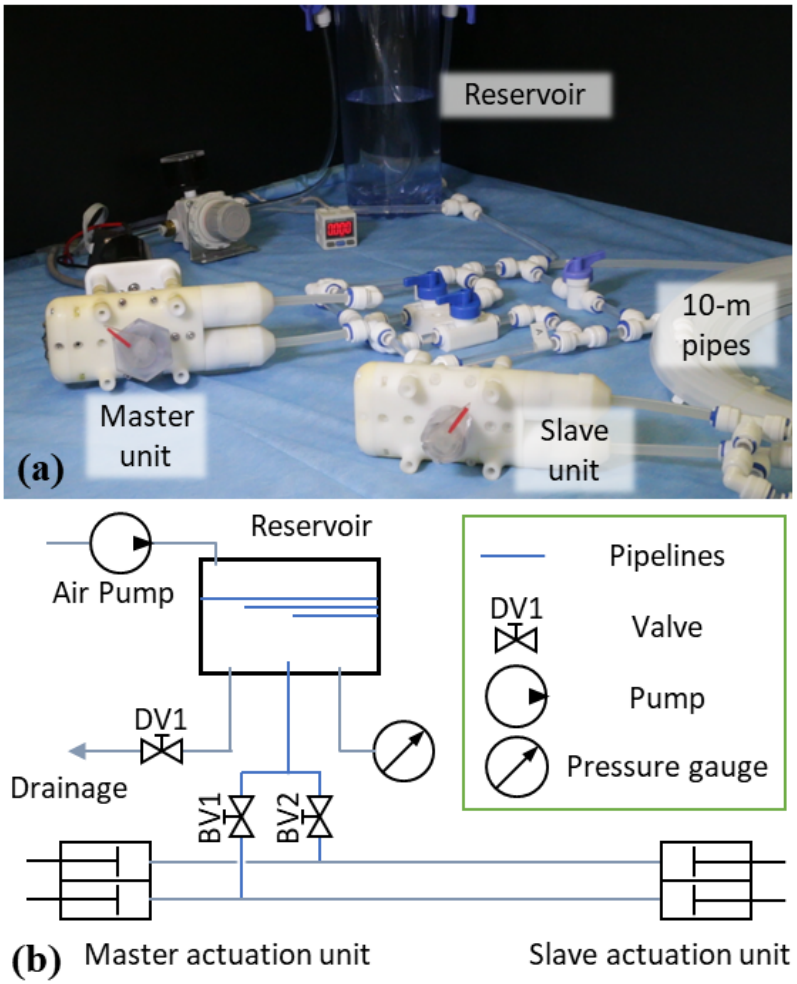

Fig. 3.12: **(a)** Setup of the preloading system for the two-cylinder actuator; **(b)** Schematic diagram showing the pipeline connection of two-cylinder actuator with preloading system.

3.6 Experimental evaluation of motor performance

Several experiments have been conducted to evaluate key performance indices of the proposed hydraulic transmission, including step response, force transmission, positional frequency response and sinusoidal positional tracking. In all these experiments, master and slave units were connected by 10-meter semi-rigid nylon (PA 6) tubes, which had inner and outer diameters of ⌀4 mm and ⌀6 mm, respectively. Distilled water was chosen as the transmission media, accrediting to its incompressibility and convenient implementation. The water pressure preloaded in all pipelines was controlled by the system in **Fig. 3.12**. Not only could this eliminate backlash, but it could also ensure the symmetric folding/unfolding of rolling diaphragms, thus reducing friction during fast motion transmission.

3.6.1 MRI compatibility test

A signal-to-noise ratio (SNR) test was conducted to evaluate the electromagnetic (EM) interference to the MR images with the operation of the three-cylinder motor. The slave part of the motors involved exclusively non-metallic, non-conducting, and non-magnetic materials, thus fulfilling the MR safe classification from American Society for Testing and Materials (ASTM) standard F2503-13 [76]. The slave part of the motor was tested in a 1.5T MRI scanner (SIGNA, General Electric Company, USA) and was placed near a commercial MRI phantom (J8931, J.M. Specialty Parts, USA) at the isocenter of the scanner (**Fig. 3.13**). The T1-weighted fast field echo (FFE) and T2-weighted turbo spin echo (TSE) sequences were adopted to obtain the MR images.

Fig. 3.14a shows the resultant MR images of the MRI phantom by T1 and T2-weighted sequences under four different conditions: i) *Phantom*: only the MRI phantom was placed in the scanner; ii) *Static*: motor was placed in the scanner and remains powered OFF; iii) *Powered*: motor was in static without motion output, with the electric power was ON; iv) *In motion*: motor in operation. No observable image artifact was found in the MR images under these motor operation scenarios. The SNR analysis followed the guidelines from ASTM F2119-07 [165], with the *phantom* condition served as the baseline for evaluation. **Fig. 3.14b-c** illustrate the results of SNR analysis under the two imaging sequences. The maximum SNR loss in the successive conditions was found within 2% only, even with the motor in full motion.

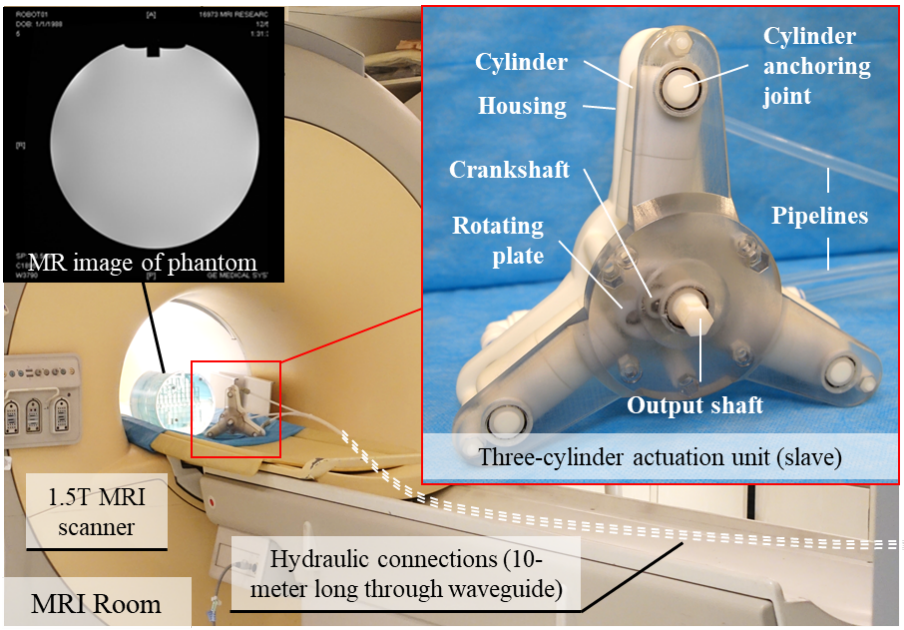

Fig. 3.13: Setup of the three-cylinder motor in the 1.5T MRI scanner. This MR safe motor was connected with three hydraulic pipelines, which transmitted motion from the master unit in the control room. The MR image of an MRI phantom placed aside the actuator indicates the negligible EM interference.

3.6.2 Step response of hydraulic transmission

Step response experiments were conducted to evaluate the force transmission behavior between two cylinders, which were connected by a hydraulic pipeline (**Fig. 3.1**). At the master side, a DC motor actuated the master cylinder through the rack-and-pinion mechanism, which converted rotational torque to linear force. The output force at slave cylinder was measured by a force sensor (MIK-LCS1, Hangzhou Meacon Automation Technology Co., Ltd) embedded on the piston rod. Water in the pipelines was preloaded at 0.05 MPa to ensure the mechanical couplings were fully engaged, which corresponded to 5 N force output on the slave cylinder at the initial state. Two step inputs, i.e. 26 N and 78 N, were applied to the master cylinder. The corresponding measured force responses are shown in **Fig. 3.15**. Simulated results deduced by the dynamics model in **Section 3.4** are also overlaid, predicting a similar response to the measured results. The response time was within 40 ms from the signal input and the 10%-to-90% rise time was 25 ms for both step input forces. This rise time remains constant for different input forces, depicting an important feature for a linear time-invariant system. The settling time with 5% error band was about 0.17 s, indicating that the proposed hydraulic transmission could rapidly transmit the force, even via a 10-meter long pipeline. These characteristics are crucial to the highly responsive force transmission required in many tele-operated robot systems.

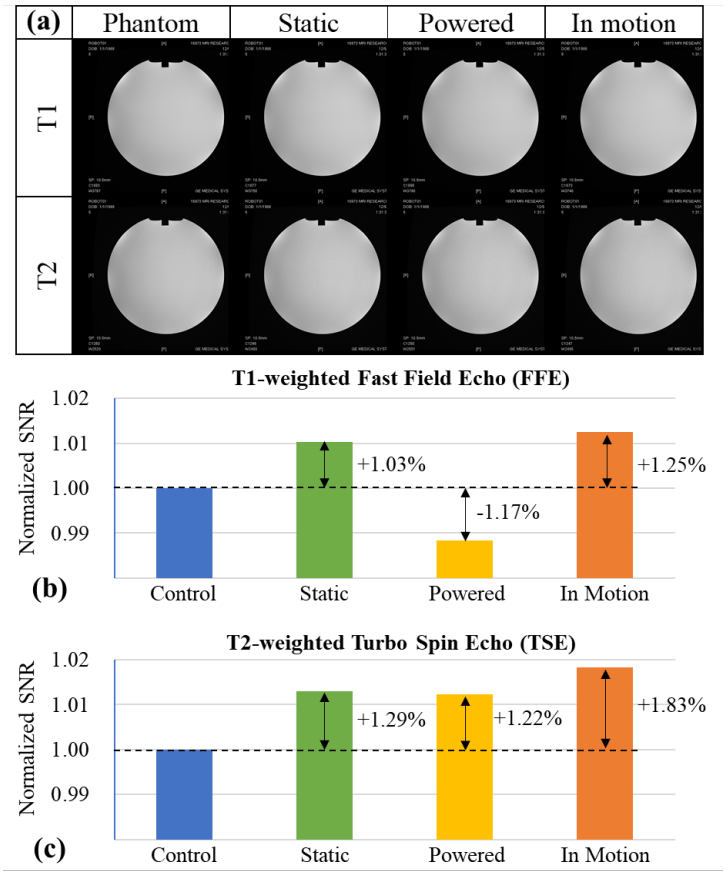

Fig. 3.14: **(a)** MR images of an MRI phantom placed aside the robot indicating the negligible electromagnetic (EM) interference in four operating conditions. Signal-to-noise ratio (SNR) test results with sequence of **(b)** T1-weighted fast field echo (FFE); **(c)** T2-weighted turbo spin echo (TSE). Both sequences show the SNR losses below 2% in all conditions.

3.6.3 Transmission hysteresis

Hysteresis is the primary concern for interventions that requires accurate manipulation of instruments with high resolution. The hysteresis of the pair of two-cylinder actuation units was measured, with the results shown in **Fig. 3.16**. The translational positions of the master and slave pistons were measured at four levels of preloaded fluid pressure inside the pipelines (0.05-0.20 MPa). The periodic motion of the master unit was controlled by the embedded proportional–integral–derivative (PID) positional controller at a frequency of 0.1 Hz, where 70% of the stroke-length was covered. The hysteresis was generally uniform throughout the whole range of motion, particularly at higher preloaded pressures. The average values of hysteresis were 0.88 mm, 0.93 mm, 1.02 mm, 1.29 mm for preloaded pressure 0.05 MPa, 0.1 MPa, 0.15 MPa and 0.2 MPa, respectively. The hysteresis only slightly increased with the preloaded pressure, potentially due to the rise in static friction between the gears.

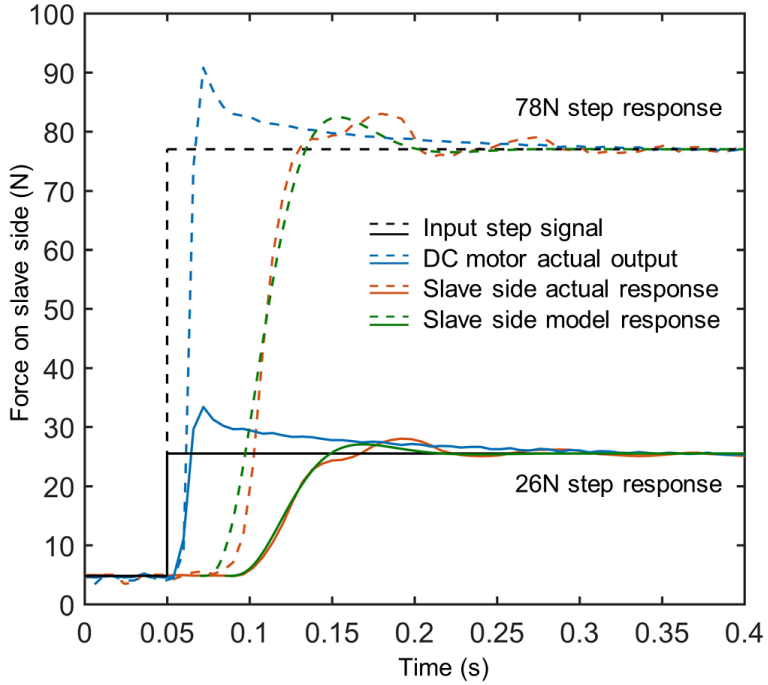

Fig. 3.15: Experimental step response of a single cylinder transmission, which were measured in two different steps of magnitudes. Actual and modeled responses are compared. Response time from the signal input was within 40 ms.

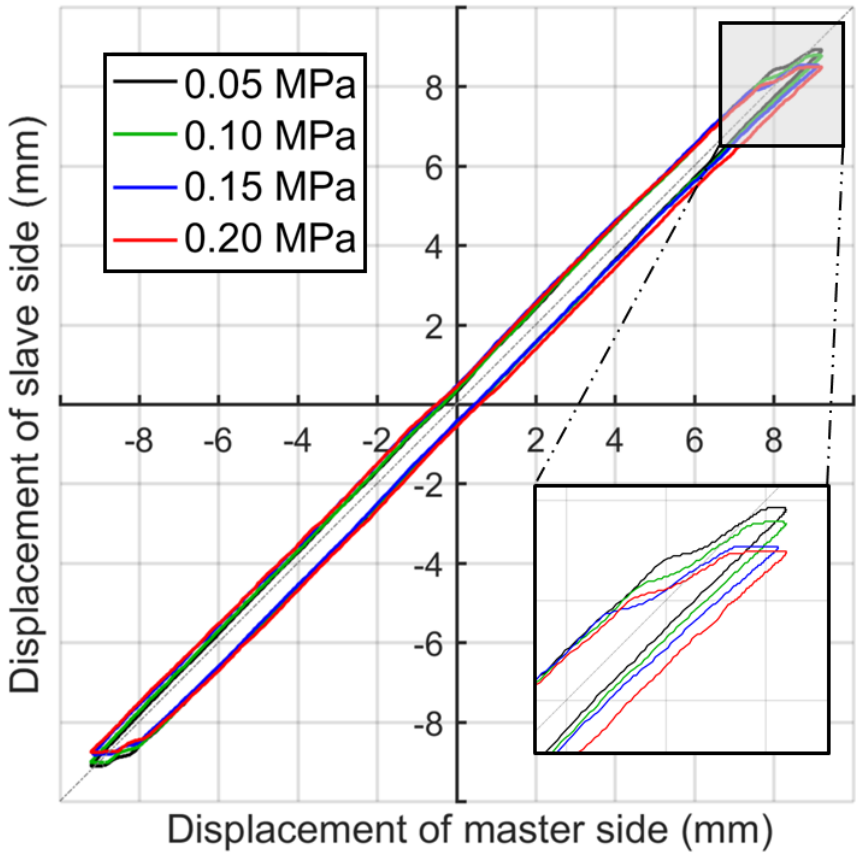

Fig. 3.16: Diagram illustrating the transmission hysteresis of the two-cylinder actuator, which were evaluated at four levels of fluid preloading pressures (0.05-0.20 MPa).

3.6.4 Sinusoidal positional tracking

To evaluate the accuracy of the hydraulic actuator under open-loop control, a positional tracking test was performed. No loading was added to the slave actuator. For both the two- and three-cylinder actuators, the slave unit was controlled to follow the periodic sinusoidal input of master actuator under open-loop control, where the angular position is $\theta = A\sin(\omega \cdot t)$. The three master cylinders were controlled based on the inverse kinematics derived in **Section 3.4**. The output angular position was measured by a differential encoder coupled with the output shaft. The frequency of periodic sinusoidal input at the master side was kept low, which was 0.1 Hz, in order to minimize the dynamics effect such as fluid damping.

Two-cylinder configuration: **Fig. 3.17** depicts that the slave actuation unit of two-cylinder configuration could precisely follow a sinusoidal trajectory of the master unit. The maximum absolute positional error was 0.67 mm. The motion range was short (18 mm) for this configuration, due to the limited cylinder stroke.

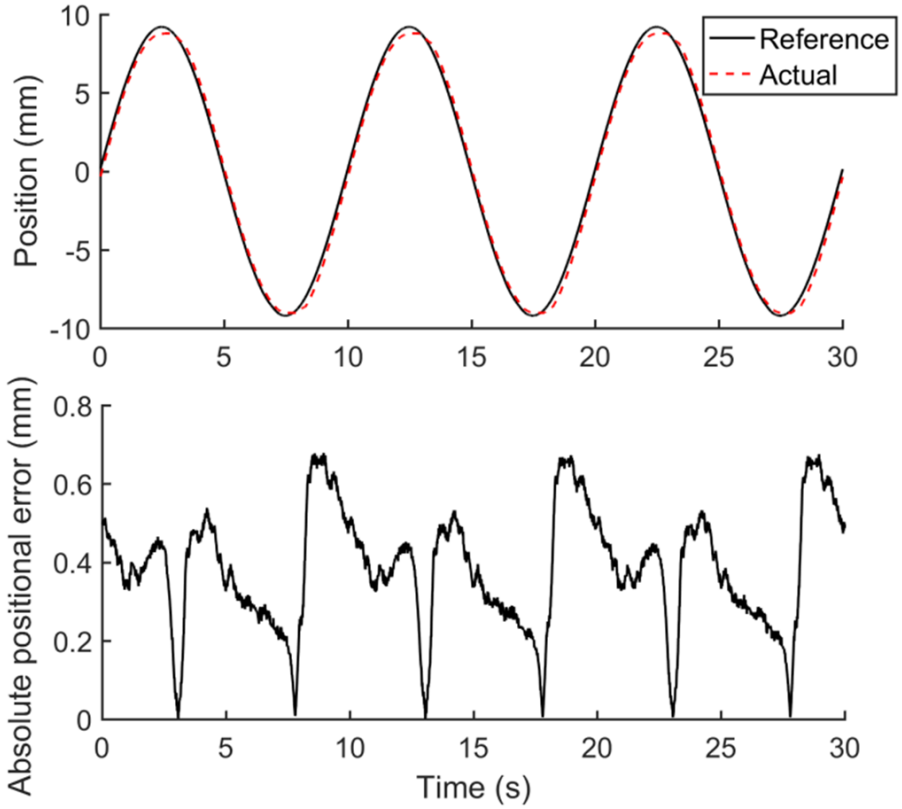

Fig. 3.17: Sinusoidal angular positional tracking of the two-cylinder actuator. The angular position of the slave actuation unit can accurately follow input from the master unit at 0.1 Hz.

Three-cylinder configuration: In the experiment, the periodic sinusoidal input at the master side covered a larger motion range of 360°. This sinusoidal tracking performance is illustrated in **Fig. 3.18**, which shows the input and output angular motion profile, as well as the corresponding error in angular displacement. It also demonstrates the three-cylinder continuous actuator can track the positional input over the range of 360°. The average error between the input and output within one cycle was 0.64°, demonstrating an accurate feed-forward control performance.

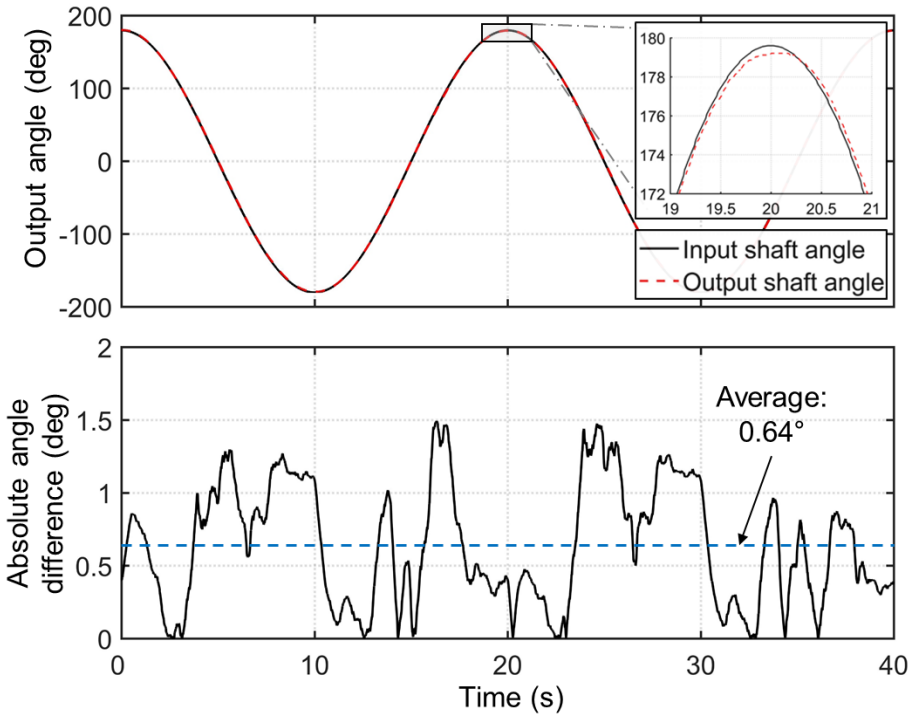

Fig. 3.18: Sinusoidal tracking of angular displacement during the three-cylinder actuation throughout two cycles in 40s. Precise feed-forward control can be observed, with an average absolute error of 0.64°.

3.6.5 Transmission stiffness

Transmission stiffness is a critical index which can characterize the response and steadiness of a hydraulic actuator. The stiffness of the presented master-slave two-cylinder actuator (**Fig. 3.3**) was experimentally measured. The input shaft at the master side was actuated by a DC motor. The input torque and angular displacement were measured by a torque sensor and differential encoder, respectively. With the slave side fixed, transmission stiffness could be deduced by the torque and angular position at the master side. In every test cycle, the input torque was alternated between the positive and negative extremes. This torque was changed in a quasi-static manner, once per 10 seconds (≈0.1 Hz), in order to minimize the dynamics effect such as fluid damping. This test was repeated under four different conditions of fluid

preloading levels, i.e. 0.05, 0.10, 0.15 and 0.20 MPa.

Fig. 3.19 shows the torque-angle diagram. The recorded data at four preloading levels were linearly fitted using least square regression. A highly linear relation between torque and angular displacement can be found, corresponding to a spring-like stiffness behavior of the hydraulic transmission. Furthermore, there is a clear trend that the increase in preloaded pressure can improve the transmission stiffness. This is consistent with the prediction in **Section 3.5.1**. In the mechanical model, the hydraulic fluid (water) is assumed to be incompressible, and the transmission stiffness is mainly attributed to the compliance of nylon hydraulic pipes. Preloading on fluid can pre-stretch, thus stiffen the nylon pipes. Meanwhile, the torque transmission hysteresis reveals in the same diagram (**Fig. 3.19**) as well. The area inside the hysteresis profile, enclosed by forward and backward transmission, indicates the energy loss during one cycle. Higher preloading pressure would also lead to more significant hysteresis, as it can tighten the gears to reduce backlash, but inevitably giving rise to the friction between gears.

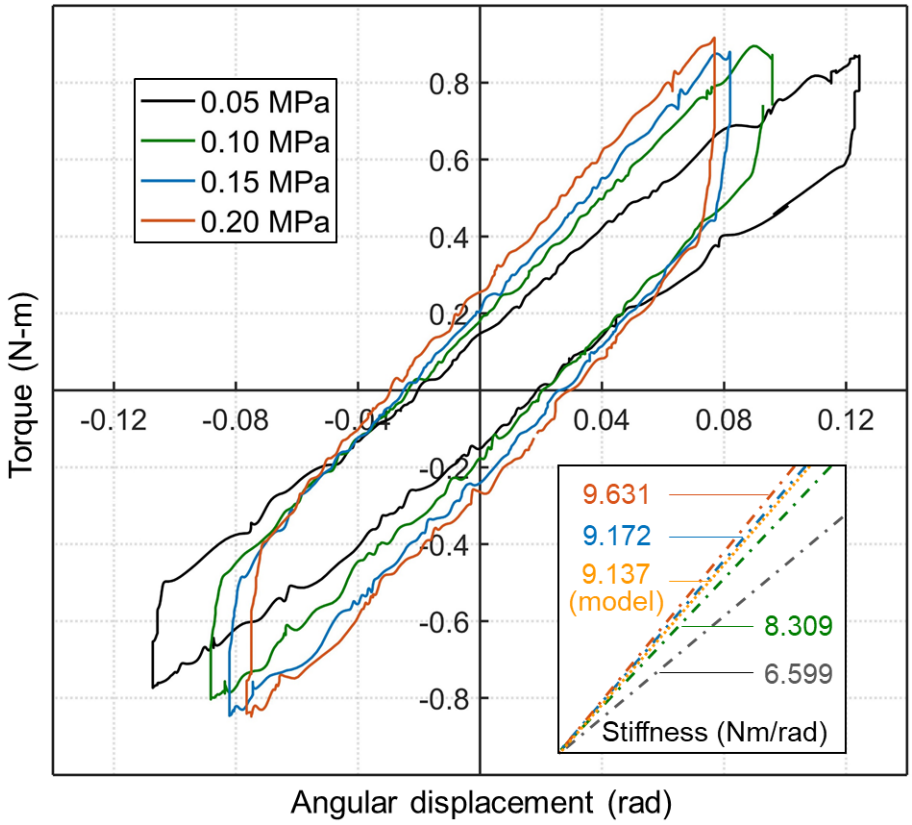

Fig. 3.19: Torque-displacement trials of two-cylinder actuation under four levels of hydraulic pressure (0.05-0.20 MPa) preloaded. Motion hysteresis can also be observed from the corresponding enclosure area, and the stiffness profiles can be denoted by the overall regression slope, ranging from 6.60 to 9.63 Nm/rad.

3.6.6 Force transmission performance

Two-cylinder configuration: The force transmission performance of the master–slave actuator was evaluated by a weight-lifting experiment. In this experiment, a rotary slave actuator depicted in **Fig. 3.3a** was coupled to a winch with 5-cm radius. With the hydraulic fluid preloaded at 0.1 MPa, the master–slave actuator was capable of lifting a 3-kg mass at a constant velocity of 10.01 cm/s, corresponding to an output torque of 1.47 Nm and net power of 2.93 W. The input torque at the motor axis on master side was also monitored by a torque sensor, which was used to estimate the hydraulic force transmission efficiency as 70%.

Three-cylinder configuration: Force transmission performance of the three-cylinder continuous motor was evaluated in a weight-lifting experiment, in which three master cylinders were individually actuated by electric motors through leadscrew drives. The output shaft was coupled to a winch of diameter ⌀40 mm. With the hydraulic fluid preloaded at 0.1 MPa, the master-slave actuator could lift a 2.5-kg load at a constant velocity of 50.24 mm/s, corresponding to an output torque of 0.49 Nm and a net power of 1.23 W. The volumetric power density of the hydraulic transmission was 2.46 kW/m^3. The torque/power outputs of this motor were mainly determined by the electric motor inputs at the master side. In principle, the continuous motor can generate power as much as the electric motors can afford, until the weakest component with lower strength limit fails, such as tiny gear teeth and thin rolling diaphragms.

In fact, the maximum torque of the present prototype is limited by the mechanical strength of the 3D printed components. In the practice for animal/human trials, the robot prototype ought to be fabricated with standard industrial machining procedures. Wider choices of MR safe materials, such as Acetal, Nylon or any strong resilient plastic, will be used to comprise more robust structure for promising durability and enhanced actuation torque.

3.6.7 Frequency response of the transmission

Two-cylinder configuration: For a linear time-invariant system, the frequency response at steady state can be described by $\tau_{ss} = M \cdot sin(\omega t + \xi)$, where M is the "magnification" and the ξ is the "phase-shift". The Bode plot of the two-cylinder hydraulic transmission is illustrated in **Fig. 3.20**. The magnitude plot shows a growing trend of the transmission magnification when the preloaded fluid pressure increases. The peak of the magnification was at around 5 Hz, which could be regarded as the natural frequency of the overall hydraulic transmission. The increase of preloaded fluid pressure did not significantly affect the natural frequency. The transmission phase lag remained around 25° within the low actuation frequency ($\leq$ 1 Hz), and was not influenced by the preloaded fluid pressure. Small time delay could be observed for the transmission at 0.2-MPa preloaded pressure, with values of 45 ms and 66 ms at the frequency 1 Hz and 15 Hz, respectively. The natural frequency and phase-shift could be attributed to the compliance of the rolling diaphragms and 10-m long semi-rigid tubes, as well as the micro air bubbles in the fluid.

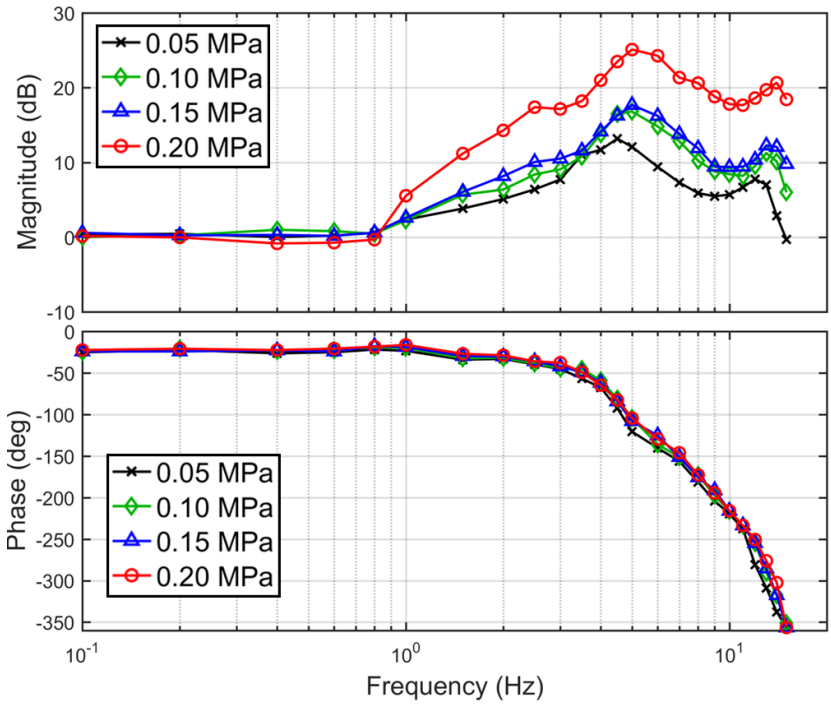

Fig. 3.20: Bode plot showing torque transmission response of the master-slave hydraulic actuation unit at four preloaded fluid pressures (0.05-0.20 MPa). The magnitude (top) and phase shift (bottom) are shown. The data was collected in 10 cycles at the steady state.

Three-cylinder configuration: The dynamics performance of a three-cylinder continuous actuator (**Fig. 3.5**) was investigated with a frequency response method. No loading was added to the slave actuator. The three master cylinders were controlled based on the inverse kinematics derived in **Section 3.3.2**. The slave actuator could thus follow the periodic sinusoidal input of master actuator under open-loop control, where the angular position $\theta = A\sin(\omega \cdot t)$. The amplitude was 5° and the test frequency was from 0.1 Hz to 7 Hz. The output angular position was measured by a differential encoder coupled with the output shaft. **Fig. 3.21** illustrates the Bode plots of magnitude M and the phase-shift ξ of the continuous actuator at steady state. Note that for a linear time-invariant system, the frequency response at steady state becomes $\tau_{ss} = M \cdot A\sin(\omega \cdot t + \xi)$. The magnitude plot indicates that the magnification increases with higher preloaded fluid pressures. The magnification value peaked at around 5 Hz, which corresponded to the natural frequency of the overall hydraulic transmission. The phase lag of the transmission was kept at around 20.3° for low actuation frequency ($\leq$ 2 Hz). It was also found that the increase of the preloaded fluid pressure did not significantly affect the natural frequency and phase lag. The transmission with preloaded fluid pressure 0.2 MPa had small time delay only: 60 ms and 52 ms at actuation frequency 1 Hz and 5 Hz, respectively.

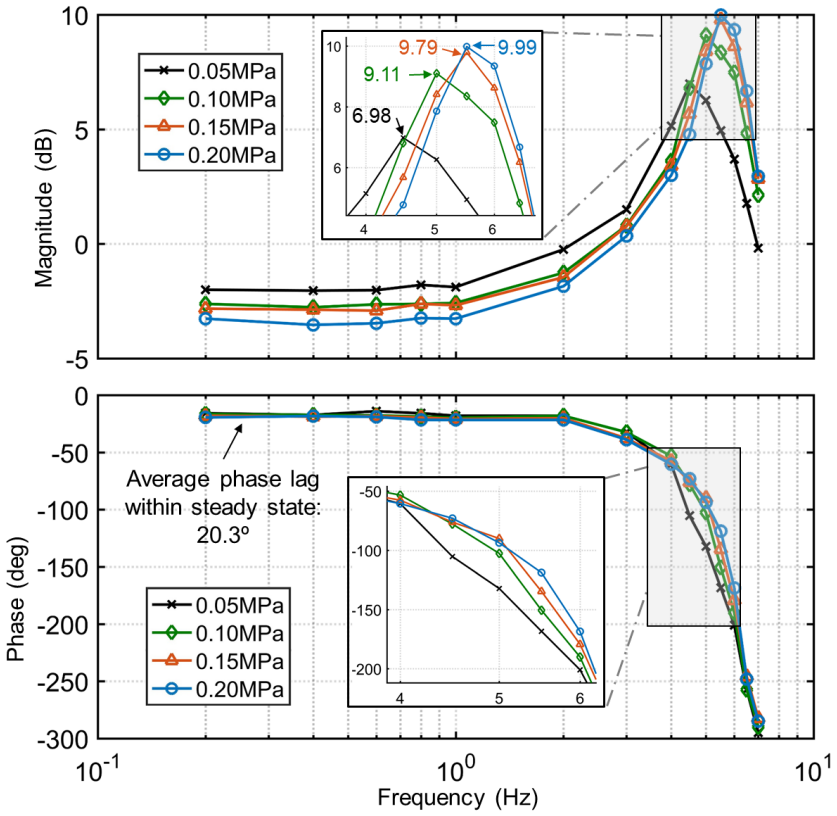

Fig. 3.21: Experimental frequency response of the three-cylinder actuation at four levels of hydraulic pressure. The input is positional signal, and the output displacement was measured by encoder at slave-side actuation unit.

In summary, the master-slave actuator had fast step response ($<$ 40 ms), high transmission stiffness (9.63 Nm/rad at 0.2 MPa), quick frequency response (60 ms at 1 Hz and 0.2 MPa), and precise feed-forward control (average error of 0.64°). Higher transmission stiffness could be attained by increasing the fluid preloading level, as shown in the stiffness plot (**Fig. 3.19**). The performance in step response (**Fig. 3.15**) and frequency response (Bode plot, **Fig. 3.21**) has demonstrated that sufficiently low latency of force/position transfer could be maintained in a range of 0.1-2.0 Hz.

3.7 Conclusion

In this chapter, MR safe hydraulic motors are presented, which incorporate rolling-diaphragm-sealed cylinders for high-fidelity robotic tele-operation. The configurable MR safe motor is capable of offering continuous bidirectional rotation with unlimited range. These capabilities would be comparable to the conventional electric motor for versatile applications even involving high payload manipulation. It also features fast response (rise time $<$ 40 ms), precise open-loop control of position (average error of 0.64°) and high output torque (0.49 N-m) through 10-meter long hydraulic pipelines. Currently, there is no such kind of MR safe hydraulic master-slave follower. Both kinematics and dynamics models of the motor have also been devised to identify the key design parameters governing the system performance, namely transmission stiffness and latency. Their design tradeoffs are presented in an analytical study.

The current limitation of the proposed MR safe hydraulic actuators is mainly on the relatively large size (two-cylinder: $85\times60\times28$ mm^3; three-cylinder: $150\times140\times46$ mm^3). The large actuator size would cause obstacle to reduce robot overall dimension, particularly for the robots involving high number of DoF and used inside/under the head/body coils with confined workspace. In our future work, we intend to miniaturize the size of hydraulic actuators in two approaches: 1) optimizing the motor structure with more compact design; 2) customizing the rolling diaphragm with reduced size.

In summary, the proposed hydraulic actuation methods, particularly the three-cylinder configuration, would offer many opportunities for MR safe/conditional robot. The motors could be further implemented to other interventions demanding for intra-op MRI guidance, such as breast and prostate biopsy. MRI-guided robotic catheter platform for cardiac EP (**Chapter 5**) and robotic manipulator for functional stereotactic neurosurgery (**Chapter 4**)

are our recent examples. It is anticipated that, not only would the surgical workflow be simplified by the presented tele-operation of robot from the control room to MRI suite, but it would also add much confidence to surgeons with clear MR-based guidance revealing on multiple displays in control room, which is particularly crucial to cardiac EP.

Chapter 4

MRI-guided Needle Placement Robotic Systems

4.1 Introduction

In **Chapter 2**, the current development status of neurosurgery and percutaneous interventions is reviewed. Various robotic systems have been developed in an attempt to improve the accuracy and effectiveness of needle/probe targeting and placement. However, few systems could achieve sufficient compactness to be placed within magnetic resonance imaging (MRI) head/body coils, as well as fully magnetic resonance (MR) safe to ensure zero imaging interference during consecutive MR scanning. In light of the unmet technical challenges, MR safe needle positioning robotic systems are proposed and introduced in this chapter, aiming to facilitate improved needle placement accuracy and shortened operational workflow.

Section 4.2 describes an intra-operative (intra-op) MRI-guided robot for bilateral stereotactic procedures. Its compact design can enable robot operation inside the standard MRI head coil with constrained space. MR safe, high-performance hydraulic transmissions (**Chapter 3**) were incorporated in the robot. The robot performance was experimentally validated, as present in **Section 4.4**. The system also incorporated novel MR-based wireless tracking markers, which are capable of offering real-time three-dimensional (3D) instrument localization with a frequency of 30-40 Hz. With assistance of the MR-based tracking system, a navigation test was conducted under standard MRI settings. The hydraulic-actuated robotic platform was proven to have minimal interference to MR

imaging by a signal-to-noise ratio (SNR) test.

A semi-automated robotic system is designed for MRI-guided percutaneous needle procedures (**Section 4.3**), which could be further modified for neurosurgery or other instrument placement procedures. The compact and lightweight structure can enable the direct fixture on patient body as well as needle targeting at multiple locations with several robots. The instrument manipulation can be conducted in a more interactive way, with fine adjustment conducted by the robot following the coarse initial placement by the surgeon.

4.2 Tele-operated robotic system for bilateral stereotactic neurosurgery

After reviewing the current robotic systems for MRI-guided stereotaxy in **Chapter 2**, compactness and MRI compatibility can be concluded as two crucial matters affecting the efficiency and flexibility of robot setup in the hospital. However, quite a few robotic systems could be implemented into the MRI head coil, as well as to conduct the manipulation without diminishing the imaging quality during consecutive MR imaging. No platform could provide bilateral deep brain stimulation (DBS), which is currently the prevalent approach for Parkinson's disease (PD) [89]. Besides, for most of the previous systems, the positional tracking of the instrument was achieved by either passive MR fiducials or optical tracking system, which may introduce large errors during the registration between the coordinates of robot and imaging [90]. In summary, no existing robotic system could conduct stereotactic manipulation for functional neurosurgery inside the MRI bore. To this end, the contributions can be differentiated from previous works in three major aspects:

1. Development of a tele-operated manipulator for bilateral neuro-stereotaxy under intra-op MRI guidance. The robot can be anchored based on a single platform on the patient's skull. Navigation for both bilateral targets can be performed independently and simultaneously;

2. Light-weight (145.4g) and compact ($110.6 \times 206.8 \times 33.2$ mm^3) robot design. It can enable the robotic operation inside an MR imaging head coil with limited workspace. High-performance hydraulic motors were incorporated to offer MR safe actuation with minimal imaging interference;

3. Intro-op MRI-guided needle navigation accomplished by wireless MR-based tracking markers. Instrument localization in imaging coordinates can be directly acquired in real-time. Offline registration can be avoided for the alignment of imaging and tracking coordinates.

4.2.1 Design criteria torwards effective MRI-guided neurosurgery

The robotic system in **Fig. 4.1** aims to conduct bilateral needle placement procedures, particularly for intra-op MRI-guided DBS. The purpose of the procedure is to place an electrode in the anatomical target, subthalamic nucleus (STN), which has an ellipsoid shape and is located in the deep brain (90 mm under the skull surface) [166]. High-accuracy targeting and placement of the electrode are desired to be <3 mm, in order to optimize stimulation result. To achieve the aim, clinical consideration and robot design criteria are discussed as follows.

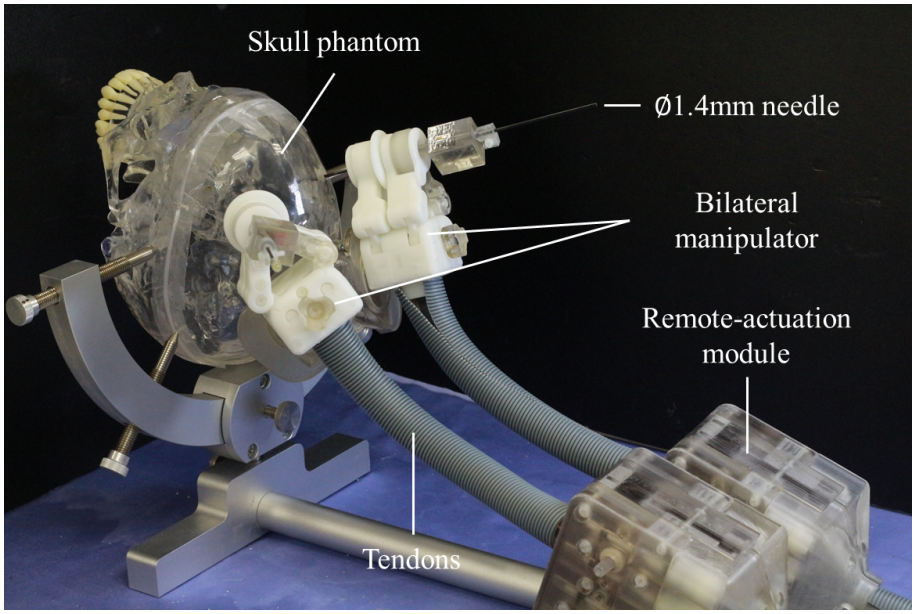

Fig. 4.1: Slave module of the proposed MR safe robot for intra-op MRI-guided bilateral stereotactic procedures.

Workspace and dexterity: Two burr holes are created on the skull for the procedure. The proposed robotic system can be anchored on the middle line of the two burr holes, with each manipulator serving one burr hole (**Fig. 4.2**). For each manipulator, 4-degree-of-freedom (DoF) actuation of the needle guide can be achieved, including pitch, roll, and offset along the parallel plane above the skull tangent surface. This can facilitate alignment of the instrument with the desired straight-line trajectory to the STN. The manipulation actuation ranges include the planar motion in X or Y direction of ± 2.5 mm, pitch angle of $\pm 33°$, and

roll angle of $\pm 26°$. These ranges can be considered to be more than sufficient to fulfill the required workspace in many cases [166].

Insertion path planning: With the 3D intra-op MR images, surgeons can identify the mid-commissural point (MCP), as well as the STN targets according to the anterior commissure-posterior commissure (AC-PC) line, and can consequently define the entry point on skull and insertion path to the target. The coordinate frame of the robotic operation should be identical to the deep brain targets, which is pre-planned based on the AC-PC line. The target location is approximately 12 mm lateral, 5-6 mm inferior, 3-4 mm posterior with respect to (w.r.t.) the MCP (**Fig. 4.2**) [167].

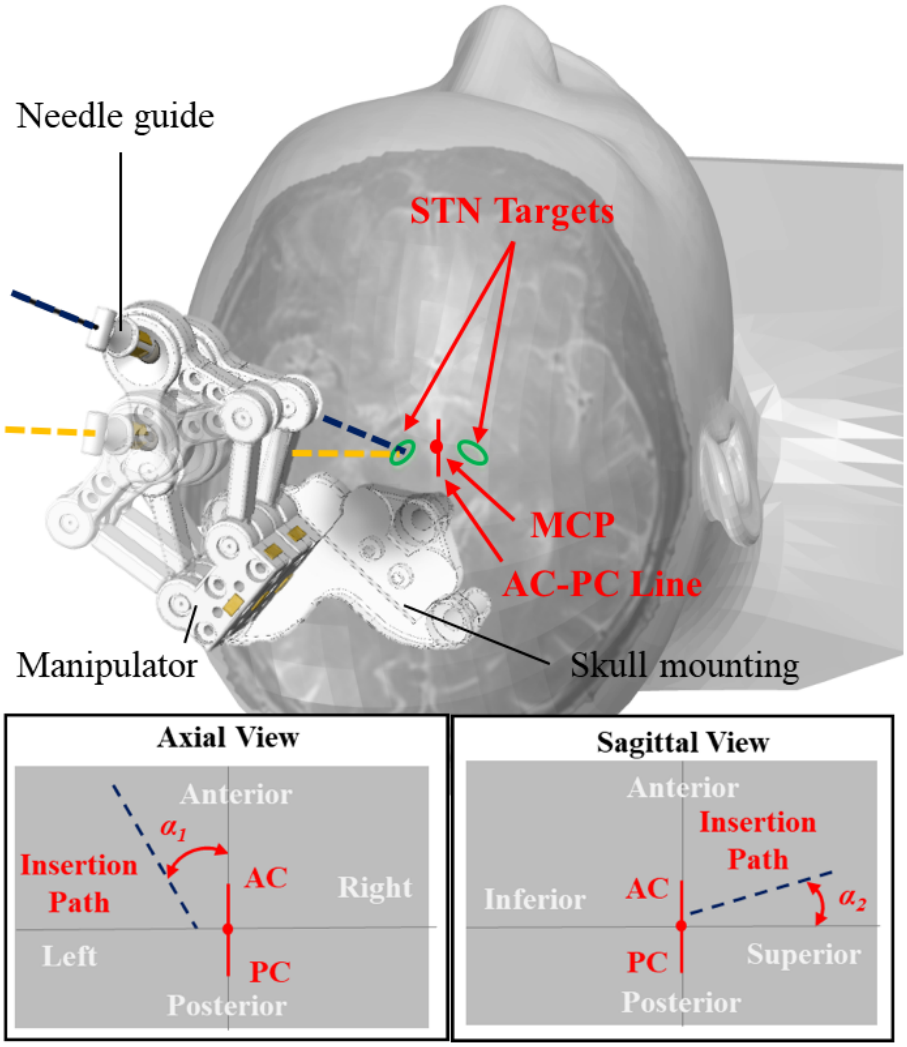

Fig. 4.2: A single manipulator shown with two possible configurations. Bound-aries of subthalamic nucleus (STN) targets highlighted in green, which could be revealed by T2-weighted MRI.

Setup and MR compatibility: The robot is designed to achieve bilateral stereotactic manipulation with the following features: i) the structure of the robot body is compact, such that the robot can be mounted on the skull within the head coil; ii) automatic path planning and instrument adjustment can be conducted; iii) bilateral manipulation can be performed independently; iv) the robotic system can fulfill the standard of American Society for Testing and Materials (ASTM) F2503-13 regarding MRI safety [76].

4.2.2 Tele-operated actuation system

A short-range tendon-driven mechanism (**Fig. 4.3**) is proposed for the slave actuation system, which intends to separate the manipulator from the bulky and heavy actuation module. As illustrated in **Fig. 4.1**, the bilateral manipulators were mounted on the patient's skull. And the actuation module could be accommodated on the operation table. The manipulator and actuation module were connected by short-range flexible tendons. The design can minimize the manipulator size to fit the limited space in MRI head coil, as well as reduce its weight, which may cause discomfort to the patient. Meanwhile, the tendon-driven mechanism can still provide a flexible manipulation as well as an acceptable actuation performance in terms of torque/force, accuracy and responsiveness. To meet the MR conditional standards, most components of the prototype were made of 3D-printed polymers (VeroClear™, Stratasys Inc., USA).

Fig. 4.3 depicts the 1-DoF actuation module for the single layer of the manipulator. The manipulator and slave part of the hydraulic actuation unit were connected by a pair of tendons (≈200 mm) to transmit bidirectional actuation. The tendons had a diameter of ⌀0.16 mm (Dyneema polyethylene (PE), Tokushima Inc., Japan) and covered by Polytetrafluoroethylene (PTFE) sheaths with outer/inner diameter of ⌀2/0.5 mm. The tendon sheath can resist axial compressing force and deformation while the tendons are pulling, which can ensure accurate transmission of force and displacement. The appropriate rigidity of the sheath can also support the tendon route while maintaining sufficient pliability, even under a high tendon pulling force. The low-friction characteristic of PTFE will greatly reduce the tendon-sheath fiction during the actuation. To reduce the actuation hysteresis, two idlers were installed to pre-stretch the tendons, with their translational positions adjustable along the grooves. Other than PTFE, we have also tried Polyetheretherketone (PEEK) for the material of tendon sheath. It has similar performance compared to PTFE, but with a higher axial rigidity to improve the transmission accuracy.

However, it is harder than PTFE and hence has a decreased pliability.

A master-slave actuation system is designed for the robotic tele-manipulation. The master and slave parts located separately in the control room and MRI room, respectively (**Fig. 4.3**). Two-cylinder hydraulic actuators (**Section 3.3**) were integrated into the robotic system. The slave unit was connected through hydraulic pipelines to the master cylinders, which were actuated by electric motors (57BYG250-80, Hongfuda Inc., China). The pipes were made of semi-rigid nylon, having an inner/outer diameter of ⌀2/4 mm and a length of 8 meters. To improve the transmission dynamics performance, the parameters of the hydraulic system were chosen according to the previous studies [138], which suggested a shorter length and larger diameter of pipelines to diminish transmission latency, fluidic friction and energy loss. Incompressible fluid (e.g. water or oil) was filled in the pipes, which were channeled through the waveguide in-between the control and MRI rooms. To further reduce the transmission hysteresis, the fluid was pre-pressured to generate a force onto the piston against the rack-and-pinion gear, reducing the gap between the teeth and hence backlash. Rolling diaphragm seals (⌀15 mm, MCS3014MOP, FEFA Inc., Germany) were adopted in the cylinders to reduce the sliding friction during actuation (**Chapter 3**). The resultant actuation response and efficiency can outperform the conventional O-rings sealings, which generally had a significant sliding friction [140]. The actuator could generate a rotary motion of 100.6°, corresponding to the 201.2° rotation at the base joint of the manipulator.

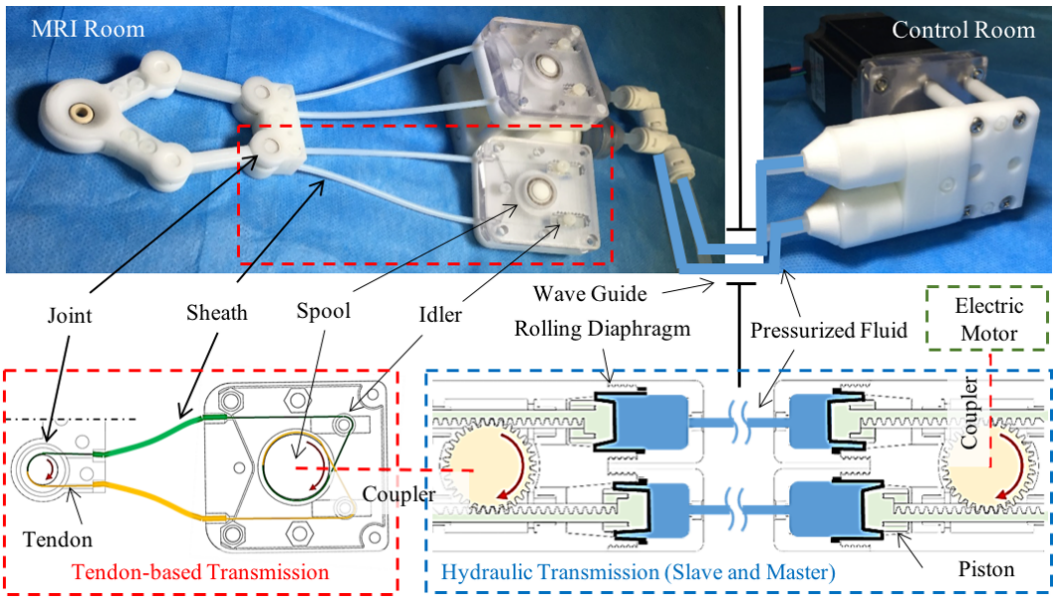

Fig. 4.3: Key components and schematic diagram of a 1-degree-of-freedom (DoF) actuation design for the single layer of manipulator. Master-slave hydraulic transmission was integrated with a tendon-driven mechanism. Hydraulic power was transmitted through 8-m long pipelines through the waveguide in-between control room and MRI room.

4.2.3 Skull-mounted manipulator design

Fig. 4.4a illustrates the structure and components of the robotic bilateral manipulator. It adopts a five-bar planar parallel mechanism for the upper and lower layers of arms, which can enhance positioning accuracy and stiffness compared to the serial-link structure. Large workspace-to-footprint ratio has also been revealed in previous studies [168, 169] for such parallel mechanism. The planar motion can be manipulated by two active revolute joints and three passive revolute joints, providing 2-DoF actuation at the end-effector of each layer. The parallel mechanism has been integrated into the robot to form 4-DoF, five-bar-linkage, double-layer manipulators in a bilateral arrangement.

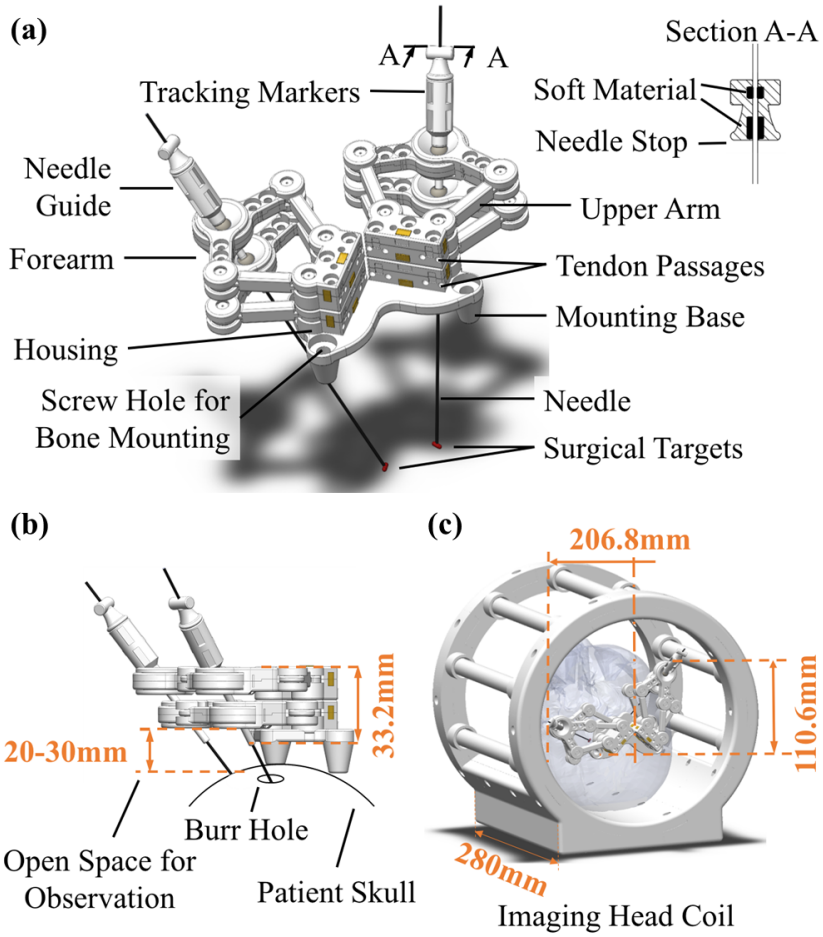

Fig. 4.4: **(a)** 3D model illustrating the robot structure and main components of the two manipulators for bilateral stereotaxy; **(b)** Sufficient space of 20-30 mm from the skull to the manipulator's lower layer, which is reserved for direct observation of burr hole; **(c)** Dimensions with the manipulator placed within a standard MRI head coil.

The bilateral manipulators can be anchored on a mounting base (**Fig. 4.5**), which was affixed to the skull via bone screws. The anchorage locations were positioned apart from the sagittal suture to avoid potential trauma to the patient's brain. The mounting base can be tailored for patient according to the pre-op images, in order to suit the patient-specific skull

curvature (**Fig. 4.4b**). In the current prototype, there was a 20-30 mm spacing between the lower arms to the burr hole, which was reserved for surgeons to have a clearer monitoring on the burr hole in case of any accident. To ensure the remote center of motion (RCM) is located on the burr hole, boundary condition can be set for the 4-DoF needle pose, which could be deduced from the robot kinematics. Eight slots were reserved on the housing surface (**Fig. 4.4a**) for embedding registration markers under MRI guidance. The bilateral manipulators can operate inside the mock head coil (inner diameter: ⌀265 mm), even with the two sides controlled to reach the actuation limits in opposite directions.

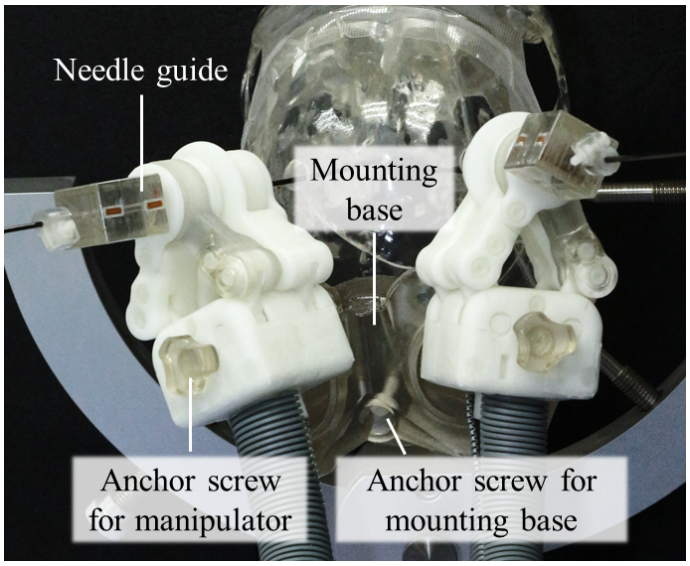

Fig. 4.5: Bilateral manipulators which can be fixed onto the mounting base through an anchor screw. The initial orientation of each manipulator can also be adjusted and fixed by the corresponding anchor screws.

For each manipulator, tendon-driven mechanism was adopted to actuate the four revolute joints and hence the forearms (**Fig. 4.4a**). At the distal end of the forearms, ball joints (igus® Inc., Germany) were incorporated at upper and lower layers. To avoid vertical backlash of the arms and keep a constant distance between the two ball joints, the upper and lower forearms are designed to maintain contact at the sliding plate (**Fig. 4.6**). It can serve as a moving contact plane for the upper forearm, which embedded sliding ceramic balls (**Fig. 4.6**) to reduce the friction. Through controlling the planar positions of the two ball joints, the needle guide orientation can be adjusted. The needle guide was fixed with the upper ball joint to avoid unexpected sliding. Before inserting needle through the needle guide, the desired insertion depth can be preset by a needle stop (**Fig. 4.6**).

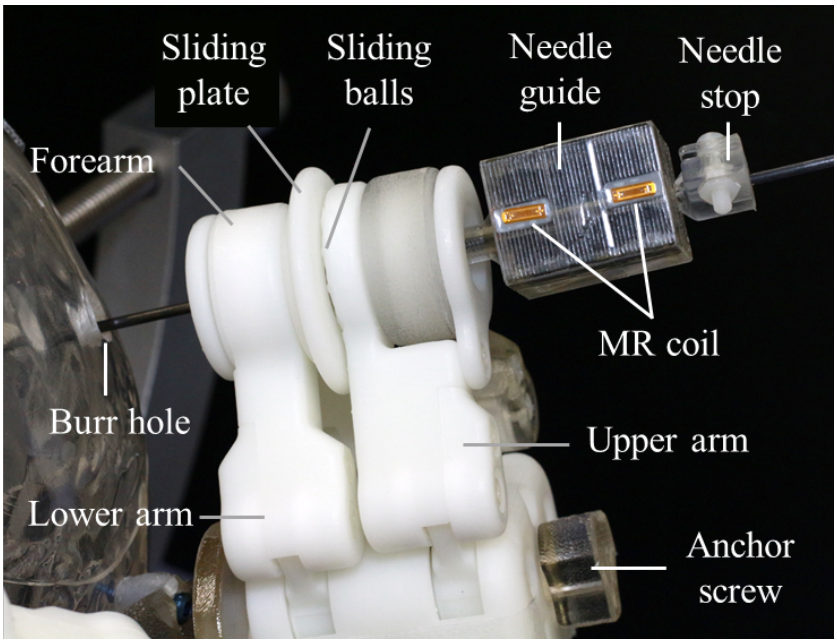

Fig. 4.6: Side view of the single robotic manipulator mounted on the skull. Upper and lower forearms are kept in contact and can move along the sliding plate. The needle guide passes through the ball joints of each layer, with the orientation controlled by the planar positions of the two joints.

4.2.4 Kinematics modeling

Fig. 4.7 describes the kinematics of the double-layer manipulator at one side. The coordinate frames at the housing base and needle tip are defined as $\{\Psi_O\}$ and $\{\Psi_E\}$ respectively. The cannula passes through the upper and lower passive joints, J_{u5} and J_{l5}, respectively. Their planar positions can be manipulated by the individual robotic actuation from the two layers, which contain the points $\mathbf{p}_{uk}$ and $\mathbf{p}_{lk}$ $(k = 1, \cdots, 5)$, where $\mathbf{p} \in \mathbb{R}^3$. These points represent the coordinates of the relevant joints J_{uk}, J_{lk} $(k = 1, \cdots, 5)$, which have the following relations:

$$\begin{cases} \|\mathbf{p}_{u3} - \mathbf{p}_{u5}\| = l_f \\ \|\mathbf{p}_{u4} - \mathbf{p}_{u5}\| = l_f \end{cases} \tag{4.1}$$

$$\begin{cases} \|\mathbf{p}_{l3} - \mathbf{p}_{l5}\| = l_f \\ \|\mathbf{p}_{l4} - \mathbf{p}_{l5}\| = l_f \end{cases} \tag{4.2}$$

The horizontal distance a of the two adjacent base joints (i.e. J_{u1} & J_{u2}, J_{l1} & J_{l2}) is 25 mm. The vertical separation b of the two layers is 16 mm. The inputs values at the actuated joint can be defined as $\mathbf{q} = [q_1, q_2, q_3, q_4]^T$. The actuation ranges of the active joints can be found as $q_1, q_3 \in [29.7^\circ, 195.3^\circ]$ for J_{u1}, J_{l1}, and $q_2, q_4 \in [-15.3^\circ, 150.3^\circ]$ for J_{u2}, J_{l2}. The

forward kinematics can be solved by deducing the needle orientation $\mathbf{r} \in \mathbb{R}^3$ as:

$$\mathbf{r} = \frac{\mathbf{p}_{l5} - \mathbf{p}_{u5}}{\|\mathbf{p}_{l5} - \mathbf{p}_{u5}\|} \tag{4.3}$$

Singularity exists in this five-bar linkage mechanism [170] in two types: (1) the condition when the forearms are collinear; (2) the condition when the arms are fully stretched. To eliminate the collinear condition, a mechanical limit is set for the relative rotational positions of the forearms. For example, joint J_{l5} will be controlled outside quadrangle area of $J_{l1}\,J_{l2}\,J_{l3}\,J_{l4}$. The second condition does not exist in the presented design.

The linear distances between the target and the joints J_{u5} and J_{l5} are defined as d_u and d_l respectively. Then the needle tip position $\mathbf{p}_t$ could be obtained as:

$$\mathbf{p}_t = \mathbf{p}_{u5} + d_u \cdot \mathbf{r} \tag{4.4}$$

Inverse kinematics can be deduced by calculating the joint angles $\mathbf{q} = [q_1, q_2, q_3, q_4]^T$ from the desired needle position, which is obtained by MR imaging. The desired needle position $\mathbf{p}_t$ and orientation $\mathbf{r}$ are defined in $\{\Psi_O\}$. Positions of $\mathbf{p}_{u5}$, $\mathbf{p}_{l5}$ could then be obtained by estimating the needle intersecting locations on the layers:

$$\mathbf{p}_{l5} = \mathbf{p}_t - d_l \cdot \mathbf{r} \quad \text{and} \quad \mathbf{p}_{u5} = \mathbf{p}_t - d_u \cdot \mathbf{r} \tag{4.5}$$

The coordinates of $\mathbf{p}_{u5}$, $\mathbf{p}_{l5}$ are within the triangle $\Delta J_{u1}J_{u3}J_{u5}$ and $\Delta J_{l1}J_{l3}J_{l5}$, respectively. Afterwards, the angle $\angle J_{u3}J_{u1}J_{u5}$ (θ_{u1}) and $\angle J_{u4}J_{u2}J_{u5}$ (θ_{u2}) can be calculated by cosine laws within their triangles:

$$l_f^2 = l_u^2 + \|\mathbf{p}_{u2} - \mathbf{p}_{u5}\|^2 - 2l_u \|\mathbf{p}_{u2} - \mathbf{p}_{u5}\| \cos\theta_{u2} \tag{4.6}$$

$$l_f^2 = l_u^2 + \|\mathbf{p}_{u5} - \mathbf{p}_{u1}\|^2 - 2l_u \|\mathbf{p}_{u5} - \mathbf{p}_{u1}\| \cos\theta_{u1} \tag{4.7}$$

The angles $\angle J_{u2}J_{u1}J_{u5}$ (α_{u1}) and $\angle J_{u5}J_{u2}J_{u1}$ (α_{u2}) can be solved in the triangle $\Delta J_{u1}J_{u2}J_{u5}$. The actuation angles q_3, q_4 can be calculated similarly through the above procedures.

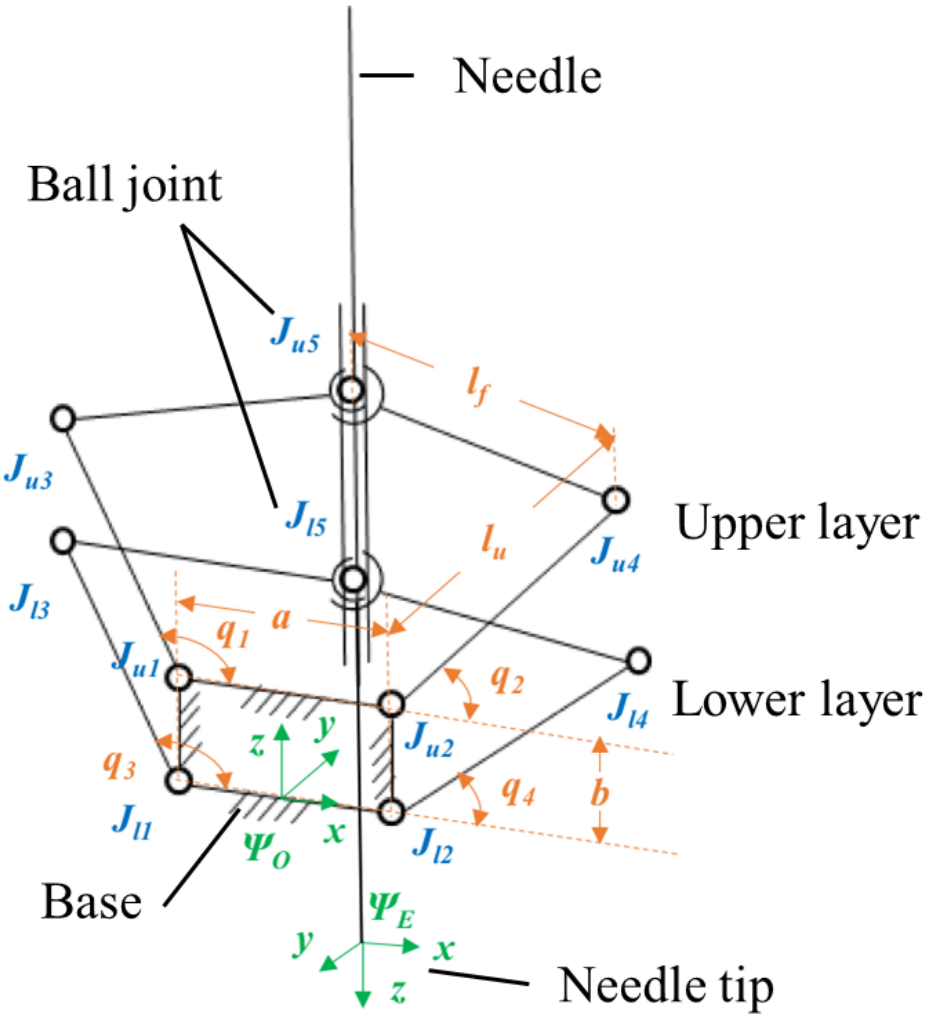

Fig. 4.7: Schematic diagram showing the manipulator kinematics. Mechanism of five-bar linkage is adopted for the upper and lower layers.

4.3 Interactive needle placement robot for percutaneous interventions

This section describes a small-sized patient-mounted robotic system for MRI-guided needle placement, which allows needle targeting and insertion at multiple locations with several robots. The overall procedure time could be shortened by reducing the demand of rescanning, repositioning, and inserting needles for each target. The key contributions are listed as:

1. A patient-mounted robotic device designed for MRI-guided percutaneous procedures. The needle manipulator is semi-automated, with fine adjustment actuated by the robot after coarse initial placement by the surgeon. Visual feedback from light indicator is provided to the surgeon during manual operation for clear, interactive operation;
2. Lightweight (189 g) and compact ($\varnothing$108 mm$\times$115 mm height) robot structure, which allows mounting on the patient and operation with standard loop coils under MRI, even for needle targeting at multiple locations. Fine adjustment can be performed by soft fluid-driven actuators to ensure minimal MR imaging artifacts. Granular jamming was adopted for the locking of the needle guide to prevent undesired movement;

4.3.1 Robot design criteria for MRI-guided percutaneous procedures

The considerations regarding the design and surgical application of the proposed robot are summarized as follows:

1. *Dexterity*: In order to achieve an RCM manipulation for single-port intervention, at least pan and tilt DoFs are required. An ample angle (-32° to 24° about normal from the patient's skin [22]) is desired for flexible adjustment of needle inserting trajectories, particularly for tumors with large dimension ($>\varnothing$3 cm) that require ablation at multiple sites.
2. *Size and weight*: A compact robot structure ($<\varnothing$110 mm) is desired, in order to facilitate flexible anchoring on the patient body within the MRI bore. The robot should be capable of placing in the standard MRI loop coil (Part No. 10185554, Siemens Medical Solutions, USA), which has a diameter of $\varnothing$110 mm. Moreover, multiple incisions with several robots should be considered. The robot should be

lightweight to allow convenient handling by the surgeon, as well as to minimize the burden on the patient.

3. *Positioning accuracy*: By referring to the smallest size of tumor for radiofrequency (RF) ablation, the needle targeting accuracy should be maintained as $<$3 mm [171] at the probe tip.

4. *MR-safety*: The robot should be made of materials that satisfy the MRI compatibility standard ASTM F2503-13 [76]. The material is restricted to those that are not conductive, metallic or magnetic [76]. Besides, electromagnetic (EM) interference should be minimized during the operation of the robot, which may deteriorate the MR imaging quality or device tracking accuracy.

4.3.2 Clinical workflow with proposed robotic system

Four stages are included in the proposed workflow, namely preparation, planning, targeting, and intervention (**Fig. 4.8**). The overall duration is around 3 hours, with time cost for each stage estimated as: (1) Preparation in 20 minutes; (2) Planning in 72 minutes (26 minutes for each MR scan [172]); (3) Targeting in 56 minutes; (4) Intervention in 30 minutes [173]. The overall procedure time is similar to the RF ablation for hepatic malignancies under MRI guidance, generally lasting for 2–5 hours [97]. For the treatment of multiple tumors, the proposed compact and lightweight robot design can offer a more efficient option using several robots for targeting and intervention. Detailed descriptions of each stage are list below:

Stage 1: Preparation. Based on the pre-operative MRI images for early observation and diagnosis, the target location for treatment or biopsy can be roughly estimated. At this stage, the patient is placed on the MRI table.

Stage 2: Planning. The patient undergoes pre-interventional imaging to obtain a high-resolution 3D dataset for the region of interest. The needle insertion path, incision port and hence the robot position can be determined by the surgeon based on this image set. The robot is then attached to the patient body accordingly by adhesive pads and a fastening belt. Robot registration is then performed with a second round of MR scans to localize the robot relative to the target.

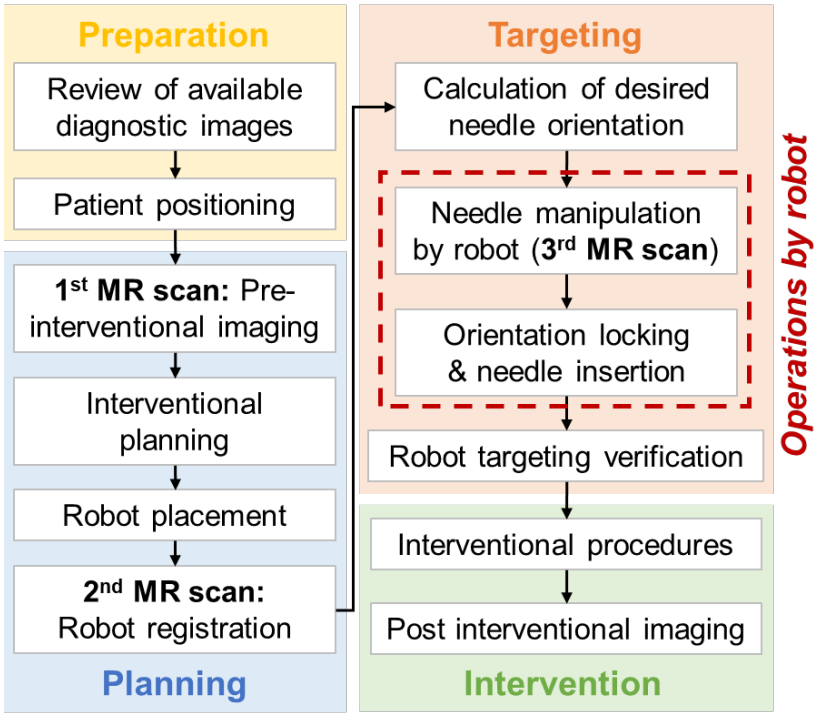

Fig. 4.8: Workflow of MRI-guided percutaneous intervention using the proposed needle robot. The robotic operation is involved in the targeting stage.

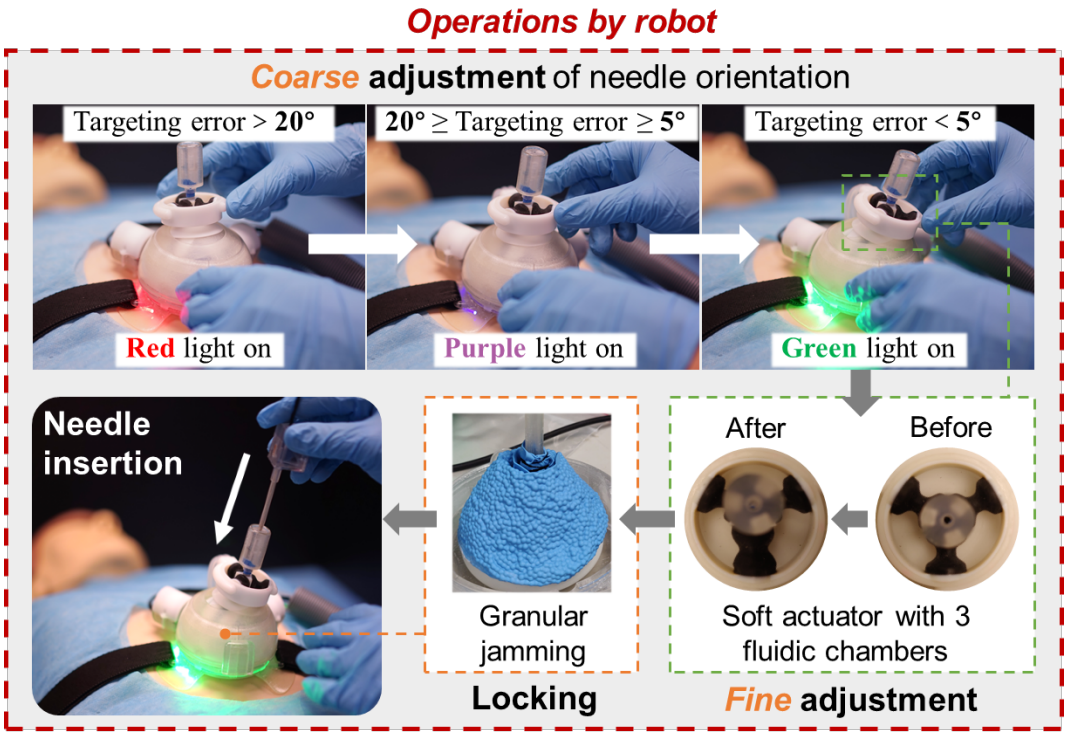

Fig. 4.9: Coarse adjustment of the needle guide while the patient is being outside the scanner bore. Fine adjustment will be tele-operated while being in the bore. The angular error of needle guide can be indicated by colored lighting during the coarse adjustment. The needle guide can be locked by the operator using granular jamming for a precise needle insertion.

Stage 3: Targeting. Targeting can be divided into three steps (**Fig. 4.9**): 1) The orientation of the needle guide is adjusted manually by the surgeon following lighting instructions. When the error between the desired orientation and the actual orientation becomes larger than 20°, between 5° and 20° or less than 5°, the red light, purple light or the green light can be turned on respectively (**Fig. 4.9**). This step is called *coarse* adjustment of the robot. 2) Manual locking can be applied by operating a switch on the outer shell of the robot. 3) The patient is moved into the MRI bore for automatic needle guide positioning, which is *fine* adjustment, under real-time MR tracking. Afterwards, the needle guide is further locked by the granular jamming module inside the robot.

Stage 4: Interventional procedures. The patient is moved out of the MRI bore for manual needle insertion by the surgeon. The allowable insertion depth is preset by a needle stop. The patient is then moved into the MRI bore for treatment/biopsy. Intra-op imaging can be performed based on the surgical requirement. Post-operative imaging can then be performed as needed for detailed analysis of ablation lesions.

4.3.3 Design of robot components

The proposed robot platform is designed to be anchored onto the patient or on a loop coil to mitigate the effects of patient movement. Three attaching pads with adhesive and a fasten belt were employed as anchorage (**Fig. 4.10**). To minimize interference with MR imaging, the main structure of the robot was 3D-printed with biocompatible polymers (MED610, Stratasys Inc., USA). The remaining components were also made of non-conductive, non-metallic or non-ferromagnetic materials.

The overall robot size is $\varnothing$108 mm $\times$ 115 mm height, with a weight of 189 g. The compact and lightweight features can permit a flexible setup within the confined MRI bore. The needle guide installed on the robot has 2-DoF actuation, pivoting about a ball joint at the bottom of robot. The robot can be anchored on the patient's body, with the ball joint placed above the entry port on the abdomen skin and serving as an RCM for needle guide. The robotic system can offer semi-automated needle positioning with the core features: i) active alignment of needle direction in small range, which can be actuated by a soft fluid-driven actuator; ii) passive needle holder manipulated manually by the surgeon for coarse adjustment of orientation, which can cover a large ($\pm$ 30°) orientation range; iii) granular jamming locking mechanism (**Fig. 4.10**) incorporated to provide a rigid fixture for needle insertion. This semi-automated actuation design can reduce the actuator's

performance requirements in terms of motion range and output force, but without sacrificing the needle targeting precision. Compared to the fully automatic systems with large structural size ($>$ 200 mm length $\times$ 200 mm width [24, 106]), the small size of our robot can enable improved flexibility and convenience in practice. In this way, the setup of multiple robots on patient's body becomes possible for the scenarios with multiple needle insertions, providing reduced operational time and simplified scanning procedures.

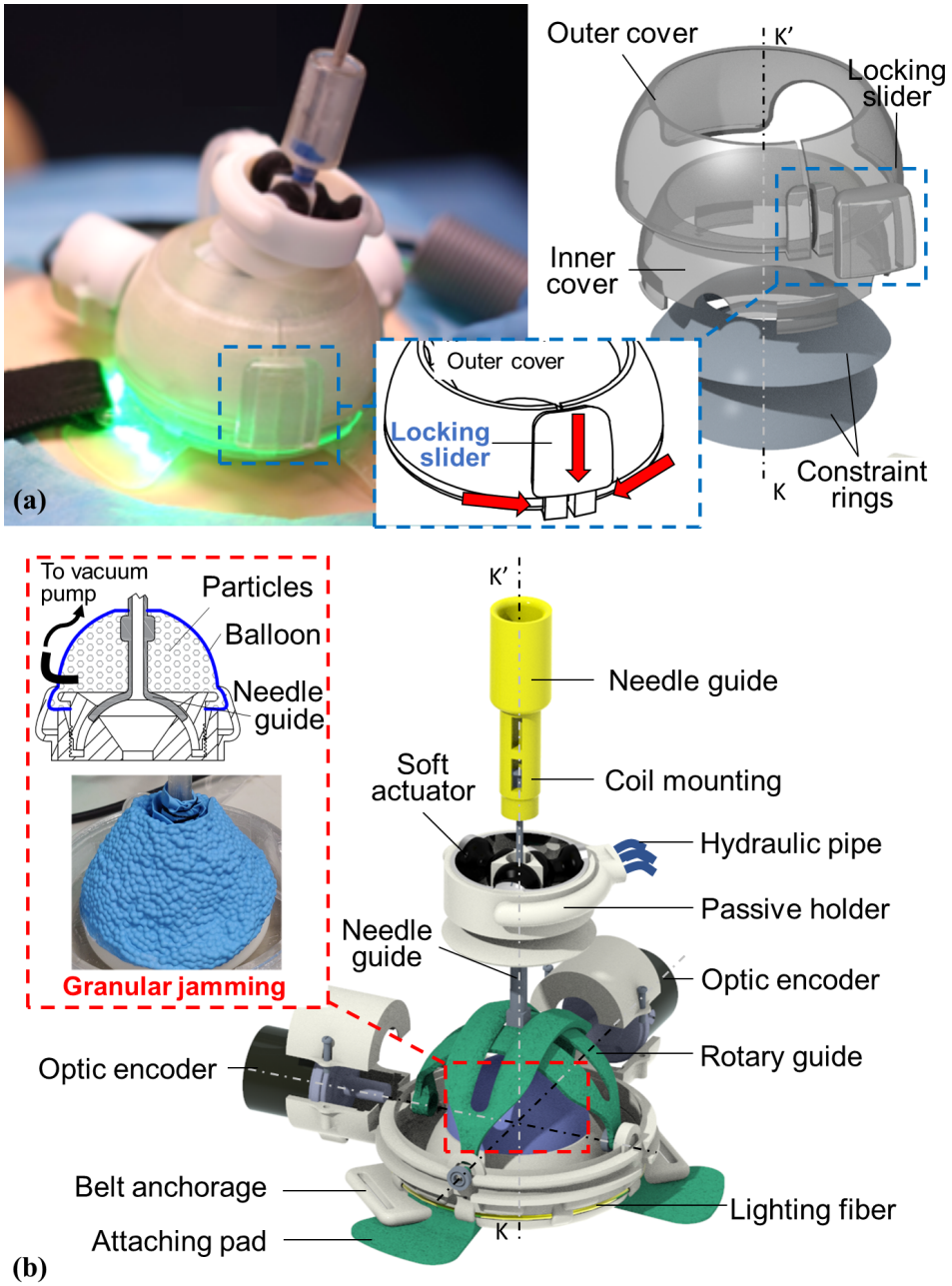

Fig. 4.10: Exploded view of the robot interior structure. A locking slider is used to manually fix the passive holder orientation. A small pack of particles can enclose the needle guide, ensuring rigid fixture for needle insertion.

During coarse adjustment of the needle guide, the surgeon can grip the passive holder, which is labeled in **Fig. 4.10a**. The outer and inner covers constrain the motion of passive holder into merely pivoting around the RCM. A slider (**Fig. 4.10a**) can be pushed downwards to lock the passive holder through a friction-lock mechanism. The desired needle guide orientation and corresponding optical encoder angles can be calculated based on the target selected from preliminary MR imaging. Fiber-optic lighting (**Fig. 4.9**) can transmit light signals to the surgeon to indicate the angular error range of the needle guide orientation.

After the coarse adjustment, the orientation of needle guide can be actively manipulated by a soft fluid-driven actuator [174] ($\varnothing$40 mm $\times$ 10 mm height) for fine alignment. The fluidic chambers were 3D-printed with soft polymers (Agilus 30, Stratasys Inc., USA). The three chambers can achieve 2-DoF planar motion (**Fig. 4.10b**). The chambers were connected through 10-m long pipelines to the master cylinders, which were actuated by electric motors. Low-latency and high-stiffness transmission can be conducted by this hydraulic actuation approach [175, 176]. The soft actuator was connected to the needle guide, offering two-direction fine adjustment with $\pm$ 5° motion range. Although the full-range automatic positioning would be sacrificed, the actuator can retain small size with lower requirements for motion range and output force. It could also ensure safety by minimizing the potential damage to the patient upon any undue mechanical failure. Besides, the soft actuator can achieve feedback control by incorporating the MR safe optical absolute rotary encoders (ZapFREE® MR431, Micronor Inc., Camarillo, USA), which can provide 2-DoF angular measurement with a resolution of 0.044° for the needle guide.

In addition to the manual locking mechanism for the needle holder, a granular jamming module (**Fig. 4.10b**) was incorporated into the robot, acting as a second level of locking after the fine adjustment. A small package of granular particles was sealed in a flexible cover, which wrapped around the needle guide. Upon the vacuum is induced, stiffness of the granular chamber will increase, hence fixing the needle guide orientation. The granules were polyvinyl chloride spheres with 2-mm diameter, having sufficient smoothness on their surface to reduce the hindrance against needle guiding movement.

4.3.4 Targeting kinematics

The schematic diagram of the robot is depicted in the **Fig. 4.11a-b**. A coordinate frame $\{\Psi_O\}$ is defined at the RCM point $\mathbf{p}_O \in \mathbb{R}^3$, about which the needle guide can revolve. When the actuator is at rest, the actuation block is at the center point $\mathbf{p}_N$, and the needle guide is perpendicular to the plane of the soft actuator. A coordinate frame $\{\Psi_A\}$ is defined at the point $\mathbf{p}_N$ and moves with the actuator.

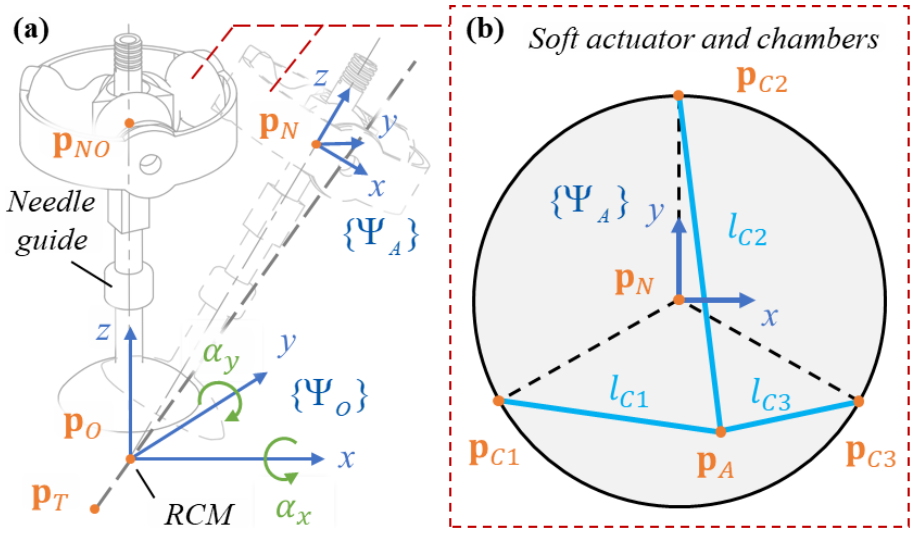

Fig. 4.11: **(a)** Schematic diagram showing the DoFs of the needle guide. Its initial (vertical) and inclined pose are both constrained by the remote center of motion (RCM) at the incision point. Angles α_x and α_y about the X- and Y-axis of the frame Ψ_O, respectively, denote the needle guide orientation; **(b)** Schematic of the soft actuator with the length of i^{th} fluidic chamber denoted by l_{Ci}.

The initial pose of the needle guide is along the Z-axis of the frame $\{\Psi_O\}$. After the coarse adjustment of the robot, the angular positions of the needle guide with respect to (w.r.t.) the coordinates X and Y of $\{\Psi_O\}$ can be denoted as α_x and α_y respectively. The three-dimensional rotation matrix ${}^A_O\mathbf{R}(\phi) \in \mathbb{R}^{3\times3}$ from the coordinate frame $\{\Psi_A\}$ to $\{\Psi_O\}$ can be described with ZYX Euler angles:

$$ {}^A_O\mathbf{R}(\phi) = \mathbf{R}_z(\varphi) \cdot \mathbf{R}_y(\theta) \cdot \mathbf{R}_x(\gamma) \tag{4.8} $$

where the angles $\phi = [\ \varphi \quad \theta \quad \gamma\ ]^T$ represent rotations defined w.r.t. the frame $\{\Psi_O\}$ along the Z-, Y- and X-axis respectively. The values of each angle can be found as $\varphi = 0$, $\theta = \alpha_x$, and γ can be derived based on α_y according to the geometric relations. Then the position of $\mathbf{p}_N$ can be obtained as:

$$ \mathbf{p}_N = {}^A_O\mathbf{R}(\phi) \cdot \mathbf{p}_{NO} \tag{4.9} $$

where $\mathbf{p}_{NO}$ is the center coordinate of the actuator at the initial pose. In the same way, the

coordinates of the soft chamber base points $\mathbf{p}_{C1}$, $\mathbf{p}_{C2}$ and $\mathbf{p}_{C3}$ can also be obtained.

For an array of inputs from the actuator chambers $\mathbf{q} = [l_{C1},\ l_{C2},\ l_{C3}]^T$, the new position of the actuation block $\mathbf{p}_A$ can be solved by the equation set:

$$l_{Ci} = \|\mathbf{p}_A - \mathbf{p}_{Ci}\|,\ i = 1,\ 2,\ 3 \tag{4.10}$$

The motion range of the chambers are $l_{C1},\ l_{C2},\ l_{C3} \in [5\ mm,\ 15\ mm]$. The point $\mathbf{p}_A$ is kept within the X-Y plane of the frame $\{\Psi_O\}$ by the constraint:

$$(\mathbf{p}_A - \mathbf{p}_N) \cdot (\mathbf{p}_N - \mathbf{p}_O) = 0 \tag{4.11}$$

Then the orientation of the needle guide $\mathbf{r} \in \mathbb{R}^3$ can be denoted by:

$$\mathbf{r} = \frac{\mathbf{p}_O - \mathbf{p}_A}{\|\mathbf{p}_O - \mathbf{p}_A\|} \tag{4.12}$$

Given a needle insertion depth d_i defined from the joint $\mathbf{p}_A$ to the target, position of the needle tip $\mathbf{p}_T$ can be calculated as:

$$\mathbf{p}_T = \mathbf{p}_A + d_i \cdot \mathbf{r} \tag{4.13}$$

To solve the inverse kinematics based on the desired tip position $\mathbf{p}_T$, co-registration between image coordinate system and the robot is executed first. The robot is assumed to have been manually adjusted and fixed and the needle guide orientation is within the motion range of the actuator. The desired needle orientation $\mathbf{r}d$ can be expressed as:

$$\mathbf{r}d = \frac{\mathbf{p}_T - \mathbf{p}_O}{\|\mathbf{p}_T - \mathbf{p}_O\|} \tag{4.14}$$

Then the desired coordinate of actuation block $\mathbf{p}_A$ can be obtained by solving the equation sets of **Eq. 4.11** and **Eq. 4.12**, with the conditions that $\mathbf{p}_A$ is located simultaneously in the direction of $\mathbf{r}d$ and on the X-Y plane of $\{\Psi_O\}$. In the end, the desired inputs of each chamber $\mathbf{q} = [l_{C1},\ l_{C2},\ l_{C3}]^T$ can be solved by substituting $\mathbf{p}_A$ into the equation set **Eq. 4.10**. The desired encoder angles α_x and α_y can also be calculated based on the needle orientation $\mathbf{r}d$.

4.4 Experimental validation

The performance of the robotic system for stereotactic neurosurgery presented in **Section 4.2** has been validated by the following experiments, including actuation stiffness, robotic targeting accuracy, MR tracking performance, and MRI compatibility. To verify the proposed DBS workflow, a pre-clinical trail has been carried out under MRI guidance by the robotic system.

4.4.1 Transmission stiffness of robotic actuation

Transmission stiffness is one of the primary factors governing the ability to resist external disturbance. A stiffness test was carried out for the one DoF of hydraulic actuation, which was from the master side to the manipulator's base joint. The manipulator's arm was fixed to lock the joint rotation. A pair of 10-m long pipes connected the master and slave units, which were filled with distilled water. A direct current (DC) motor was employed to actuate the master unit with an encoding resolution of 1.39°. The applied torque by the motor was measured by a torque sensor with 5 mN-m sensitivity (HLT131, Hualiteng Technology Co. Ltd., China). The tests were performed repeatedly (10 cycles) under the bi-directional load. Fluid preloading pressures at 0.05, 0.1, 0.15 and 0.2 MPa were examined. The external loads were gradually increased, while recording the corresponding piston displacements.

The force-displacement diagram in **Fig. 4.12** illustrates the increasing trend of transmission stiffness with higher fluid pressure pre-loaded. The maximum stiffness can reach 24.35 N/mm at 0.2 MPa preloading pressure, which was linearly fitted by the least-square regression. In comparison, the interaction force is commonly less than 0.8 N [86, 177] between the brain tissue and the instrument, which shows that the incorporated hydraulic actuator has sufficient stiffness to provide precise tissue manipulation under external load. The existing compliance in the hydraulic transmission could be attributed to three main reasons: 1) structure deformation of the plastic components under load; 2) diaphragms elongation; 3) expansion of the pipes under internal pressure. The transmission stiffness can be enhanced by utilizing more rigid materials. In addition, shorter pipelines can help to increase the transmission stiffness, as well as to reduce fluid friction and inertia [138].

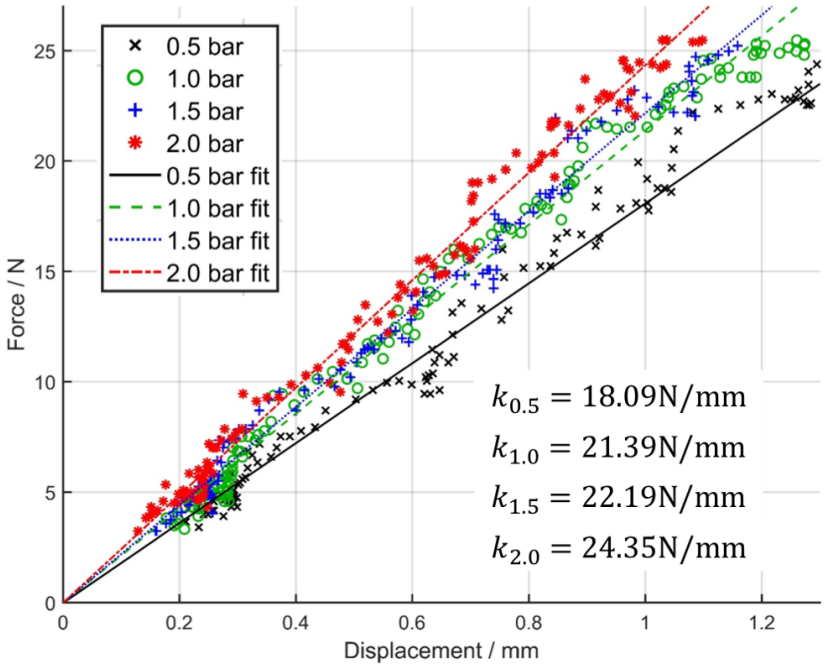

Fig. 4.12: Transmission stiffness of the hydraulic actuator illustrated by the force-displacement diagram. Four preloading pressures (0.05, 0.1, 0.15 and 0.2 MPa) were investigated for the experiment.

4.4.2 Needle targeting accuracy of manipulator

In the needle targeting experiment, the 3D coordinates of any point defined in the experimental setup were measured by an EM tracking system (Aurora, NDI Medical, Canada). The STN targets were simulated with 10 points pre-defined on a plate. The robotic manipulator was placed approximately 100 mm above the targets, which was the average depth of stereotactic targets under the human skull. These measured targets coordinates were registered with the robot coordinate system. A ⌀1.4-mm simulated needle was used, which was similar to a DBS cannula. A 6-DoF EM marker was attached on the needle tip to record its position.

The robot pose, needle guide configuration and the insertion depth were continuously measured and calculated during the experiment. After confirming the needle guide orientation towards the target, the needle was manually inserted. 10 trails were taken for each target. When the needle tip was considered to reach the pre-defined target, 500 times of measurement were taken and an average value was calculated. The measurement was taken for the deviation from the needle tip to the target, as well as for the orthogonal distance from the target to the axis of needle. The average error was less than 2 mm, and the standard deviation was smaller than 1 mm (**Table 4.1**). This targeting accuracy is comparable to the current stereotaxy application [83].

Table 4.1: Needle targeting accuracy test results

	Needle tip		Normal to the needle	
Accuracy (mm)	Left 1.73±0.75	Right 1.21±0.63	Left 1.61±0.72	Right 1.15±0.62

4.4.3 Validation of MR-based tracking system

MR-based wireless tracking coils has been incorporated into the proposed robotic system, which is the first time for such applications. The conventional passive tracking [178, 179] could not provide sufficient signal contrast to the background, which was not reliable to be used for real-time and automatic localization. Passive tracking markers would have prolonged processing time due to the 2D image reconstruction in prior to the markers' visualization. In comparison, the proposed *wireless* marker can pick up the MR gradient signal along three principal scanning directions, and resonate with the signals transmitted to the MRI scanner receiver [180–182]. 1-D projection techniques [183] could be utilized without the process of image reconstruction.

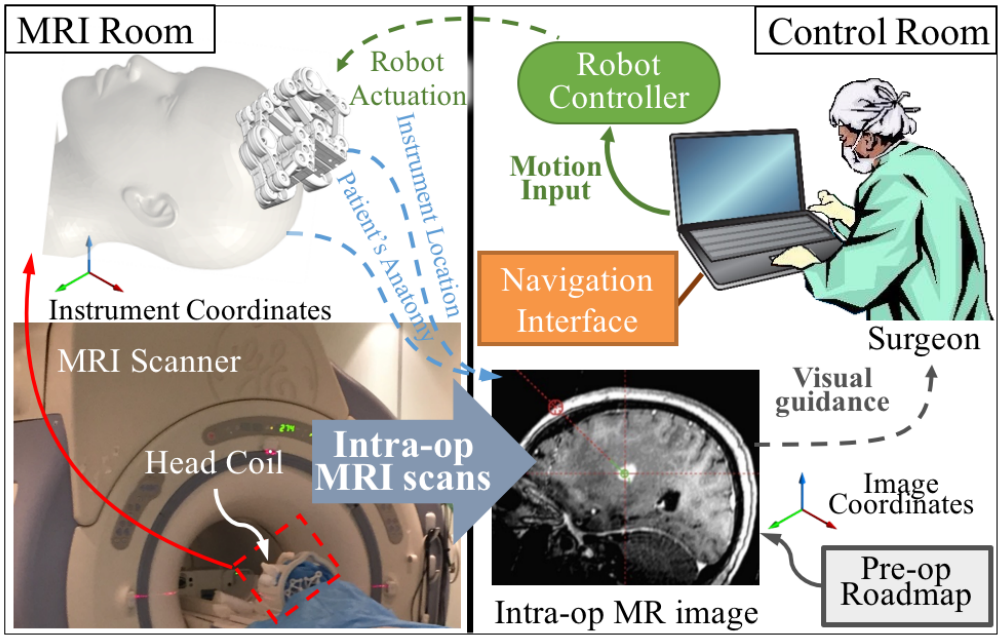

Fig. 4.13: System schematic of the MRI-guided robot-assisted stereotaxy.

A navigation test was conducted using a diagnosis MRI scanner. **Fig. 4.13** shows the setup of robotic system for MRI-guided stereotaxy. The brain simulator was fabricated by molding the agar gel (Biosharp Inc., China) into a skull model. It can be revealed in MR images and used to improve the image contrast for needle targeting. In the test, the robot was anchored on the skull model and placed within an imaging head coil. Two MR tracking

markers in $1.5\times5\times0.2$ mm^3 were incorporated for robot navigation, which were embedded in the needle guide (**Fig. 4.14a**). 3D fast spoiled gradient recalled-echo (FSPGR) sequence was used to assess the location and orientation of the needle guide. The sequence parameters are listed in **Table 4.2**. A needle made of carbon fiber was then inserted and scanned with the same imaging sequence.

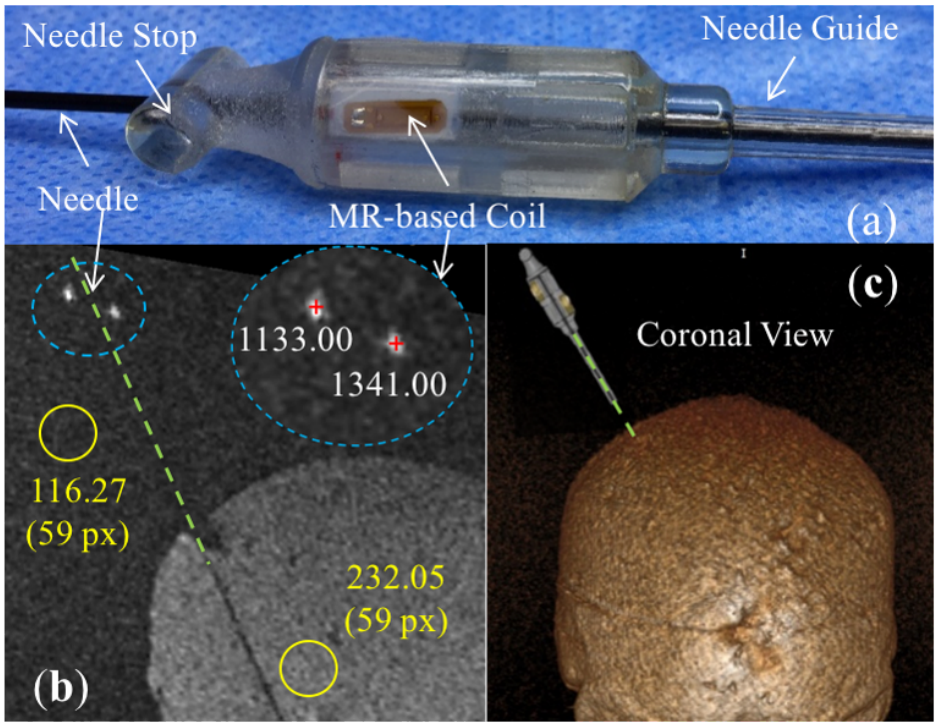

Fig. 4.14: (a) Needle guide embedded with two MR-based tracking coil units; **(b)** MR image of the brain simulator (in the coronal view) revealing the two tracking markers by the corresponding bright spots; **(c)** Virtual configurations of the instrument augmented on those high-contrast markers, which were posed above the 3D-reconstructed brain simulator.

Table 4.2: MRI scan parameters

	w/o needle inserted	w/ needle inserted	SNR test
FOV (mm)	240×240	240 × 240	280 × 280
Matrix	256 × 256	256 × 256	256 × 256
Acquisition	FSPGR	FSPGR	T2-FSE
TR (ms)	68.0	68.0	2000.0
TE (ms)	2.8	2.8	76.8
Flip angle (°)	10	10	90

The MR image in coronal view is illustrated in **Fig. 4.14b**, with a clear visualization of inserted needle and coils. The bright spots with red crosses represent the two coils, with signal intensities of 1133.00 and 1341.00. In contrary, the average intensities were measured as 16.27 and 232.05 for the background and agar-gel brain (yellow circles), respectively. The contrast of the MR coils can be further improved by dedicated excitation at lower flip angles (e.g. 1°) to minimize the background signals. The dark straight line in **Fig. 4.14b** indicates the negative artifact of the needle. The two spots are zoomed in and enclosed in the blue dash ellipse. Two red crosses indicate the signal intensities of the coils, which are much higher than the average intensities within the other two yellow circles: on the background and agar-gel brain simulator. The marker's inherent precision was 0.12 mm and maximum position error was 0.50 mm, which were measured at 48-mm distance from the isocenter. Due to the gradient field nonlinearities, these errors may increase if the marker is located farther from the isocenter.

4.4.4 MRI compatibility test

The MRI compatibility of the robotic platform was tested in a 1.5T MRI scanner (SIGNA HDxt, GE Healthcare, USA). A square MRI phantom (Part Number: 150027, USA Instruments, Inc.) was placed at the scanner's isocenter. An image without the robot was obtained for baseline utilizing T2-weighted fast spin echo (FSE) MRI sequence (**Table 4.2**). This acquisition sequence is usually used for localization in stereotactic neurosurgery. After placing the robot alongside the MRI phantom in the scanner, three robot operating conditions were set to acquire the MR images (**Fig. 4.15**): i) *Static*: robot remained powered off and was placed in the scanner; ii) *Powered*: robot was powered on, but remained static without motion output; iii) *Operating*: robot was in full operation. Then the SNRs of MR images were examined by referring to the standard from the National Electrical Manufacturer's Association [184].

Fig. 4.15 shows the results with $< 3\%$ SNR loss, even with the robot in actuation. Artifacts of MR images were analyzed according to the evaluation method in ASTM [165], which may result from the robot's presence and operation. The images under the four operating conditions were analyzed. Pixels were considered as artifacts with the intensity variation larger than 30% [124], which would be shown in the binary map (FSE Artifact, **Fig. 4.15**) as white spots. The robotic operation had zero generation of imaging interference, with no artifact observed within the MRI phantom area in the images.

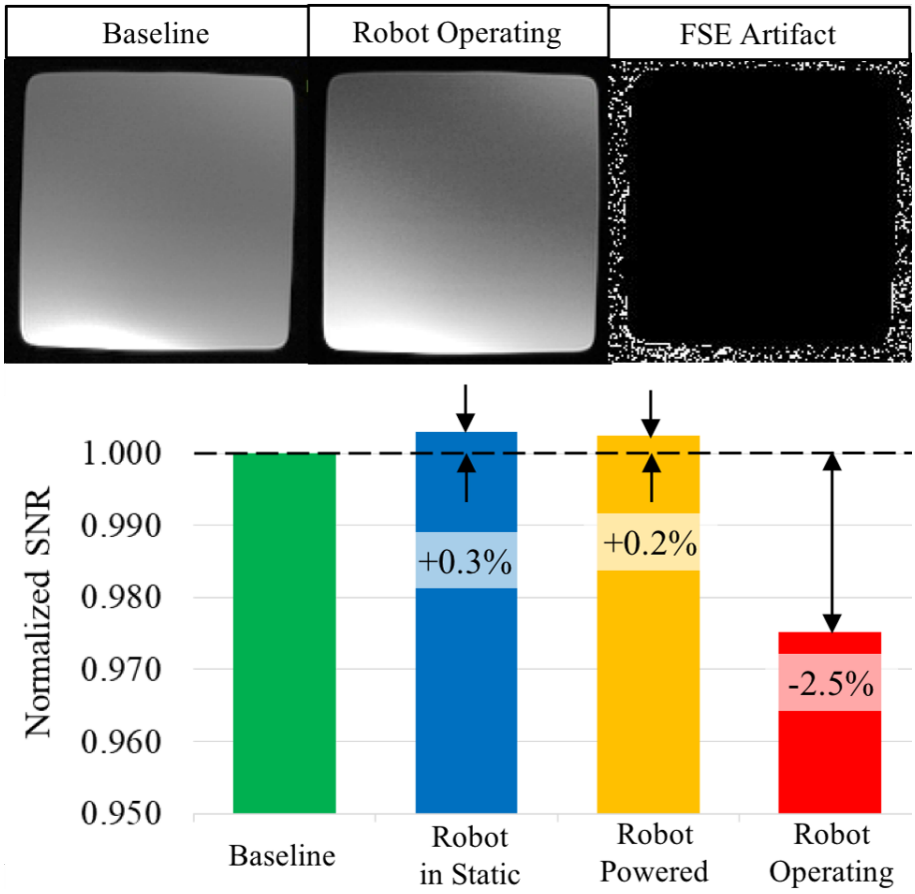

Fig. 4.15: Upper: T2-weighted FSE images of an SNR phantom. No artifact was observed within the phantom area. Lower: SNR test results. Minimal influence on SNR has been demonstrated for the four robot conditions.

4.4.5 MRI-guided pre-clinical trial

The MRI-guided bilateral robotic system and the proposed DBS workflow have been validated by a pre-clinical trial. System setup and workflow are shown in **Fig. 4.16** and **Fig. 4.17**. A human cadaver was utilized for the experiment, with the DBS targets simulated by capsules containing Vitamin-E. The targets were placed inside the cadaver head before moving the subject to the MRI room. To reduce the duration of experiment, pre-op procedures including MRI scanning and planning were omitted. The anchoring base was fixed on the skull by three titanium screws. Afterward, based on the robot's workspace, the surgeon conducted the skin incision, burr hole creation, as well as dural opening. Two fiducial rings were anchored and aligned at the center of burr holes. A head fixator (inner/outer diameter: ⌀220/250 mm) made of MR safe materials was employed to anchor the subject, which had an inner diameter of ⌀300 mm and could be placed into the imaging head coil.

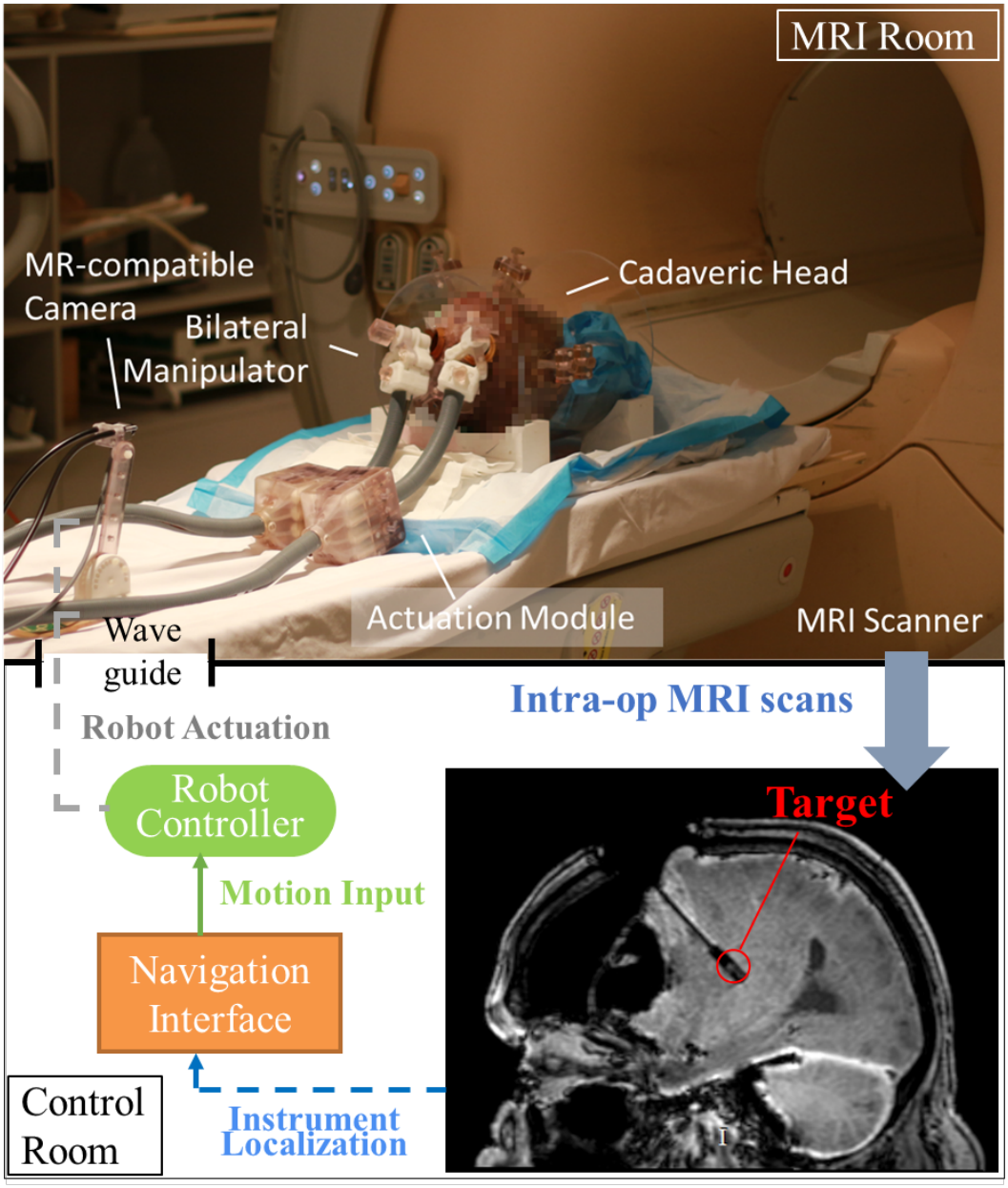

Fig. 4.16: Pre-clinical trial conducted by the proposed bilateral robotic system for MRI-guided stereotaxy.

After completion of all the preparation works, the subject was moved to the MRI room for robotic needle positioning (**Fig. 4.16**). A 1.5T diagnostic MRI scanner (Achieva, Philips Healthcare) was utilized for imaging. The head fixator together with the subject was anchored tightly inside the MRI head coil during the scanning. 3D volumetric MR scan was conducted with a selective volume covering the brain, targets, as well as the fiducial markers. The images were stored in the computers placed in the control room through Digital Imaging and Communications in Medicine (DICOM) connection. The 3D location of points were chosen in the DICOM files, including the fiducial markers on robot, fiducial rings at burr holes, as well as the targets. Then the 3D coordinates of these points were

used for robot registration and needle insertion trajectory calculation. Note that it is just a preliminary trajectory by directly connecting the burr hole center and target points. The surgeon might conduct fine-tuning of the trajectory by adjusting the entry locations at the burr hole, forming final optimized needle insertion paths.

After the confirmation of the preparatory trajectory, needle guide localization was carried out by MR tracking sequence for robot guidance. The robot actuation states at each joint can then be reversely determined based on the position and orientation of needle guide. Angular errors at each joint could be estimated by comparing the actuation states calculated from the current and desired needle trajectories. Based on the errors, the desired joint motions could be input in the program to control the robot. Alternatively, the angular position of each joint can be individually adjusted to reduce the alignment error. This alignment procedure needed to be performed repeatedly to aim the needle guide at the target.

When the MR-guided robotic manipulation was completed, the subject was transferred out of the isocenter. The desired insertion distance could be calculated according to the robot kinematics. A clip was installed on the needle to fix the insertion distance. The distance from the tip to the clip was equal to the desired insertion distance. Afterward, the surgeon conducted the needle advancement manually towards the target. The subject was translated into the MRI isocenter again for the post-operative MRI scan to assess the targeting accuracy.

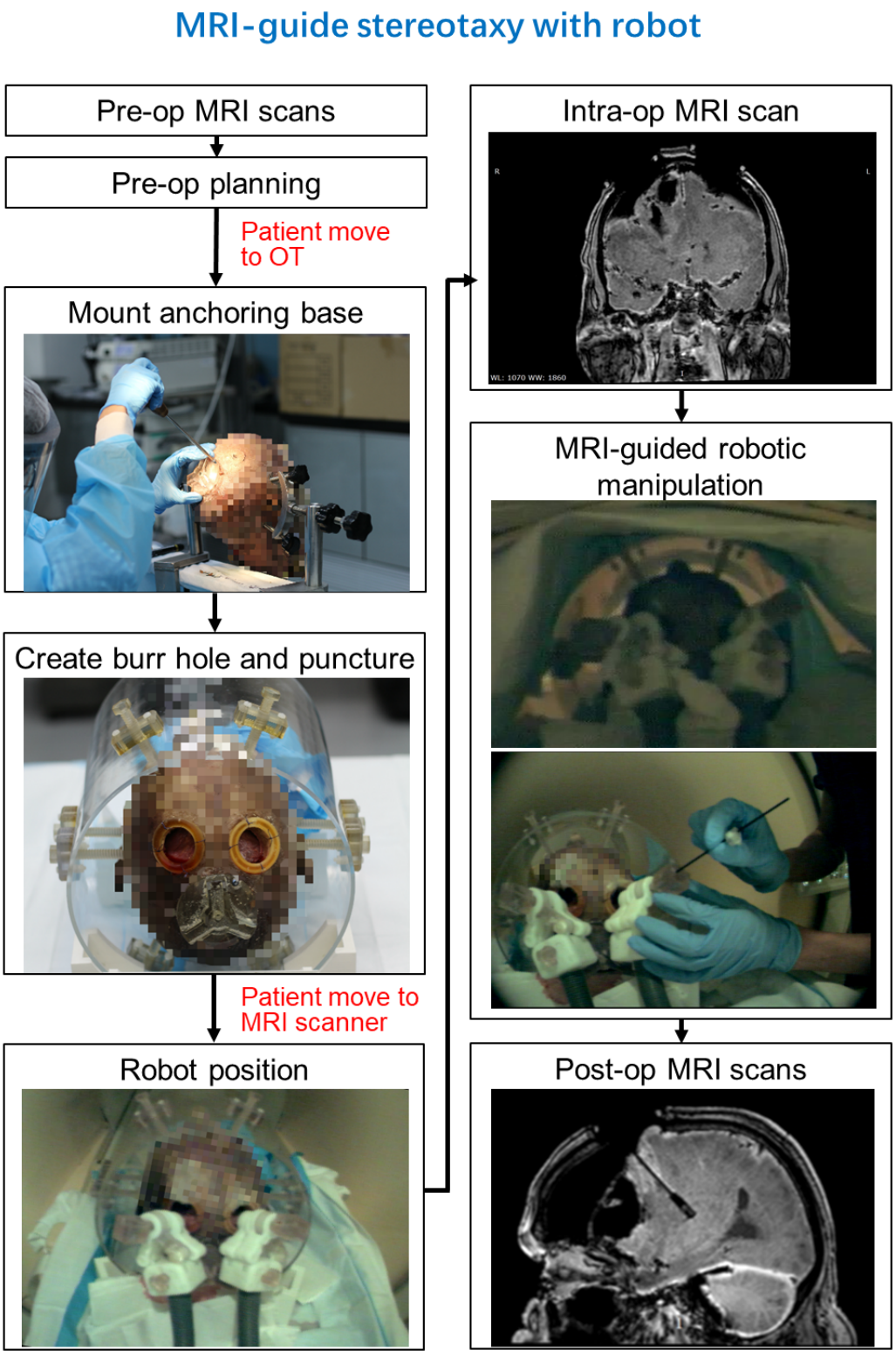

Fig. 4.17: Proposed workflow of the MRI-guided stereotaxy with assistance of the tele-operated robotic system.

4.5 Conclusion

This chapter presents compact robotic manipulators for MRI-guided needle placement procedures, including stereotactic neurosurgery and percutaneous intervention. The manipulator for MRI-guided stereotactic neurosurgery can perform bilateral needle targeting towards both STNs simultaneously. The manipulator features compact ($110.6 \times 206.8 \times 33.2$ mm^3) and light-weight (145.4 g), which could be operated in the head coil with confined workspace. The patient-mount design can avoid the repeated adjustment of the needle orientation if patient's head is moved during the surgery. The current robot size has been optimized to ensure sufficient dynamics performance to achieve safe and effective stereotactic procedures. The design trade-off between the robot dimension and performance (e.g. accuracy, stiffness) needs to be further studied for different applications. The high-fidelity hydraulic actuators, which are introduced in **Chapter 3**, have been incorporated in the robot. The manipulation could achieve a maximum stiffness of 24.35 N/mm. The needle targeting accuracy was verified by a simulated DBS task, indicating the robot could provide a much sufficient accuracy than the regular requirement. A pre-clinical trial under MRI guidance has been carried out to verify the surgical workflow with the assistance of the proposed robotic system. In addition, a semi-automated needle placement robot is proposed towards interactive manipulation for instrument positioning. The lightweight (189 g) and compact ($\varnothing$108 mm$\times$115 mm height) features can enable the setup of several robots for needle targeting at multiple locations.

In stereotactic neurosurgery, the continuous update of the brain map with the intra-op MRI can greatly improve the instrument placement accuracy by monitoring the brain shift. The bilateral needle insertion approach can also minimize this brain shift with no need for extra anchorage on the skull. The proposed MR safe robotic system with integration of the wireless MR tracking system can benefit from the utilization of fast MR imaging/tracking sequences. Risks for damaging the crucial brain structures can be avoided by real-time visualization of the instruments and targets with the robotic tele-manipulation in situ. Local anesthesia with the patient awake could also be avoided. Lastly, it is anticipated that the operational time could be greatly saved, which was usually due to the repeated image alignment and instrument adjustment. In this way, the overall expense can be remarkably reduced, which can also cover the high cost of MRI.

The current limitation of the proposed MR safe needle placement manipulators is mainly on the lack of automated needle insertion mechanism. The needle insertion

by manual would prolong the operation duration and reduce the targeting accuracy. In our future work, compact ($\sim$ $\varnothing$30 mm $\times$ 60 mm) needle insertion module with tendon-driven mechanism will be developed. The module will be integrated with the proposed manipulators to provide a fully-automated needle placement operation.

For commercialization of the proposed needle placement systems, several challenges are still encountered. The robot design will be modified by taking account of the sterilization standards. The materials will be carefully selected for robot components and the cost will be examined to achieve the disposable feature. The robot effectiveness will also be evaluated by pre-clinical trials with anatomical simulators or animals, followed by clinical studies in prior to the market approval from relevant agency (e.g. Food and Drug Administration (FDA)).

Chapter 5

Robotic Catheter Platform for MR-guided Cardiac Catheterization

5.1 Introduction

This chapter introduces a robotic manipulator to achieve robot-assisted intra-cardiac catheterization under magnetic resonance imaging (MRI) guidance. MRI can offer high-resolution images to visualize soft tissue features such as scars or edema, as well as can localize the catheter tip precisely with respect to (w.r.t.) the MR image/roadmap coordinates. It is hypothesized that robotic catheterization, combined with the enhanced monitoring of lesions creation using MRI intra-operatively, will significantly improve the procedural safety, accuracy and effectiveness for cardiac electrophysiology (EP). However, despite the benefits of robot-assisted catheterization and the advances of intra-operative (intra-op) MRI, no existing commercial robotic catheterization platform could be used under MRI guidance.

To this end, the first magnetic resonance (MR) safe robot for intra-cardiac EP intervention has been developed. The robot incorporates the MR safe, high-performance hydraulic actuators presented in **Chapter 3**, demonstrating the promising ability to tele-manipulate a cardiac EP catheter. Detailed design and hydraulic actuation mechanism are described in **Section 5.4**. A human-robot control interface to assist the tele-operation is presented in **Section 5.5**. Experiments are reported in **Section 5.6** to evaluate the tele-manipulation effectiveness of a standard cardiac catheter.

5.2 Clinical motivation for MRI-guided robot-assisted catheterization

Heart rhythm disorder (arrhythmias) is one of the most prevalent cardiovascular diseases worldwide. There are more than 2.7 million patients suffering from this disease each year in the United States. And the estimated patient number is expected to be 16 million by 2050 [185]. The symptoms of cardiac arrhythmias vary from conditions. Mild symptoms include irregular or skipping of heartbeat, which may be seldom noticed by patients. However, certain types of arrhythmia, such as ventricular tachycardia (VT), may induce unexpected cardiac death, causing over half a million death in the United States annually. As population age increases, the number of death would rise accordingly. At least 80% of these deaths could be avoided through timely diagnosis and proper treatment. A basic classification of heart rhythm disorder is by heart rate, which includes bradycardia (slower heart rhythm) and tachycardia (faster heart rhythm).

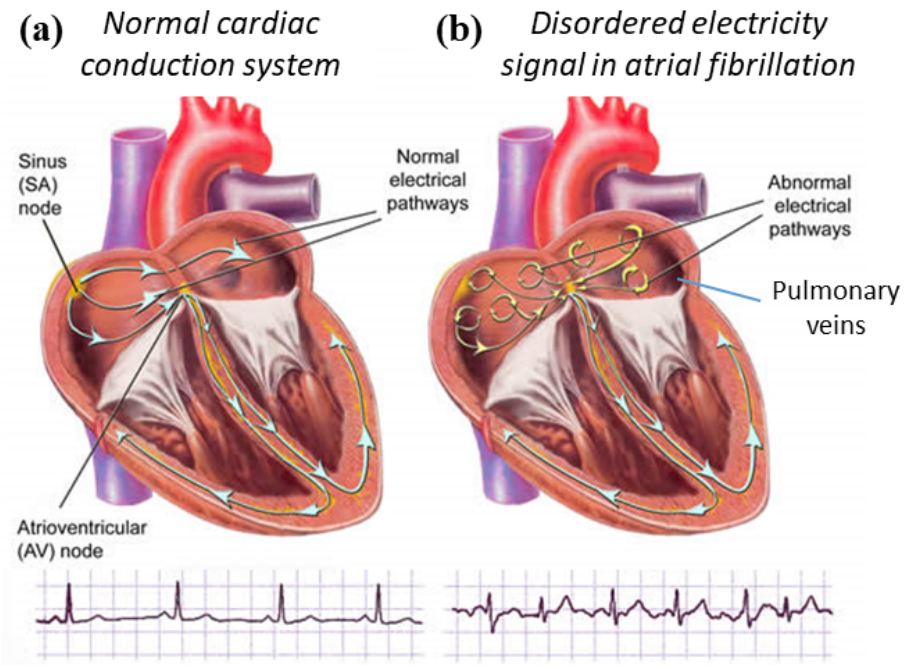

Fig. 5.1: (a) Normal cardiac conduction system. The electricity signal is initiated from the sinus (SA) node, and transmitted to atriums and ventricles in a regular pattern; **(b)** Disordered electricity signal in atrial fibrillation. The signal becomes disordered in the atria and adjacent parts of the pulmonary veins, causing irregular heart rhythm. **Image Source**: [38].

Atrial fibrillation is a common case of heart rhythm disorder. For the normal cardiac conduction system, the bioelectricity signal is initiated from the sinus (SA) node and propagated throughout the atriums first (**Fig. 5.1a**). Then the signals are concentrated on the atrioventricular (AV) node and spread to the ventricles. Under healthy condition, this electric

signal should be transmitted in a regular pattern, governing the heart muscle to contract and pump the blood. However, for atrial fibrillation, the signal would become disordered in the atria or adjacent parts of the pulmonary veins (**Fig. 5.1b**), causing disordered heart rhythm.

Among a variety of treatments, cardiac EP is an effective interventional approach for atrial fibrillation, which has drawn growing interests [108, 109]. In the procedure, a long (∼1.5 m) and thin (∼⌀2.7 mm) catheter (**Fig. 5.2a**) is inserted from femoral vein to heart chamber (**Fig. 5.2c**). The electrodes on the catheter tip then conduct radiofrequency (RF) ablation on the target tissue (**Fig. 5.2b**). The destroyed tissue can block the irregular electrophysiological signals that induce arrhythmias. Two key procedures are conducted repeatedly during the EP procedure: electroanatomical mapping (EAM) and RF ablation.

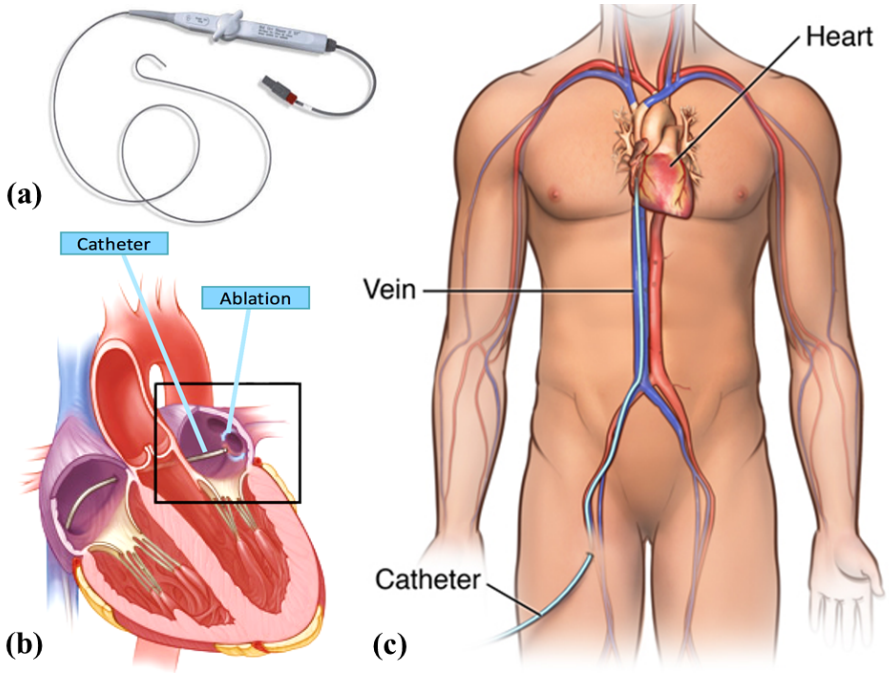

Fig. 5.2: (a) Electrophysiology (EP) catheter with a diameter of ∼⌀2.7 mm and length of ∼1.5 m; **(b)** Radiofrequency (RF) ablation conducted on the target tissue by the catheter tip; **(c)** Insertion path of catheter to the heart chamber, passing through the femoral vein, inferior vena cava and right atrium. **Image Source**: [39–41].

Electroanatomical mapping (EAM): Electrodes at the catheter tip are manipulated to contact with atrial/ventricle tissues. Electrical activations can be collected at different phases of cardiac cycle, together with the tracked location of catheter tip. The contact locations with electrical signal information form the electroanatomical (EA) map, which is based on the cardiac roadmap obtained by the pre-operative (pre-op) imaging (**Fig. 5.3a**). EP surgeons will refer to the EA map for catheter positioning and further RF ablation (**Fig. 5.3b**).

Radiofrequency (RF) ablation: In the ablation process, RF energy is delivered by the catheter tip to destroy the tissues which are the origins of abnormal electrical signals (**Fig. 5.3b-c**). The non-conductive scars created by ablation, usually on the ostia of the pulmonary veins, can isolate abnormal EP signals to treat heart rhythm disorders [146]. The typical procedure is called pulmonary vein isolation (PVI). The ablation progress could only be roughly estimated based on the tissue impedance decay, contact force, ablation temperature, and intra-cardiac surface electrocardiograms (ECGs) under conventional fluoroscopic guidance.

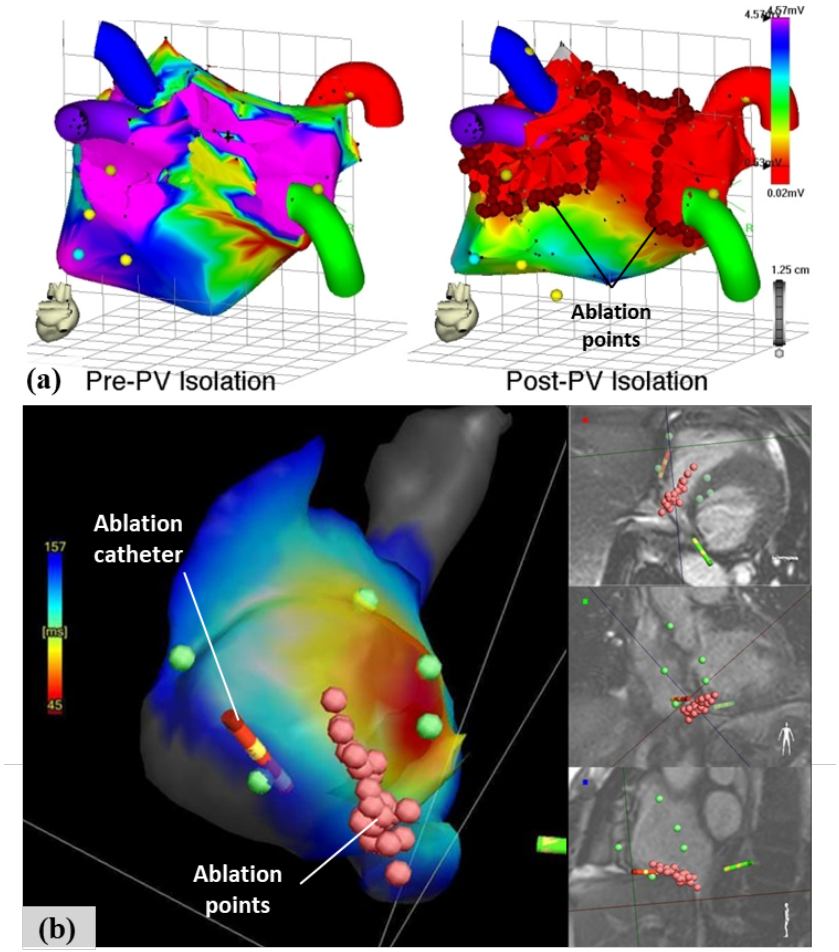

Fig. 5.3: (a) Electroanatomical mapping (EAM) of the left atrium (LA) during sinus rhythm. The electrogram voltage became relative low in the red areas after ablation (red points); **(b)** EAM during real-time MR–guided cardiovascular EP intervention conducted by Imricor Medical Systems. The catheter could be localized by MR-based tracking within MR image coordinates, with ablation points recorded. **Image Source**: [42, 43].

A safe and effective cardiac EP procedure depends on two crucial factors: i) the capability of monitoring the ablation progress during intra-op imaging, as well as evaluating lesions and their locations; ii) effective manipulation of EP catheters in heart chamber for EAM and RF ablation [110–112]. However, for conventional EP procedure under

X-Ray or ultrasound guidance (**Fig. 5.4a-b**), it is still challenging for surgeons to manipulate the compliant EP catheter under the dynamic disturbance in heart chamber. Apart from dexterous maneuvering of cardiac catheters to the target tissues, the ability to intra-operatively assess lesion locations and their ablation progress is crucial to enhance the safety and efficacy of the EP procedure. The arrhythmia recurrence chances would rise due to the formation of edema instead of necrosis on the tissues, which were generally caused by inaccurate or incomplete electrical-circuit isolation, or insufficient RF ablation on the lesion [113]. On the contrary, excessive tissue ablation may cause perforation of the cardiac wall.

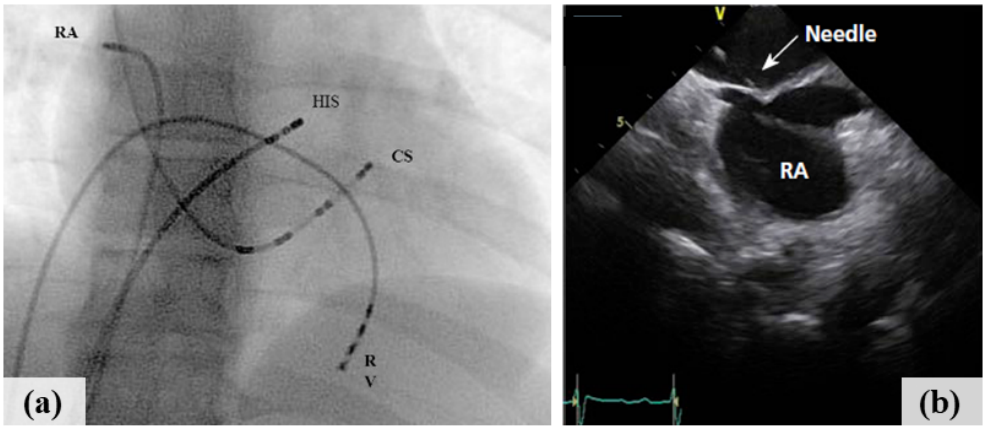

Fig. 5.4: **(a)** Catheters under X-ray fluoroscopy; **(b)** Ultrasound image showing the trans-conduit puncture. **Image Source**: [44, 45].

These difficulties have stimulated the study on tele-operated robotic systems for dexterous catheter manipulation [122–124]. Several commercial platforms have been developed, including Hansen Sensei® X, Amigo Remote Catheter System, and Stereotaxis Niobe® system [125]. These robotics platforms have shown the great potential to improve the catheter manipulation dexterity and accuracy for intra-cardiac EP intervention. However, due to the lack of continuous and real-time updates on patient-specific cardiac EP roadmaps, catheter navigation still remained complicated and inaccurate. The electrophysiologists would be conservative to deliver a large amount of RF ablation, due to the probably large misalignment (>5 mm) between the actual and reconstructed catheter tip positions shown in the roadmap or EA map.

In light of these challenges, MRI can provide high-contrast imaging for cardiovascular soft tissue visualization (**Fig. 5.5a**) and construction of cardiac roadmap in three-dimensional (3D) [114, 115]. The edema [117] or scar tissue [116] can be promptly visualized and distinguished under MRI (**Fig. 5.5b**), which results from inadequate or successful RF ablation respectively. The ablation temperature and thermal dose can

also be monitored by MR thermometry in real-time (**Fig. 5.5c**). In addition, with the MRI-based real-time tracking techniques [36, 50, 186], the position of catheter tip can be localized precisely, relative to the MR image/roadmap coordinates (**Fig. 5.3b**, **Fig. 5.5d**), eliminating the potential misalignment occurred in conventional imaging modality (i.e. X-ray). Numerous clinical trials have been conducted by research groups (e.g. [118–121]), verifying the vital advantages of intra-op MRI for EP. Despite the benefits of robot-assisted catheterization and intra-op MRI, there is no complete system which can be used for MRI-guided EAM and RF ablation. To this end, an MR safe robotic manipulator is developed to improve the accuracy and dexterity of catheter manipulation for cardiac EP intervention.

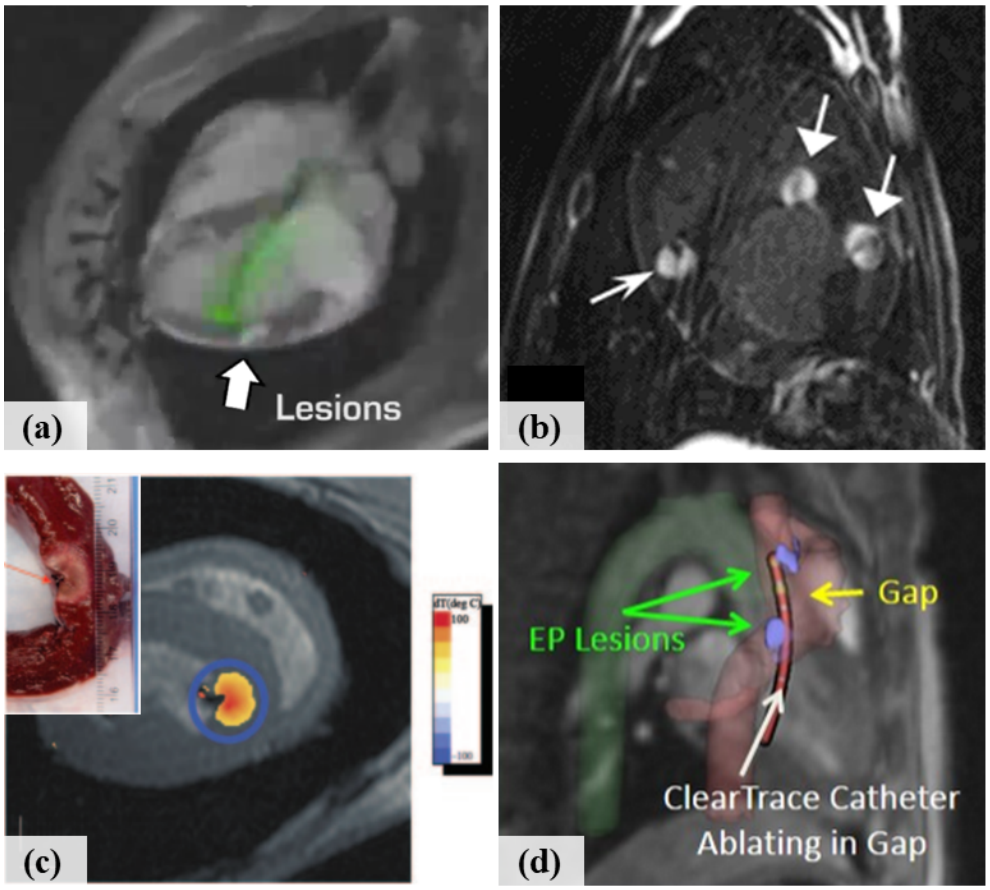

Fig. 5.5: (a) Ablation progress visualized in MR images; **(b)** Post-ablation edema indicates progress of ablation under MRI; **(c)** Ablation temperature monitored by MR thermometry; **(d)** Catheter tip position localized by MRI-based real-time tracking coils, relative to the MR image coordinates. **Image Source**: [1, 46–48].

5.3 Robot design criteria towards effective MRI-guided catheterization

The design of robotic catheter platform should comply with the following considerations towards surgical requirements. The key robotics components are introduced in the following sections with fulfillment of these requirements.

1. *MR safety*. The robot operation should not pose any hazard to the patient as well as the MRI scanner, and not adversely affect the quality of MR images;

2. *Manipulability*. Necessary degrees of freedom (DoFs) should be involved to achieve the cardiac catheter manipulation, including catheter advancement, rotation, and catheter tip steering. Each DoF should also have sufficient motion range for effective catheter manipulation.

3. *Dexterity*. The cardiac EP catheter will deliver ablation inside left atrium (LA). Heartbeat, blood flow as well as the interaction with tissue would cause unexpected motion of catheter tip. Therefore, the actuation of the robotic platform should feature high accuracy, high dexterity and fast response, in order to facilitate effective and safe catheter manipulation under the dynamic disturbance.

4. *Size and weight*. The robotic platform should be compact and lightweight, which could be accommodated on the MRI operation table near or inside the scanner bore. It should be sufficiently compact to be placed adjacent to patient's leg, in order to accommodate the catheter inserting location.

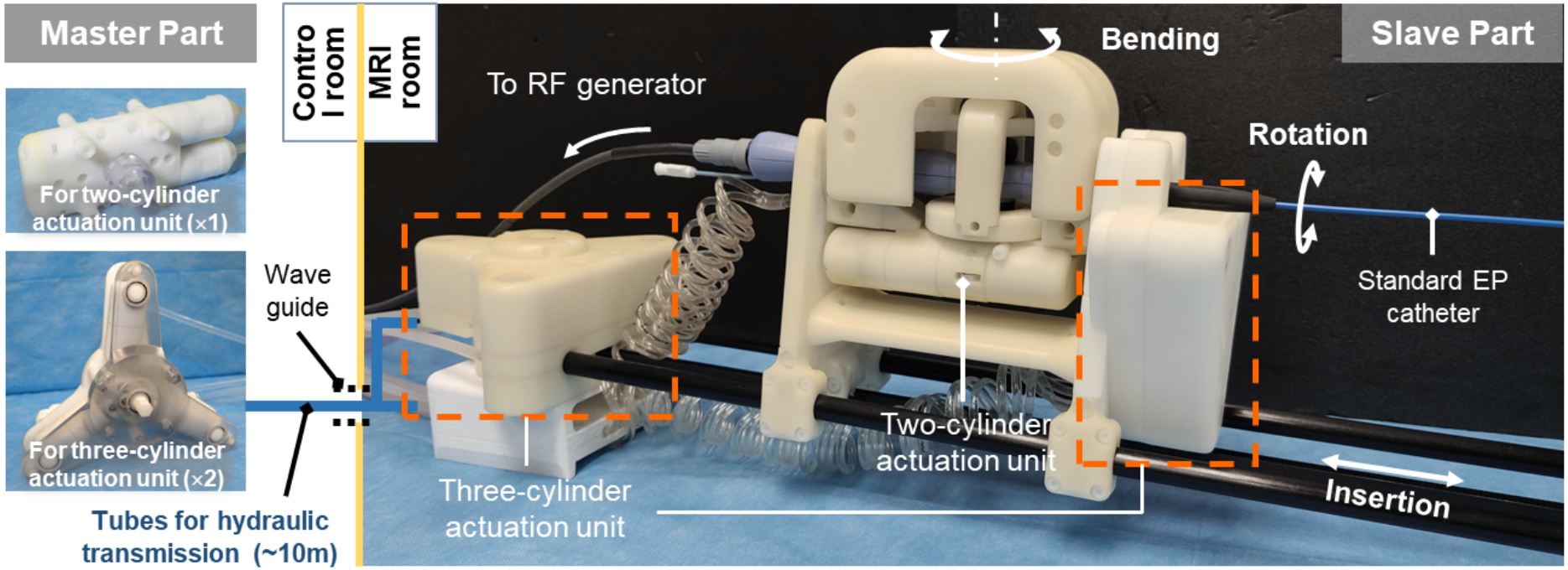

Fig. 5.6: MR safe robot prototype incorporating three sets of hydraulic transmission actuation units, which can manipulate the standard EP catheter in 3 DoFs. Master-slave motion transmission from control room and MRI room was conducted through 10-meter long hydraulic pipelines. The waveguide is EM-shielded and channels those three pairs of pipelines, which is the only channel connecting the two rooms.

5.4 Design of tele-operated robotic catheter system

The proposed MR safe robotic catheter system incorporated the high-performance hydraulic motors (**Chapter 3**) to tele-manipulate a standard EP catheter. Master-slave hydraulic actuation can be transmitted from control room to MRI room through a pair of 10-meter long pipelines (**Fig. 5.6**), which could be channeled through the waveguide in-between the two rooms. A full view of the robotic system is illustrated in **Fig. 5.6**, with the specification summarized in **Table 5.1**. Detailed descriptions are introduced in the following sections.

Table 5.1: Specification of robotic catheter platform

Size	$800 \times 105 \times 210$ mm^3
Weight	3.59 kg
Motion range of robotic platform	
Bending	$-60° \sim 60°$
Rotation	Unlimited
Insertion	$0 \sim 340$ mm
Catheter manipulation range	
Cardiac catheter	Thermocool® SmarttouchTM Bi-Directional Catheter, Biosense Webster Inc.
Bending	$-180° \sim 180°$
Rotation	Unlimited
Insertion	$0 \sim 340$ mm
Hydraulic transmission	
Pipelines	Length: 10 m; Outer/Inner diameter: 6/4 mm (Nylon: DG-5431101, Daoguan Inc.)
Transmission media	Distill water
Pressure	0.1 Mpa
Rolling diaphragm	Type A: 18-mm diameter, 35-mm stroke Type B: 10-mm diameter, 20-mm stroke
Power source	24V DC motors

5.4.1 MR safe hydraulic actuation

The present catheter platform relies upon robotic actuation with MR safe hydraulic motors (**Chapter 3**). The motors were fabricated with non-metallic materials and can be driven by fluid-based power, e.g. hydraulic. The whole actuation unit is MR safe and has minimal imaging interference in the MR environment, which can fulfill the criteria (1). The hydraulic actuation unit contained pairs of hydraulic piston-actuators connected with long flexible tubes ($\approx$10 meters). As shown in **Fig. 5.6**, the master and slave parts of the robot were separately placed in control room and MRI room. The slave part was placed inside or near MRI bore, while the master part was being in the control room. The actuation units in master

part were coupled with direct current (DC) motors. Each master actuation unit can drive the corresponding slave one through 10-m pipelines, which passed through the waveguide in-between the control room and the MRI room.

To enhance the hydraulic transmission performance and address the criteria (3), the actuator's cylinders were sealed by rolling diaphragm [140], as shown in **Fig. 3.1**. The rolling diaphragm can act as flexible seals to separate the fluid inside pipelines from outside air. Compared to O-ring seals which were generally used in conventional hydraulic systems, rolling diaphragm can offer effective transnational motion with negligible friction between the piston and the inner wall of the cylinder. This kind of elastomeric sealing is made of MR safe, non-metallic material reinforced by fabric to withstand the high internal fluid pressure. The hydraulic pipelines were filled with pressurized fluid to minimize the transmission hysteresis. This can be achieved and maintained by an automatic circulation system, which will be introduced in **Section 5.4.4**. Bubbles in the fluid can also be readily removed to increase the hydraulic transmission stiffness, hence enhancing the robotic actuation performance.

5.4.2 Robotic actuation in 3 DoFs

Three hydraulic actuation units were integrated in the robot to manipulate the cardiac catheter in 3 DoFs, i.e., allowing translation, rolling and steering control over the catheter, as illustrated in **Fig. 5.6**. The linear translational motion (insertion) can be driven by a three-cylinder hydraulic motor (**Section 3.3.2**) to provide continuous and long-range actuation. Not only can it enable the catheter advancement to the human body in a long range of 340 mm, but it can also ensure high fidelity of pushing/pulling the catheter in short range, which is crucial for delicate EP tasks, such as EAM and RF ablation. The rotational output of the motor can be transmitted into linear motion through the main pulley and a timing belt (**Fig. 5.7a-b**), which can then drive the robot moving along the two linear rails. To tighten the belt and reduce hysteresis, two tension pulleys were installed in the basement (**Fig. 5.7b**). Guide rollers with plastic bearings were incorporated to couple with the linear rails, in order to reduce the friction in the translational motion (**Fig. 5.7c**).

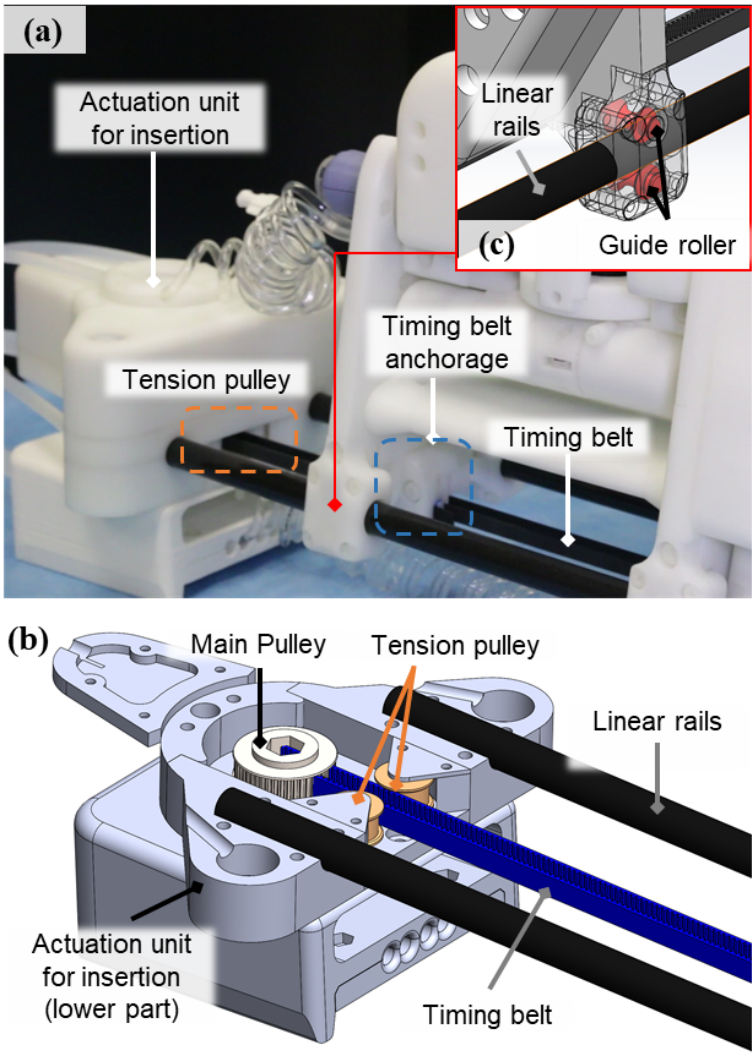

Fig. 5.7: **(a)** Belt-driven system for translational motion, which was actuated by a three-cylinder actuation unit; **(b)** Inner structure of the belt-driven system. Two tension pulleys are installed to tighten the belt, in order to maintain a tension for the belt and reduce hysteresis.

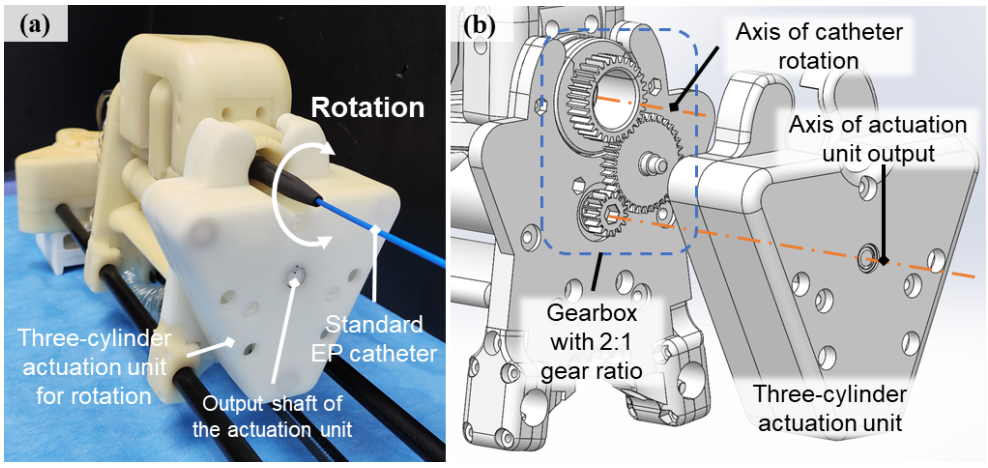

Fig. 5.8: **(a)** Three-cylinder actuation unit for rotation of the robotic platform. It can enable unlimited motion range of catheter rotation; **(b)** Inner structure of the gearbox, which has a gear ratio of 2:1 to gear-down the output of the actuation unit.

The rolling motion (rotation) of the robot is also actuated by a three-cylinder hydraulic motor (**Fig. 5.8a**). It can provide an unlimited rotational range for the catheter. Although the catheter tip can be manipulated to cover the workspace with ±180° rotational range ideally, surgeon may need a larger motion range to compensate the potential twist of the long catheter body. Thus the unlimited rotational range could well fulfill the criteria (2) for effective catheter manipulation. A gearbox was incorporated for the rotational output, as shown in **Fig. 5.8b**, which had a gear ratio of 2:1. This gearbox with a gear-down ratio can improve the performance by increasing the actuation accuracy and stiffness, as well as reduce the hysteresis.

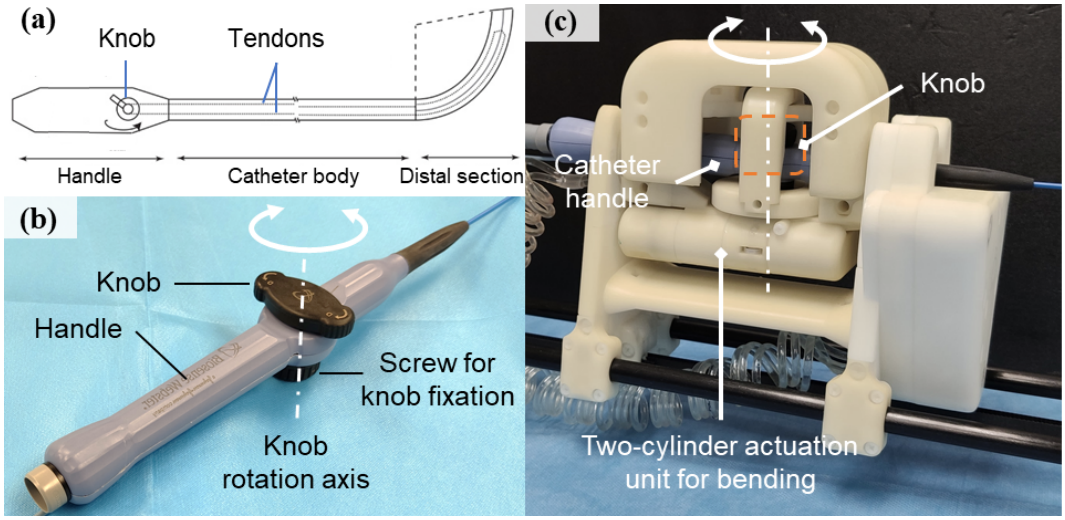

Fig. 5.9: (a) Schematic illustrating the steering mechanism of catheter distal shaft, which is driven by two tendons inside catheter; **(b)** Catheter handle containing the knob for pulling tendons and the screw for knob fixation; **(c)** Robotic platform incorporated with the catheter handle. **Image source**: [49].

The steering (bending) of catheter distal section is driven by two tendons inside catheter (**Fig. 5.9a**), which can be pulled by rotating the knob on catheter handle (**Fig. 5.9b**). A screw on the handle can be tightened to fix the knob's rotation, thus locking the catheter bending shape. By incorporating the catheter with robot, the knob rotation can be actuated by the two-cylinder hydraulic motor because of less motion range required (**Section 3.3.1**). The axis of actuator output shaft is coincide with the knob rotation axis (**Fig. 5.9c**). The hydraulic motor has a motion range of ±60°, which is corresponding to the steering of ±180° for the EP catheter (Thermocool® Bi-Directional Catheter, Biosense Webster Inc.). The two-cylinder actuator can maintain a compact robot size while providing sufficient motion range for catheter steering.

To address criteria (3), the angular positions of the master gears can be precisely controlled using the motors' built-in proportional–integral–derivative (PID) controllers. Since pipeline diameter and length also contribute to the fluid dynamics [175], stiff pipelines made of nylon (**Table 5.1**) were employed to minimize the pipe deformation when subjected to transmission force, thereby maintaining high precision output at the slave gears.

To minimize the EM interference to the MR images, all the components of the slave part were made of exclusively non-metallic, non-conducting, and non-magnetic materials, thus fulfilling the MR safe classification from American Society for Testing and Materials (ASTM) standard F2503-13 [76]. The main structural components were 3D-printed using acrylic compounds (VeroWhitePlus/VeroClear, Stratasys, USA). The key actuation components were made of MR safe materials, including gears of nylon, a transmission belt of rubber, and auxiliary parts of polymers (e.g. Polyvinyl Chloride (PVC), Polyetherimide (PET)). This master-slave system has been tested to withstand rapid actuation ($\leq$ 15 Hz) under high fluid pressure ($\leq$ 0.3 MPa). Regarding sterilization, this small-sized slave body can be enclosed by disposable surgical equipment drapes. The insertion guide (**Fig. 5.10a**), which is made of low-cost acrylic compounds, is also disposable and can be sterilized beforehand.

5.4.3 Quick plug-in catheter holder

The robotic catheter platform employs modularized catheter holders (**Fig. 5.10a**), which can be tailor-made to accommodate various types of steerable EP catheters (e.g. Biosense Webster Inc. or St. Jude Medical). In this way, the platform is switchable for catheterization systems by replacing the detachable catheter holders. Furthermore, these catheter holders can be 3D-printed to account for future upgrade of any new catheter handle design. A "plug-in" design is also included to quickly attached or detached the catheter from the robotic platform, even during the EP procedure. As illustrated in **Fig. 5.10b**, the catheter can be installed into the upper passive holder and mounted on the robot. In EP procedure, the catheter can be inserted firstly by surgeon into patient's vein, and then be incorporated on the robot for further navigation or targeting. The catheter together with the holder can also be quickly detached from the robot, even during the operation. In this way, the robot design can facilitate safe and flexible arrangements for EP procedure.

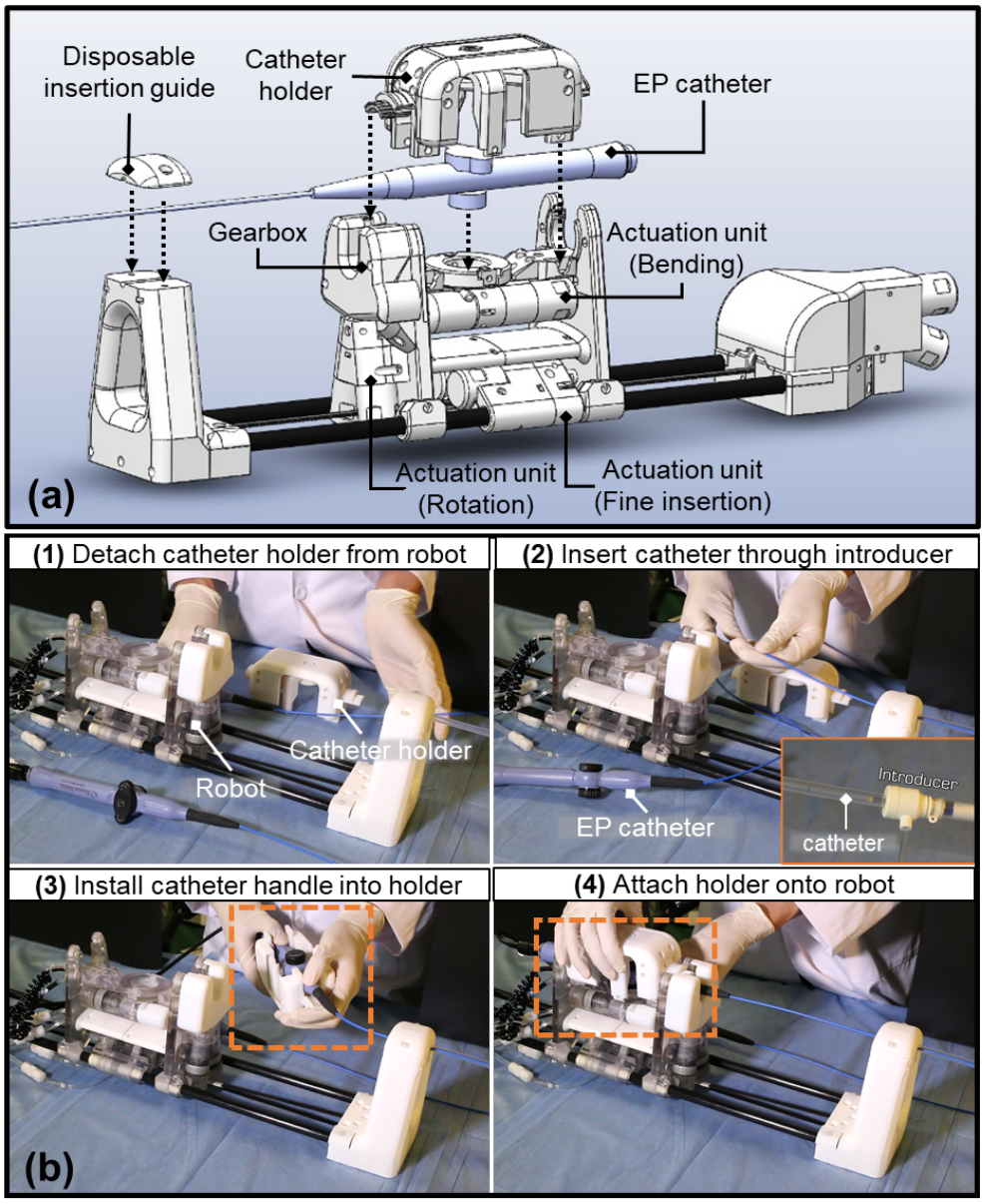

Fig. 5.10: **(a)** Main components of the MR safe robotic manipulator (the slave system) which can operate in the MRI room. A cardiac EP catheter can be tightly mounted on a tailor-made catheter holder; **(b)** Robot deployment procedure including four steps: 1) detach the holder from the robot; 2) insert catheter through introducer; 3) install catheter handle into holder; 4) attach the holder with catheter onto the robot.

5.4.4 Master console and automatic fluid circulation system

The console contains all the master actuation units to tele-operate the slave robot (**Fig. 5.11**) through hydraulic transmission. DC motors, controller and corresponding circuits were installed for actuation and control. As the console should be accommodated in control room, it does not need to fulfill the MR safety requirement. The master console also contains an automatic fluid circulation system to supports the high-performance operation of the hydraulic system. The functions of the circulation system are summarized as following:

1. *Preloading of hydraulic transmission system*. Except for the pipelines connecting the master and slave units, additional pipes link them to a water reservoir to prevent entering of air. Before the robotic operation, valves are opened and pressure (0.05-0.2 MPa) can be introduced into the hydraulic system through a pressurized air source or an air pump. Then the input/output positions of the master and slave units can be aligned. Upon the motor actuation, the valves are closed to isolate the fluid in pipelines, thus enabling the master-slave hydraulic actuation.

2. *Automatic fluid circulation*. The system can circulate the fluid within the hydraulic system. The fluid circulation can drive the air bubbles out of the pipelines into water container, where the compressible air would introduce significant reduction of transmission stiffness and increase of hysteresis. **Fig. 5.11** illustrates the schematic of circulation system. An additional supply pipe is added together with the pipelines of actuation units. MR safe single-way valves can be installed near the slave side to prevent the reverse flow through the supply pipe. The pump can circulate the fluid to the water container, which can hence drive air bubbles out of the pipelines.

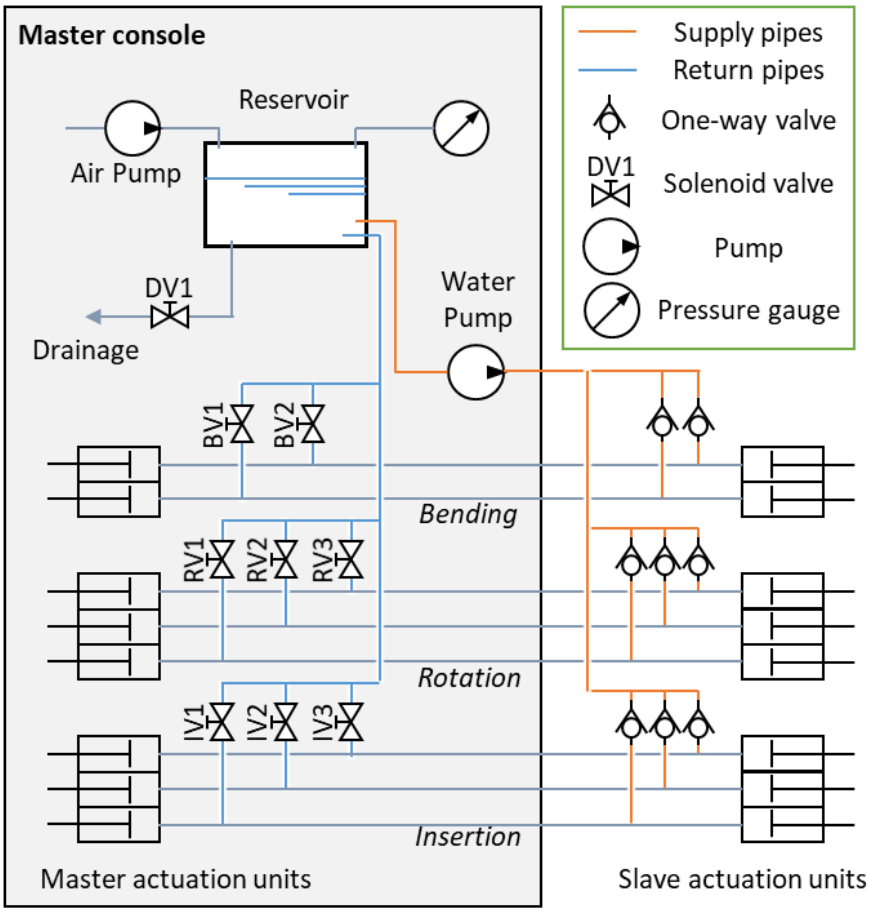

Fig. 5.11: Schematics illustrating the components and pipeline connections of the hydraulic actuation and circulation system.

5.5 Human-robot control interface

We also developed a graphical control interface to provide effective tele-operated control for cardiac EP catheters. The graphical interface can display the pre-operative or intra-operative MR images in 2-D or 3-D space. This allows a physician to have visual guidance towards the targets prior to and/or during the treatment (e.g. ablation). The graphical interface can also display the 3D EAM, ECG and/or other physiological data related to the patient.

Multiple virtual 3D roadmaps of the patient anatomy obtained by MR imaging or other imaging techniques can be overlaid on the graphical interface with or without the MR image slices, as shown in **Fig. 5.12**. This 3D roadmap can be overlaid with virtual 3D models of catheter to locate the measured catheter position inside or outside the patient body. The positional information of catheter could be provided by one or multiple MR-based tracking markers. The graphical display can also overlay the pre-planned ablation targets together with the completed RF ablation lesion, which are illustrated in the endoscopic view and LA roadmap as yellow and red targets in **Fig. 5.12**.

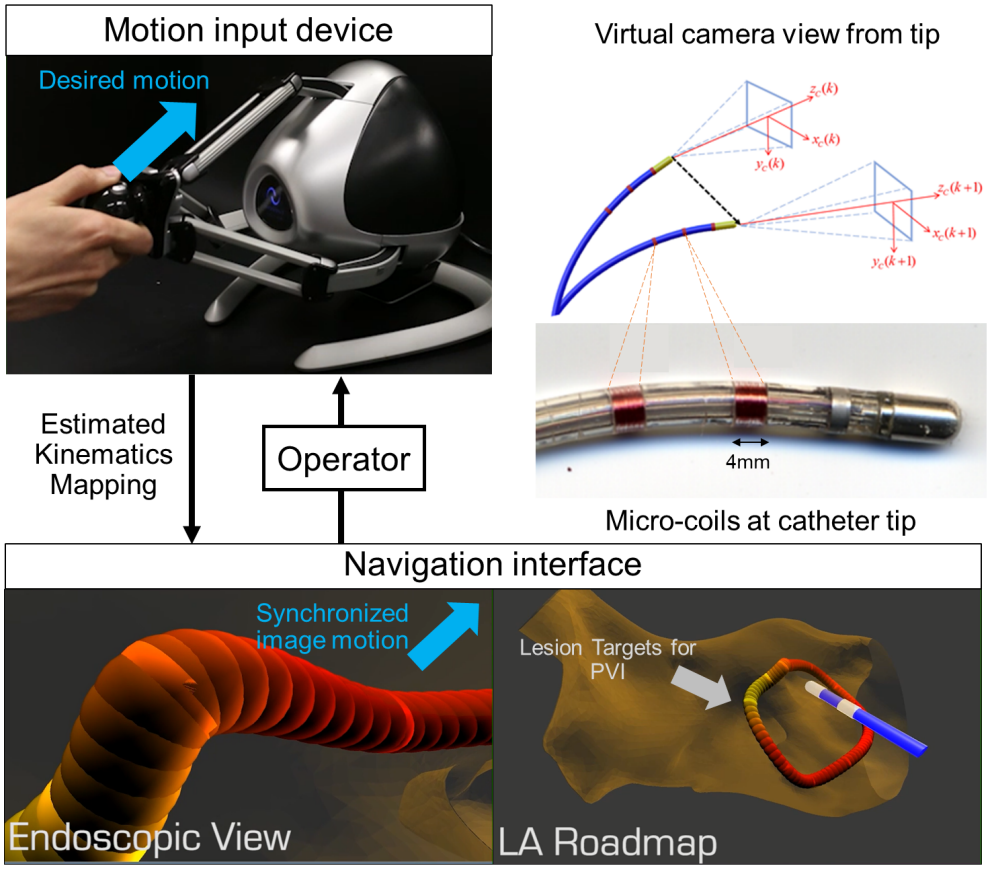

Fig. 5.12: Human-robot control interface for effective and precise catheterization. Cardiac roadmap is indicated with circular lesion target in red. The virtual camera has the same point of view with catheter tip.

A viewpoint looking from the catheter tip towards its normal direction can be simulated. As illustrated in **Fig. 5.12**, an endoscopic view (virtual camera view) is established based on the catheter tip. It can provide the operator with intuitive visual coordination at the catheter tip, which directly aims at the lesion targets, instead of merely the fixed viewpoint. **Fig. 5.12** (bottom) illustrates an exemplary viewing perspective that displays the virtual catheter and 3D roadmap of cardiovascular tissue, as well as its ablated status. The targets in red depict the completion of RF ablation obtained from the intra-operative MR images.

Fig. 5.12 (bottom-left) shows an endoscopic view (virtual camera view) virtually rendered from the viewpoint of catheter distal tip (see dotted lines in **Fig. 5.12**). The figure at the right-up corner of **Fig. 5.12** illustrates the coordinates of virtual camera, which are aligned with the catheter tip. The virtual endoscopic view can be particularly reliable when the position of catheter tip is tracked by the MR-signal in the intra-op imaging coordinates, where the 3D roadmap is also constructed [187]. In conventional imaging modalities, registration was needed to fuse the positional tracking with the imaging system, where misalignment usually exists. In the proposed approach, the MR-based catheter tracking takes place in the same MR imaging coordinates, which can avoid the registration and hence eliminate the misalignment. The robotic system can be operated by a motion input device (e.g. joystick shown in **Fig. 5.12**) that can remotely control the actuation of the robotic catheter. The robot operator can stay in the control room to tele-manipulate the robot catheter with the visual interface. Other than master-slave tele-operation, the robotic system could be automatically controlled by positional and curvature feedback to manipulate catheters towards pre-defined targets, as introduced in **Section 6.3**.

5.6 Experimental validation

The performance of the robotic catheter platform for cardiac EP catheterization has been validated by three experiments: 1) signal-to-noise ratio (SNR) test to evaluate EM interference of the robot to MR images; 2) long-range navigation test to validate the robot performance during the navigation from the simulated femoral vein to LA; 3) short-range navigation task simulating catheter tip targeting for PVI [188].

5.6.1 MRI compatibility test

An SNR test was conducted to evaluate the EM interference to MR images during operation of the robotic catheter platform. In the test, the slave part of the robot was operated inside a 1.5T MRI scanner (SIGNA, General Electric Company, USA) and was placed near a commercial MRI phantom (J8931, J.M. Specialty Parts, USA) at the isocenter of the scanner (**Fig. 3.13**). The T1-weighted fast field echo (FFE) and T2-weighted turbo spin echo (TSE) sequences were adopted to acquire MR images of the MRI phantom, in order to evaluate the potential EM interference generated by the slave robotic manipulator.

Fig. 5.13b shows the resultant MR images of the MRI phantom by T2-weighted TSE under four different conditions: i) *Phantom*: only the MRI phantom was placed in the scanner; ii) *Static*: robot was involved and remained power OFF; iii) *Powered*: robot was kept still, but with the hydraulic and electric powered ON; iv) *In motion*: robot was in operation. The SNR analysis followed the guidelines provided by ASTM F2119-07 [165], with the control condition served as the baseline for evaluation. The MR images had a maximum SNR loss less than 2% and no observable image artifact was found in the MR images under the robot operation scenarios.

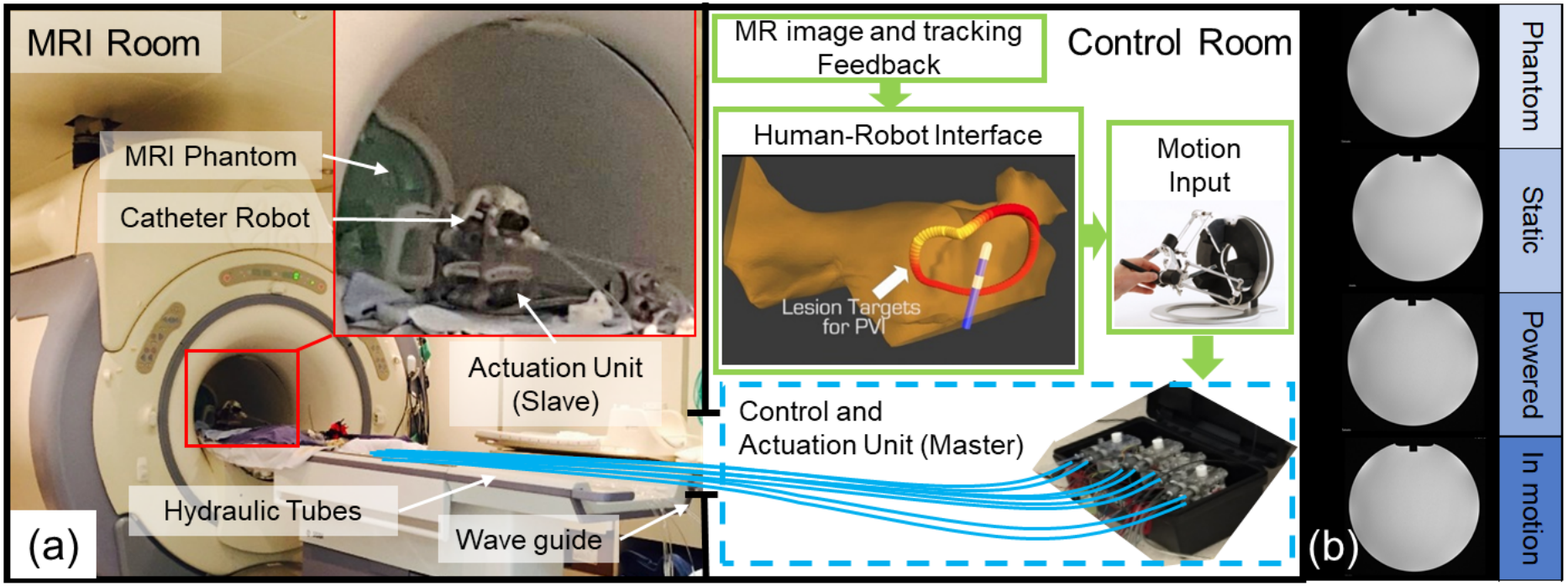

Fig. 5.13: (a) Experimental setup of SNR test for the presented robot. Key components were connected between the MRI and the control rooms via the waveguide. The operator can tele-manipulate the catheter using the catheter navigation interface. **(b)** MR images of an MRI phantom placed aside the robot indicate the negligible EM interference in four different operating conditions.

5.6.2 Long-range catheter navigation

The test of long-range catheter navigation has been designed and conducted to simulate the catheter navigation, from the femoral vein to left atrium. *Eleven* rings (ID = ⌀7 mm) were placed serially along 310-mm distance with an average spacing of 31 mm (**Fig. 5.14**). The detailed dimensions are stated in **Table 5.2**. A smooth curve linking the ring centers in serial simulated a path along the vessel to heart chamber (**Fig. 5.15**). This task would be found more difficult relative to the navigation in human vein (inner diameter ≈⌀9.4 mm) and inferior vena cava (inner diameter ≈⌀20 mm) [189, 190].

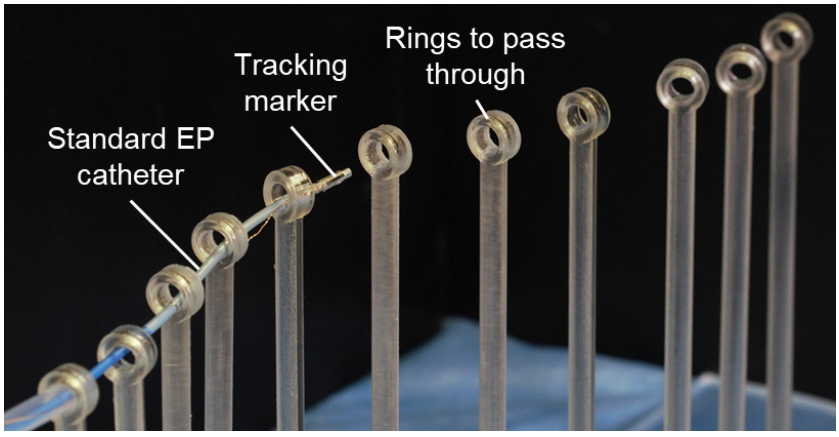

Fig. 5.14: EP ablation catheter tele-manipulated to pass through a series of 11 rings. The 3-D position of catheter tip was EM-tracked in real-time;

Table 5.2: Key parameters of the experimental setup and the catheterization performance indices

Experimental settings	
No. of rings	11
Inner diameter of the rings (mm)	7.0
Dimension of the setup (L×W×H mm)	310×70×32
Avg. spacing of rings along x-axis (mm)	31.0
Robot performance	
Total time (s)	96.0
Average time interval per ring (s)	9.6
Min./max. interval between two rings (s)	1.9/19.8
Average value of deviation (mm)	3.03

In the task, a standard catheter with an outer diameter of 8 Fr (≈⌀2.7 mm) was manipulated by the robot, which was tele-controlled by a 3D motion input device (Novint Falcon, NF1-L01-004). To record the real-time position and orientation (pose) of the catheter, a 5-DoF EM positional sensor (NDI Medical Aurora) was attached near the catheter tip (**Fig. 5.14**). A subject, who was familiar with the robot operation, was invited to perform the task. The subject could look at the catheter tip to adjust the manipulation so as to pass through all those eleven rings.

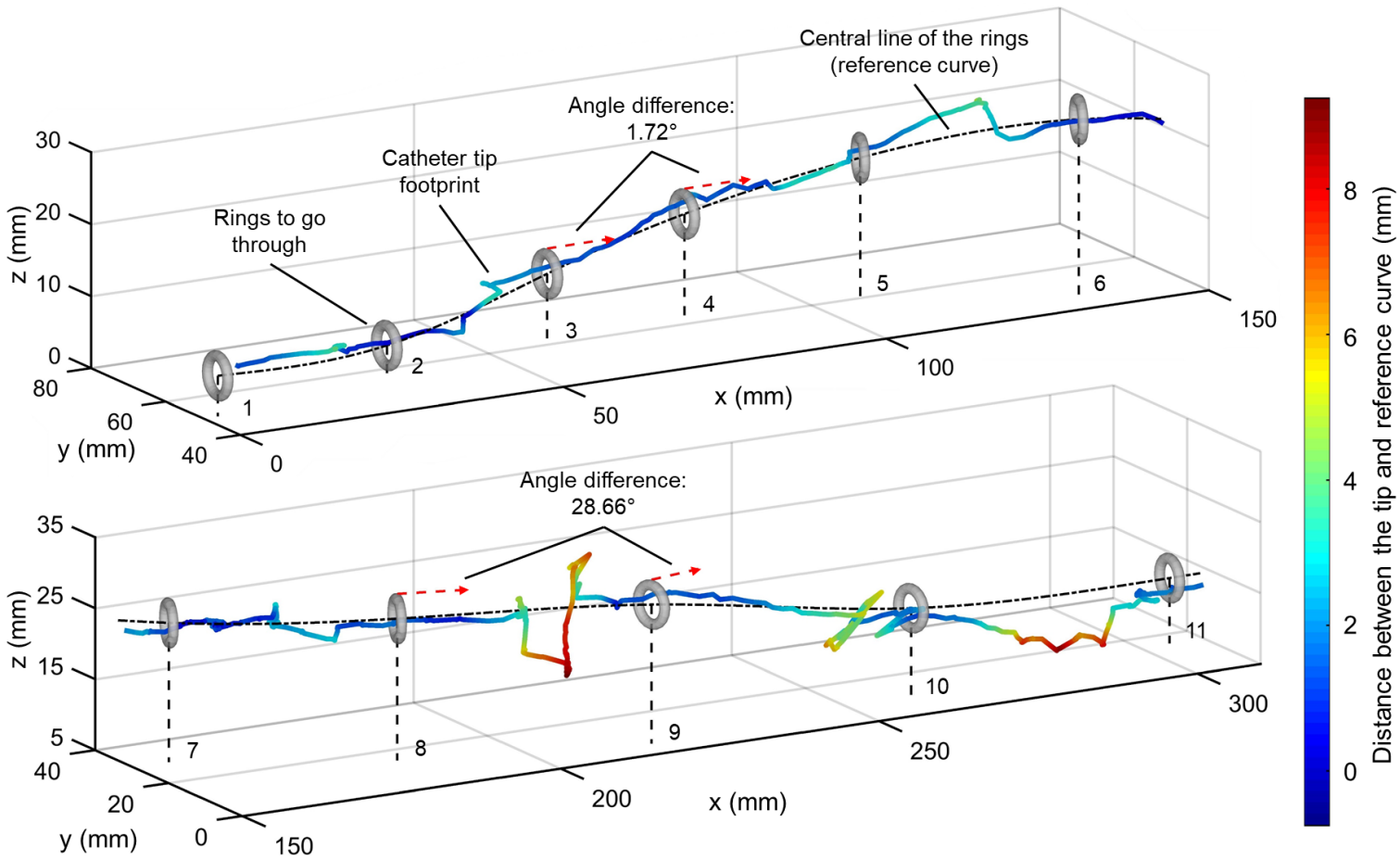

Fig. 5.15: Actual footprint of the catheter tip compared with the reference curve along the series of rings of 1st–6th (Upper) and 7th–11th (Lower). More the catheter tip deviated from the reference curve, warmer the color of its tip footprint. Large difference in the orientation of two adjacent rings, e.g. from the 8th to the 9th, made the navigation challenging.

The diagrams in **Fig. 5.15** depict the catheter tip footprint along the series of 11 rings. The deviation from catheter tip to the reference curve is indicated by the color gradient. A mean value of deviation, 3.03 mm, was found throughout the entire trajectory. Most sections of navigation are smooth and closed along with the reference curve. But several sections of the tip footprint involve more deviations, particular when the orientation difference of adjacent rings is relatively large. The subject may somehow feel challenging to drag the catheter into the ring hole without graphic user interface (GUI)-aided navigation.

5.6.3 Short-range catheter tip targeting

A short-range navigation task was conducted to simulate catheter tip targeting for PVI. An LA simulator was designed and constructed based on a patient-specific imaging data. It was 3D-printed with soft material (AgilusClear, Stratasys, USA) (**Fig. 5.16**). A semi-rigid sheath was fixed near the end to ensure the location of the outlet was similar to the transseptal puncture through atrial septum to the LA in PVI task.

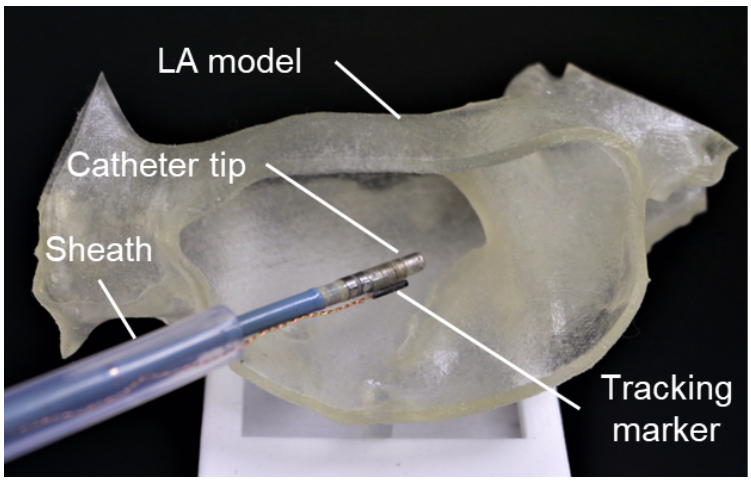

Fig. 5.16: Catheter navigation test conducted in a soft left atrial (LA) simulator. EM tracking marker was attached on the catheter tip. A standard EP ablation catheter was tele-manipulated to reach a series of targets around the pulmonary vein ostium;

The same subject, as in the last navigation task, tele-manipulated the catheter through the aid of a human-robot control interface (**Section 5.5**), by which a virtual endoscopic view looking from the catheter tip's viewpoint could be rendered and provided [187, 191]. This endoscopic view on cardiac EP roadmap can be well constructed with accurate alignment, as the MR imaging and tracking can be both acquired within the same MR coordinate system. The MR-based tracking can offer fast and accurate feedback of catheter tip position [36]. MR-tracking tiny coils can be integrated close to the tip. Meanwhile, the fast MR images can be acquired in the region around the catheter tip such that the RF ablated lesion can be

registered/realigned on the EP roadmap [148, 192]. In this way, the relevant physiological features can be updated in situ on the same roadmap for making the instant decision on the next move of the catheter tip.

In the lab-based experiment, the endoscopic view was generated based on the tracked catheter tip. A virtual LA model was registered to the actual simulator so as to align both coordinates of tracking and model into a single coordinate frame. Six landmarks were predefined on the support of LA simulator. The virtual endoscopic view can facilitate fine placement of the catheter tip while approaching the "lesion" targets that has revealed on the virtual LA model around the pulmonary vein ostium. Note that this virtual model acted as an EP roadmap in our simulated task. By stepping on the foot pedal, the subject could create "lesion" when the catheter tip contacts the virtual LA model surfaces.

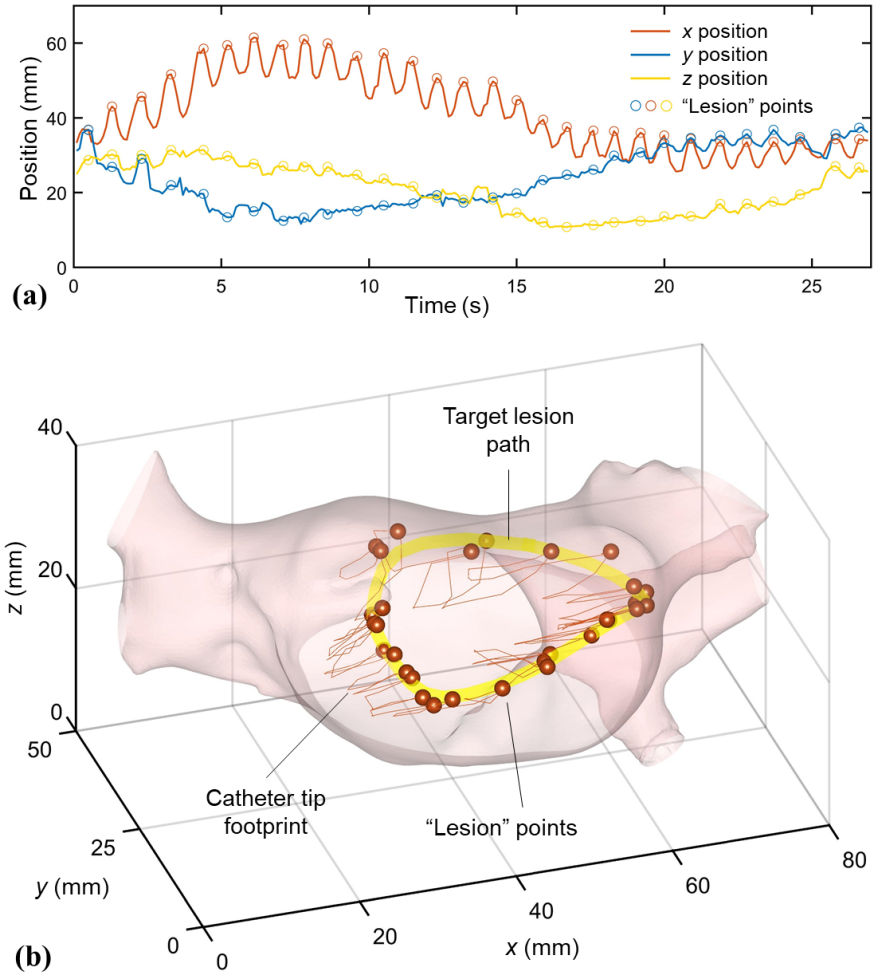

Fig. 5.17: (a) Catheter tip trajectory decoupled 3 axes against time (in 27 seconds). Fast reciprocating motions could be observed from the *x*-axis displacement profile; **(b)** Front view showing the catheter tip footprint, the 30 targeted ablation points – "lesions", and also the desired lesion targets (yellow). The footprint (red line) indicates the reciprocating motions towards the "lesions".

Fig. 5.17a illustrates the tip trajectory in x-, y- and z-coordinates, which was created in one go during the aforementioned task in 27 seconds. Note that the catheter insertion was aligned close to the x-axis. The reciprocating motions of catheter tip could be obvious in x axis, with an average frequency of 1.1 Hz over the time range. It demonstrated our robot capable of providing dexterous reciprocating motions for RF ablation and EAM construction with delicate and precise tip-tissue contact. **Fig. 5.17b** and **Fig. 5.18** show different views of the virtual LA model, along with the circumferential lesion targeted nearby the pulmonary vein ostia. The red dots, with a total number of 30, represent the "lesion" points. The subject aimed to follow the circumferential ablation path with the reciprocating catheter motion tele-operated by the robot. The deviation of catheter tip from this path could be measured at the frequency of 40 Hz. Such deviation in average and maximum were, respectively, 1.1 mm and 3.2 mm, as measured. It is worth noting that the "lesions" were conducted clockwise from the view of **Fig. 5.18**, in which the catheter tip footprint also reveals along the circumferential path.

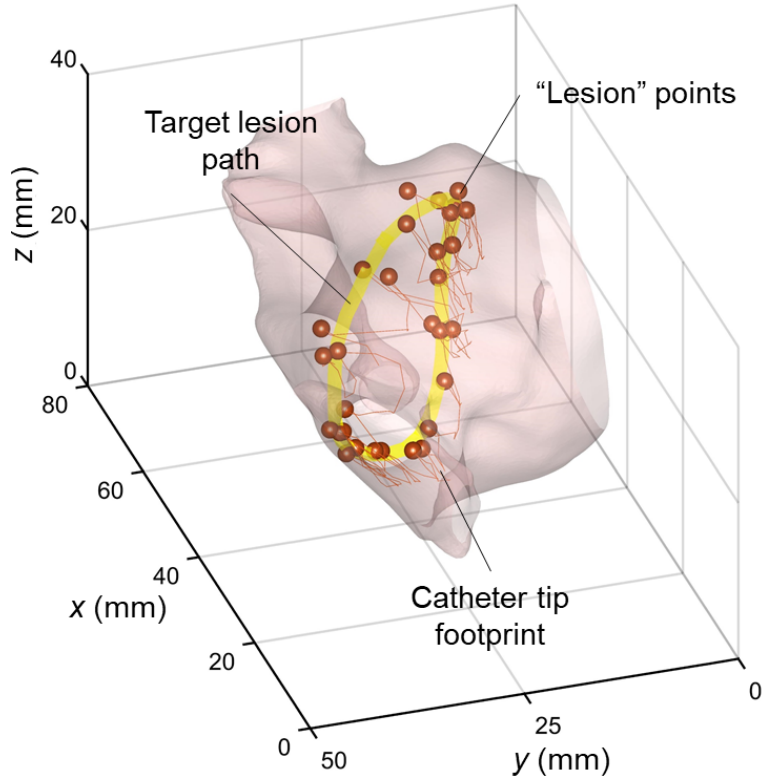

Fig. 5.18: Side view showing the catheter footprint fully covers along the "lesions".

5.7 Towards realization of robot-assisted cardiac EP under intra-operative MRI

Over the last decade, there have been many MRI-guided cardiac EP procedures conducted in clinical settings, despite without any robot-assisted one. It is worth noting that the EP operator needs many cardiac data references from multiple computer screens (> 4 usually) throughout the procedure. Limited space in interventional MRI suite, or EM shielding of multiple screens, still remain the obstacles to smoothen the surgical workflow. The operator would have to access in and out MRI suite and control room frequently. The proposed MR safe robotic catheter tele-manipulation will allow the operator to perform EAM and RF ablation inside the control room, also given with sufficient references in screens.

In addition, real-time MR-based tracking of the catheter position is crucial to close the robot control loop. MR-*active* tracking can enable precise, fast and continuous 3-D locations of the catheter tip in the MR imaging coordinates. Wireless MR-based tracking markers can be embedded with the catheter body or close to its tip. It is the state-of-the-art without having to connect the coil units with MRI scanner receivers through any coaxial cables [193]. Such coil units can resonate with Larmor frequencies (1.5T: 63.8 MHz or 3T: 123.5 MHz) by means of wireless inductive coupling with the MRI system [180]. Such wireless setting can avoid generating any RF interference to imaging, also any heating hazards along the cables.

5.8 Conclusion

The proposed MR safe robotic manipulator is the first of its kind that can offer sufficient DoFs to tele-manipulate a cardiac catheter under intra-op MRI guidance [182]. The robot fulfills the MR safe standard (ASTM F2503-13), as it solely comprises of non-conductive, non-metallic and non-magnetic materials. Currently, there is no such commercial system that is MR safe. The proposed manipulator incorporates the high-fidelity hydraulic transmission using rolling-diaphragm seals (**Chapter 3**). We have emulated the catheter navigation and PVI tasks to validate the robot performance of long-range advance and subtle lesion targeting. These experiments have altogether demonstrated that the robot can offer effective manipulation towards MRI-guided EP procedure with sufficient workspace and dexterity, which is the first of its kind. Regarding the material cost of current prototype, the disposable part (slave part) in MRI room is around US$ 1400, and the console (master part)

in control room is about US$ 2000.

The major challenge of the MR safe robotic catheter system is the lack of well-established clinical settings towards intra-op MRI-guided EP procedure, such as MRI-based cardiac mapping system, 12-lead ECG acquisition device, defibrillator in MRI, as well as RF ablation system. In our future work, pre-clinical animal trials will be conducted on a live porcine prepared with arrhythmia. The proposed robotic system will be integrated with commercial MR conditional systems of 12-lead ECG acquisition and RF ablation (ClearTrace^{TM}, MRI Interventions, Inc. or Imricor Medical System). The necrosis created by RF ablation, and its efficacy, will also be examined with the post-mortem histology.

For commercialization of the robotic catheter system, numerous studies need to be carried out. Pre-clinical animal trials will be conducted to evaluate the robot overall performance. Modifications on the robotic system will be made based on the surgeons' feedback. In prior to market approval from relevant agency (e.g. Food and Drug Administration (FDA)), the system will go through clinical studies to verify the safety and effectiveness in surgical routine. The major challenge towards commercialization is the synergic use of multiple MR conditional systems provided by several parties (e.g. Imricor Medical System Inc., MRI Interventions, Inc.), including MRI-based cardiac mapping system, 12-lead ECG acquisition device, and RF ablation system.

In summary, the advent of the proposed MRI-guided robotic catheter system will increase surgeon's confidence to perform effective RF ablation, while improving the catheter navigation safety. As a result, it may reduce nerve damage, esophageal fistula creation, pulmonary vein stenosis and stroke, as well as the chance of post-procedural disease recurrence (currently 30% in atrial fibrillation and 50% in ventricular tachycardia). This will contribute to justifying the use of MRI, while reducing the overall healthcare expenditure of the treatments.

Chapter 6

High-performance Control Interfaces for Robotic Catheter System

6.1 Introduction

Cardiac electrophysiology (EP) is an effective treatment for arrhythmias, in which a long and flexible catheter is delivered to the heart chamber for radiofrequency (RF) ablation. In **Chapter 5**, an MR safe robotic platform is present, which is capable of manipulating the standard cardiac EP catheter under intra-operative (intra-op) magnetic resonance imaging (MRI) guidance. However, it is still challenging to realize effective catheter control due to the disorientation in tele-manipulation. To improve the control effectiveness towards the cardiac catheter, kinematics modeling methods have been investigated in **Section 6.2**, with model-free and model-based control approaches implemented on the robotic platform for quantitative comparison and evaluation.

A shape tracking system is also present in **Section 6.3** for the standard cardiac catheter, integrating the tracking coils and a multi-core optical fiber with fiber Bragg gratings (FBGs). Both shape and positional tracking of the catheter bendable section could be achieved. A learning-based modeling method is developed for cardiac catheters, which can utilize FBG-reconstructed three-dimensional (3D) curvatures to characterize the model parameter and update the motion mapping. The proposed shape tracking and modeling methods have been implemented on an MRI-guided robotic platform, which can achieve feedback control of a cardiac catheter. Their overall performance was demonstrated by a simulated pulmonary vein isolation (PVI) task with *ex-vivo* tissue ablation.

6.2 Kinematics modeling for robotic catheter

In this section, kinematics modeling for robotic catheter with model-free control method is introduced. Compared to model-based approaches, model-free control method can avoid the complicated procedures of system identification by estimating the robot kinematics online. It can benefit in particular to the modeling of cardiac EP catheters, which consist of composite materials with unknown properties. A control mapping for hand-to-eye coordination was implemented based on the virtual endoscopic view. The model-based controller was designed based on the constant curvature kinematics model [155, 156]. The model-free controller can utilize positional feedback to update the kinematic Jacobian [194]. Experimental evaluations were carried out using a standard cardiac catheter, which was tele-manipulated via an MR safe robotic manipulator (**Fig. 5.6**) under a virtual endoscopic guidance (**Fig. 6.1**). The major contributions include: 1) Control mapping for hand-to-eye coordination based on the virtual endoscopic view utilizing model-based and model-free control methods; 2) Experimental validation of model-based and model-free control approaches for the robotic catheter platform.

6.2.1 Generation of endoscopic view

As illustrated in **Fig. 6.1a**, an endoscopic view (virtual camera view) is established based on the catheter tip, where the z-axis matches the tip axial direction. The 6-dimension (6-D) endoscopic pose can be determined by the MRI tracking system. In this work, user's input motion can be correlated to the catheter tip motion in the endoscopic view. Firstly, the catheter tip position is derived for the transformation from the Cartesian space to the X-Y frames inside the 2D endoscopic view. The incremental movement of the virtual camera at the catheter tip with respect to (w.r.t.) the coordinate frame of endoscopic view $\{\boldsymbol{C}\}$ and the world coordinate frame (Cartesian space) $\{\boldsymbol{W}\}$ can be denoted respectively as:

$$\Delta \boldsymbol{p}_{\mathrm{c}} = \begin{bmatrix} \Delta x_{\mathrm{c}} & \Delta y_{\mathrm{c}} & \Delta z_{\mathrm{c}} \end{bmatrix}^{\mathrm{T}} \tag{6.1}$$

$$\Delta \boldsymbol{p}_{w} = \begin{bmatrix} \Delta x_{w} & \Delta y_{w} & \Delta z_{w} \end{bmatrix}^{\mathrm{T}} \tag{6.2}$$

where the unit vector Δz_{c} is set to follow the forward direction of catheter tip.

The rolling of the camera along the z-axis is fixed during the movement, which is to guarantee the consistency of the catheter steering direction. A unit vector $\boldsymbol{z}_{\mathrm{c}} \in \mathbb{R}^3$ denotes

the axial direction of rolling. Hence the horizontal/vertical axes in the plane of camera view $\begin{bmatrix} \Delta x_c & \Delta y_c \end{bmatrix}^T$ are equivalent to the x- and y-axis of the camera's coordinate frame. The rotation matrix of $\mathbb{R}^{3\times3}$ from the world to camera coordinate frame can be formed as ${}^{C}_{W}\boldsymbol{R} = \begin{bmatrix} \boldsymbol{x}_c & \boldsymbol{y}_c & \boldsymbol{z}_c \end{bmatrix}^T$. By omitting the z_c in the last row, the 2-dimension ($\mathbb{R}^{2\times3}$) matrix ${}^{C}_{W}\widehat{\boldsymbol{R}} = \begin{bmatrix} \boldsymbol{x}_c & \boldsymbol{y}_c \end{bmatrix}^T$ can represent the transformation of tip displacement, relative to its image plane coordinate, i.e. $\Delta \boldsymbol{p}_c = {}^{C}_{W}\boldsymbol{R}\,(\Delta \boldsymbol{p}_w)$.

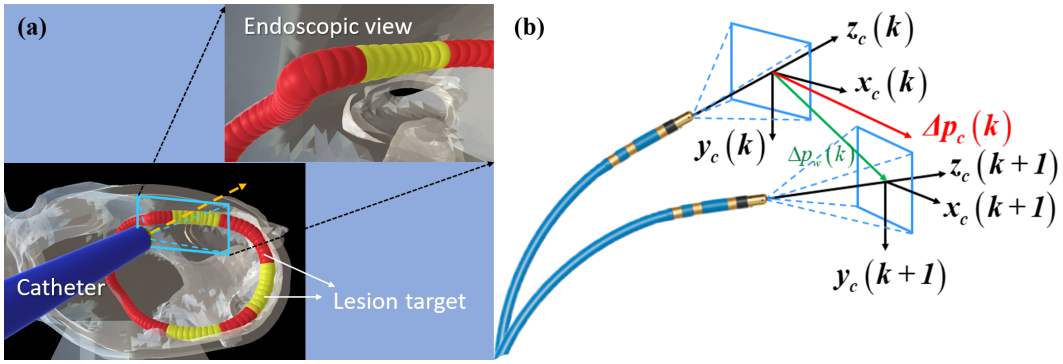

Fig. 6.1: (a) Virtual lesion targets pre-defined in EP roadmap, with ablated sections in yellow and incomplete regions in red. The orientation of endoscopic view is set to follow the axial direction of catheter tip; **(b)** Diagram illustrating the catheter tip displacement between the step k and $(k+1)$.

6.2.2 Model-based control

In prior to implementation of control algorithm to the robot, the kinematics/dynamics model of the flexible catheter needs to be established. Various modeling approaches for continuum robots have been investigated by previous works, including constant curvature model [155, 156], beam model [157], n-rigid links model [158]. For standard cardiac catheter, it can be steered into two directions within the same plane by pulling tendons. The kinematics modeling has been deduced in [155] based on Denavit–Hartenberg (D-H) parameters. Two assumptions are taken: constant bending curvature and zero torsion along the catheter body. **Fig. 6.2** illustrates the equivalent model.

Three degrees of freedom (DoFs) exist in the catheter distal bending section, as illustrated in **Fig. 6.2a**. Relevant parameters include the axial translation d_i, the rotation angle θ_r, and the bending angle θ_b. The catheter tip motion can be driven by the manipulation from the catheter handle, which is illustrated in **Fig. 6.2b**. The twisting angle of the knob, insertion distance, and rotation angle of the handle are denoted by ϕ, d, and α respectively.

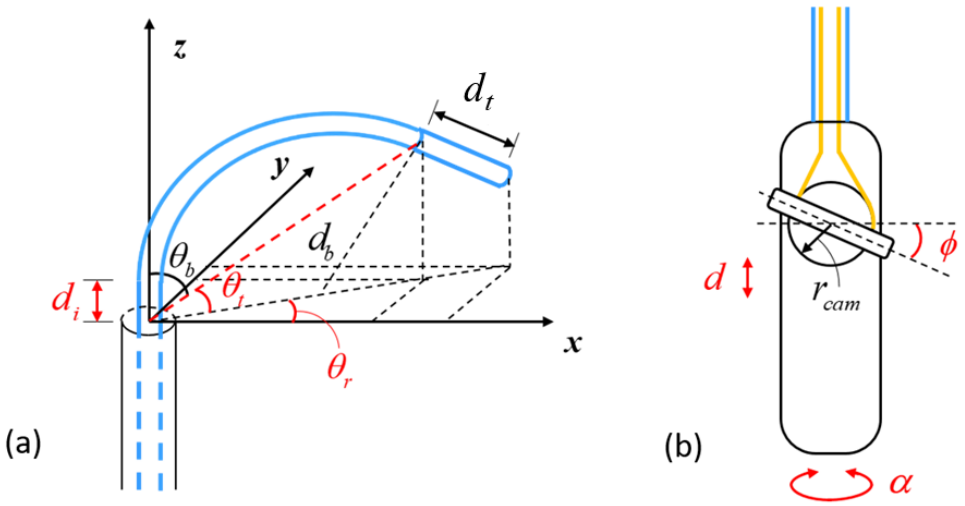

Fig. 6.2: Schematics illustrating the manipulation mechanism of a typical catheter. **(a)** Catheter distal bending section represented by constant curvature geometry; **(b)** Three-degree-of-freedom (3-DoF) manipulation of the catheter handle, including twisting angle ϕ, insertion distance d, and rotating angle α.

The insertion distance d of the catheter handle can be approximately regarded as the axial translation of the catheter tip d_i, such that $d \approx d_i$. The rotation at the tip θ_r is calculated by multiplying a torsional transmission coefficient K to the rotating angle of handle α as $\theta_r = K\alpha$. In the experiment, a value of 1 was taken, because of the negligible friction between the catheter body and Polytetrafluoroethylene (PTFE) pipeline. According to the assumption of constant curvature, the bending of catheter tip section can be described based on the knob angle ϕ with the relation:

$$(\pi - 2\theta_t)\,\Delta R = (1+k)\,r_{cam}\phi,\ \theta_t + \theta_b = \pi/2 \tag{6.3}$$

where r_{cam} is the cam radius of the catheter knob, ΔR is the difference of bendable section radius between the outer and inner arc. In the equation, a backlash factor k is included to address the cable displacement due to tension [156]. It has a value of 1 with the assumption that both pulling wires are in tension during operation.

The position of the catheter tip can be deduced as following based on d, ϕ, and α within the coordinate system in **Fig. 6.2**:

$$\boldsymbol{p} = \begin{bmatrix} \left(d_t \mathrm{s}\,(2M\phi) + \frac{L}{M\phi}\mathrm{s}^2\,(M\phi)\right)\mathrm{c}\,(K\alpha) \\ \left(d_t \mathrm{s}\,(2M\phi) + \frac{L}{M\phi}\mathrm{s}^2\,(M\phi)\right)\mathrm{s}\,(K\alpha) \\ d_t \mathrm{c}\,(2M\phi) + \frac{L}{2M\phi}\mathrm{s}\,(2M\phi) + d \end{bmatrix},\ M = \frac{r_{cam}\,(1+k)}{\Delta R} \tag{6.4}$$

where L is the total length of catheter bendable section, d_t represents the total length of

the tip rigid section. The symbols $\mathrm{c}(\cdot)$ and $\mathrm{s}(\cdot)$ respectively represent the full expression of $\cos(\cdot)$ and $\sin(\cdot)$. The added and initial lengths of bending arc are respectively denoted by ΔL and L_b. Here, ΔL can be ignored because of the relatively small value compared to L_b:

$$L = \Delta L + L_b = 2r_{cam}\theta_t + L_b \approx L_b \tag{6.5}$$

The relation can then be described from the actuator inputs $\boldsymbol{q} = \begin{bmatrix} \phi & \alpha & d \end{bmatrix}^{\mathrm{T}}$ to the catheter tip position $\boldsymbol{p}_c = \begin{bmatrix} x_c & y_c & z_c \end{bmatrix}^{\mathrm{T}}$ by referring to the frame of camera view $\{\boldsymbol{C}\}$. Its differential function can be denoted as

$$\dot{\boldsymbol{p}}_c = \boldsymbol{J}\dot{\boldsymbol{q}} \tag{6.6}$$

where $\boldsymbol{J} \in \mathbb{R}^{3\times 3}$ is the Jacobian matrix. It can be obtained by differentiating $\boldsymbol{p}_w$ w.r.t. $\boldsymbol{q}$, where $\boldsymbol{p}_c = {}^{C}_{W}\boldsymbol{R} \cdot \boldsymbol{p}_w$.

After the calculation of Jacobian matrix for forward kinematics, the function for inverse kinematics can be derived as $\dot{\boldsymbol{q}} = \boldsymbol{J}^{-1}\dot{\boldsymbol{p}}_c$, which has the discretized form as

$$\Delta\boldsymbol{q} = \boldsymbol{J}^{-1}\Delta\boldsymbol{p}_c \tag{6.7}$$

Since the overall aim is to synchronize the input motion with the catheter tip movement, the input value from the 3D motion input device can be assigned as $\Delta\boldsymbol{p}_c$, and then the inverse Jacobian matrix $\boldsymbol{J}^{-1}$ could be derived based on the values in the last time step. Then the actuator variables $\Delta\boldsymbol{q}$ can be calculated based on the two variables.

6.2.3 Model-free control

Other than the control method based on the pre-defined model, the model-free control method has also been investigated. The algorithm is from the optimal control approach in [194], but without the consideration of force. Continuous update of Jacobian matrix can be conducted during the operation based on real-time data. A simple initialization of the Jacobian matrix is needed at the beginning. Then the robot can be controlled with an updating mapping scheme. The following content describes the control flow.

(1) *Initialization of Jacobian matrix*: The initialization is conducted by sequentially actuating the three DoFs of the robot with a discrete value $\Delta\boldsymbol{q}_i$ $(i = 1,2,3)$, and recording

the resultant positional movements at the tip $\Delta \boldsymbol{p}_{ci}$. Thus the Jacobian matrix $\boldsymbol{J}$ could be initialized:

$$\boldsymbol{J} = \begin{bmatrix} \boldsymbol{J}_1 & \boldsymbol{J}_2 & \boldsymbol{J}_3 \end{bmatrix}, \tag{6.8}$$

where $\boldsymbol{J}_i$ could be obtained as $\boldsymbol{J}_i = \Delta \boldsymbol{p}_{ci} / \Delta \boldsymbol{q}_i$. With introduce of a weighting matrix $\boldsymbol{W} = \text{diag}\left(\|\boldsymbol{J}_1\|, \|\boldsymbol{J}_2\|, \|\boldsymbol{J}_3\|\right)$, the kinematics described in **Eq. 6.6** could be denoted as:

$$\dot{\boldsymbol{p}}_c = \widehat{\boldsymbol{J}} \boldsymbol{W} \dot{\boldsymbol{q}}, \quad \widehat{\boldsymbol{J}} = \boldsymbol{J} \boldsymbol{W}^{-1} \tag{6.9}$$

which has a discrete form as

$$\Delta \boldsymbol{p}_c = \widehat{J} \boldsymbol{W} \Delta \boldsymbol{q} \tag{6.10}$$

(2) *Updating of Jacobian matrix*: The online update of Jacobian matrix is based on the continuous deduction of quadratic programming process below:

$$\begin{aligned} &\text{minimize} \quad \text{abs}\left(\Delta \widehat{\boldsymbol{J}}(\text{k})\right) \\ &\text{subject to} \quad \widehat{\boldsymbol{J}}(k+1) = \widehat{\boldsymbol{J}}(k) + \Delta \widehat{\boldsymbol{J}}(k), \Delta \boldsymbol{p}_c(k) = \widehat{\boldsymbol{J}}(k+1) \boldsymbol{W} \Delta \boldsymbol{q}(k) \end{aligned} \tag{6.11}$$

where Jacobian matrices $\widehat{\boldsymbol{J}}(k)$ and $\widehat{\boldsymbol{J}}(k+1)$ are obtained at the step k and $k+1$ respectively, $\Delta \widehat{\boldsymbol{J}}(k)$ is the optimization variable. The displacements are denoted by $\Delta \boldsymbol{p}_c(k)$ in camera view and $\Delta \boldsymbol{q}(k)$ in actuator output for the single step from k to $k+1$. The Frobenius norm (L_2-norm) of $\Delta \widehat{\boldsymbol{J}}(k)$ is minimized to achieve a smooth transition of the Jacobian's column vectors. After deducing the newest Jacobian, the actuation command can be derived as

$$\Delta \boldsymbol{q}(k+1) = \left(\widehat{\boldsymbol{J}}(k+1) \boldsymbol{W}\right)^{-1} \Delta \boldsymbol{p}_c{}^*(k+1) \tag{6.12}$$

where $\Delta \boldsymbol{p}_c{}^*(k+1)$ represents the target movement shown in the camera view. At each step, the new Jacobian matrix $\widehat{\boldsymbol{J}}(k+1)$ is obtained by finding the difference between the actual tip motion and the predicted tip motion calculated from $\widehat{\boldsymbol{J}}(k)$. As the updating scheme is to compensate the error existing in the current Jacobian $\widehat{\boldsymbol{J}}(k)$, the mapping error will be reduced rather than accumulated in the Jacobian updating process (**Eq. 6.12**).

6.2.4 Experimental validation

6.2.4.1 Experimental setup

MR-safe Robotic Catheter Platform: The above-mentioned control algorithms were implemented on an MR safe catheter robot (**Chapter 5**) [182, 195]. This robot features a master-slave hydraulic transmission that can manipulate a standard cardiac catheter in 3 DoFs. Each master unit was actuated by an electric direct current (DC) motor located in the control room. The fluid power was delivered to the slave unit via the long hydraulic transmission pipelines ($\approx$ 10 meters). The master-slave actuation design can separate the components with ferromagnetic materials from the MRI scanner, ensuring negligible electromagnetic (EM) interference to the MR images. The robot can provide sufficient workspace to perform RF ablation for pulmonary vein isolation, as shown in [195].

Left Atrial Model: The 3D anatomical model of left atrium (LA) (**Fig. 6.3a**) was obtained from MRI scanning and 3D-printed with soft material (AgliusClear, Stratasys Inc.). The shore hardness of the material is A30-35 and the polymerized density is 1.14-1.15 g/cm^3. To conduct RF ablation inside LA, EP catheter is inserted at femoral vein, through the inferior vena cava to the right atrium. After puncturing the atrial septum, it will reach LA for RF ablation [196]. In our experiment, a tube (Polytetrafluoroethylene (PTFE)) was used to form the pathway, guiding catheter towards the LA model with similar entering direction and position compared to EP procedure.

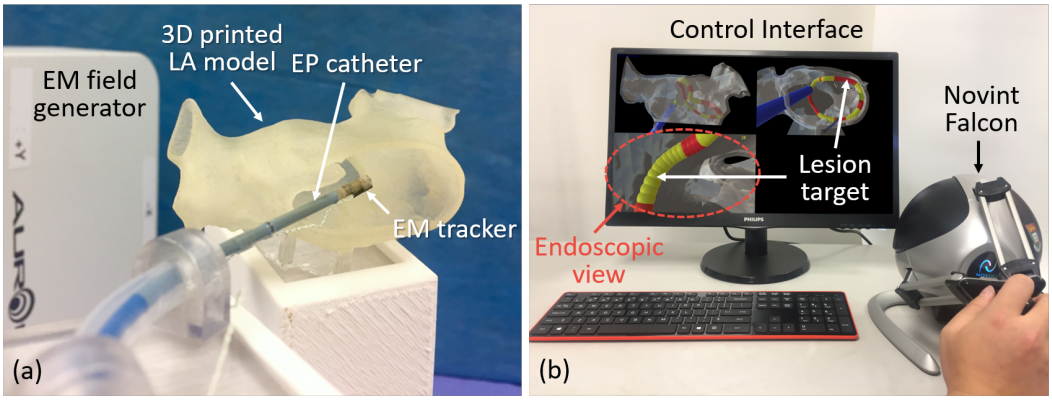

Fig. 6.3: (a) Experimental setup including an EP ablation catheter and a left atrial (LA) model; **(b)** Human-robot control interface including rendered cardiac roadmap in three perspectives. The operator can use a motion input device to tele-operate the robot through the interface.

Position Tracking System: To record the position and orientation of the catheter tip, an EM tracking system (Aurora V3, Northern Digital Inc.) (**Fig. 6.3a**) was adopted. In MRI setting, MR-based tracking coils [36] can replace the EM tracking system for

catheter localization with comparable performance. Active coil wired to the receiver system could realize a tracking resolution as high as $0.6 \times 0.6 \times 0.6$ mm^3 [36]. Although the positional tracking may not be linear due to MRI distortion, the tracking accuracy can be still maintained within the MR imaging coordinate, where the distortion would take place for both tracking and imaging. The use of 1D-projection pulse-sequence [180] allows acquisition of the marker's 3D positional signal along each axis, enabling fast localization up to 30 Hz. With an MRI real-time control interface, RTHawk (Heartvista™), the raw scanning data can also be streamed out at low latency ($<$20 ms).

Robot control interface: Before the experiment, registration of the LA simulator to the coordinates in Unity 3D were performed to align the spacial frames. The LA simulator made of soft material was anchored on a rigid pedestal. Six points were pre-defined on the pedestal for registration between the virtual environment and EM coordinate. Upon establishment of the reference points' transformation, the 3D-printed LA simulator could be registered with the virtual LA model in the interface. As described in "Position tracking system" paragraph, a 6-DoF EM tracker (Aurora #610029, Northern Digital Inc.) was attached to the distal end of the catheter, to capture the position and orientation. Hence, the relative geometric configuration between LA model and catheter could be measured in real time for visualization and evaluation. The robot control interface included three virtual views, as shown in **Fig. 6.3b**, including top, side and endoscopic views. Subjects can look at these sub-views during the subject test. A 3D haptic device (Novint Falcon haptics controller) was used to control the catheter tip movement. Assisted by the endoscopic view and the 3D input, the operator can readily recognize the spatial position and manipulate the catheter tip. Thus a consistent hand-to-eye coordination can be achieved.

6.2.4.2 Simulated ablation task

A 3D roadmap of "lesion" targets (red) were shown in the navigation interface (**Fig. 6.4**). It was formed by 121 sections located on the virtual LA model around the pulmonary vein ostium. Registration was performed for the lesion targets and the 3D-printed LA simulator, which was discussed in the previous section. The lesion targets were consistently aligned with the virtual LA model, since the highly compliant catheter only imposed limited deformation ($\leq$ 2 mm) on the LA simulator and even less on the "lesion" targets. This deformation caused by the catheter tip was insignificant to the resultant accuracy evaluation. When valid ablation (ablation duration and tip-to-target distance were satisfied) performed

on the lesion targets, the color of target would turn yellow gradually, representing the corresponding section was successfully ablated. Experimental data were stored at 20 Hz for offline analysis, including (1) time, (2) catheter tip position, (3) deviations from the tip to the lesion targets, (4) ablation status in ON/OFF, and (5) ablation process for each lesion target.

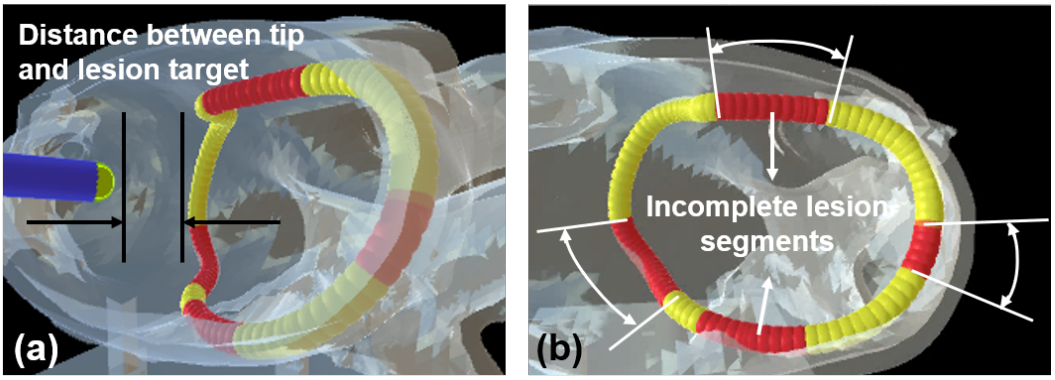

Fig. 6.4: Two major performance indices, namely accuracy and efficiency defined based on **(a)** proximity distance measured from tip to lesion target around the pulmonary vein ostia and **(b)** total length of incomplete lesion segments (red).

The experiment involved 10 subjects (age between 20 and 30, 3 women and 7 men). The subjects conducted the tasks by the two control methods in a random order. In this way, the variance induced by individual differences could be minimized, since the subjects act as their individual standard for comparison [197]. All the subjects had no experience in EP procedures. They were briefly introduced about the robot manipulation task before the operation. For each subject, a time limit was set as 3 minutes to conduct the simulated RF ablation.

6.2.4.3 Results and discussion

Accuracy and efficiency are of upmost importance to the surgical practice, which were hence defined for assessment in the task (**Fig. 6.4**). The accuracy could be assessed in terms of: i) the proximity distance measured from catheter tip to lesion target during the ablation; ii) number of times that ablation had been turned on; iii) average ablation duration. The efficiency could be evaluated by: i) the missed proportion of lesion target segments; ii) the maximum number of continuously missed lesion targets; iii) the total travel distance of the catheter tip (**Fig. 6.5**).

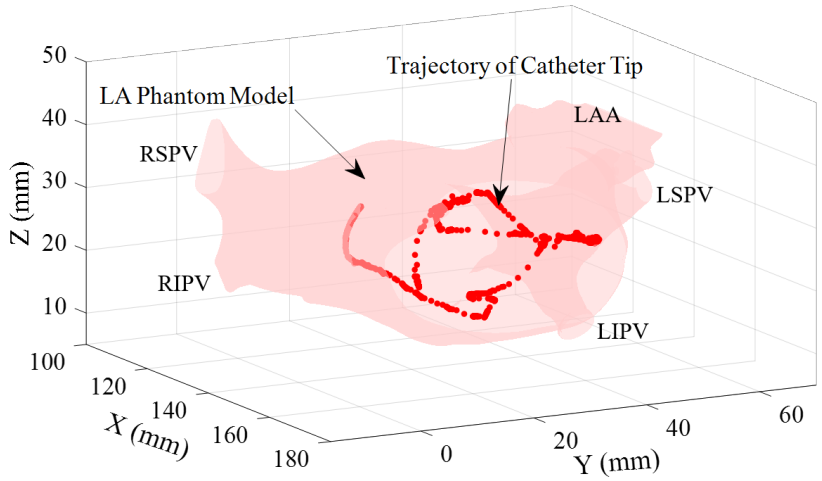

Fig. 6.5: Actual footprint of the catheter tip recorded by the EM tracking system. The LA model is overlaid under the same coordinate.

Table 6.1 shows the performance evaluation result of the subject test, where model-based and model-free control methods in robotic catheterization are compared for each index. Here, the improvement percentage was calculated by the increment of model-free method referring to the model-based method.

Accuracy: The average distance between catheter tip to the closest lesion target during ablation was 19.1% for the model-free control method, which was shorter than the model-based one, indicating the advantage of model-free control to approach static target. Compared to model-free method, the model-based method has lower accuracy, as it was analyzed by the inherent kinematic properties without considering interactions between catheter and atrium model. But the EP procedure would be inevitable on complicated interaction with endocardial environment. In comparison, the model-free control can adapt to the interaction by updating the inverse Jacobian, particularly under the circumstance of soft contact with the LA simulator.

Efficiency: The model-free control method demonstrated a remarkable reduction in the missed lesion targets (35.8%) and the maximum number of continuous missed lesion target spheres (46.2%). Both of them corresponded to a low p-value (≤ 0.05). For the total travel distance of the catheter tip in the task, the model-free method demonstrated a slight disadvantage (-7.65%). It shows that the model-free method has the ability to provide a more sensitive and faster response to the operator's input.

Table 6.1: Measured performance indices averaged across 10 subjects in performing the robotic catheterization

Model	**Model-based**		**Model-free**		**Improvement**
Accuracy	**Mean**	**STD**	**Mean**	**STD**	**% *p-val.**
Mean tip-to-target distance during ablation (mm)	6.94	1.34	5.61	1.31	19.1% *0.08
Mean times of ablation turning on (sec)	23.7	10.9	24.1	7.2	-1.88% *0.89
Ablation duration (sec)	1.49	0.36	1.76	0.48	-18.7% *0.07
Efficiency	**Mean**	**STD**	**Mean**	**STD**	**% *p-val.**
Mean proportion of missed targets (%)	51.9	14.7	33.3	11.9	35.8% *0.03
Maximum number of continuously missed targets	55.1	24.1	29.7	3.16	46.2% *0.01
Total travel distance (mm)	649	176	699	320	-7.65% *0.60

Conclusion: The proposed experimental validation platform, comprising an MR safe robotic manipulator and a human-robot interface, could realize both model-based and model-free methods for catheter control. Subject test that emulated an ablation task was conducted to quantitatively evaluate the performance of both control methods. Accuracy indices (e.g. mean of the closest distance between catheter tip and the closest target during ablation) and efficiency indices (e.g. proportion of missed lesion target) were adopted. Compared to model-based control method, model-free method achieved higher accuracy, with 19.1% improvement in the tip-to-target ablation distance. In terms of efficiency, model-free method had 35.8% reduction in the missed-target proportion and 46.2% reduction in the number of continuous missed targets.

6.3 Shape tracking and feedback control of cardiac catheter

6.3.1 Clinical motivation for shape sensing of continuum manipulator

Cardiac EP procedure is an effective treatment for atrial fibrillation. Electroanatomic mapping (EAM) and RF ablation are two key procedures repeated in EP. The procedures require precise maneuvering of thin ($\sim$ ⌀2.7 mm), long ($\sim$1.5 m) and flexible catheters inside the heart chamber to measure electrical signals and deliver ablation energy. MRI is a powerful imaging modality that has gained traction for guiding EP procedures [108], accredited to its superior high-contrast images of cardiovascular soft tissue and absence of harmful ionizing radiation. It can be used to form a detailed 3D cardiac roadmap, to visualize physiological changes of cardiac tissues and also to assess the ablation lesion formation intra-operatively [50, 121]. MR-based tracking [183, 186] could provide instrument localization under the same coordinate frame as imaging, avoid any image registration that would pose spatial error. Commercial MRI-guided catheterization systems (e.g. Imricor, ClearTrace, St. Jude Medical) have adopted active tracking coils for the positional feedback of catheter tip [48, 50, 198]. However, the sole use of discrete positional tracking coils (**Fig. 6.6a**) could not provide precise information of the catheter morphology for either visualization or motion control. Although the catheter shape could be visualized by MRI [199] (**Fig. 6.6b**), the prolonged time for image reconstruction would cause significant tracking delay. Accurate intra-op shape tracking of catheters under MRI remains challenging.

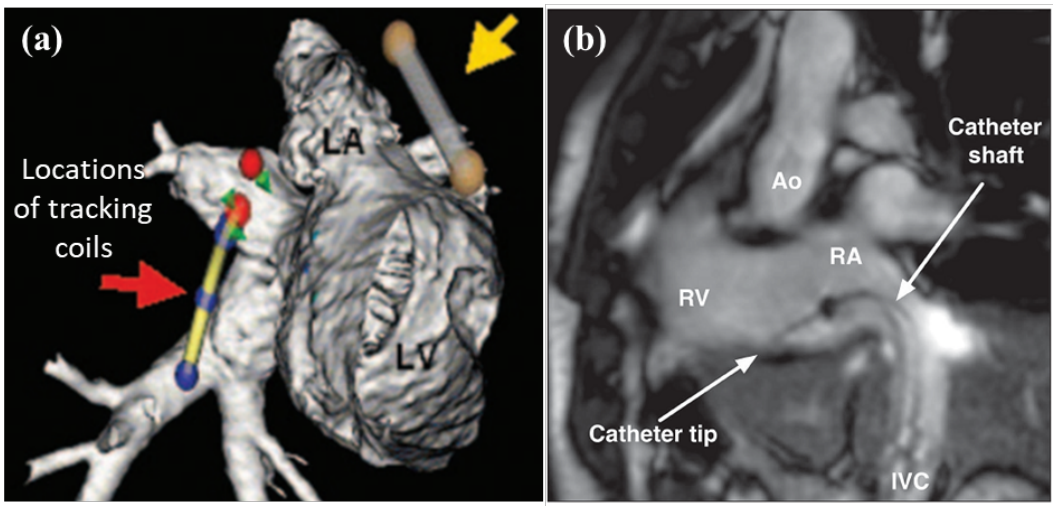

Fig. 6.6: (a) Catheters shape reconstructed by discrete MR tracking coils; **(b)** Catheter shape shown in MR image. **Image Source**: [50, 51].

Optical fiber-based sensors using FBGs (**Fig. 6.7**) have attracted interest for their ability to measure morphological deformation of flexible surgical instruments. It can achieve real-time shape estimation with high sampling rates (>100 Hz) with thin, sub-millimeter diameters footprints. FBGs have excellent multiplexing capabilities, where many sensing points can be employed along a fiber without increasing its size [200]. The use of multi-core fibers with FBGs can further increase the sensor density and enable shape estimation of the fiber itself [201]. The flexibility of optic fiber also has minimal effect on structural stiffness of the instrument, allowing it to be integrated with delicate devices, such as needles and catheters. These distinctive advantages have prompted the use of FBG shape sensing in many applications, including navigation of medical instruments [202, 203], shape estimation and control of steerable interventional needles [204, 205], as well as force sensing of instruments [206]. Additionally, because of the inherent electromagnetic immunity optical fibers possess [207], FBG fibers are entirely compatible with MRI and have been incorporated with MR safe/conditional instruments [208, 209].

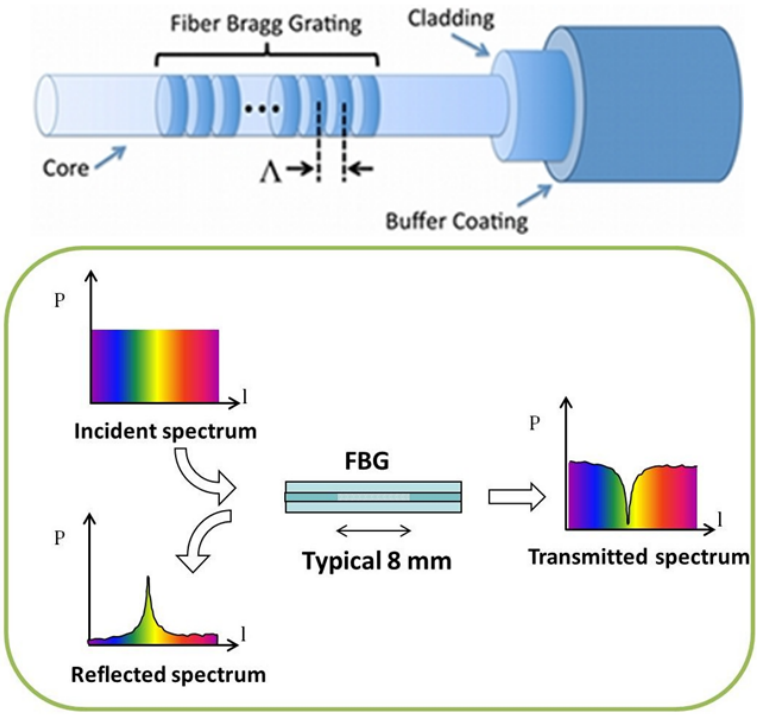

Fig. 6.7: Working principle of the optical fiber-based sensor using fiber Bragg gratings (FBGs). Gratings on the optic fiber can reflect light with specific wavelength. The reflected wavelength would vary under diverse local bending behaviors. **Image Source**: [52].

Despite the increasing use of FBGs for shape sensing, few studies have applied it to enhance the closed-loop control performance of surgical continuum manipulators [210, 211]. In the cardiac EP procedure, complicated and repeated tasks introduce difficulties to manual operation of catheters, even for experienced operators. It is expected that fast and

accurate robot-assisted catheter positioning could significantly reduce operation times and difficulty when compared to manual operation [212]. Previous studies have investigated various modeling/control methods to improve the accuracy and effectiveness of robotic catheter systems [213, 213, 214]. However, most of these catheters were custom-made with their known or deterministic structural parameters that facilitate precise modeling. For a standard cardiac catheter consisting of composite materials, its mechanical properties remain unknown, which induces difficulty in modeling and control. It creates strong incentive for utilizing shape sensing in robotic catheter control to achieve dexterous and precise manipulation, particularly under MRI guidance.

In this section, we aim to develop a shape tracking method to provide both positional and morphological sensing of flexible cardiac catheter. To achieve accurate and effective feedback control, shape information obtained from the FBGs are used for characterization of catheter kinematics as well as real-time autonomous control. The contributions are summarized below:

1. Design and implementation of a shape tracking system integrating a multi-core FBG fiber and tracking coils with a standard cardiac catheter. Both shape and positional tracking of the bendable section could be achieved;

2. Development of a learning-based modeling method for cardiac catheters, which uses FBG-reconstructed 3D curvatures to initialize the model and update the motion mapping. The proposed modeling method was implemented on an MRI-guided robotic platform to achieve feedback control of a cardiac catheter;

3. Experimental validations of the shape tracking system and control algorithm. The overall robot control performance was demonstrated by targeting and path following tasks. An autonomous PVI task was conducted with *ex-vivo* tissue ablation inside an LA simulator.

6.3.2 Shape tracking with FBG sensors

6.3.2.1 Shape sensing with multi-core FBG fiber

FBGs are sensors inscribed directly into optical fibers for measuring local and 1D strain. Multiple FBGs can be inscribed along a single fiber to obtain strain sensing points without additional input or output connections. In the previous work [215], a sensor was designed capable of reconstructing its surface shape by embedding a single-core FBG fiber in a flexible substrate. However, for flexible and thin surgical instruments that are designed to access deep regions in the body, such as biopsy needles and cardiac catheters, a fiber with only a single core of FBGs is insufficient for reconstructing its 3D curvature. Alternatively, multiple single-core fibers could be grouped [216] for co-located strain measurements. However, this would come at the cost of sensor size and fabrication complexity. A more reliable approach was to adopt a fiber fabricated with multiple optical cores (multi-core fiber) and FBGs [201]. It can allow shape sensing of the fiber geometry itself while maintaining a thin cross-sectional size.

A continuous-grating multi-core fiber (FBGS International) with optical frequency domain reflectometry (OFDR) interrogation (RTS125+, Sensuron) was used for shape sensing of the cardiac catheter. The fiber was 12-m long with a diameter of $\varnothing$0.2 mm. As illustrated in **Fig. 6.8b**, seven cores run along the length of fiber, with one core centered around by other 6 cores equally spaced at 60° intervals. Shape sensing can be conducted by measuring off-axis strain from the FBGs sensors located within the fiber cross-section. Strain measurements can be obtained at the distal 1-m tip of the fiber with a spatial resolution of 3.17 mm. Note that the adopted multi-core fiber features with a high-density grating fiber structure; therefore, continuous strain measurement can be conducted. By contrast, the typical wavelength division multiplexing (WDM)-based fiber systems have discretely placed FBGs that are divided by bare fiber segments. A comparison between the fiber systems using WDM and OFDR techniques are summarized in **Table 6.2**.

Table 6.2: Comparison of WDM and OFDR optic fiber systems

Wavelength division multiplexing (WDM)	**Optical frequency domain reflectometry (OFDR)**
– Discretely placed FBGs	– High-density continuous FBGs
– Low spatial resolution	– High spatial resolution
– High refresh rate > 1000Hz	– Refresh rate up to 100Hz
– Low cost	– Expensive

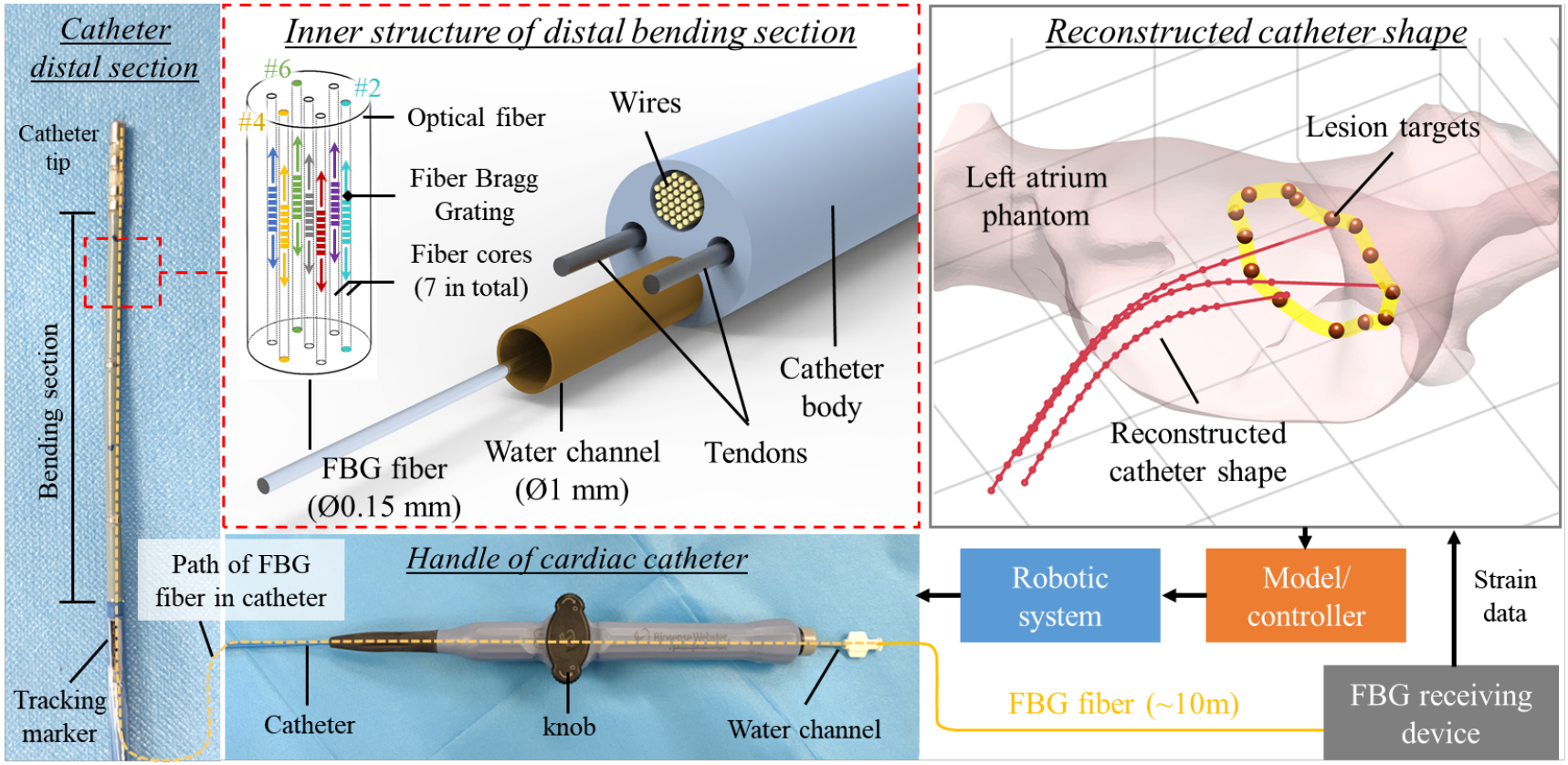

Fig. 6.8: Diagram showing the architecture of shape sensing for robotic catheter system. **(a)** Catheter distal bending section integrating a multi-core FBG fiber (12 m long) and the tracking marker for shape tracking; **(b)** Inner structure of distal bending section, with multi-core FBG fiber put throughout the water channel; **(c)** Handle of cardiac catheter, where the FBG fiber was fixed at the water channel entrance; **(d)** Real-time shape reconstruction can be achieved by continuously acquiring the strain data from FBGs. The 3D curvature of the catheter bending section can then be fed back to the robotic catheter platform for autonomous control.

There are two common approaches towards multi-core fiber shape reconstruction from strain data: i) Adopting the piecewise constant curvature (PCC) model with the assumption of circular bending shape for each FBG segment. The overall fiber shape can be constructed by accumulating the sum of discrete curvatures and corresponding bending directions, which are measured and calculated from a set of sensors at a particular cross-section of the fiber [217]; ii) Utilizing the Frenet-Serret formulas to describe 3D curves, which can take account of the torsion effect [218].

To optimize the reconstruction speed and sensing performance, the PCC-based approach was used in accredit to its faster convergence w.r.t. sensing segment length and superior noise handling ability [219]. For 3D curvature reconstruction, at least three cores are needed to estimate the 2-DoF section bending along the fiber cross-section. More fiber cores could be employed to improve reconstruction accuracy and reduce overall sensing noise.

6.3.2.2 Fusing and calibration of shape and positional feedback

For shorter and more rigid instruments like biopsy needles, MR-based positional tracking markers can be located at a fixed base of the instrument to provide a reliable reference frame. However, this approach is not suitable for long ($\sim$1.5 m) and flexible cardiac catheters, since its handle would be placed far from the MR imaging volume. In order to monitor the 3D curvature of a standard cardiac catheter, as well as its tip pose, the coordinate frame of the fiber's reconstructed curvature has to be co-registered with MR images. Note that the 3D curvature reconstruction error can also be accumulated much along with the increasing sensing length.

To this end, we incorporated only distal section of a multi-core fiber to cover and feedback the bending of 63.4-mm long catheter tip. Three cores were used, each containing 21 FBGs for strain measurement. In our preliminary test, the FBG fiber was put throughout the water channel of EP catheter (Thermocool® Bi-Directional Catheter, Biosense Webster Inc.) (**Fig. 6.8b-c**). The water irrigation function would not be affected as the fiber diameter ($\varnothing$0.2 mm) is negligible, relative to that of the water channel ($\varnothing$1 mm). Alternatively, the fiber could be integrated into the wire channel (**Fig. 6.8b**) of the catheter in the future manufacture. To minimize the noise induced by fiber tip contact, the fiber was offset approximately 2 mm from the distal end and fixed at the water channel entrance to prevent sliding (**Fig. 6.8c**).

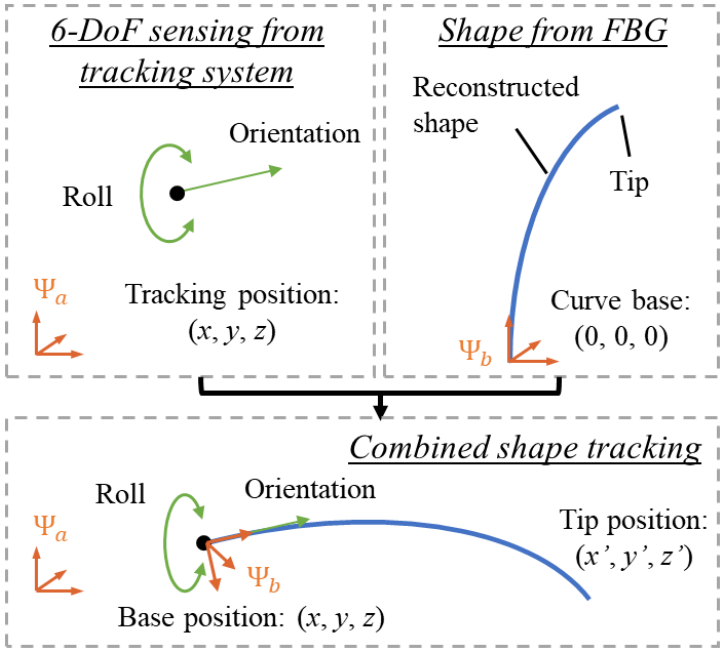

Fig. 6.9: Diagram illustrating the shape tracking method by *fusing* the 3D curvature from FBGs and the positional sensing from the tracking coil.

Although the fiber can be used to reconstruct its 3D curvature, the origin and orientation of reconstructed shape are not defined within the robot or MRI coordinate system. In addition, as the fiber was fixed at the catheter handle, the catheter rolling could not be measured by the shape reconstruction. Therefore, we propose the use of real-time MR-based positional tracking coils that could be integrated into the catheter to provide this information (**Fig. 6.9**). Three coils located closely before the active bending section are expected to provide 6-DoF information in the MR imaging coordinate, and also map it to the catheter model. In our lab-based experimental validations, EM tracking coils and field generator (NDI Aurora) could be used as a comparable proxy for the MR-based tracking system. Preliminary validation of the MR tracking coils distributed along a catheter has been conducted and introduced in **Section 6.3.2.3**.

Sensor calibration can be performed with the catheter bendable section placed in free space. The catheter was actuated to steer in opposite bending directions, while the FBG-reconstructed positions along the catheter bendable section were being collected. The bending plane was generated by fitting through least squares of the normal distances, which we defined as $\mathscr{P}_m$. Similarly, the bending plane generated by FBG-reconstructed points can be obtained as $\mathscr{P}_w$. The transformation to align $\mathscr{P}_w$ to $\mathscr{P}_m$ can then be calculated by point-by-point optimization. In this way, the FBG-reconstructed shape can be registered with the MR tracking coordinates, thereby in the same domain as the imaging model, e.g. EAM.

6.3.2.3 Towards shape tracking in MRI

MR tracking markers [220] can be used for 3D localization of catheters under MRI. MR active coil wired to the receiver system could realize a tracking resolution as high as $0.6 \times 0.6 \times 0.6\ \text{mm}^3$ [179]. MR-guided active tracking for cardiac EP has been demonstrated by human trials, where active markers enabled real-time tracking and overlay of EP catheters on MR images [199]. Additionally, wireless multilayer markers [176, 193, 221] have potential to further simplify the integration with catheters. Fabricated with amplifying circuits, MR tracking markers can provide high-contrast MR signal against anatomical surroundings, thus allowing positional localization in the MR image coordinate (**Fig. 6.10a**).

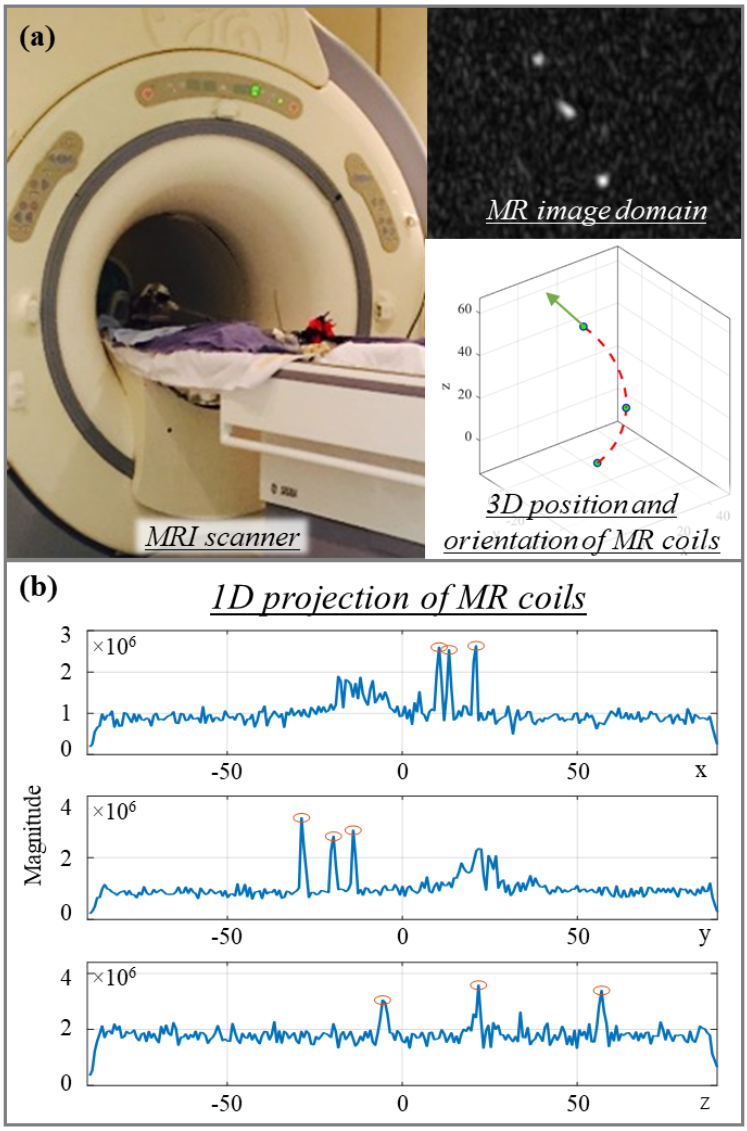

Fig. 6.10: **(a)** MR image revealing the MR tracking markers and the reconstructed 3D positions from the 1D projection pulse-sequence; **(b)** 1D projection of the three tracking markers along the orthogonal axes. Three RF signal peaks can be found in each projection.

The adoption of 1D-projection pulse-sequence [180] can enable acquisition of the marker's positional signal along each axis, facilitating fast localization up to 30 Hz. The raw scanning data can also be streamed out at low latency (<20 ms) with the MRI real-time control interface, RTHawk (Heartvista™). The 1D-projection signals of three markers attached longitudinally and at diverse separations along a catheter body can be seen in **Fig. 6.10b**. The peaks along each coordinate could be readily detected, and further back-projected to 3D marker positions by matching the geometry constraints, e.g. distances between each marker pairs. An arc was fitted to pass through the three markers and approximate the 3D catheter shape (**Fig. 6.10a**). Benefiting from the small size and high accuracy (∼0.48 mm), three markers could be mounted on the catheter in three separated circumferential directions in the future integration. The catheter orientation and rotation could be obtained by calculating the pose of cross-sectional triangle formed by the markers.

6.3.3 Modeling and control of cardiac catheter

6.3.3.1 Modeling of catheters

We implemented the FBG shape tracking system on our previously developed MR safe catheter robot [195] (**Chapter 5**), which is capable of tele-operating the catheter under intra-op MRI. The robot was designed to accommodate standard cardiac EP catheters. Detailed design and configurations of this robotic platform are introduced in **Chapter 5**. The steerable catheter can be regarded as a typical robotic continuum manipulator after integrated into the actuation platform. To achieve accurate and effective autonomous control of catheters, particularly commercial ones, a reliable model is needed to provide precise motion mapping from the robotic actuator to the catheter tip.

Regarding modeling of the continuum manipulator, a common approach was to consider each of its bending sections as a constant-curvature arc [155]. The forward and inverse kinematics models can then be derived [191]. There are other more complex modeling approaches using beam theory [157] or Cosserat rod theory [222], mimicking a more accurate deflection but requiring longer computation time. However, for commercial cardiac catheters consisting of composite materials, its mechanical properties remain unknown, which induces difficulty in modeling and control. It is also time-consuming and impractical to characterize the parameters of each cardiac catheter before use.

In view of this, we developed a modeling approach based on the assumption of PCC. The bendable distal shaft is modeled as a combination of n piecewise circular arcs, with curvatures represented by κ_i, $i = 1,2,\cdots,n$. The distal section is assumed to deform in a plane determined by the two tendons. Regarding the base of bendable section as the origin, we define the arc length, s, from the origin to a point on the bendable section, the angle between axis Z and tangent to the curve at that point as $\theta(s)$ (**Fig. 6.11**). The arc length of each segment is l_i, $i = 1,2,\cdots,n$. Without considering the rotation DoF, the catheter would bend in a fixed plane (x-z plane as in **Fig. 6.11**) w.r.t. the robot coordinate. According to [213], the position of each point along the bendable section can be determined by

$$\begin{cases} x(s) = \int_0^s \sin\theta(\zeta)\, d\zeta \\ z(s) = \int_0^s \cos\theta(\zeta)\, d\zeta \end{cases} \tag{6.13}$$

where the angle $\theta_i(s)$ on the i^{th} segment is

$$\theta_i(s) = \kappa_i s + \sum_{j=1}^{i-1} l_j(\kappa_j - \kappa_i) \tag{6.14}$$

where κ_0=0 at the origin. The position (x_p, z_p) of bendable section end on the bending plane without rotation can be calculated based on **Eq. 6.13** as

$$\begin{cases} x_p = \sum\limits_{i=1}^{n} \int_{a_i}^{b_i} \sin\theta_i(\zeta)\, d\zeta \\ z_p = \sum\limits_{i=1}^{n} \int_{a_i}^{b_i} \cos\theta_i(\zeta)\, d\zeta \end{cases} \tag{6.15}$$

where the lower and upper limits of integration are respectively

$$a_i = \sum_{j=0}^{i-1} l_j \quad \text{and} \quad \mathrm{b_i} = \sum_{\mathrm{j}=0}^{\mathrm{i}} \mathrm{l_j}, \quad \mathrm{i} = 1,2,\ldots,\mathrm{n} \tag{6.16}$$

Substituting **Eq. 6.14** into **Eq. 6.15** and defining $l_0 = 0$, the final expression of position (x_p, z_p) can be obtained.

The constant length of distal straight tip is defined as d_0, and the insertion distance and rotation angle of end-effector as d and α, respectively. Thus the spatial position $\boldsymbol{p} = (x,y,z)$ of catheter end-effector in a coordinate as in **Fig. 6.11** could be represented as

$$\begin{cases} x = (x_p + d_0 \sin\theta_n)\cos\alpha \\ y = (x_p + d_0 \sin\theta_n)\sin\alpha \\ z = z_p + d_0\cos\theta_n + d \end{cases} \tag{6.17}$$

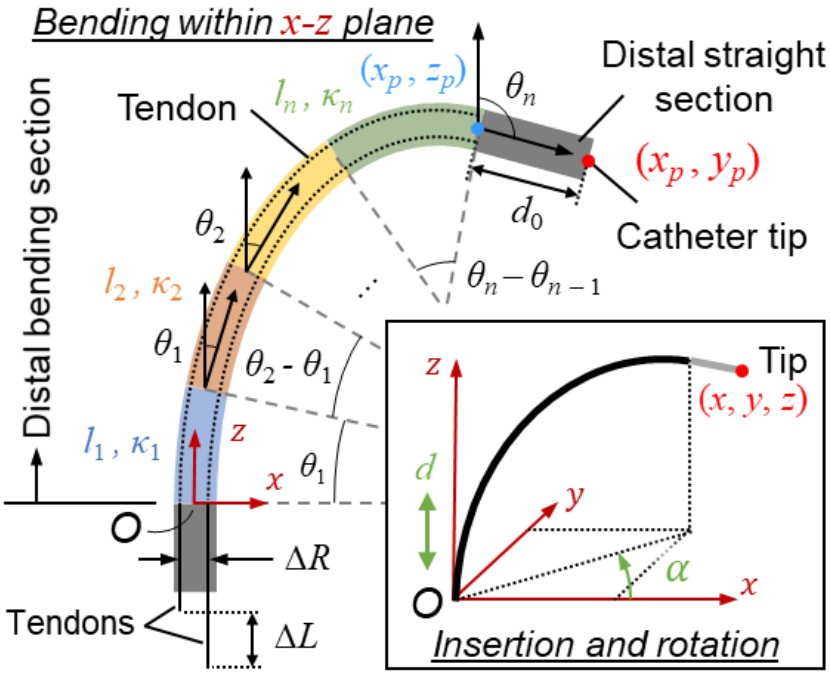

Fig. 6.11: Configuration of the catheter approximated by several curve segments. The curvature of i^{th} segment can be represented by κ_i. A straight section is added at the distal end on top of the piecewise constant curvature (PCC) segments, which represents the rigid tip of catheter.

The catheter deformation is determined by the relative position of two tendons. Here we represent the distance between two tendons as ΔR. The tendons are pulled and pushed by the knob on the catheter handle, whose radius is represented by r_{cam} and steering angle by ϕ (i.e., the rotation angle of steering knob [156]). A relationship based on the representation of tip bending angle θ_n can be obtained as

$$\theta_n = \sum_{i=1}^{n} \kappa_i l_i = \frac{2 \cdot r_{cam} \sin\phi}{\Delta R} \tag{6.18}$$

The axial displacement difference between two tendons is

$$\Delta L = 2 \cdot r_{cam} \sin\phi \tag{6.19}$$

In this end, the mapping between configuration and task spaces is derived [151], i.e. the relationship between catheter tip position and bending curvatures κ_i, $i = 1, 2, \cdots, n$. However, for the bending DoF of robotic catheter, the mapping between actuation space and configuration space is still unknown, that is, the relationship between knob rotation ϕ and bending curvatures κ_i, $i = 1, 2, \cdots, n$. We aim to find the mapping from ϕ to each κ_i, as well as to resolve the un-modeled characteristics by a learning-based method. Therefore, the kinematics between actuation and task spaces could be established.

6.3.3.2 System characterization with learning-based method

As described in **Section 6.3.3.1**, the forward model would be established only in the condition that all the segment curvatures or their ratios are available. We define the curvature ratio as

$$\boldsymbol{k}_c = \begin{bmatrix} k_{c1} & k_{c2} & \cdots & k_{cn} \end{bmatrix}^{\mathrm{T}}, \sum_{i=1}^{n} k_{ci} = 1 \tag{6.20}$$

In the PCC model, ΔL from **Eq. 6.19** could also be divided into n elements and represented as a vector in the following form

$$\Delta \boldsymbol{l} = \begin{bmatrix} \Delta l_1 & \Delta l_2 & \cdots & \Delta l_n \end{bmatrix}^{\mathrm{T}}, \Delta L = \sum_{i=1}^{n} \Delta l_i \tag{6.21}$$

where $\Delta \boldsymbol{l}$ is proportional to the curvature ratio $\boldsymbol{k}c$. A learning-based method is adopted to obtain the curvature ratio among all the segments.

Aforementioned in **Section 6.3.2.1**, the multi-core FBG fiber can reconstruct the curves by approximately consecutive points. The 3D positions and the radii between adjacent points can both be obtained, represented by $\boldsymbol{p}_j^s \in \mathbb{R}^{3\times 3}$ $(j = 1,2,\ldots,M)$ and r_j^s $(j = 1,2,\ldots,M-1)$, respectively, where M is the total number of effective points in the reconstruction. Positions and radii at time step k are $\boldsymbol{p}_j^s(k)$ and $r_j^s(k)$, respectively. Corresponding to the segmentation in PCC model, each segment's curvature $\kappa_i(k)$, $i = 1,2,\ldots,n$ (**Section 6.3.3.1**) can be obtained as the reciprocal of the average radius. The knob steering angle at time step k is $\phi(k)$, which drives the catheter tendon displacement. The curvatures from FBG shape reconstruction can be regarded as ground truth, and used to train the mapping between the steering angle $\phi(k)$ and the curvature ratio $\boldsymbol{k}_c$.

Besides the multi-segment curvatures, we also consider the hysteresis resulting from friction and/or tendon looseness. The backlash would appear particularly when changing bending direction (i.e. steering direction of the knob). Differences between the analytical model and actual bending performance can be compensated by imposing additional input l_c to the ΔL during the robot manipulation.

Therefore, the actual relative position after the learning-based compensation can be calculated by

$$\Delta \boldsymbol{l} = \boldsymbol{k}_c \cdot (\Delta L + l_c) \tag{6.22}$$

The parameters to be trained are $\boldsymbol{k}_c$ (**Eq. 6.20**) and l_c, corresponding to the specific knob steering angle ϕ.

Training of motion mapping: In the pre-training procedure, the radii r_j^s, $j = 1,2,\ldots,M-1$ at each time step has to be collected, as well as the motor's position $q(t)$ that is correlated to the knob steering angle $\phi(t)$. To cover the whole bending workspace, the knob is rotated with a predefined actuation sequence

$$\boldsymbol{Q} = \begin{bmatrix} q(1) & q(2) & \cdots & q(N) \end{bmatrix} \tag{6.23}$$

where N is the sampling number. A value $s(t)$ is introduced to represent the actuation direction change between current and previous steps, which can be derived as:

$$s(t) = \text{sign}(q(t) - q(t-1)), t = 1,2,\ldots,N \tag{6.24}$$

where the function $\text{sign}(\cdot)$ is to differentiate positive and negative values. The sequence of curvatures could be obtained as:

$$\boldsymbol{C} = \begin{bmatrix} \boldsymbol{c}(1) & \boldsymbol{c}(2) & \cdots & \boldsymbol{c}(N) \end{bmatrix} \tag{6.25}$$

where $\boldsymbol{c}(t) = \begin{bmatrix} c_1(t) & c_2(t) & \cdots & c_n(t) \end{bmatrix}^{\mathrm{T}}$ and $c_i(t)$ is the curvature of the i^{th} segment in accord with **Section 6.3.3.1**. The curvature ratio in **Eq. 6.20** could be obtained by normalizing $\boldsymbol{c}(t)$.

The parameter l_c could be derived based on the tip bending angle θ_n, which is independent of $\delta\boldsymbol{l}$ and could be calculated from δL. For each actuation input, the actual tip bending angle θ_A can be obtained from the FBGs. The predicted tip bending angle θ_P can be calculated from the forward PCC model. Thus, a compensation-related parameter f_c is available for training:

$$f_c = \exp(\Delta R \cdot (\theta_A - \theta_p)) \tag{6.26}$$

The input of training data is

$$\boldsymbol{U} = \begin{bmatrix} \boldsymbol{u}(1) & \boldsymbol{u}(2) & \cdots & \boldsymbol{u}(N) \end{bmatrix} \tag{6.27}$$

where

$$\boldsymbol{u}(t) = \begin{bmatrix} q(t) & s(t) \end{bmatrix}^{\mathrm{T}}, t = 1,2,\ldots,N \tag{6.28}$$

The output of training data is

$$\boldsymbol{O} = \begin{bmatrix} \boldsymbol{o}(1) & \boldsymbol{o}(2) & \cdots & \boldsymbol{o}(N) \end{bmatrix} \tag{6.29}$$

where

$$\boldsymbol{o}(t) = \begin{bmatrix} \boldsymbol{k}_c(t)^{\mathrm{T}} & f_c(t) \end{bmatrix}^{\mathrm{T}}, t = 1,2,\ldots,N \tag{6.30}$$

Using the feedforward neural network in the deep learning toolbox of MATLAB®, with $\boldsymbol{U}$ as input and $\boldsymbol{O}$ as output, we can train a mapping as

$$\boldsymbol{o}(t) = f(\boldsymbol{u}(t)),\ t = 1,2,\ldots,N \tag{6.31}$$

Prediction of motion mapping: During robot motion, the curvature ratio $\boldsymbol{k}_c(k)$ among different segments and the compensation-related $l_c(k)$ at the k^{th} step can be calculated by

$$[k_c(k),\ \ f_c(k)] = f(q(k),\ s(k)),\ \ k = 1,2,\ldots \tag{6.32}$$

The enhanced estimation of relative positions between two tendons $\delta\boldsymbol{l}$ can be calculated by **Eq. 6.21**, where $l_c(k)$ can be derived as

$$l_c(k) = \ln(f_c(k)) \tag{6.33}$$

The predicted $\boldsymbol{k}_c$ and l_c would link up ϕ and κ_i, $i = 1,2,\ldots,n$, completing the mapping between actuation and configuration spaces of bending DoF. Combined with **Eq. 6.17**, the complete forward kinematics are available for robotic control

$$\dot{\boldsymbol{p}} = \boldsymbol{J}\begin{bmatrix} \dot{\alpha} & \dot{\phi} & \dot{d} \end{bmatrix}^{\mathrm{T}} \tag{6.34}$$

where $\boldsymbol{J}$ is the Jacobian matrix.

6.3.3.3 Autonomous motion control and ablation

For the autonomous ablation task, targets in the model coordinates $\{\boldsymbol{C}\}$ are predefined around the pulmonary vein ostium in the LA simulator. The real-time tip position $\boldsymbol{p}_w$ could be provided by the shape tracking system in the world coordinates $\{\boldsymbol{W}\}$. $\boldsymbol{p}_c$ and $\boldsymbol{p}_w$ are transformed using the rotation matrix $\boldsymbol{R}_w^c$ and translation vector calculated by registration approach.

In each targeting cycle, the target could be appointed either automatically in sequence or selected by the operator. The error between current tip position $\boldsymbol{p}_c$ and desired position $\boldsymbol{p}^*$ can be calculated and normalized with constant step size as $\Delta\boldsymbol{p}_c$. The robot actuation

is derived by multiplying inverse Jacobian matrix and $\Delta \boldsymbol{p}_c$. A tolerance distance from the catheter tip would be set for each target. The ablation process would be automatically triggered by simultaneously satisfying the two conditions: i) tissue contact is detected with an appropriate impedance for ablation (e.g. $< 200\ \Omega$ [223]); ii) targeting error is within the tolerance distance. During the ablation process, the robot would keep still for RF ablation on the tissue. The control block diagram in **Fig. 6.12** shows the key processing components including the kinematic control and autonomous ablation.

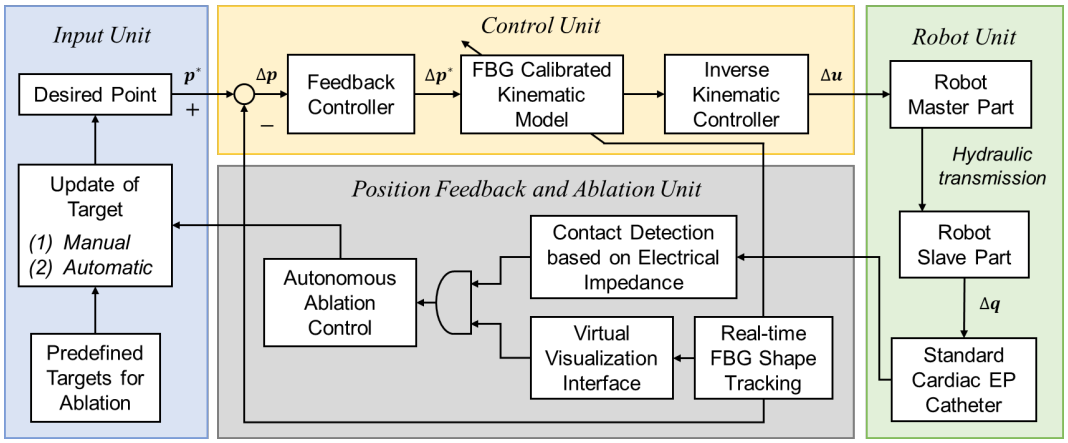

Fig. 6.12: Control architecture of the autonomous ablation procedure. Parameters of the PCC model can be automatically tuned by a learning-based algorithm, which can enable accurate positional control of the catheter end-effector. The 3D curvature of catheter can be obtained in real-time from the FBG feedback. RF ablation can be triggered when the catheter tip reaches the target and contacts tissue.

6.3.4 Experimental setup

6.3.4.1 MR safe robotic catheter platform

The proposed shape sensing method and control algorithms were implemented, then evaluated on the MR-safe robotic catheter system [182, 195] (**Fig. 5.6**), which is capable of tele-operating the catheter under intra-op MRI. The robot features a master-slave hydraulic transmission system in order to provide high-accuracy and low-latency actuation. The master units were driven by electric motors located in the control room. Actuation from master units could be transmitted to the slave units through 10-meter long hydraulic pipelines. The robot could manipulate a standard EP catheter (Thermocool® Bi-Directional Catheter, Biosense Webster Inc.) in 3 DoFs, namely bending, insertion and rotation. The robotic system is upgraded from the previous prototype [195], incorporating our previously designed three-cylinder actuation units [175] (**Section 3.3.2**) for rotation and insertion DoFs of the catheter. It can enable a large motion range for catheter advancement (340 mm) and rotation ($\pm 360°$), as well as high-fidelity catheter manipulation. Such improved robotic actuation performance would enable feedback control implementation for effective autonomous catheter manipulation, thereby delicate cardiac EP tasks, such as EAM and RF ablation.

6.3.4.2 Left atrial simulator

To perform the simulated PVI task, an LA anatomical model was designed based on patient-specific imaging data (**Fig. 6.13a**). The simulator was molded by silicone [224] in an attempt to mimic the LA tissues consisting of myocardium and endocardium. A semi-rigid sheath was fixed at the puncture on the simulator's wall, simulating a path along the femoral vein, inferior vena cava, right atrium to left atrium. Pulsatile liquid flow can be generated by a water pump through pipelines to the LA simulator. The flow direction is indicated by the arrows in **Fig. 6.13a**, which follows the direction of LA blood flow from pulmonary veins to left ventricle. The LA pressure and resultant motion during EP procedure could be simulated by controlling the magnitude and frequency of pulsatile flow, which could be gated with the patient-specific electrocardiogram (ECG) signal. **Fig. 6.13b** shows the simulated liquid pressure compared to the human ECG and LA pressure [225, 226]. **Fig. 6.13c** shows the simulated pressure curves at fast and slow pulsatile rates. The rates could be adjusted within the range, covering the common patient heartbeat rate during EP procedure.

To conduct the *ex-vivo* tissue ablation, a slice of swine tissue with 3-mm thickness was attached on the LA simulator's inner surface around pulmonary veins. In EP procedure, a neutral electrode is usually attached on patient's body to form a close electric circuit with catheter and RF generator, in order to monitor tissue resistance and conduct RF ablation. In this setup with LA simulator, the *ex vivo* tissue was linked to a neutral electrode through electrical wires, which was connected to an RF generator (Biosense Webster Stockert 70). The control program was gated with the generator to automatically trigger the RF ablation when the catheter tip reached the target range and contacted with the tissue.

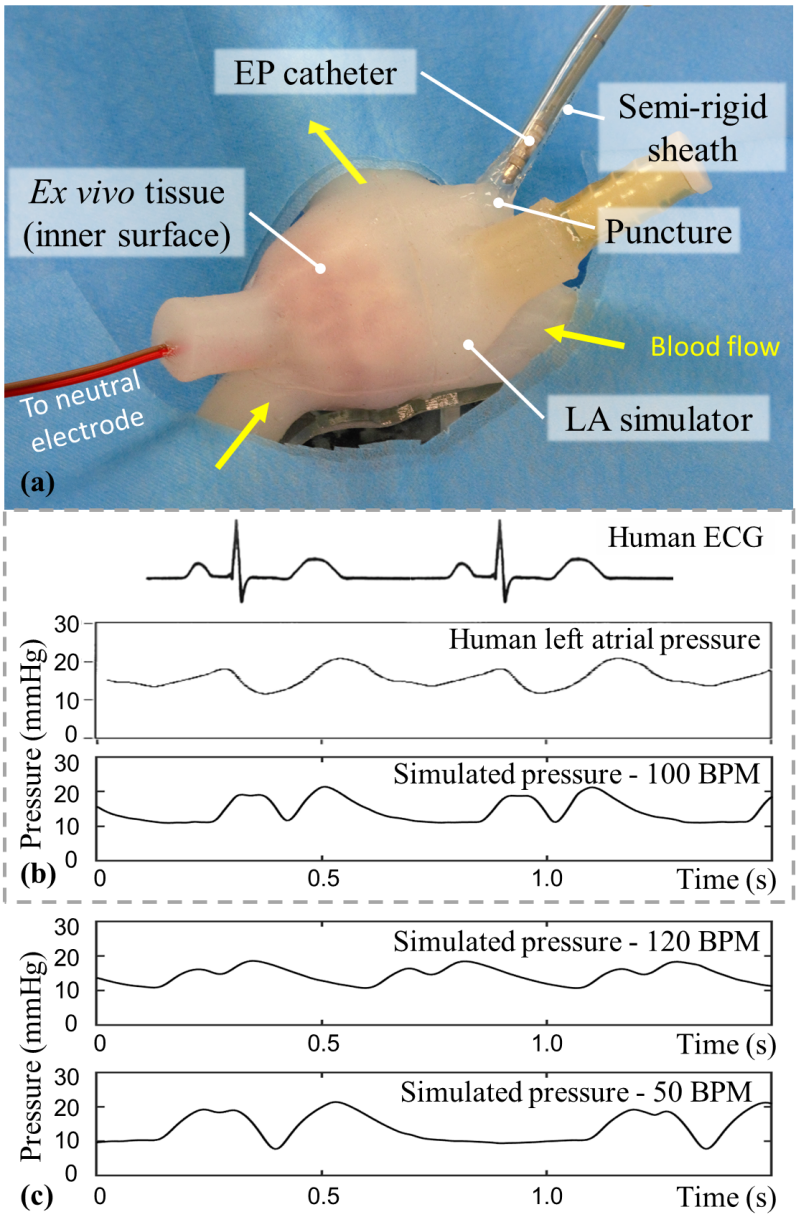

Fig. 6.13: **(a)** LA simulator filled with liquid, of which the pulsatile flow was generated by a hydraulic pump. A slice of swine tissue was attached on the inner surface at target ablation area; **(b)** Simulated liquid pressure compared to the human electrocardiogram (ECG) and LA pressure; **(c)** Simulated pressures with fast and slow rates. The simulated pulsatile rate could be adjusted within the range.

6.3.5 Experimental validation

6.3.5.1 Shape sensing performance of the multi-core FBG fiber

To validate the FBG shape sensing performance when integrated with the cardiac catheter, a fixed curvature test was conducted on the two symmetric bending curvature templates, as shown in **Fig. 6.14a**. The templates were 3D-printed with fixed curvature grooves of 2.7-mm width, which is approximately equal to the outer diameter of EP catheter. The bending angles of the curved section were from 0° to 105° on each side. The length of the constant-curvature arc section was 55 mm. The integration of FBG fiber and cardiac catheter followed the method in **Section 6.3.2.1**. The shape of 63.4-mm distal catheter section was reconstructed by three cores in the fiber, with each core containing 21 FBG segments. The catheter was placed into the template grooves for measuring its 3D curvature. For each measurement, the location of first FBG segment was aligned to the start position of the constant-curvature arcs. The reconstructed 3D curvature was obtained by taking average of 100 consecutive data captures for the entire sensing section.

The reconstructed catheter shapes are plotted in **Fig. 6.14b**, with the position of first FBG section set as the origin (0,0). Curves for the ground truths are also plotted, following the same shape of corresponding grooves. The overall average angular error of all FBG sensors was 2.33°. And the average tip bending angle was 2.35° for all curvatures. **Fig. 6.14c** illustrates the average errors of the tip bending angle among the fifteen groups of predefined bending angle. Other than the sensor error of FBGs, the misalignment between the reconstructed shape and ground truth could be partially attributed to the large gap between the FBG fiber (⌀0.2 mm) and the water channel (⌀1 mm). In future manufacture, the fiber could be put through a sheath with slightly larger diameter to minimize such interspace, thus to improve the overall sensing accuracy. The sheath could also be integrated into the wire channel of catheter to free up the water channel for irrigation function.

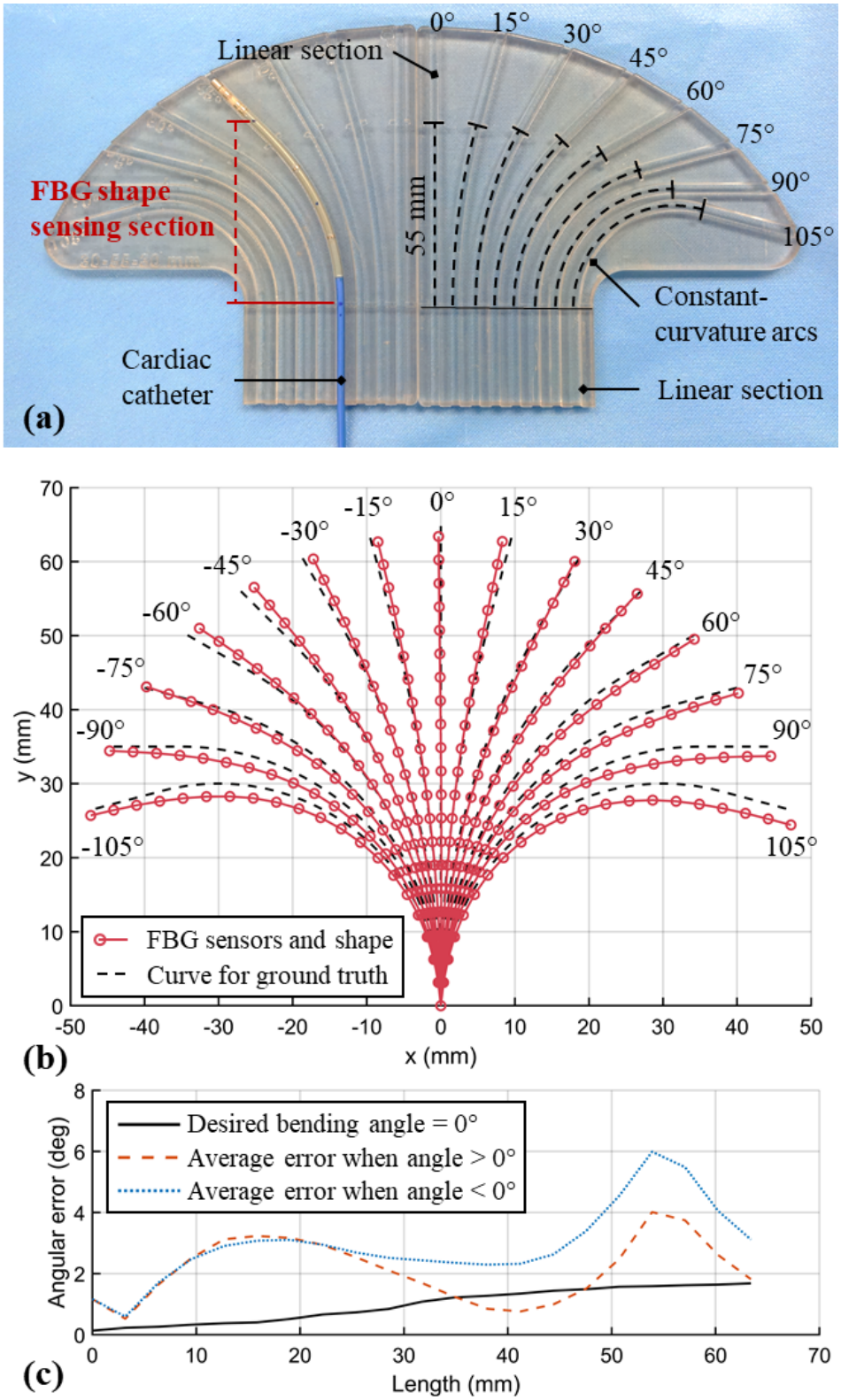

Fig. 6.14: **(a)** Bending curvature templates used to evaluate the shape sensing performance of the multi-core FBG fiber. Eight curvatures are included at each bending direction, with an absolute value from 0° to 105°; **(b)** Reconstruction catheter shapes compared with the ground truth curves. The starting positions are all aligned at (0,0); **(c)** Bending angle errors along the shape sensing section.

6.3.5.2 Shape tracking under active bending

The shape tracking performance was further evaluated with active catheter manipulation. The integration method of FBG fiber with the catheter remained the same as in **Section 6.3.5.1**. A 6-DoF EM positional sensor (⌀0.8×9 mm, NDI Medical Aurora) was attached to the catheter at the location of first FBG sensor. Before data collection, the coordinate frames of the reconstructed shape and EM tracking system were aligned following the procedure in **Section 6.3.2.2**. In the test, the cardiac catheter was actuated by the robotic platform for bending in two directions. The shape and positional data of the catheter were recorded under seven knob steering angles, which are summarized in the table in **Fig. 6.15a**. For each input angle, the 3D curvature for ground truth was represented by 25 evenly distributed points, which were captured along the catheter by an EM tracking probe (NDI Medical Aurora).

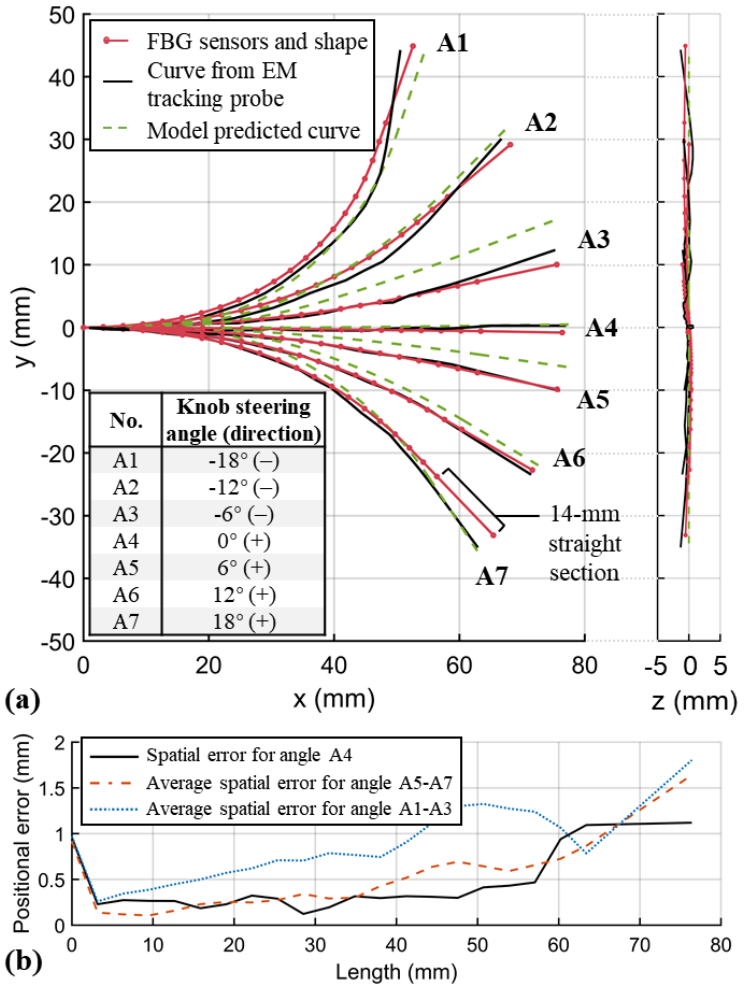

Fig. 6.15: (a) Top and side views of catheter shapes obtained from FBG shape sensing (red), EM tracking system (black), as well as model prediction (green). The catheter was actuated by the robotic platform with seven knob steering angles, which were also used for model input; **(b)** Spatial differences along the shape sensing section by comparing curves from FBGs and the EM tracking system.

The diagrams in **Fig. 6.15a** depict the shape of catheter bending section under the seven knob steering angles. To obtain the catheter tip position, a 14 mm straight section was added to the tip of reconstructed 3D curvature based on the orientation of last FBG segment. Simulated shapes deduced by the learning-based model in **Section 6.3.3.2** are also overlaid in the diagram, predicting similar shapes and positions to the measured results. The side view of the shape tracking curves is plotted in **Fig. 6.15a**, indicating that the catheter used for the experiment had a nearly planar bending behavior. The reconstructed shapes from FBG fiber were consistent with the actual shape, implying there was no significant twist between the FBG fiber and the catheter. The spatial positional errors of shape tracking for the bending section are shown in **Fig. 6.15b**. The average positional error of 21 FBG sensing segments was 0.63 mm, and 1.64 mm at the tip. The largest tip error was 2.46 mm for A7, which is within the tolerance of targeting error ($\sim$5 mm [227]) in EP procedure.

6.3.5.3 Learning-based PCC vs CC

The proposed learning-based PCC model was compared to the conventional CC model by simulation. The structure-related parameters of the two models (e.g. length, diameter) were set to be identical. In the PCC model, we divided the bendable section into three segments (i.e. n = 3 in **Section 6.3.3.1**). The knob steering angles ϕ in a range of -20° to 20° were input to both models. For the proposed learning-based PCC model, the actuation direction $s(t)$ is also considered as an input, as introduced in **Eq. 6.24**.

Fig. 6.16a illustrates the simulated catheter planar curves with five inputs of knob steering angle, A1-A5. For the learning-based PCC model, each knob angle could generate two curves in two actuation directions, namely positive (+) and negative (–). The variation trends of curvature and tip bending angle are depicted in **Fig. 6.16b-c** respectively, w.r.t. the knob steering angles. The CC model exhibits a linear increase with a larger magnitude in both cases. Regarding the learning-based PCC model, a nonlinear relation between the knob input and curvatures of three segments could be predicted, as well as the tip bending angle. These predictions conform with the observed bending behavior of commercial cardiac catheters, which could be attributed to the tendon-sheath friction, manufacturing tolerance and non-ideal material conditions.

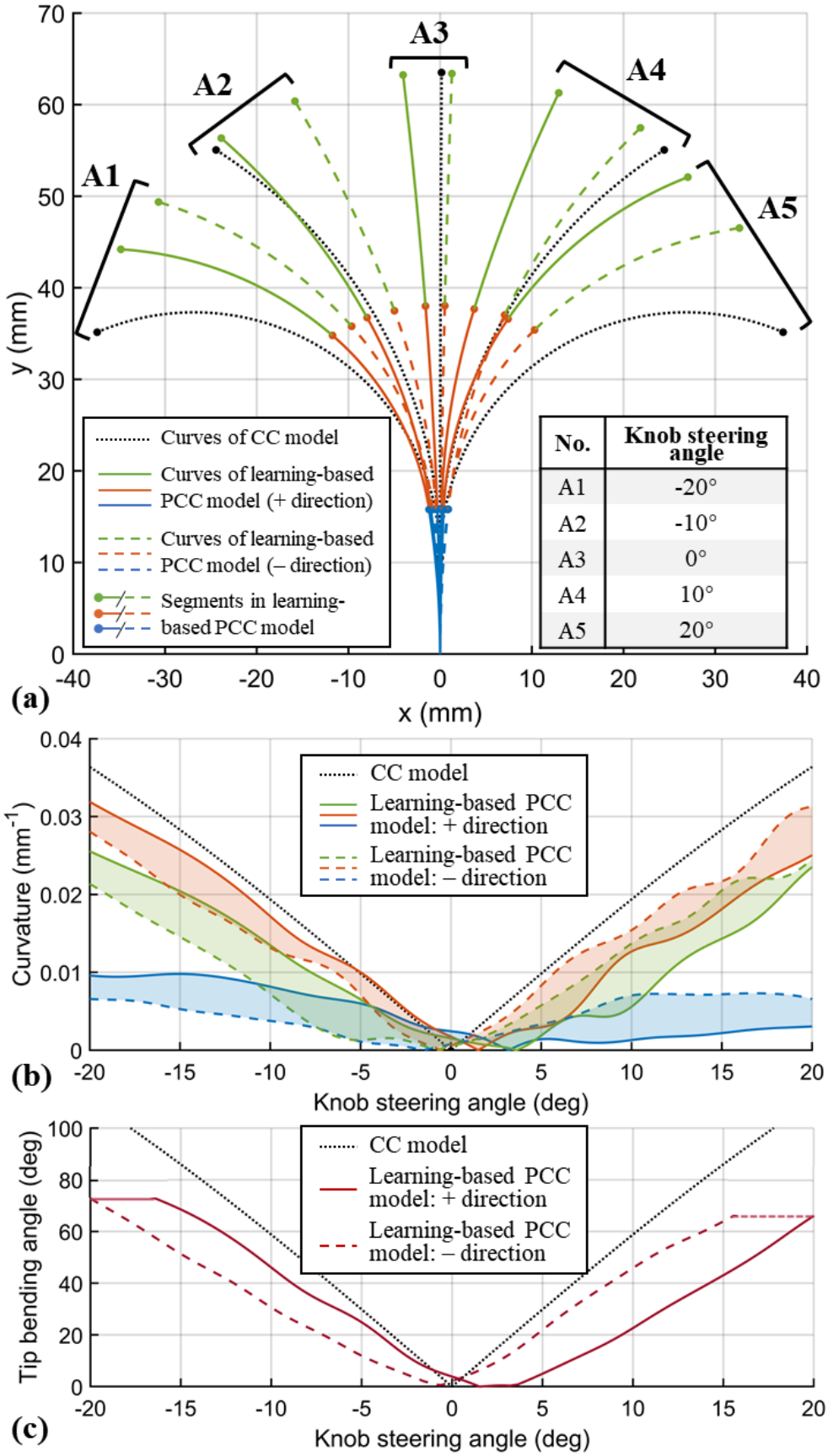

Fig. 6.16: (a) Simulated catheter bending curves by the CC model and the learning-based PCC model with five knob steering angles (I1-I5); **(b)-(c)** Diagrams showing the curvature and tip bending angle variation trends for CC model and learning-based PCC model. The learning-based PCC model can predict the actuation hysteresis by considering the actuation direction.

The learning-based PCC model could also reveal the bending hysteresis of catheter by involving the actuation directions. As illustrated in **Fig. 6.16c**, the tip bending angle would follow the solid (/dashed) curve when the knob steering angle is increasing (/decreasing), corresponding to the + (/–) actuation direction. The transition between the two curves occurs when the actuation direction changes, which are at $\pm 20^\circ$ in this case. The tip angle would remain unchanged while the input angle increasing/decreasing, which could represent the bending hysteresis of catheter. The hysteresis could be predicted for every knob input within the actuation range, leading to a more accurate mapping between the catheter task space and actuation space.

6.3.5.4 Autonomous targeting

An autonomous targeting experiment was carried out by implementing the proposed shape tracking and learning-based modeling on the robotic platform. Five targets (T1 to T5 in **Fig. 6.17a**), which were in a volume of $78.4 \times 75.7 \times 46.3$ mm^3, were chosen within the workspace of catheter tip. The EP catheter passed through a Polytetrafluoroethylene (PTFE) pipeline with 0.8-m length and 4-mm inner diameter, which started at the robotic platform and ended before the catheter bendable section. The catheter's bending section could move freely in the workspace. The PTFE pipeline simulated a path along the vessel to heart chamber. In the task, the catheter was automatically manipulated by the robotic platform to reach the targets in a sequence from T1 to T5. The tip position and catheter shape were recorded and fed back by the proposed shape tracking method. The pre-trained catheter model introduced in **Section 6.3.5.3** was used to control the robot.

The footprint of catheter tip during autonomous targeting is shown in **Fig. 6.17a**, with the trajectories represented by different colors. The red curves with dots indicate the reconstructed catheter shape and position when its tip reached the targets. The deviations from the tip to targeting points in the five stages are illustrated in **Fig. 6.17b**. The average duration towards each target was 16.9 s, with the maximum duration of 25.8 s (T3). The longer duration towards T3 could be attributed to the larger targeting distance (85.8 mm), as the tip maximum speed was limited in the control algorithm to ensure a safe catheter manipulation. The results indicated a fast and efficient autonomous targeting performance of the robotic system incorporating with the shape tracking and control systems.

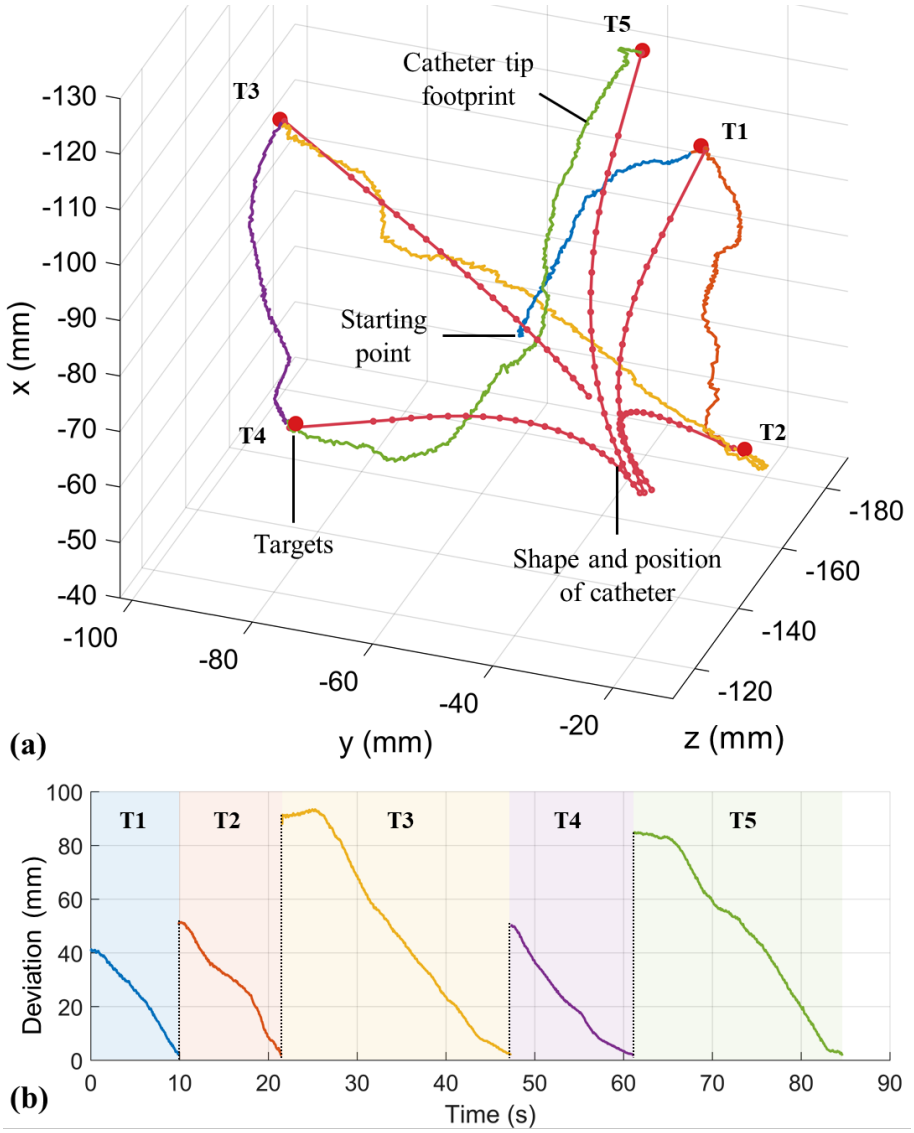

Fig. 6.17: **(a)** Diagrams showing the catheter tip trajectory towards the five targets during the autonomous targeting. The reconstructed catheter shape and position are plotted for the instances when the tip reached the targets; **(b)** Deviation from the tip to the targets in the five stages.

6.3.5.5 Path following

To further investigate the overall feedback control performance of the robotic catheter system, a path following task was conducted. The static reference path was pre-defined in the shape of a sideways figure eight ("∞"), which has a dimension of 60×30 mm. The learning-based PCC model was implemented on the robot. The catheter tip was autonomously controlled to trace the reference path periodically, with the duration of each loop set to 60 seconds.

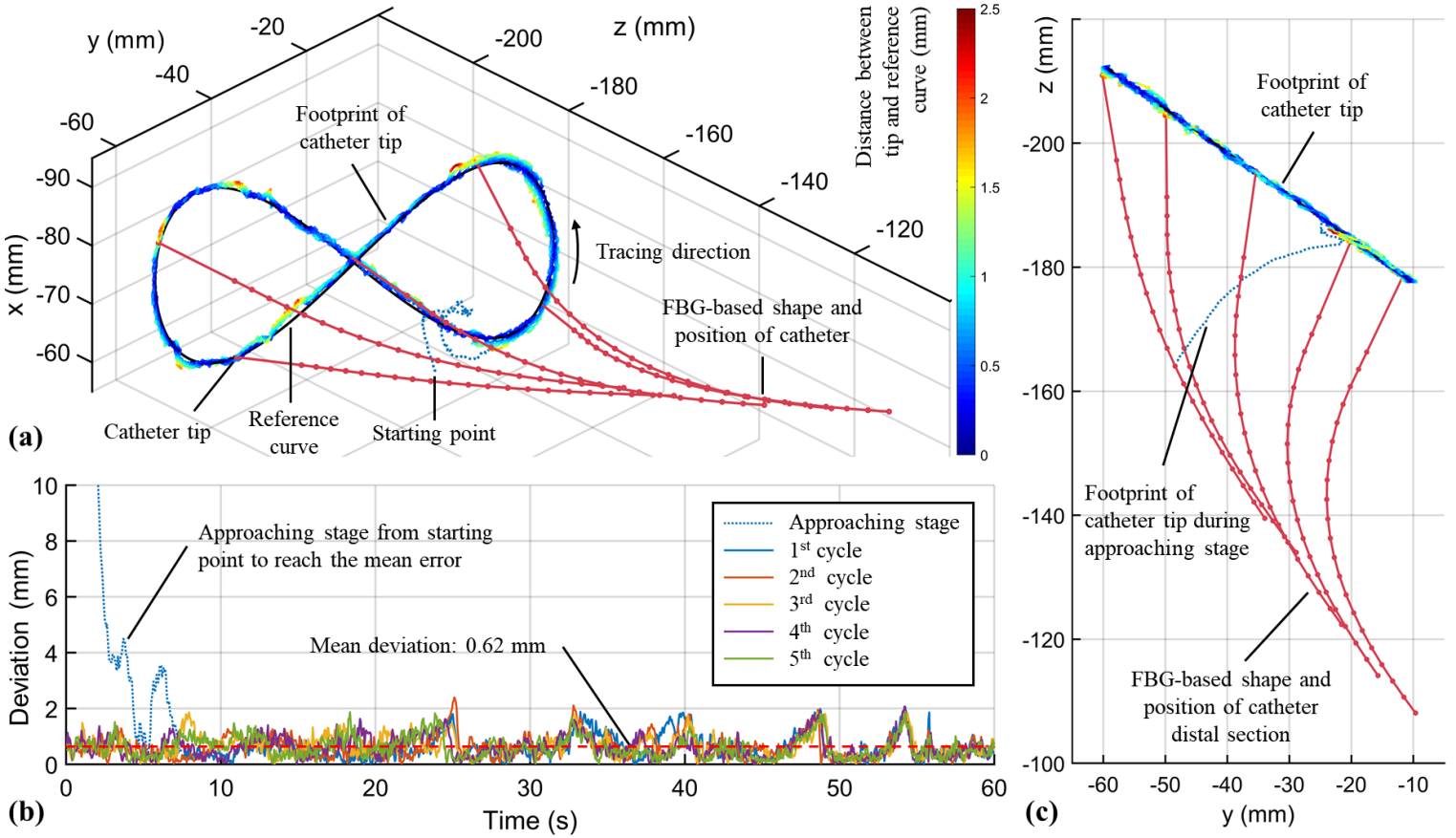

Fig. 6.18: **(a)** Catheter tip footprint in 5 cycles under autonomous path following using the learning-based PCC model. Larger the catheter tip deviation from the reference curve, warmer the color of its tip footprint. The reconstructed catheter shapes and positions were obtained from the proposed shape tracking approach; **(b)** Deviation from the tip to the reference curve in 5 cycles. The catheter was controlled to quickly trace the path during the approaching stage; **(c)** Top view showing the catheter bending shapes at the five instances.

The diagram in **Fig. 6.18a** depicts the tip footprint recorded by the shape tracking system over 5 cycles. The deviation from the tip to the reference curve is indicated by the warm color gradient. **Fig. 6.18b** illustrates the corresponding tip deviation over the 5 tracing cycles. A mean value of deviation, 0.62 mm, could be found throughout the trajectory after the approaching stage. Most segments of the trajectory tracking are smooth and closed along with the reference curve. Several sections of the tip footprint have larger deviations (max. 2.34 mm), which is mainly due to the backlash and nonlinearity of the catheter manipulation and robotic actuation. The reconstructed curves of the catheter are also overlaid on the diagrams as red curves with dots, representing the instantaneous shape and position of the bending section at 12s, 24s, 36s, 48s and 50s in the 1st cycle. A close tracing between the tip footprint and reference curve could be clearly observed in **Fig. 6.18c**, together with the reconstructed catheter shapes in various bending curvatures.

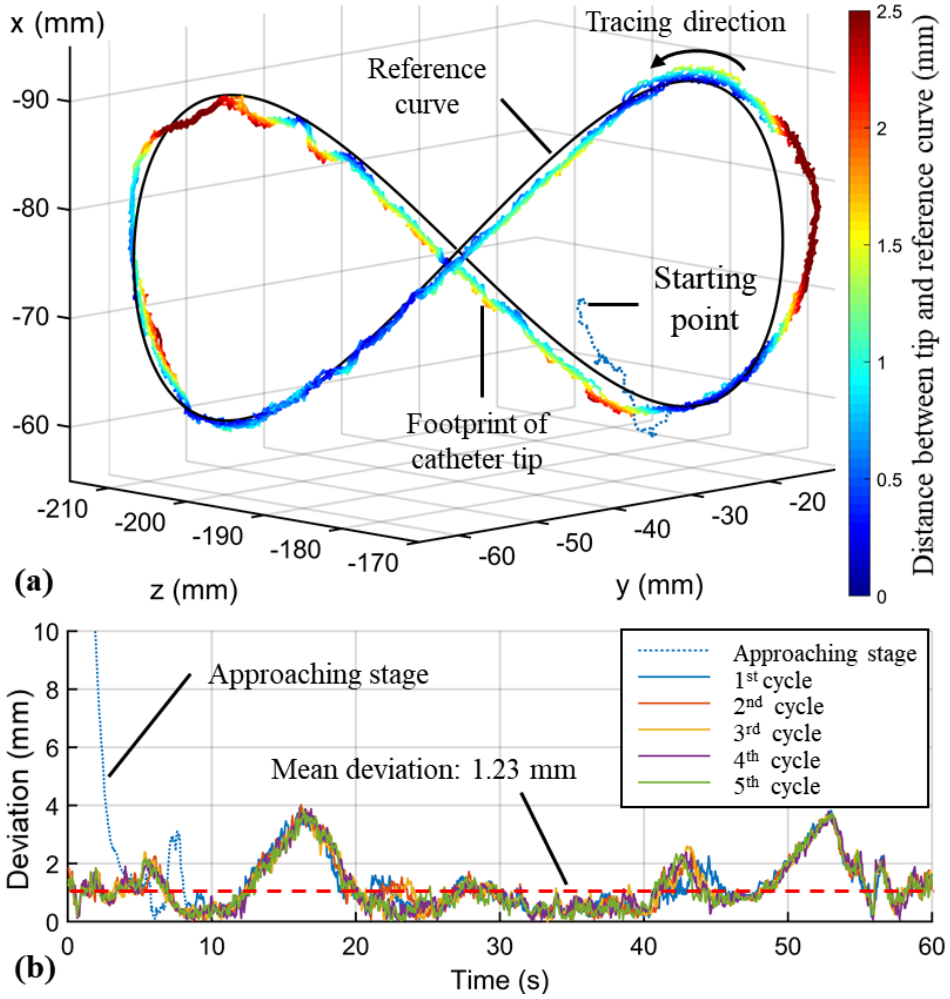

Fig. 6.19: (a) Catheter tip footprint under autonomous control with the CC model. Large deviation can be found at segments with red color; **(b)** Tip deviation from the reference curve. Slow and delayed retracement can be observed at several segments due to the inaccurate estimation of kinematic mapping done by the CC model.

As a comparison, the CC model was implemented on the robot for a path flowing task as well. All the initial parameters of the CC model and controller remained the same as the proposed model, with the only difference in the modeling method and absence of training process. The footprint recorded by shape tracking system over 5 cycles is shown in **Fig. 6.19a**. The deviation from tip to reference curve is illustrated in **Fig. 6.19b**, which had an average value of 1.23 mm and a maximum value of 4.02 mm. It can be seen that the path controlled by CC model had a larger deviation, which could be attributed to the overestimation of bending by the model. In contrast, the learning-based PCC model could reflect the catheter configuration characteristics more precisely, thus offering a more accurate mapping between the robotic actuation and the tip motion.

6.3.5.6 *Ex vivo* tissue ablation with simulated pulsatile flow

A simulated PVI task with *ex-vivo* tissue ablation was conducted to assess the overall performance of the shape tracking and controller. The experiment was performed inside the LA model with simulated pulsatile liquid flow. In the task, the catheter was manipulated by the robot to reach the predefined ablation targets (**Fig. 6.20a**). A 2-mm tolerance was set for each target. The ablation process was automatically triggered by an RF generator (Biosense Webster Stockert 70) when the catheter tip reached the target region and had tissue contact with impedance $<$200 Ω, as introduced in **Section 6.3.3.3**. After conducting ablation at each target point, the robot was reset to the initial position for another targeting process. This reset aimed to separate the catheter tip with the ablated tissue, as well as to avoid the collision with the LA simulator's wall during the next targeting.

As shown in **Fig. 6.20a**, the red spheres represent the predefined ablation targets, which have a total number of 15 and are in a volume of $20.9\times23.0\times11.1$ mm^3. These targets form a yellow line corresponding to the circumferential lesion targeted path nearby the pulmonary vein ostia. The footprint (blue line) indicates the targeting motions towards the lesions. 12 out of the 15 (80.0%) lesion targets were successfully reached by the catheter tip to conduct RF ablation. For the unsuccessful cases, the catheter was blocked by the tissue on the targeting path. **Fig. 6.20b** shows the actual lesion points on the *ex-vivo* tissue. The average time taken to complete the targeting process was 7.76 s, with the average traveling distance of 43.4 mm. The results demonstrate stable and accurate control achieved by the proposed feedback control methods, even under dynamic disturbance with simulated pulsatile liquid flow. In **Fig. 6.20a**, the red curves with dots indicate the reconstructed catheter shape and

position when the tip reached three of the targets. Other than providing feedback control for the robotic system, the catheter shape tracking can also offer informative visual feedback of the current catheter shape and tip targeting orientation. This additional information could help surgeons keep track of the targeting progress and evaluate the ablation result, thus improving the treatment safety and effectiveness.

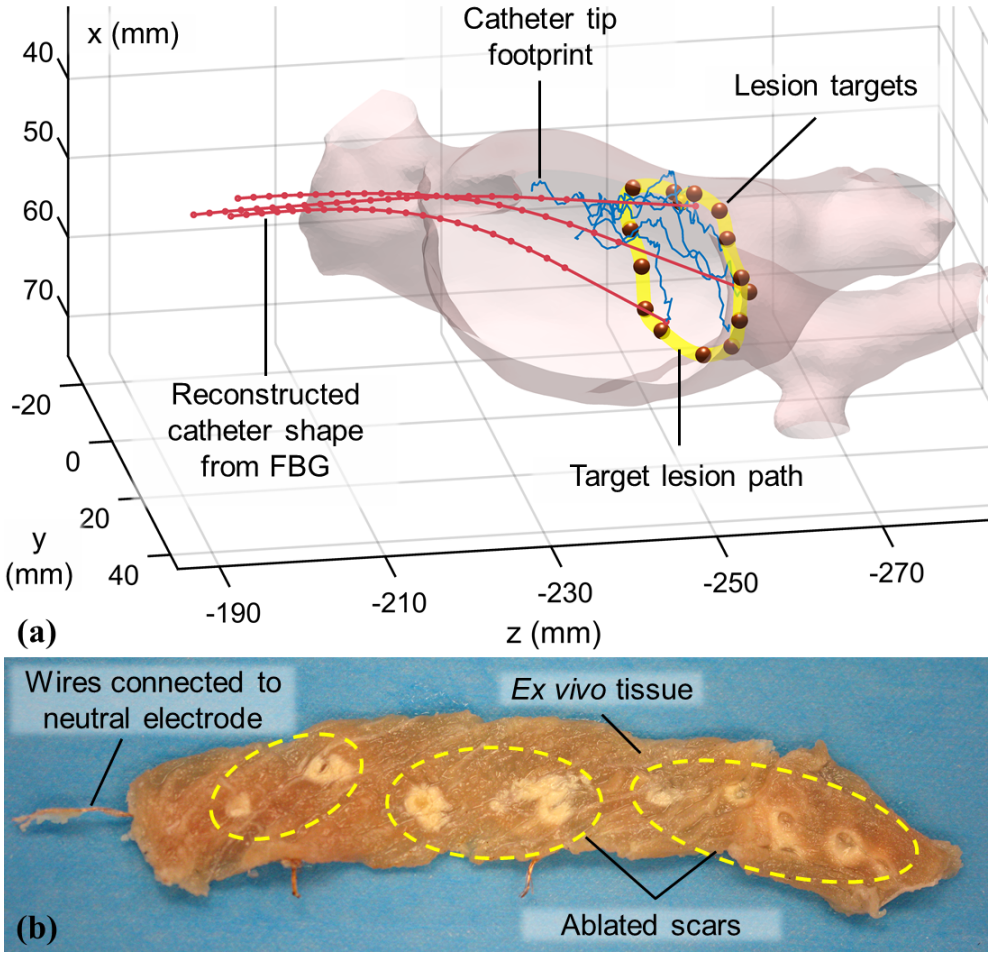

Fig. 6.20: Results of the pulmonary vein isolation (PVI) task conducted in the LA simulator. A standard EP catheter was autonomously controlled to reach a series of targets around the pulmonary vein ostium. **(a)** Front view showing the catheter tip footprint, the targeted ablation points, and the desired lesion path (yellow). The footprint (blue line) indicates the selective tip trajectories towards the targets; **(b)** Tissue with ablated points (yellow circle).

6.4 Conclusion

To improve the tele-operated control effectiveness of cardiac catheters, kinematics modeling methods have been investigated with model-based and model-free modeling approaches, which were implemented on the MR safe robotic catheter platform. Subject test was conducted to evaluate the performance of both control methods quantitatively. Compared to the model-based control method, it could be seen that model-free method achieved higher accuracy (19.1% improvement in the tip-to-target ablation distance) and higher efficiency (35.8% reduction in the missed-target proportion and 46.2% reduction in the number of continuously missed targets).

Shape tracking and feedback control methods are also proposed for standard cardiac catheters. Sensing information from multi-core FBG fiber and positional tracking coils was integrated to enable catheter shape estimation under MRI, which was subsequently incorporated with an MR safe robotic catheter system. A learning-based modeling method is proposed for the cardiac catheter, with the FBG shape tracking used for system characterization. Comparing with conventional CC models for continuum robots, the proposed modeling method can resolve the modeling uncertainties from heuristic parameter tuning and tendon backlash. The shape sensing using multi-core FBG fiber could achieve 2.33° average error for each sensing segment, and 1.52 mm positional accuracy for the catheter tip. Autonomous targeting of five points within the robot workspace showed effective convergence rates (average 16.9 s). Performance of the proposed learning-based PCC and conventional CC models were compared in a path following task, where the average deviations were 0.62 mm (max. deviation 2.34 mm) and 1.23 mm (max. deviation 4.02 mm), respectively. A simulated PVI task with *ex-vivo* tissue ablation has also been conducted to demonstrate the overall performance of the shape tracking and controller.

Chapter 7

Conclusion

7.1 Summary of thesis achievements

This thesis presents several research attempts aiming to solve the unmet technical challenges of tele-operated robotic systems, which are applied for intra-operative (intra-op) magnetic resonance imaging (MRI)-guided interventions. High-performance magnetic resonance (MR) safe hydraulic actuator has been developed, serving as the essential component for robotic tele-operation. With incorporation of the hydraulic motors, the needle placement robots and the robotic catheter system are developed, offering accurate and dexterous manipulation of instrument. Real-time shape tracking and motion control methods are also proposed with the robotic catheter platform. These concepts and techniques involved in the works can be further applied to other types of interventions demanding intra-op MRI guidance, such as breast and prostate biopsy. It is expected the successful integration of high-performance tele-operated robotic system would present a significant improvement in accuracy, efficiency and safety for MRI-guided interventions. The major achievements are summarized as follows:

1. *High-performance MR safe hydraulic actuation*: MR safe hydraulic motors are developed with incorporation of rolling-diaphragm-sealed cylinders for high-fidelity tele-operation. The configurable MR safe motor is capable of providing continuous bidirectional rotation with unlimited range. It also features fast response (rise time $<$40 ms), accurate open-loop positional control (average error of 0.64°) with high output torque (0.49 N-m), even through 10-meter long hydraulic pipelines. Both kinematics and dynamics models of the hydraulic motor have been studied to identify

the key design parameters that affect the system performance. Their design tradeoff is presented in an analytical study. The proposed hydraulic motors, particularly the three-cylinder configuration, would offer many opportunities to facilitate the MR safe/conditional robot development. The motors could be implemented into robotic systems for interventions demanding intra-op MRI guidance. MRI-guided catheter robot for cardiac electrophysiology (EP) (**Chapter 5**) and robotic manipulator for stereotactic neurosurgery (**Chapter 4**) are two examples.

2. *Compact robotic manipulator for bilateral stereotactic neurosurgery*: The intra-operative MRI-guided robot can perform bilateral needle targeting towards both subthalamic nucleus (STNs) simultaneously. The compact robot structure ($110.6 \times 206.8 \times 33.2$ mm^3) can enable its operation within the limited space of an MRI head coil. The high-fidelity hydraulic motors were integrated for robotic actuation, which can achieve a maximum stiffness of 24.35 N/mm. The needle targeting accuracy was verified by a simulated deep brain stimulation (DBS) task, demonstrating sufficient targeting accuracy compared to the regular requirement. A pre-clinical trial under MRI guidance has been conducted to verify the surgical workflow assisted by the proposed robotic system. It is expected that the robotic system can greatly reduce the operation time from the repeated instrument placement/adjustment, as well as the image alignment with head frame. The overall healthcare expenditure could be significantly reduced, also compensating the high cost of using MRI.

3. *Interactive needle placement robot for percutaneous intervention*: The proposed robot can offer semi-automated instrument positioning under MRI guidance. The instrument manipulation can be interactively conducted, with coarse initial placement operated by the surgeon and fine adjustment actuated by the robotic system. The compact and lightweight robot design allows not only the direct mounting onto the patient body, but also needle targeting at multiple locations with several robots alongside the loop coils. Granular jamming was also implemented to lock the needle position in place once after the fine automated adjustments have been made. The entire system is expected to improve ablation probe access to lesions and reduce recurrence rate of tumor ablation.

4. *Robotic catheter platform for MRI-guided cardiac catheterization*: The proposed MR safe robotic manipulator can offer sufficient degrees of freedom (DoFs) to tele-manipulate a cardiac catheter under intra-op MRI guidance. High-fidelity

hydraulic motors using rolling-diaphragm seals have been incorporated. We have simulated the navigation and pulmonary vein isolation (PVI) tasks to validate the robot performance in terms of long-range catheter advancement and subtle lesion targeting. These experiments have demonstrated that the robot can provide functional manipulation towards MRI-guided EP with sufficient workspace and dexterity. The advent of the proposed MRI-guided robotic catheter system can increase effectiveness to perform radiofrequency (RF) ablation, while improving the navigation safety. As a result, the system may reduce nerve damage, esophageal fistula creation, pulmonary vein stenosis and stroke, as well as the chance of post-procedural disease recurrence, which is currently 30% in atrial fibrillation and 50% in ventricular tachycardia. This will also contribute to justifying the use of MRI, while reducing the overall healthcare expenditure of the treatments.

5. *Experimental validation of control interface for tele-operation of the robotic catheter platform*: To improve the effectiveness of tele-operated control for cardiac catheters, kinematics modeling methods have been investigated, with model-based and model-free approaches implemented on the MR safe robotic catheter platform. Subject test, which emulated an ablation task, was conducted to evaluate the performance of both control methods quantitatively. Compared to the model-based control method, it could be seen that model-free method achieved higher accuracy, with 19.1% improvement in the tip-to-target ablation distance. Model-free method also achieved a higher efficiency, with 35.8% reduction in the missed-target proportion and 46.2% reduction in the number of continuously missed targets.

6. *Shape tracking and feedback control of cardiac catheter*: Shape tracking and feedback control methods are developed for standard cardiac catheters in MRI-guided EP procedures. The shape tracking of cardiac catheter can be achieved by integrating the multi-core optical fiber with fiber Bragg gratings (FBGs) and positional tracking coils, which was subsequently incorporated with an MR safe robotic catheter system. A learning-based modeling method is proposed for the cardiac catheter, with the FBG-based shape tracking used for characterizing modeling parameters. Experiments have been conducted to evaluate the shape tracking and feedback control performance. A simulated PVI task with *ex-vivo* tissue ablation was carried out to demonstrate the overall performance of the robotic system.

7.2 Future work

Despite the achievements presented in the thesis, there are few directions deserving further investigations. As the essential components of tele-operated robotic system for MRI-guided interventions, the high-performance hydraulic actuator presented in **Chapter 3**, particularly the three-cylinder design, could be further implemented on other MRI-guided interventions. We also foresee that MRI-guided high-intensity focused ultrasound (HIFU) thermal therapy is another emerging intervention that could benefit from the present motor. The high-payload, continuous actuation would facilitate accurate repositioning of the large array of ultrasound transducers, hence enlarging the ablation workspace, and also smoothening the interventional workflow without having to going in-and-out the MRI room for manual repositioning.

For the robotic needle manipulators presented in **Chapter 4**, cadaveric trials will be the upcoming aims to validate their benefits and workflow. Many practical considerations need to be further investigated, such as the setup in MRI, integration with MR scanning coils, and the maintenance of the hydraulic transmission system. In addition, to improve the manipulation accuracy, MR safe optical encoders could be incorporated, with development of controller to "fuse" the sensing data with MR real-time tracking of the needle guide to obtain the pose of the tracked needle tip in the image coordinates, instead of solely by calculation from the robot kinematics. Although robotic assistance alone is a large direction for researchers aiming to improve needle-based procedures, we will have a focus on integrating other technologies that can complement the automation and precision offered by robotics. Notable examples include haptics for tele-operative needle insertion and augmented reality for guiding needle placement and insertion paths.

For the robotic catheter platform introduced in **Chapter 5**, pre-clinical animal trials will be conducted to validate the robotic catheter system for MRI-guided EP procedure. RF ablation will be carried out on a live porcine or ovine model with arrhythmia. The proposed shape tracking and controller (**Chapter 6**) will be adapted to commercial MR-conditional systems equipped with RF ablation system (e.g. ClearTrace™, MRI Interventions, Inc. or Imricor Medical System). The efficacy of RF ablation will also be examined with post-mortem histology. It is anticipated that the robotic catheter system would simplify the surgical workflow of MRI-guided EP procedures. The proposed catheter shape tracking method is expected to provide sufficient feedback for visualization and robotic control under MRI, potentially reducing workload of the surgeon as well as post-procedural disease

recurrence.

In addition, the proposed FBG-based shape tracking method (**Chapter 6**) could be implemented on other MR safe/conditional continuum manipulators for interventional procedures, such as urologic surgery, ophthalmic surgery and neurosurgery. The direct measurement and reconstruction of shape and position for continuum manipulators would reduce the computational cost of MRI, enabling high-performance feedback control and interactive instrument manipulation. It is believed that both safety and overall operational efficiency would be enhanced, with accurately and intra-operatively updated morphological information of interventional instruments.

References

[1] E. Kholmovski, R. Ranjan, J. Silvernagel, J. Blauer, and N. Marrouche, "Assessment of acute cryo and rf ablation lesions by non-contrast and contrast enhanced mri techniques: Similarities and differences," *Circulation*, vol. 130, no. Suppl_2, pp. A14649–A14649, 2014.

[2] E.-S. Cho and J.-Y. Choi, "Mri features of hepatocellular carcinoma related to biologic behavior," *Korean journal of radiology*, vol. 16, no. 3, pp. 449–464, 2015.

[3] R. Medvid, A. Ruiz, R. J. Komotar, J. Jagid, M. Ivan, R. Quencer, and M. Desai, "Current applications of mri-guided laser interstitial thermal therapy in the treatment of brain neoplasms and epilepsy: a radiologic and neurosurgical overview," *American Journal of Neuroradiology*, vol. 36, no. 11, pp. 1998–2006, 2015.

[4] V. Seifert and C. Senft, "Utilization of low-field intraoperative mri in glioma surgery–an overview," *Intraoperative MRI-Guided Neurosurgery. Stuttgart: Thieme*, pp. 99–107, 2011.

[5] "Medtronic inc." https://www.medtronic.com/us-en/index.html. Accessed: 2020-03-25.

[6] "Philips inc." https://www.philips.com/global. Accessed: 2020-04-05.

[7] "Siemens inc." https://new.siemens.com/global/en.html. Accessed: 2020-03-26.

[8] "Imris inc." https://www.imris.com/. Accessed: 2020-04-01.

[9] N. Clinic, "Mri safety week: precautions to take before an mri scan," *Newcastle Clinic News*, 2016. Available: https://newcastleclinic.co.uk/mri-safety-week-precautions-to-take-before-an-mri-scan/, Accessed: Feb 2020.

[10] T. Budrys, V. Veikutis, S. Lukosevicius, R. Gleizniene, E. Monastyreckiene, and I. Kulakiene, "Artifacts in magnetic resonance imaging: how it can really

affect diagnostic image quality and confuse clinical diagnosis?," *Journal of Vibroengineering*, vol. 20, no. 2, pp. 1202–1213, 2018.

[11] J. M. Jani, C. O. Oluigbo, and S. K. Reddy, "Anesthesia for deep brain stimulation in traumatic brain injury-induced hemidystonia," *Clinical case reports*, vol. 3, no. 6, p. 492, 2015.

[12] J.-F. Lu, H. Zhang, J.-S. Wu, C.-J. Yao, D.-X. Zhuang, T.-M. Qiu, W.-B. Jia, Y. Mao, and L.-F. Zhou, ""awake" intraoperative functional mri (ai-fmri) for mapping the eloquent cortex: is it possible in awake craniotomy?," *NeuroImage: Clinical*, vol. 2, pp. 132–142, 2013.

[13] F. R. Khan and J. M. Henderson, "Deep brain stimulation surgical techniques," in *Handbook of clinical neurology*, vol. 116, pp. 27–37, Elsevier, 2013.

[14] S. Chabardes, S. Isnard, A. Castrioto, M. Oddoux, V. Fraix, L. Carlucci, J. F. Payen, A. Krainik, P. Krack, P. Larson, *et al.*, "Surgical implantation of stn-dbs leads using intraoperative mri guidance: technique, accuracy, and clinical benefit at 1-year follow-up," *Acta neurochirurgica*, vol. 157, no. 4, pp. 729–737, 2015.

[15] "Clearpoint neuro." https://www.clearpointneuro.com/. Accessed: 2020-03-26.

[16] J. W. Motkoski and G. R. Sutherland, "Why robots entered neurosurgery," in *Experimental Neurosurgery in Animal Models*, pp. 85–105, Springer, 2016.

[17] C. J. Nycz, R. Gondokaryono, P. Carvalho, N. Patel, M. Wartenberg, J. G. Pilitsis, and G. S. Fischer, "Mechanical validation of an mri compatible stereotactic neurosurgery robot in preparation for pre-clinical trials," in *2017 IEEE/RSJ International Conference on Intelligent Robots and Systems (IROS)*, pp. 1677–1684, IEEE, 2017.

[18] "Monteris medical inc." https://www.monteris.com/. Accessed: 2020-03-26.

[19] M. Li, D. Mazilu, A. Kapoor, and K. A. Horvath, "Mri compatible robot systems for medical intervention," in *Advances in Robot Manipulators*, IntechOpen, 2010.

[20] E. Franco, M. Ristic, M. Rea, and W. M. Gedroyc, "Robot-assistant for mri-guided liver ablation: A pilot study," *Medical physics*, vol. 43, no. 10, pp. 5347–5356, 2016.

[21] D. Stoianovici, C. Jun, S. Lim, P. Li, D. Petrisor, S. Fricke, K. Sharma, and K. Cleary, "Multi-imager compatible, mr safe, remote center of motion needle-guide robot," *IEEE Transactions on Biomedical Engineering*, vol. 65, no. 1, pp. 165–177, 2017.

[22] N. Hungr, I. Bricault, P. Cinquin, and C. Fouard, "Design and validation of a ct-and mri-guided robot for percutaneous needle procedures," *IEEE transactions on robotics*, vol. 32, no. 4, pp. 973–987, 2016.

[23] J. Ghelfi, A. Moreau-Gaudry, N. Hungr, C. Fouard, B. Véron, M. Medici, E. Chipon, P. Cinquin, and I. Bricault, "Evaluation of the needle positioning accuracy of a light puncture robot under mri guidance: results of a clinical trial on healthy volunteers," *Cardiovascular and interventional radiology*, vol. 41, no. 9, pp. 1428–1435, 2018.

[24] G. Li, N. A. Patel, J. Hagemeister, J. Yan, D. Wu, K. Sharma, K. Cleary, and I. Iordachita, "Body-mounted robotic assistant for mri-guided low back pain injection," *International Journal of Computer Assisted Radiology and Surgery*, pp. 1–11, 2019.

[25] N. Patel, J. Yan, R. Monfaredi, K. Sharma, K. Cleary, and I. I. Iordachita, "Preclinical evaluation of an integrated robotic system for magnetic resonance imaging guided shoulder arthrography," *Journal of Medical Imaging*, vol. 6, no. 2, p. 025006, 2019.

[26] F. Y. Wu, M. Torabi, A. Yamada, A. Golden, G. S. Fischer, K. Tuncali, D. D. Frey, and C. Walsh, "An mri coil-mounted multi-probe robotic positioner for cryoablation," in *ASME 2013 International Design Engineering Technical Conferences and Computers and Information in Engineering Conference*, American Society of Mechanical Engineers Digital Collection, 2013.

[27] "Hansen medical." https://www.aurishealth.com/hansen-medical. Accessed: 2020-04-05.

[28] "Catheter precision inc." http://www.catheterprecision.com/. Accessed: 2020-04-05.

[29] "Stereotaxis inc." http://www.stereotaxis.com/. Accessed: 2020-04-05.

[30] "Faulhaber micromo." https://www.micromo.com/. Accessed: 2020-04-05.

[31] H. Su, D. C. Cardona, W. Shang, A. Camilo, G. A. Cole, D. C. Rucker, R. J. Webster, and G. S. Fischer, "A mri-guided concentric tube continuum robot with piezoelectric actuation: a feasibility study," in *2012 IEEE International Conference on Robotics and Automation*, pp. 1939–1945, IEEE, 2012.

[32] D. Stoianovici, A. Patriciu, D. Petrisor, D. Mazilu, and L. Kavoussi, "A new type of motor: pneumatic step motor," *IEEE/ASME Transactions On Mechatronics*, vol. 12, no. 1, pp. 98–106, 2007.

[33] V. Groenhuis, J. Veltman, F. J. Siepel, and S. Stramigioli, "Stormram 3: A magnetic resonance imaging-compatible robotic system for breast biopsy," *IEEE robotics & automation magazine*, vol. 24, no. 2, pp. 34–41, 2017.

[34] Y. Chen, K.-W. Kwok, and Z. T. H. Tse, "An mr-conditional high-torque pneumatic stepper motor for mri-guided and robot-assisted intervention," *Annals of biomedical engineering*, vol. 42, no. 9, pp. 1823–1833, 2014.

[35] Z. Guo, T. Lun, Y. Chen, H. Su, D. Chan, and K. Kwok, "Novel design of an mr-safe pneumatic stepper motor for mri-guided robotic interventions," in *Proceedings of The Hamlyn Symposium on Medical Robotics*, pp. 25–28, Imperial College London and the Royal Geographical Society London. The . . . , 2016.

[36] W. Wang, C. L. Dumoulin, A. N. Viswanathan, Z. T. Tse, A. Mehrtash, W. Loew, I. Norton, J. Tokuda, R. T. Seethamraju, T. Kapur, *et al.*, "Real-time active mr-tracking of metallic stylets in mr-guided radiation therapy," *Magnetic resonance in medicine*, vol. 73, no. 5, pp. 1803–1811, 2015.

[37] S. Weiss, T. Kuehne, F. Brinkert, G. Krombach, M. Katoh, T. Schaeffter, R. W. Guenther, and A. Buecker, "In vivo safe catheter visualization and slice tracking using an optically detunable resonant marker," *Magnetic Resonance in Medicine: An Official Journal of the International Society for Magnetic Resonance in Medicine*, vol. 52, no. 4, pp. 860–868, 2004.

[38] K. Hayatin, "Treatment using electrical energy, instead of medications, may be viable first option for treating certain type of atrial fibrillation," *Medimoon*, 2014. Available: https://medimoon.com/category/medical/, Accessed: 2020-06-25.

[39] "Boston scientific corporation." https://www.bostonscientific.com/en-US/Home.html. Accessed: 2020-06-25.

[40] "Electrophysiology study and catheter ablation: What to expect at home," *Healthwise*, 2019. Available: https://myhealth.alberta.ca/Health/aftercareinformation/pages/conditions.aspx?hwid=zy1373, Accessed: 2020-06-25.

[41] S. Bricelyn H. and P. Kevin, "Cardiac catheterization," *Johns Hopkins Medicine*. Available: https://www.hopkinsmedicine.org/health/treatment-tests-and-therapies/cardiac-catheterization, Accessed: 2020-06-25.

[42] D. Bhakta and J. M. Miller, "Principles of electroanatomic mapping," *Indian pacing and electrophysiology journal*, vol. 8, no. 1, p. 32, 2008.

[43] A. Kolandaivelu, A. C. Lardo, and H. R. Halperin, "Cardiovascular magnetic resonance guided electrophysiology studies," *Journal of Cardiovascular Magnetic Resonance*, vol. 11, no. 1, pp. 1–14, 2009.

[44] L. Organ, "Cardiac equipment (tilt studies and ep studies) to diagnose arrhythmias part iii of iv," *Elite Cardiology Group*, 2013. Available: http://ecgmedical.com/cardiac-equipment-diagnose-arrhythmias-part-iii-iv/, Accessed: 2020-06-25.

[45] U. Jae-Sun, K. Nam Kyun, P. Jin-Kyu, J. Boyoung, P. Hui-Nam, and L. Moon-Hyoung, "Atrial tachycardia in a patient with extracardiac conduit fontan circulation," *International Journal of Arrhythmia*, vol. 15, no. 4, pp. 37–44, 2014.

[46] T. Rogers, S. Mahapatra, S. Kim, M. A. Eckhaus, W. H. Schenke, J. R. Mazal, A. Campbell-Washburn, M. Sonmez, A. Z. Faranesh, K. Ratnayaka, *et al.*, "Transcatheter myocardial needle chemoablation during real-time magnetic resonance imaging: a new approach to ablation therapy for rhythm disorders," *Circulation: Arrhythmia and Electrophysiology*, vol. 9, no. 4, p. e003926, 2016.

[47] A. Kolandaivelu, M. M. Zviman, V. Castro, A. C. Lardo, R. D. Berger, and H. R. Halperin, "Noninvasive assessment of tissue heating during cardiac radiofrequency ablation using mri thermography," *Circulation: Arrhythmia and Electrophysiology*, vol. 3, no. 5, pp. 521–529, 2010.

[48] R. Ranjan, E. G. Kholmovski, J. Blauer, S. Vijayakumar, N. A. Volland, M. E. Salama, D. L. Parker, R. MacLeod, and N. F. Marrouche, "Identification and acute targeting of gaps in atrial ablation lesion sets using a real-time magnetic resonance imaging system," *Circulation: Arrhythmia and Electrophysiology*, vol. 5, no. 6, pp. 1130–1135, 2012.

[49] M. Kouh Soltani, S. Khanmohammadi, and F. Ghalichi, "A three-dimensional shape-based force and stiffness-sensing platform for tendon-driven catheters," *Sensors*, vol. 16, no. 7, p. 990, 2016.

[50] E. J. Schmidt, R. P. Mallozzi, A. Thiagalingam, G. Holmvang, A. d'Avila, R. Guhde, R. Darrow, G. S. Slavin, M. M. Fung, J. Dando, *et al.*, "Electroanatomic mapping and radiofrequency ablation of porcine left atria and atrioventricular

nodes using magnetic resonance catheter tracking," *Circulation: Arrhythmia and Electrophysiology*, vol. 2, no. 6, pp. 695–704, 2009.

[51] H. Chubb, S. E. Williams, J. Whitaker, J. L. Harrison, R. Razavi, and M. O'Neill, "Cardiac electrophysiology under mri guidance: an emerging technology," *Arrhythmia & Electrophysiology Review*, vol. 6, no. 2, p. 85, 2017.

[52] "Fbgs." https://fbgs.com/. Accessed: 2020-06-25.

[53] T. Kahn and H. Busse, *Interventional Magnetic Resonance Imaging*. Medical Radiology, Berlin, Heidelberg: Springer Berlin Heidelberg, 2012.

[54] S.-E. Song, N. B. Cho, G. Fischer, N. Hata, C. Tempany, G. Fichtinger, and I. Iordachita, "Development of a pneumatic robot for MRI-guided transperineal prostate biopsy and brachytherapy: New approaches," in *2010 IEEE International Conference on Robotics and Automation*, pp. 2580–2585, IEEE, May 2010.

[55] G. Rahmathulla, P. F. Recinos, K. Kamian, A. M. Mohammadi, M. S. Ahluwalia, and G. H. Barnett, "Mri-guided laser interstitial thermal therapy in neuro-oncology: a review of its current clinical applications," *Oncology*, vol. 87, no. 2, pp. 67–82, 2014.

[56] M. J. LaRiviere and R. E. Gross, "Stereotactic laser ablation for medically intractable epilepsy: the next generation of minimally invasive epilepsy surgery," *Frontiers in surgery*, vol. 3, p. 64, 2016.

[57] J. Fritz, C. Thomas, S. Clasen, C. D. Claussen, J. S. Lewin, and P. L. Pereira, "Freehand real-time mri-guided lumbar spinal injection procedures at 1.5 t: feasibility, accuracy, and safety," *American Journal of Roentgenology*, vol. 192, no. 4, pp. W161–W167, 2009.

[58] M. Kinoshita, N. McDannold, F. A. Jolesz, and K. Hynynen, "Targeted delivery of antibodies through the blood–brain barrier by mri-guided focused ultrasound," *Biochemical and biophysical research communications*, vol. 340, no. 4, pp. 1085–1090, 2006.

[59] A. Tzifa, G. A. Krombach, N. Krämer, S. Krüger, A. Schütte, M. von Walter, T. Schaeffter, S. Qureshi, T. Krasemann, E. Rosenthal, *et al.*, "Magnetic resonance–guided cardiac interventions using magnetic resonance–compatible

devices: A preclinical study and first-in-man congenital interventions," *Circulation: Cardiovascular Interventions*, vol. 3, no. 6, pp. 585–592, 2010.

[60] Y. Feng, Z. Guo, Z. Dong, X.-Y. Zhou, K.-W. Kwok, S. Ernst, and S.-L. Lee, "An efficient cardiac mapping strategy for radiofrequency catheter ablation with active learning," *International journal of computer assisted radiology and surgery*, vol. 12, no. 7, pp. 1199–1207, 2017.

[61] K. Masamune, E. Kobayashi, Y. Masutani, M. Suzuki, T. Dohi, H. Iseki, and K. Takakura, "Development of an mri-compatible needle insertion manipulator for stereotactic neurosurgery," *Journal of Image Guided Surgery*, vol. 1, no. 4, pp. 242–248, 1995.

[62] K. M. Pondman, J. J. Fütterer, B. ten Haken, L. J. S. Kool, J. A. Witjes, T. Hambrock, K. J. Macura, and J. O. Barentsz, "Mr-guided biopsy of the prostate: an overview of techniques and a systematic review," *European urology*, vol. 54, no. 3, pp. 517–527, 2008.

[63] A. N. Sridhar, A. Hughes-Hallett, E. K. Mayer, P. J. Pratt, P. J. Edwards, G.-Z. Yang, A. W. Darzi, and J. A. Vale, "Image-guided robotic interventions for prostate cancer," *Nature Reviews Urology*, vol. 10, no. 8, p. 452, 2013.

[64] D. B. Comber, E. B. Pitt, H. B. Gilbert, M. W. Powelson, E. Matijevich, J. S. Neimat, R. J. Webster III, and E. J. Barth, "Optimization of curvilinear needle trajectories for transforamenal hippocampotomy," *Operative Neurosurgery*, vol. 13, no. 1, pp. 15–22, 2017.

[65] L. Saba, *Magnetic Resonance Imaging Handbook*. CRC Press, Inc., 2016.

[66] J. R. Brookeman, "MRI from Picture to Proton," *American Journal of Roentgenology*, vol. 182, pp. 592–592, mar 2004.

[67] R. Toth, D. Sperling, and A. Madabhushi, "Quantifying post-laser ablation prostate therapy changes on mri via a domain-specific biomechanical model: preliminary findings," *PloS one*, vol. 11, no. 4, 2016.

[68] N. V. Tsekos, A. Khanicheh, E. Christoforou, and C. Mavroidis, "Magnetic Resonance–Compatible Robotic and Mechatronics Systems for Image-Guided Interventions and Rehabilitation: A Review Study," *Annual Review of Biomedical Engineering*, vol. 9, pp. 351–387, aug 2007.

[69] J. S. Lewin, C. A. Petersilge, S. F. Hatem, J. L. Duerk, G. Lenz, M. E. Clampitt, M. L. Williams, K. R. Kaczynski, C. F. Lanzieri, A. L. Wise, *et al.*, "Interactive mr imaging-guided biopsy and aspiration with a modified clinical c-arm system.," *AJR. American journal of roentgenology*, vol. 170, no. 6, pp. 1593–1601, 1998.

[70] E. Salomonowitz, "Mr imaging-guided biopsy and therapeutic intervention in a closed-configuration magnet: single-center series of 361 punctures," *American Journal of Roentgenology*, vol. 177, no. 1, pp. 159–163, 2001.

[71] R. Blanco Sequeiros, R. Ojala, J. Kariniemi, J. Perälä, J. Niinimäki, H. Reinikainen, and O. Tervonen, "MR-guided interventional procedures: a review," *Acta Radiologica*, vol. 46, pp. 576–586, oct 2005.

[72] M. Schulder, D. Liang, and P. W. Carmel, "Cranial surgery navigation aided by a compact intraoperative magnetic resonance imager," *Journal of neurosurgery*, vol. 94, no. 6, pp. 936–945, 2001.

[73] G. R. Sutherland, T. Kaibara, D. Louw, D. I. Hoult, B. Tomanek, and J. Saunders, "A mobile high-field magnetic resonance system for neurosurgery," *Journal of neurosurgery*, vol. 91, no. 5, pp. 804–813, 1999.

[74] D. I. Hoult, J. K. Saunders, G. R. Sutherland, J. Sharp, M. Gervin, H. G. Kolansky, D. L. Kripiakevich, A. Procca, R. A. Sebastian, A. Dombay, *et al.*, "The engineering of an interventional mri with a movable 1.5 tesla magnet," *Journal of Magnetic Resonance Imaging*, vol. 13, no. 1, pp. 78–86, 2001.

[75] T. Kaibara, J. K. Saunders, and G. R. Sutherland, "Utility of a moveable 1.5 tesla intraoperative mr imaging system," *Canadian journal of neurological sciences*, vol. 26, no. 4, pp. 313–316, 1999.

[76] ASTM, "Standard practice for marking medical devices and other items for safety in the magnetic resonance environment," *ASTM F2503-13*, 2013.

[77] R. A. Beasley, "Medical robots: current systems and research directions," *Journal of Robotics*, vol. 2012, 2012.

[78] D. B. Camarillo, T. M. Krummel, and J. K. Salisbury Jr, "Robotic technology in surgery: past, present, and future," *The American Journal of Surgery*, vol. 188, no. 4, pp. 2–15, 2004.

[79] Y. Wang, S. E. Butner, and A. Darzi, "The developing market for medical robotics," *Proceedings of the IEEE*, vol. 94, no. 9, pp. 1763–1771, 2006.

[80] M. Hoeckelmann, I. J. Rudas, P. Fiorini, F. Kirchner, and T. Haidegger, "Current capabilities and development potential in surgical robotics," *International Journal of Advanced Robotic Systems*, vol. 12, no. 5, p. 61, 2015.

[81] T. S. Lendvay, J. Rosen, and B. Hannaford, "44 telerobotics: Its future in clinical application," *Pediatric Robotic and Reconstructive Urology*, p. 314, 2012.

[82] R.-M. deSouza, E. Moro, A. E. Lang, and A. H. Schapira, "Timing of deep brain stimulation in parkinson disease: a need for reappraisal?," *Annals of neurology*, vol. 73, no. 5, pp. 565–575, 2013.

[83] R. A. Vega, K. L. Holloway, and P. S. Larson, "Image-guided deep brain stimulation," *Neurosurgery Clinics*, vol. 25, no. 1, pp. 159–172, 2014.

[84] C. Nimsky, O. Ganslandt, P. Hastreiter, and R. Fahlbusch, "Intraoperative compensation for brain shift," *Surgical neurology*, vol. 56, no. 6, pp. 357–364, 2001.

[85] C. Sidiropoulos, R. Rammo, B. Merker, A. Mahajan, P. LeWitt, P. Kaminski, M. Womble, A. Zec, D. Taylor, J. Wall, *et al.*, "Intraoperative mri for deep brain stimulation lead placement in parkinson's disease: 1 year motor and neuropsychological outcomes," *Journal of neurology*, vol. 263, no. 6, pp. 1226–1231, 2016.

[86] G. R. Sutherland, Y. Maddahi, L. S. Gan, S. Lama, and K. Zareinia, "Robotics in the neurosurgical treatment of glioma," *Surgical neurology international*, vol. 6, no. Suppl 1, p. S1, 2015.

[87] A. H. Hawasli, S. Bagade, J. S. Shimony, M. Miller-Thomas, and E. C. Leuthardt, "Magnetic resonance imaging-guided focused laser interstitial thermal therapy for intracranial lesions: single-institution series," *Neurosurgery*, vol. 73, no. 6, pp. 1007–1017, 2013.

[88] G. Li, H. Su, G. A. Cole, W. Shang, K. Harrington, A. Camilo, J. G. Pilitsis, and G. S. Fischer, "Robotic system for mri-guided stereotactic neurosurgery," *IEEE transactions on biomedical engineering*, vol. 62, no. 4, pp. 1077–1088, 2014.

[89] F. W. Petraglia III, S. H. Farber, J. L. Han, T. Verla, J. Gallis, Y. Lokhnygina, B. Parente, P. Hickey, D. A. Turner, and S. P. Lad, "Comparison of bilateral vs. staged

unilateral deep brain stimulation (dbs) in p arkinson's disease in patients under 70 years of age," *Neuromodulation: Technology at the Neural Interface*, vol. 19, no. 1, pp. 31–37, 2016.

[90] G. Widmann, "Image-guided surgery and medical robotics in the cranial area," *Biomedical imaging and intervention journal*, vol. 3, no. 1, 2007.

[91] S. McGuire, "World cancer report 2014. geneva, switzerland: World health organization, international agency for research on cancer, who press, 2015," 2016.

[92] L. S. Poulou, E. Botsa, I. Thanou, P. D. Ziakas, and L. Thanos, "Percutaneous microwave ablation vs radiofrequency ablation in the treatment of hepatocellular carcinoma," *World journal of hepatology*, vol. 7, no. 8, p. 1054, 2015.

[93] J. Wong, K.-F. Lee, S. C.-H. Yu, P. S.-F. Lee, Y.-S. Cheung, C.-N. Chong, P. C.-T. Ip, and P. Bo-San Lai, "Percutaneous radiofrequency ablation versus surgical radiofrequency ablation for malignant liver tumours: the long-term results," *HPB*, vol. 15, no. 8, pp. 595–601, 2013.

[94] G. G. Di Costanzo, G. Francica, and C. M. Pacella, "Laser ablation for small hepatocellular carcinoma: state of the art and future perspectives," *World journal of hepatology*, vol. 6, no. 10, p. 704, 2014.

[95] K. A. Simo, S. E. Sereika, K. N. Newton, and D. A. Gerber, "Laparoscopic-assisted microwave ablation for hepatocellular carcinoma: Safety and efficacy in comparison with radiofrequency ablation," *Journal of surgical oncology*, vol. 104, no. 7, pp. 822–829, 2011.

[96] H. Fukuda, R. Ito, M. Ohto, A. Sakamoto, E. Karasawa, T. Yamaguchi, N. Shinozuka, H. Zhu, and Z.-B. Wanga, "Treatment of small hepatocellular carcinomas with us-guided high-intensity focused ultrasound," *Ultrasound in medicine & biology*, vol. 37, no. 8, pp. 1222–1229, 2011.

[97] A. H. Mahnken, A. Buecker, E. Spuentrup, G. A. Krombach, D. Henzler, R. W. Günther, and J. Tacke, "Mr-guided radiofrequency ablation of hepatic malignancies at 1.5 t: initial results," *Journal of Magnetic Resonance Imaging: An Official Journal of the International Society for Magnetic Resonance in Medicine*, vol. 19, no. 3, pp. 342–348, 2004.

[98] G. G. Di Costanzo, R. Tortora, G. D'Adamo, M. De Luca, F. Lampasi, L. Addario, A. Galeota Lanza, F. P. Picciotto, M. T. Tartaglione, G. Cordone, *et al.*, "Radiofrequency ablation versus laser ablation for the treatment of small hepatocellular carcinoma in cirrhosis: a randomized trial," *Journal of gastroenterology and hepatology*, vol. 30, no. 3, pp. 559–565, 2015.

[99] C. M. Pacella, G. Bizzarri, G. Francica, A. Bianchini, S. De Nuntis, S. Pacella, A. Crescenzi, S. Taccogna, G. Forlini, Z. Rossi, *et al.*, "Percutaneous laser ablation in the treatment of hepatocellular carcinoma with small tumors: analysis of factors affecting the achievement of tumor necrosis," *Journal of vascular and interventional radiology*, vol. 16, no. 11, pp. 1447–1457, 2005.

[100] M. W. Kroes, W. M. Busser, J. J. Fütterer, M. J. Arntz, C. M. Janssen, Y. L. Hoogeveen, F. de Lange, and L. J. Schultze Kool, "Assessment of Needle Guidance Devices for Their Potential to Reduce Fluoroscopy Time and Operator Hand Dose during C-Arm Cone-Beam Computed Tomography–guided Needle Interventions," *Journal of Vascular and Interventional Radiology*, vol. 24, pp. 901–906, jun 2013.

[101] A. Magnusson, E. Radecka, M. Lönnemark, and H. Raland, "Computed-tomography-guided punctures using a new guidance device," *Acta Radiologica*, vol. 46, no. 5, pp. 505–509, 2005.

[102] A. Melzer, B. Gutmann, A. Lukoschek, M. Mark, W. Zylka, and H. Fischer, "Experimental evaluation of an mri compatible telerobotic system for ct mri guided interventions," *Supplement to Radiology*, vol. 226, pp. 409–444, 2003.

[103] K. Chinzei, N. Hata, F. A. Jolesz, and R. Kikinis, "Mr compatible surgical assist robot: System integration and preliminary feasibility study," in *International Conference on Medical Image Computing and Computer-Assisted Intervention*, pp. 921–930, Springer, 2000.

[104] D. B. Comber, J. E. Slightam, V. R. Gervasi, J. S. Neimat, and E. J. Barth, "Design, additive manufacture, and control of a pneumatic mr-compatible needle driver," *IEEE Transactions on Robotics*, vol. 32, no. 1, pp. 138–149, 2016.

[105] S. B. Park, J.-G. Kim, K.-W. Lim, C.-H. Yoon, D.-J. Kim, H.-S. Kang, and Y.-H. Jo, "A magnetic resonance image-guided breast needle intervention robot system: overview and design considerations," *International journal of computer assisted radiology and surgery*, vol. 12, no. 8, pp. 1319–1331, 2017.

[106] R. Monfaredi, I. Iordachita, E. Wilson, R. Sze, K. Sharma, A. Krieger, S. Fricke, and K. Cleary, "Development of a shoulder-mounted robot for mri-guided needle placement: phantom study," *International journal of computer assisted radiology and surgery*, vol. 13, no. 11, pp. 1829–1841, 2018.

[107] C. Baegert, C. Villard, P. Schreck, and L. Soler, "Multi-criteria trajectory planning for hepatic radiofrequency ablation," in *International Conference on Medical Image Computing and Computer-Assisted Intervention*, pp. 676–684, Springer, 2007.

[108] F. Morady, "Radio-frequency ablation as treatment for cardiac arrhythmias," *New England Journal of Medicine*, vol. 340, no. 7, pp. 534–544, 1999.

[109] M. Haissaguerre, P. Jaïs, D. C. Shah, A. Takahashi, M. Hocini, G. Quiniou, S. Garrigue, A. Le Mouroux, P. Le Métayer, and J. Clémenty, "Spontaneous initiation of atrial fibrillation by ectopic beats originating in the pulmonary veins," *New England Journal of Medicine*, vol. 339, no. 10, pp. 659–666, 1998.

[110] M. Boulos and L. Gepstein, "Electroanatomical mapping and radiofrequency ablation of an accessory pathway associated with a large aneurysm of the coronary sinus," *EP Europace*, vol. 6, no. 6, pp. 608–612, 2004.

[111] J. Ector, S. De Buck, J. Adams, S. Dymarkowski, J. Bogaert, F. Maes, and H. Heidbüchel, "Cardiac three-dimensional magnetic resonance imaging and fluoroscopy merging: a new approach for electroanatomic mapping to assist catheter ablation," *Circulation*, vol. 112, no. 24, pp. 3769–3776, 2005.

[112] J. Dong, H. Calkins, S. B. Solomon, S. Lai, D. Dalal, A. C. Lardo, E. Brem, A. Preiss, R. D. Berger, H. Halperin, *et al.*, "Integrated electroanatomic mapping with three-dimensional computed tomographic images for real-time guided ablations," *Circulation*, vol. 113, no. 2, pp. 186–194, 2006.

[113] A. C. Lardo, E. R. McVeigh, P. Jumrussirikul, R. D. Berger, H. Calkins, J. Lima, and H. R. Halperin, "Visualization and temporal/spatial characterization of cardiac radiofrequency ablation lesions using magnetic resonance imaging," *Circulation*, vol. 102, no. 6, pp. 698–705, 2000.

[114] E. M. Aliot, W. G. Stevenson, J. M. Almendral-Garrote, F. Bogun, C. H. Calkins, E. Delacretaz, P. D. Bella, G. Hindricks, P. Jaïs, M. E. Josephson, *et al.*, "Ehra/hrs expert consensus on catheter ablation of ventricular arrhythmias: developed in a

partnership with the european heart rhythm association (ehra), a registered branch of the european society of cardiology (esc), and the heart rhythm society (hrs); in collaboration with the american college of cardiology (acc) and the american heart association (aha)," *Europace*, vol. 11, no. 6, pp. 771–817, 2009.

[115] P. Sommer, M. Grothoff, C. Eitel, T. Gaspar, C. Piorkowski, M. Gutberlet, and G. Hindricks, "Feasibility of real-time magnetic resonance imaging-guided electrophysiology studies in humans," *Europace*, vol. 15, no. 1, pp. 101–108, 2013.

[116] J. Ren, K. A. McIsaac, R. V. Patel, and T. M. Peters, "A potential field model using generalized sigmoid functions," *IEEE Transactions on Systems, Man, and Cybernetics, Part B (Cybernetics)*, vol. 37, no. 2, pp. 477–484, 2007.

[117] D. Peters, J. Hsing, K. Kissinger, B. Goddu, R. Nezafat, J. Taclas, M. Josephson, J. Wylie, and W. Manning, "T2-weighted imaging of the left atrium acutely after pulmonary vein isolation demonstrates wall thickening and edema," in *Proceedings of the 17th Annual Meeting of ISMRM*, p. 4433, 2009.

[118] A. N. Raval, P. V. Karmarkar, M. A. Guttman, C. Ozturk, R. DeSilva, R. J. Aviles, V. J. Wright, W. H. Schenke, E. Atalar, E. R. McVeigh, *et al.*, "Real-time mri guided atrial septal puncture and balloon septostomy in swine," *Catheterization and cardiovascular interventions*, vol. 67, no. 4, pp. 637–643, 2006.

[119] S. R. Dukkipati, R. Mallozzi, E. J. Schmidt, G. Holmvang, A. d'Avila, R. Guhde, R. D. Darrow, G. Slavin, M. Fung, Z. Malchano, *et al.*, "Electroanatomic mapping of the left ventricle in a porcine model of chronic myocardial infarction with magnetic resonance–based catheter tracking," *Circulation*, vol. 118, no. 8, pp. 853–862, 2008.

[120] R. C. Susil, C. J. Yeung, H. R. Halperin, A. C. Lardo, and E. Atalar, "Multifunctional interventional devices for mri: a combined electrophysiology/mri catheter," *Magnetic Resonance in Medicine: An Official Journal of the International Society for Magnetic Resonance in Medicine*, vol. 47, no. 3, pp. 594–600, 2002.

[121] R. Razavi, D. L. Hill, S. F. Keevil, M. E. Miquel, V. Muthurangu, S. Hegde, K. Rhode, M. Barnett, J. van Vaals, D. J. Hawkes, *et al.*, "Cardiac catheterisation guided by mri in children and adults with congenital heart disease," *The Lancet*, vol. 362, no. 9399, pp. 1877–1882, 2003.

[122] M. Shurrab, R. Schilling, E. Gang, E. M. Khan, and E. Crystal, "Robotics in invasive cardiac electrophysiology," *Expert review of medical devices*, vol. 11, no. 4, pp. 375–381, 2014.

[123] M. A. Tavallaei, Y. Thakur, S. Haider, and M. Drangova, "A magnetic-resonance-imaging-compatible remote catheter navigation system," *IEEE Transactions on Biomedical Engineering*, vol. 60, no. 4, pp. 899–905, 2012.

[124] M. A. Tavallaei, M. Lavdas, D. Gelman, and M. Drangova, "Magnetic resonance imaging compatible remote catheter navigation system with 3 degrees of freedom," *International journal of computer assisted radiology and surgery*, vol. 11, no. 8, pp. 1537–1545, 2016.

[125] A. Aryana, A. D'Avila, E. K. Heist, T. Mela, J. P. Singh, J. N. Ruskin, and V. Y. Reddy, "Remote Magnetic Navigation to Guide Endocardial and Epicardial Catheter Mapping of Scar-Related Ventricular Tachycardia," *Circulation*, vol. 115, pp. 1191–1200, mar 2007.

[126] C. Cheung, K. Lee, Z. Guo, Z. Dong, M. Leong, Y. Chen, A. Lee, and K. Kwok, "Kinematic-model-free positional control for robot-assisted cardiac catheterization," in *Proceedings of the Hamlyn symposium on medical robotics*, pp. 80–81, 2016.

[127] J. Cao, M. Ma, H. Li, Y. Zhang, and Z. Luo, "A survey on security aspects for lte and lte-a networks," *IEEE communications surveys & tutorials*, vol. 16, no. 1, pp. 283–302, 2013.

[128] S. Avgousti, E. G. Christoforou, A. S. Panayides, S. Voskarides, C. Novales, L. Nouaille, C. S. Pattichis, and P. Vieyres, "Medical telerobotic systems: current status and future trends," *Biomedical engineering online*, vol. 15, no. 1, p. 96, 2016.

[129] A. Krieger, S.-E. Song, N. B. Cho, I. I. Iordachita, P. Guion, G. Fichtinger, and L. L. Whitcomb, "Development and evaluation of an actuated mri-compatible robotic system for mri-guided prostate intervention," *IEEE/ASME Transactions on Mechatronics*, vol. 18, no. 1, pp. 273–284, 2011.

[130] K. El Bannan, B. A. Chronik, and S. P. Salisbury, "Development of an mri-compatible, compact, rotary-linear piezoworm actuator," *Journal of Medical Devices*, vol. 9, no. 1, 2015.

[131] Y. Wang, G. A. Cole, H. Su, J. G. Pilitsis, and G. S. Fischer, "Mri compatibility evaluation of a piezoelectric actuator system for a neural interventional robot," in *2009 Annual International Conference of the IEEE Engineering in Medicine and Biology Society*, pp. 6072–6075, IEEE, 2009.

[132] D. Stoianovici, C. Kim, D. Petrisor, C. Jun, S. Lim, M. W. Ball, A. Ross, K. J. Macura, and M. E. Allaf, "Mr safe robot, fda clearance, safety and feasibility of prostate biopsy clinical trial," *IEEE/ASME Transactions on Mechatronics*, vol. 22, no. 1, pp. 115–126, 2016.

[133] V. Groenhuis, F. J. Siepel, J. Veltman, and S. Stramigioli, "Design and characterization of stormram 4: An mri-compatible robotic system for breast biopsy," in *2017 IEEE/RSJ International Conference on Intelligent Robots and Systems (IROS)*, pp. 928–933, IEEE, 2017.

[134] H. Sajima, H. Kamiuchi, K. Kuwana, T. Dohi, and K. Masamune, "Mr-safe pneumatic rotation stepping actuator," *Journal of Robotics and Mechatronics*, vol. 24, no. 5, pp. 820–827, 2012.

[135] Y. Chen, C. D. Mershon, and Z. T. H. Tse, "A 10-mm mr-conditional unidirectional pneumatic stepper motor," *IEEE/ASME Transactions on Mechatronics*, vol. 20, no. 2, pp. 782–788, 2014.

[136] R. Secoli, M. Robinson, M. Brugnoli, and F. Rodriguez y Baena, "A low-cost, high-field-strength magnetic resonance imaging–compatible actuator," *Proceedings of the Institution of Mechanical Engineers, Part H: Journal of Engineering in Medicine*, vol. 229, no. 3, pp. 215–224, 2015.

[137] D. G. H. Bosboom, J. J. Fütterer, and J. Bosboom, "Motor system, motor, and robot arm device comprising the same," Oct. 18 2016. US Patent 9,469,026.

[138] G. Ganesh, R. Gassert, E. Burdet, and H. Bleuler, "Dynamics and control of an mri compatible master-slave system with hydrostatic transmission," in *IEEE International Conference on Robotics and Automation, 2004. Proceedings. ICRA'04. 2004*, vol. 2, pp. 1288–1294, IEEE, 2004.

[139] L. Lindenroth, J. Back, A. Schoisengeier, Y. Noh, H. Würdemann, K. Althoefer, and H. Liu, "Stiffness-based modelling of a hydraulically-actuated soft robotics manipulator," in *2016 IEEE/RSJ International Conference on Intelligent Robots and Systems (IROS)*, pp. 2458–2463, IEEE, 2016.

[140] J. P. Whitney, T. Chen, J. Mars, and J. K. Hodgins, "A hybrid hydrostatic transmission and human-safe haptic telepresence robot," in *2016 IEEE International Conference on Robotics and Automation (ICRA)*, pp. 690–695, IEEE, 2016.

[141] P. Ghanouni, K. B. Pauly, W. J. Elias, J. Henderson, J. Sheehan, S. Monteith, and M. Wintermark, "Transcranial mri-guided focused ultrasound: a review of the technologic and neurologic applications," *American Journal of Roentgenology*, vol. 205, no. 1, pp. 150–159, 2015.

[142] Y. Meng, S. Suppiah, K. Mithani, B. Solomon, M. L. Schwartz, and N. Lipsman, "Current and emerging brain applications of mr-guided focused ultrasound," *Journal of therapeutic ultrasound*, vol. 5, no. 1, p. 26, 2017.

[143] S. Patil, O. Bieri, P. Jhooti, and K. Scheffler, "Automatic slice positioning (asp) for passive real-time tracking of interventional devices using projection-reconstruction imaging with echo-dephasing (pride)," *Magnetic Resonance in Medicine: An Official Journal of the International Society for Magnetic Resonance in Medicine*, vol. 62, no. 4, pp. 935–942, 2009.

[144] J. L. Duerk, E. Y. Wong, and J. S. Lewin, "A brief review of hardware for catheter tracking in magnetic resonance imaging," *Magnetic Resonance Materials in Physics, Biology and Medicine*, vol. 13, no. 3, p. 199, 2001.

[145] A. Glowinski, G. Adam, A. Bücker, J. Neuerburg, J. J. van Vaals, and R. W. Günther, "Catheter visualization using locally induced, actively controlled field inhomogeneities," *Magnetic resonance in medicine*, vol. 38, no. 2, pp. 253–258, 1997.

[146] M. E. Josephson, *Clinical cardiac electrophysiology: techniques and interpretations*. Lippincott Williams & Wilkins, 2008.

[147] W. Wongcharoen, H.-M. TSAO, M.-H. WU, C.-T. TAI, S.-L. CHANG, Y.-J. LIN, L.-W. LO, Y.-J. CHEN, M.-H. SHEU, C.-Y. CHANG, *et al.*, "Morphologic characteristics of the left atrial appendage, roof, and septum: implications for the ablation of atrial fibrillation," *Journal of cardiovascular electrophysiology*, vol. 17, no. 9, pp. 951–956, 2006.

[148] K.-W. Kwok, K.-H. Lee, Y. Chen, W. Wang, Y. Hu, G. C. Chow, H. S. Zhang, W. G. Stevenson, R. Y. Kwong, W. Luk, *et al.*, "Interfacing fast multi-phase cardiac image

registration with mri-based catheter tracking for mri-guided electrophysiological ablative procedures," *Circulation*, vol. 130, no. suppl_2, pp. A18568–A18568, 2014.

[149] M. Bock, S. Müller, S. Zuehlsdorff, P. Speier, C. Fink, P. Hallscheidt, R. Umathum, and W. Semmler, "Active catheter tracking using parallel mri and real-time image reconstruction," *Magnetic Resonance in Medicine: An Official Journal of the International Society for Magnetic Resonance in Medicine*, vol. 55, no. 6, pp. 1454–1459, 2006.

[150] K.-W. Kwok, Y. Chen, T. C. Chau, W. Luk, K. R. Nilsson, E. J. Schmidt, and T. T. Zion, "Mri-based visual and haptic catheter feedback: simulating a novel system's contribution to efficient and safe mri-guided cardiac electrophysiology procedures," *Journal of Cardiovascular Magnetic Resonance*, vol. 16, no. 1, p. O50, 2014.

[151] R. J. Webster III and B. A. Jones, "Design and kinematic modeling of constant curvature continuum robots: A review," *The International Journal of Robotics Research*, vol. 29, no. 13, pp. 1661–1683, 2010.

[152] A. Bajo and N. Simaan, "Kinematics-based detection and localization of contacts along multisegment continuum robots," *IEEE Transactions on Robotics*, vol. 28, no. 2, pp. 291–302, 2011.

[153] I. A. Gravagne and I. D. Walker, "On the kinematics of remotely-actuated continuum robots," in *Proceedings 2000 ICRA. Millennium Conference. IEEE International Conference on Robotics and Automation. Symposia Proceedings (Cat. No. 00CH37065)*, vol. 3, pp. 2544–2550, IEEE, 2000.

[154] M. Mahvash and P. E. Dupont, "Stiffness control of surgical continuum manipulators," *IEEE Transactions on Robotics*, vol. 27, no. 2, pp. 334–345, 2011.

[155] Y. Ganji, F. Janabi-Sharifi, *et al.*, "Catheter kinematics for intracardiac navigation," *IEEE Transactions on Biomedical Engineering*, vol. 56, no. 3, pp. 621–632, 2009.

[156] Y. Ganji and F. Janabi-Sharifi, "Kinematic characterization of a cardiac ablation catheter," in *2007 IEEE/RSJ International Conference on Intelligent Robots and Systems*, pp. 1876–1881, IEEE, 2007.

[157] T. Liu and M. C. Çavuşoğlu, "Three dimensional modeling of an mri actuated steerable catheter system," in *2014 IEEE international conference on robotics and automation (ICRA)*, pp. 4393–4398, IEEE, 2014.

[158] T. Greigarn and M. C. Çavuşoğlu, "Task-space motion planning of mri-actuated catheters for catheter ablation of atrial fibrillation," in *2014 IEEE/RSJ International Conference on Intelligent Robots and Systems*, pp. 3476–3482, IEEE, 2014.

[159] J. Back, L. Lindenroth, K. Rhode, and H. Liu, "Model-free position control for cardiac ablation catheter steering using electromagnetic position tracking and tension feedback," *Frontiers in Robotics and AI*, vol. 4, p. 17, 2017.

[160] M. C. Yip and D. B. Camarillo, "Model-less hybrid position/force control: a minimalist approach for continuum manipulators in unknown, constrained environments," *IEEE Robotics and Automation Letters*, vol. 1, no. 2, pp. 844–851, 2016.

[161] S. P. Buerger, *Stable, high-force, low-impedance robotic actuators for human-interactive machines*. PhD thesis, Massachusetts Institute of Technology, 2005.

[162] T. Helbich, M. Rudas, A. Haitel, P. Kohlberger, M. Thurnher, M. Gnant, P. Wunderbaldinger, G. Wolf, and G. Mostbeck, "Evaluation of needle size for breast biopsy: comparison of 14-, 16-, and 18-gauge biopsy needles.," *AJR. American journal of roentgenology*, vol. 171, no. 1, pp. 59–63, 1998.

[163] P. J. Pritchard, R. W. Fox, and A. T. McDonald, *Introduction to fluid mechanics*. John Wiley & Sons, 2010.

[164] D. A. Thorley, *Fluid transients in pipeline systems*. No. BOOK, ASME Press, 2004.

[165] ASTM, "Standard test method for evaluation of mr image artifacts from passive implants," 2001.

[166] P. S. Larson, P. A. Starr, G. Bates, L. Tansey, R. M. Richardson, and A. J. Martin, "An optimized system for interventional magnetic resonance imaging-guided stereotactic surgery: preliminary evaluation of targeting accuracy," *Operative Neurosurgery*, vol. 70, no. suppl_1, pp. ons95–ons103, 2012.

[167] D. Tarsy, J. L. Vitek, and A. M. Lozano, *Surgical treatment of Parkinson's disease and other movement disorders*. Springer Science & Business Media, 2002.

[168] J.-P. Merlet, "Parallel robots: Open problems," in *Robotics research*, pp. 27–32, Springer, 2000.

[169] L. Campos, F. Bourbonnais, I. A. Bonev, and P. Bigras, "Development of a five-bar parallel robot with large workspace," in *ASME 2010 International Design Engineering Technical Conferences and Computers and Information in Engineering Conference*, pp. 917–922, American Society of Mechanical Engineers Digital Collection, 2010.

[170] A. Figielski, I. A. Bonev, and P. Bigras, "Towards development of a 2-dof planar oparallel robot with optimal workspace use," in *2007 IEEE International Conference on Systems, Man and Cybernetics*, pp. 1562–1566, IEEE, 2007.

[171] S.-E. Song, J. Tokuda, K. Tuncali, A. Yamada, M. Torabi, and N. Hata, "Design evaluation of a double ring rcm mechanism for robotic needle guidance in mri-guided liver interventions," in *2013 IEEE/RSJ International Conference on Intelligent Robots and Systems*, pp. 4078–4083, IEEE, 2013.

[172] V. Granata, M. Petrillo, R. Fusco, S. V. Setola, E. de Lutio di Castelguidone, O. Catalano, M. Piccirillo, V. Albino, F. Izzo, and A. Petrillo, "Surveillance of hcc patients after liver rfa: Role of mri with hepatospecific contrast versus three-phase ct scan—experience of high volume oncologic institute," *Gastroenterology research and practice*, vol. 2013, 2013.

[173] M. W. Lee, H. K. Lim, H. Rhim, D. I. Cha, T. W. Kang, K. D. Song, J. H. Min, G.-Y. Gwak, S. Kim, and D. S. Lu, "Percutaneous radiofrequency ablation of small (1–2 cm) hepatocellular carcinomas inconspicuous on b-mode ultrasonographic imaging: usefulness of combined fusion imaging with mri and contrast-enhanced ultrasonography," *Canadian Journal of Gastroenterology and Hepatology*, vol. 2018, 2018.

[174] L. H. Blumenschein and Y. Mcngüç, "Generalized delta mechanisms from soft actuators," in *2019 2nd IEEE International Conference on Soft Robotics (RoboSoft)*, pp. 249–256, IEEE, 2019.

[175] Z. Dong, Z. Guo, K.-H. Lee, G. Fang, W. L. Tang, H.-C. Chang, D. T. M. Chan, and K.-W. Kwok, "High-performance continuous hydraulic motor for mr safe robotic teleoperation," *IEEE Robotics and Automation Letters*, vol. 4, no. 2, pp. 1964–1971, 2019.

[176] Z. Guo, Z. Dong, K.-H. Lee, C. L. Cheung, H.-C. Fu, J. D. Ho, H. He, W.-S. Poon, D. T.-M. Chan, and K.-W. Kwok, "Compact design of a hydraulic driving robot

for intraoperative mri-guided bilateral stereotactic neurosurgery," *IEEE Robotics and Automation Letters*, vol. 3, no. 3, pp. 2515–2522, 2018.

[177] Ö. Bebek, M. J. Hwang, and M. C. Cavusoglu, "Design of a parallel robot for needle-based interventions on small animals," *IEEE/ASME Transactions on Mechatronics*, vol. 18, no. 1, pp. 62–73, 2011.

[178] H. Busse, R. Trampel, W. Gründer, M. Moche, and T. Kahn, "Method for automatic localization of mr-visible markers using morphological image processing and conventional pulse sequences: Feasibility for image-guided procedures," *Journal of Magnetic Resonance Imaging: An Official Journal of the International Society for Magnetic Resonance in Medicine*, vol. 26, no. 4, pp. 1087–1096, 2007.

[179] Y. Chen, W. Wang, E. J. Schmidt, K.-W. Kwok, A. N. Viswanathan, R. Cormack, and Z. T. H. Tse, "Design and fabrication of mr-tracked metallic stylet for gynecologic brachytherapy," *IEEE/ASME Transactions on Mechatronics*, vol. 21, no. 2, pp. 956–962, 2015.

[180] M. A. Rube, A. B. Holbrook, B. F. Cox, J. G. Houston, and A. Melzer, "Wireless mr tracking of interventional devices using phase-field dithering and projection reconstruction," *Magnetic resonance imaging*, vol. 32, no. 6, pp. 693–701, 2014.

[181] M. B. Ooi, M. Aksoy, J. Maclaren, R. D. Watkins, and R. Bammer, "Prospective motion correction using inductively coupled wireless rf coils," *Magnetic resonance in medicine*, vol. 70, no. 3, pp. 639–647, 2013.

[182] K. W. Kwok, Z. Dong, Z. Guo, K. C. D. Fu, K. H. Lee, and C. L. Cheung, "Robotic catheter system for mri-guided cardiovascular interventions," Dec. 28 2017. US Patent App. 15/630,406.

[183] F. Galassi, D. Brujic, M. Rea, N. Lambert, N. Desouza, and M. Ristic, "Fast and accurate localization of multiple rf markers for tracking in mri-guided interventions," *Magnetic Resonance Materials in Physics, Biology and Medicine*, vol. 28, no. 1, pp. 33–48, 2015.

[184] *Determination of signal-to-noise ratio (SNR) in diagnostic magnetic resonance images*. Rosslyn, VI, USA: NEMA, MS 1–2008 (R2014), 2008.

[185] A. A. Grace and D. M. Roden, "Systems biology and cardiac arrhythmias," *The Lancet*, vol. 380, no. 9852, pp. 1498–1508, 2012.

[186] S. Zuehlsdorff, R. Umathum, S. Volz, P. Hallscheidt, C. Fink, W. Semmler, and M. Bock, "Mr coil design for simultaneous tip tracking and curvature delineation of a catheter," *Magnetic Resonance in Medicine: An Official Journal of the International Society for Magnetic Resonance in Medicine*, vol. 52, no. 1, pp. 214–218, 2004.

[187] Y. Chen, K.-W. Kwok, J. Ge, Y. Hu, M. Fok, K. Ronald Nilsson, and Z. T. Ho Tse, "Augmented reality for improving catheterization in magnetic resonance imaging-guided cardiac electrophysiology therapy," *Journal of Medical Devices*, vol. 8, no. 2, 2014.

[188] H. Oral, C. Scharf, A. Chugh, B. Hall, P. Cheung, E. Good, S. Veerareddy, F. Pelosi Jr, and F. Morady, "Catheter ablation for paroxysmal atrial fibrillation: segmental pulmonary vein ostial ablation versus left atrial ablation," *Circulation*, vol. 108, no. 19, pp. 2355–2360, 2003.

[189] J. Mortensen, S. Talbot, and J. A. Burkart, "Cross-sectional internal diameters of human cervical and femoral blood vessels: Relationship to subject's sex, age, body size," *The Anatomical Record*, vol. 226, no. 1, pp. 115–124, 1990.

[190] M. Prince, R. Novelline, C. Athanasoulis, and M. Simon, "The diameter of the inferior vena cava and its implications for the use of vena caval filters.," *Radiology*, vol. 149, no. 3, pp. 687–689, 1983.

[191] X. Wang, K.-H. Lee, D. K. Fu, Z. Dong, K. Wang, G. Fang, S.-L. Lee, A. P. Lee, and K.-W. Kwok, "Experimental validation of robot-assisted cardiovascular catheterization: model-based versus model-free control," *International journal of computer assisted radiology and surgery*, vol. 13, no. 6, pp. 797–804, 2018.

[192] K.-W. Kwok, G. C. Chow, T. C. Chau, Y. Chen, S. H. Zhang, W. Luk, E. J. Schmidt, and T. T. Zion, "Fpga-based acceleration of mri registration: an enabling technique for improving mri-guided cardiac therapy," *Journal of Cardiovascular Magnetic Resonance*, vol. 16, no. S1, p. W11, 2014.

[193] C. L. Cheung, J. D.-L. Ho, V. Vardhanabhuti, H.-C. Chang, and K.-w. Kwok, "Design and fabrication of wireless multilayer tracking marker for intraoperative mri-guided interventions," *IEEE/ASME Transactions on Mechatronics*, 2020.

[194] M. C. Yip and D. B. Camarillo, "Model-less feedback control of continuum manipulators in constrained environments," *IEEE Transactions on Robotics*, vol. 30, no. 4, pp. 880–889, 2014.

[195] K.-H. Lee, K. C. D. Fu, Z. Guo, Z. Dong, M. C. Leong, C.-L. Cheung, A. P.-W. Lee, W. Luk, and K.-W. Kwok, "Mr safe robotic manipulator for mri-guided intracardiac catheterization," *IEEE/ASME Transactions on Mechatronics*, vol. 23, no. 2, pp. 586–595, 2018.

[196] M. J. Kern, P. Sorajja, and M. J. Lim, *Cardiac Catheterization Handbook E-Book*. Elsevier Health Sciences, 2015.

[197] R. H. Hoyle, *Statistical strategies for small sample research*. Sage, 1999.

[198] M. Grothoff, M. Gutberlet, G. Hindricks, C. Fleiter, B. Schnackenburg, S. Weiss, S. Krueger, C. Piorkowski, T. Gaspar, S. Wedan, *et al.*, "Magnetic resonance imaging guided transatrial electrophysiological studies in swine using active catheter tracking–experience with 14 cases," *European radiology*, vol. 27, no. 5, pp. 1954–1962, 2017.

[199] S. Hilbert, P. Sommer, M. Gutberlet, T. Gaspar, B. Foldyna, C. Piorkowski, S. Weiss, T. Lloyd, B. Schnackenburg, S. Krueger, *et al.*, "Real-time magnetic resonance-guided ablation of typical right atrial flutter using a combination of active catheter tracking and passive catheter visualization in man: initial results from a consecutive patient series," *Europace*, vol. 18, no. 4, pp. 572–577, 2016.

[200] B. A. Childers, M. E. Froggatt, S. G. Allison, T. C. Moore Sr, D. A. Hare, C. F. Batten, and D. C. Jegley, "Use of 3000 bragg grating strain sensors distributed on four 8-m optical fibers during static load tests of a composite structure," in *Smart Structures and Materials 2001: Industrial and Commercial Applications of Smart Structures Technologies*, vol. 4332, pp. 133–142, International Society for Optics and Photonics, 2001.

[201] G. Flockhart, W. MacPherson, J. Barton, J. Jones, L. Zhang, and I. Bennion, "Two-axis bend measurement with bragg gratings in multicore optical fiber," *Optics letters*, vol. 28, no. 6, pp. 387–389, 2003.

[202] K. Mandal, F. Parent, S. Martel, R. Kashyap, and S. Kadoury, "Vessel-based registration of an optical shape sensing catheter for mr navigation," *International journal of computer assisted radiology and surgery*, vol. 11, no. 6, pp. 1025–1034, 2016.

[203] S. C. Ryu and P. E. Dupont, "Fbg-based shape sensing tubes for continuum robots," in *2014 IEEE International Conference on Robotics and Automation (ICRA)*, pp. 3531–3537, IEEE, 2014.

[204] S. C. Ryu, Z. F. Quek, J.-S. Koh, P. Renaud, R. J. Black, B. Moslehi, B. L. Daniel, K.-J. Cho, and M. R. Cutkosky, "Design of an optically controlled mr-compatible active needle," *IEEE Transactions on Robotics*, vol. 31, no. 1, pp. 1–11, 2014.

[205] N. J. van de Berg, J. Dankelman, and J. J. van den Dobbelsteen, "Design of an actively controlled steerable needle with tendon actuation and fbg-based shape sensing," *Medical engineering & physics*, vol. 37, no. 6, pp. 617–622, 2015.

[206] T. Li, C. Shi, and H. Ren, "Three-dimensional catheter distal force sensing for cardiac ablation based on fiber bragg grating," *IEEE/ASME Transactions on Mechatronics*, vol. 23, no. 5, pp. 2316–2327, 2018.

[207] K. O. Hill and G. Meltz, "Fiber bragg grating technology fundamentals and overview," *Journal of lightwave technology*, vol. 15, no. 8, pp. 1263–1276, 1997.

[208] Y.-L. Park, S. Elayaperumal, B. Daniel, S. C. Ryu, M. Shin, J. Savall, R. J. Black, B. Moslehi, and M. R. Cutkosky, "Real-time estimation of 3-d needle shape and deflection for mri-guided interventions," *IEEE/ASME Transactions On Mechatronics*, vol. 15, no. 6, pp. 906–915, 2010.

[209] R. Seifabadi, E. E. Gomez, F. Aalamifar, G. Fichtinger, and I. Iordachita, "Real-time tracking of a bevel-tip needle with varying insertion depth: Toward teleoperated mri-guided needle steering," in *2013 IEEE/RSJ International Conference on Intelligent Robots and Systems*, pp. 469–476, IEEE, 2013.

[210] R. J. Roesthuis, S. Janssen, and S. Misra, "On using an array of fiber bragg grating sensors for closed-loop control of flexible minimally invasive surgical instruments," in *2013 IEEE/RSJ International Conference on Intelligent Robots and Systems*, pp. 2545–2551, IEEE, 2013.

[211] R. J. Roesthuis and S. Misra, "Steering of multisegment continuum manipulators using rigid-link modeling and fbg-based shape sensing," *IEEE transactions on robotics*, vol. 32, no. 2, pp. 372–382, 2016.

[212] H. Rafii-Tari, C. J. Payne, and G.-Z. Yang, "Current and emerging robot-assisted endovascular catheterization technologies: a review," *Annals of biomedical engineering*, vol. 42, no. 4, pp. 697–715, 2014.

[213] S. Hasanzadeh and F. Janabi-Sharifi, "Model-based force estimation for intracardiac catheters," *IEEE/ASME Transactions on Mechatronics*, vol. 21, no. 1, pp. 154–162, 2015.

[214] S. B. Kesner and R. D. Howe, "Position control of motion compensation cardiac catheters," *IEEE Transactions on Robotics*, vol. 27, no. 6, pp. 1045–1055, 2011.

[215] T. L. T. Lun, K. Wang, J. D. Ho, K.-H. Lee, K. Y. Sze, and K.-W. Kwok, "Real-time surface shape sensing for soft and flexible structures using fiber bragg gratings," *IEEE Robotics and Automation Letters*, vol. 4, no. 2, pp. 1454–1461, 2019.

[216] S. Sefati, F. Alambeigi, I. Iordachita, M. Armand, and R. J. Murphy, "Fbg-based large deflection shape sensing of a continuum manipulator: Manufacturing optimization," in *2016 IEEE SENSORS*, pp. 1–3, IEEE, 2016.

[217] B. Childlers, D. Gifford, R. Duncan, M. Raum, and M. Vercellino, "Fiber optic position and shape sensing device and method relating thereto," Jan. 19 2006. US Patent App. 11/180,389.

[218] C. Shi, S. Giannarou, S.-L. Lee, and G.-Z. Yang, "Simultaneous catheter and environment modeling for trans-catheter aortic valve implantation," in *2014 IEEE/RSJ International Conference on Intelligent Robots and Systems*, pp. 2024–2029, IEEE, 2014.

[219] S. Jäckle, T. Eixmann, H. Schulz-Hildebrandt, G. Hüttmann, and T. Pätz, "Fiber optical shape sensing of flexible instruments for endovascular navigation," *International journal of computer assisted radiology and surgery*, vol. 14, no. 12, pp. 2137–2145, 2019.

[220] C. L. Dumoulin, S. Souza, and R. Darrow, "Real-time position monitoring of invasive devices using magnetic resonance," *Magnetic resonance in medicine*, vol. 29, no. 3, pp. 411–415, 1993.

[221] Z. He, Z. Dong, G. Fang, J. D.-L. Ho, C.-L. Cheung, H.-C. Chang, C. C.-N. Chong, J. Y.-K. Chan, D. T. M. Chan, and K.-W. Kwok, "Design of a percutaneous

mri-guided needle robot with soft fluid-driven actuator," *IEEE Robotics and Automation Letters*, vol. 5, no. 2, pp. 2100–2107, 2020.

[222] M. B. Rubin, *Cosserat theories: shells, rods and points*, vol. 79. Springer Science & Business Media, 2013.

[223] M. Barkagan, M. Rottmann, E. Leshem, C. Shen, A. E. Buxton, and E. Anter, "Effect of baseline impedance on ablation lesion dimensions: A multimodality concept validation from physics to clinical experience," *Circulation: Arrhythmia and Electrophysiology*, vol. 11, no. 10, p. e006690, 2018.

[224] Y. Fan, K.-W. Kwok, Y. Zhang, G. S.-H. Cheung, A. K.-Y. Chan, and A. P.-W. Lee, "Three-dimensional printing for planning occlusion procedure for a double-lobed left atrial appendage," *Circulation: Cardiovascular Interventions*, vol. 9, no. 3, p. e003561, 2016.

[225] B. K. Foucha, "The abcs of a to v: Right atrial/ left atrial (pcw) pressures," *CathLab Digest*, vol. 17, no. 5, 2009.

[226] S. Nakatani, M. J. Garcia, M. S. Firstenberg, L. Rodriguez, R. A. Grimm, N. L. Greenberg, P. M. McCarthy, P. M. Vandervoort, and J. D. Thomas, "Noninvasive assessment of left atrial maximum dp/dt by a combination of transmitral and pulmonary venous flow," *Journal of the American College of Cardiology*, vol. 34, no. 3, pp. 795–801, 1999.

[227] C. G. Robinson, P. P. Samson, K. M. Moore, G. D. Hugo, N. Knutson, S. Mutic, S. M. Goddu, A. Lang, D. H. Cooper, M. Faddis, *et al.*, "Phase i/ii trial of electrophysiology-guided noninvasive cardiac radioablation for ventricular tachycardia," *Circulation*, vol. 139, no. 3, pp. 313–321, 2019.